

# Silicon-Based Low-Dimensional Nanomaterials and Nanodevices

Boon K. Teo<sup>\*,†</sup> and X. H. Sun<sup>‡,§</sup>

Department of Chemistry, University of Illinois at Chicago, Chicago, Illinois 60607, and Department of Chemistry, University of Western Ontario, London, Ontario, Canada

Received June 16, 2006

## Contents

1. Introduction	1455	7.1.1. FTIR Probe of Etching	1476
2. Silicon vs Carbon: Similarities and Differences	1457	7.1.2. Scanning Tunneling Microscopic Observations	1477
3. Silicon Nanowires vs Silicon Nanotubes: Why and Why Not?	1457	7.2. Etched SiNWs: Why H-Terminated?	1477
3.1. String-Bean-like Silicon Nanotube Structures	1458	7.3. Stabilities of SiNWs	1478
3.2. Gearlike Silicon Nanotube Structures	1458	7.4. Etching SiNWs with HF and NH <sub>4</sub> F	1478
3.3. Predictions on the Structures and Properties of Silicon Nanotubes	1460	7.5. Similarities and Differences in Etching Behavior between 1-D and 2-D Silicon	1479
3.4. Crystalline Silicon Nanotubes	1461	8. Silicon Nanowires as Platforms and Templates	1480
3.5. Theoretical Studies of SiCNT Structures	1461	8.1. AuAgND÷SiNW: Reductive Growth of Ligated Metal Nanodots on SiNWs	1480
3.6. Theoretical Studies of Silicon Nanotubes with Encapsulated Metals	1461	8.2. SiNW⊂CNT and SiNW⊂HCNT: Syntheses of Carbon and Hydrocarbon Nanostructures on SiNW (as Templates)	1482
4. Nanotechnologies: General Remarks	1462	8.2.1. CNT(O)s vs HCNT(O)s via Sonochemical Reactions Using SiNWs as Molds	1482
4.1. Five Steps to Nanodevices in the Bottom-Up Approach	1463	8.2.2. SiNW⊂HCNT and SiNW⊂CNT	1482
5. Categorization of Nanomaterials: Terms and Symbols	1463	8.2.3. Templating Effect and Formation Pathway(s)	1483
6. Synthesis of Silicon Nanowires and Silicon Nanodots	1465	8.3. CNT⊂SiCNT: Synthesis of SiCNTs using CNTs as Reactive Templates	1485
6.1. Oxide-Assisted Growth Technique	1465	8.4. Formation of Gold Nanocables on SiNWs: SiNW⊂AuNT	1486
6.1.1. Mechanism of Oxide-Assisted Growth: Theoretical Insights	1466	8.4.1. Formation of AuNW⊂SiO <sub>2</sub> NT: SiNWs as Sacrificial Templates	1486
6.2. Vapor–Liquid–Solid Method	1467	9. Silicon-Based Low-Dimensional Nanomaterials	1487
6.3. Growth Habits of Silicon Nanowires	1467	9.1. 0-D on 0-D	1487
6.3.1. Silicon Nanowires Prepared by Oxide Assisted Growth	1467	9.1.1. Silicon-Based Core–Shell Heterostructures	1487
6.3.2. Silicon Nanowires Prepared by VLS Growth	1468	9.1.2. Silica-Based Core–Shell Heterostructures	1488
6.4. Rational Growth Controls	1468	9.1.3. Core–Multishell Heterostructures	1488
6.4.1. Diameter Control	1468	9.2. 0-D on 1-D	1489
6.4.2. Orientation Control	1471	9.2.1. Nanodots on Nanowires: ND÷NW	1489
6.4.3. Position Control	1471	9.2.2. Nanodots in Nanowires: ND⊂NW	1490
6.4.4. Composition Control	1472	9.2.3. Nanodots on Nanotubes: ND÷NT	1492
6.5. Preparation of Crystalline Silicon Nanotubes via Various Templates	1474	9.2.4. Nanodots in Nanotubes: ND⊂NT	1492
6.5.1. SiO <sub>2</sub> NW⊂cSiNT: Crystalline Silicon Nanotubes Filled with Silica	1475	9.2.5. CNT and cSiNTs as Nano-Test-Tubes/Nanoreactors	1494
6.5.2. Using AAO as Templates	1476	9.2.6. CNTs and cSiNTs as Nanotemplates/Nanomolds	1494
6.5.3. “Template Replication” Technique	1476	9.3. 1-D on 1-D	1494
6.5.4. Using ZnS Nanowires as Templates	1476	9.3.1. Axial Heterostructures	1495
7. Surface Treatments: Etching of Silicon Nanowires	1476	9.3.2. Radial Heterostructures	1498
7.1. Surface Speciation of Etched SiNWs	1476	9.3.3. Biaxial, Triaxial, Tetraaxial, and Higher-Order Heterostructures	1502
		9.4. 0-D on 2-D	1503
		9.4.1. Solid Nanodots on Silicon Wafer	1503
		9.4.2. Hollow Nanospheres on Silicon Wafer	1503
		9.5. 1-D on 2-D	1504

\* To whom correspondence should be addressed. E-mail: boonkteo@uic.edu.

† University of Illinois.

‡ University of Western Ontario.

§ Present address: Center for Nanotechnology, NASA Ames Research Center, Moffett Field, California 94035. E-mail: xsun@arc.nasa.gov.

9.5.1. Nanowires Parallel to Silicon Wafer: NW <sub>  </sub> Si	1504
9.5.2. Nanowires Perpendicular to Silicon Wafer: NW <sub>⊥</sub> Si	1504
9.5.3. Nanotubes Parallel to Silicon Wafer: NT <sub>  </sub> Si	1506
9.5.4. Nanotubes Perpendicular to Silicon Wafer: NT <sub>⊥</sub> Si	1506
9.5.5. 1-D in 2-D: 1-D <sub>⊂</sub> 2-D	1506
9.6. 2-D on 2-D	1507
9.6.1. Quantum Wells	1507
10. Nanomachining, Nanomanipulating, and Nanoassembling Techniques	1508
10.1. Nanomachining Crystalline Silicon Nanowires into Nanodots and Nanorods	1508
10.2. Nanomanipulating Using Scanning Probe Microscopy and Lasers	1509
10.2.1. Nanomanipulating Using SPMs and SEM	1509
10.2.2. Nanomanipulating Using Lasers	1509
10.3. "Grown-in-Place" Approach	1509
10.4. Langmuir–Blodgett Technique	1510
10.5. Electrical Field Directed Assembly	1510
10.6. Microfluidics Assembly	1510
10.7. Other Techniques	1510
11. Quantum-Size Effects	1510
11.1. Photoluminescence	1512
11.1.1. 0-D on 0-D: SiND <sub>⊂</sub> SiO <sub>2</sub> ND	1512
11.1.2. 0-D in 1-D: Chainlike SiND <sub>⊂</sub> SiO <sub>2</sub> NW	1512
11.1.3. 1-D in 1-D: Ultrafine SiNW <sub>⊂</sub> SiO <sub>2</sub> NT	1513
11.1.4. Silicon Nanowires	1514
11.2. Band Gaps	1514
11.3. Theoretical Calculations	1514
12. Fabrication of Nanodevices	1515
12.1. Top-Down Approach	1516
12.2. Bottom-Up Approach	1516
12.3. Hybrid Approach	1517
12.4. Beyond Nanotechnologies	1517
12.5. Nanodevices	1517
12.5.1. Nanoelectronics	1517
12.5.2. Nanophotonics	1518
12.5.3. Nanosensors	1519
12.5.4. Nanospintronics	1521
12.5.5. Nanobiology and Nanomedicine	1522
13. Atomic- and Molecular-Scale Technologies	1523
13.1. Atomic- and Molecular-Scale Imprinting on Surfaces	1523
13.2. Single-Atom/Single-Molecule Chemistry: Reaction Dynamics and Spectroscopy	1524
14. Interconnection and Integration	1525
15. Conclusions and Future Prospects	1526
16. Acronyms	1526
17. Acknowledgments	1527
18. References	1527



Boon K. Teo received his B.Sc. (Hons, First Class) degree from the Chinese University of Hong Kong in 1969 and his Ph.D. degree from the University of Wisconsin (Madison) in 1973. He then worked at AT&T Bell Labs (Murray Hill, NJ) for a dozen years before joining the University of Illinois at Chicago in 1986 as a tenured professor. He is author or coauthor of hundreds of publications (including 20 reviews and book chapters), three books, and two patents. Professor Teo has a very broad research interest, including the synthesis, structure, bonding, and properties of supersized metal clusters, supramolecular chemistry, molecular and crystal engineering, molecular orbital and density function calculations, X-ray crystallography, synchrotron radiation research (EXAFS, XANES), nonlinear optical materials (optical limiters), and, more recently, nanomaterials (silicon nanowires and carbon nanotubes), and nanotechnology. One of his publications, *J. Am. Chem. Soc.* 1979, 101, 2815, was selected as one of the "all-time 125 most-cited JACS publications" in the 125th volume of the journal in 2003. He is also the cofounder and current coeditor of *J. Cluster Sci.* Professor Teo dedicates his free time to helping countless underprivileged students by building/donating primary schools in impoverished regions of the world, especially the Midwest of China.

top-down approach<sup>1,2</sup> and the bottom-up strategy.<sup>3</sup> The first steps in either approach are the synthesis and characterization of nanomaterials and the study of their chemical and physical properties. In fact, nanochemistry allows revolutionary changes of the fundamental properties of matter (often drastically different from those of the bulk phase), giving rise to novel materials and, hopefully, new applications.

Low-dimensional nanomaterials are of particular interest in that they may exhibit anisotropic and/or dimension-tunable properties, both of which are important attributes in nanodevice applications. Recently, two classes of one-dimensional (1-D) nanomaterials, carbon nanotubes (CNTs) and silicon nanowires (SiNWs), have attracted much attention because of their unique properties. Carbon nanotubes<sup>4–8</sup> are important low-dimensional nanomaterials because of their highly interesting properties, such as small diameter, high aspect ratio, high mechanical strength, high thermal and chemical stabilities, excellent heat conduction, and interesting electrical and electronic properties, etc.<sup>9–19</sup> In fact, carbon nanotubes can be either metallic or semiconducting, with the semiconducting band gap depending upon the tube diameter, geometry, and chirality. Since its discovery in 1991, CNTs have found its way into many industries. Flat panel color displays exploiting the field emission property of CNTs are just one example.<sup>20–24</sup>

SiNWs<sup>25–28</sup> are also important in nanotechnology because Si-based nanoelectronics is compatible with the Si-based microelectronics. SiNWs in the nanosize regime exhibit quantum confinement effects and are expected to play a key role as interconnection and functional components in future nanosized electronic and optical devices. It has been suggested that semiconductor wires finer than 100 nm in

## 1. Introduction

Nanotechnology is a culmination of many facets of scientific and technological developments in the nanorealm, including nanofabrication, nanomachineries, quantum devices, molecular machines, and molecular computers, etc. In principle there are two approaches to nanotechnology: the



Xuhui Sun received his B.Sc. and M.Sc. degrees from the Department of Chemistry, Tsinghua University, China, in 1993 and 1996, respectively, under the supervision of Prof. W. X. Pan. He received his Ph.D. degree from the City University of Hong Kong in 2002 under the directions of Professors N. B. Wong and S. T. Lee at City University of Hong Kong, Professor T. K. Sham at the University of Western Ontario, and Professor Boon K. Teo at the University of Illinois at Chicago. His Ph.D. thesis focuses on the synthesis, characterization, and surface chemistry of the semiconductor nanomaterials. After a postdoctoral fellowship with Prof. T. K. Sham at the University of Western Ontario where he did synthesis and electronic structure studies of low-dimensional metal and semiconductor nanomaterials, he joined the Center for Nanotechnology at NASA Ames Research Center in 2005 as a postdoctoral scholar in Dr. B. Yu's group, doing research on nanowire-based nanoelectronics for computing and information storage technologies. He also has broad research interests with regard to nanoscience and nanotechnology, including the synthesis, characterization, and applications of nanoscale materials (one-dimensional semiconductor nanomaterials in particular) and the development of synchrotron radiation techniques, etc.

diameter can be used to develop 1-D quantum-wire high-speed field effect transistors and light-emitting devices with extremely low power consumption.<sup>29</sup>

The contrast between carbon-based and silicon-based nanomaterials, in terms of their structures and properties, is deeply rooted in the attributes of the two elements and their disparate atomic properties. In other words, despite the fact carbon and silicon belong to the same group (group IV) in the Periodic Table, the two elements are very different in terms of their structural, chemical, and physical properties. For example, while CNTs are relatively easy to make, the corresponding silicon nanotubes (SiNTs), composed of rolled-up graphite-like sheets, are yet to be synthesized.

While SiNTs are difficult to make, many synthetic routes have been developed in recent years to obtain bulk quantities of SiNWs, using both gas-phase, condensed-phase and solution techniques.<sup>25–28</sup> A number of interesting properties such as the morphology, structure, photoluminescence, electron field emission, thermal and electronic conductivities, and surface chemical properties of SiNWs have also been reported.

Obviously the roles carbon-based and silicon-based nanomaterials will play in the future development of nanoscience and nanotechnology hinge upon their properties. Many excellent reviews and books are available in the literature regarding carbon-based nanomaterials and nanodevices.<sup>10,30–36</sup> This review, instead, focuses on silicon-based low-dimensional nanomaterials and nanodevices with special emphasis on building the materials base for a wide variety of nanostructures potentially useful in future nanotechnological applications. We shall begin with a brief discussion of the similarities and differences between silicon and carbon

in section 2, followed by theoretical considerations of silicon nanowires vs nanotubes in section 3. In section 4, a general discussion on the various approaches to nanotechnology is given. In particular, the bottom-up approach to nanotechnology is divided into five basic steps. The first is to tailor *make* nanomaterials of controlled dimensions and compositions (including doping) with desirable properties. The second is to etch (*clean*), prepare, or functionalize the surfaces, or fill the interior of the nanomaterials for specific applications. The third is to precision *cut* or machine the nanomaterials into individual components. The fourth step is to *assemble* various components or elements into nanodevices. And, finally, the last step is to link (*interconnect*) individual nanodevices together and *integrate* them into functional devices and connect them to the microworld, and eventually to the macroworld. Obviously the last two steps are critical to the future of bottom-up nanotechnology, yet they are the least developed to date. In this review, we shall focus our attention on the first three aspects. The fourth and the last aspects will only be discussed briefly.

A simple scheme, with special terms and symbols useful in categorizing various nanostructures, is introduced in section 5. We shall then discuss the synthesis (section 6) of SiNWs and silicon nanodots (SiNDs), with emphasis on the rational controls of diameter, orientation, position, and composition, etc. Section 7 deals with the surface treatments (etching) and the surface speciation of SiNWs. The use of low-dimensional silicon materials as platforms, templates, and molds in doing chemistry and in creating other composite nanomaterials will be described in section 8. With role reversal, utilizing other materials such as CNTs, zeolites, and anodized aluminum oxide (AAO) as templates, a wide variety of silicon-based nanomaterials can also be made. Section 9 provides a systematic discussion of the controlled syntheses of a wide variety of nanomaterials of different structural types. Section 10 describes several nanomachining and nanomanipulating techniques for nanomaterials. Quantum-size effects and properties such as photoluminescence are discussed in section 11. Though not the focus of this review, brief discussions on the fabrication of various nanostructural elements and the assembly of these individual components into fundamental nanodevice units are discussed in section 12. This is followed by atomic- and molecular-scale technologies in section 13. Finally the interconnection and integration of nanodevices and their interface with the microworld, and eventually to the macroworld, will be presented in section 14.

The pros and cons of the bottom-up and top-down approaches to nanotechnology are also discussed in section 12. It is widely held that the present top-down semiconductor technology has not exploited the physics and chemistry (e.g., quantum-size effects) of nanomaterials on the one hand and has not taken advantage of the development of bottom-up nanotechnology on the other. We shall discuss reasons for this viewpoint. While each approach has its advantages and disadvantages, it is our view that future development of nanotechnology will probably encompass both approaches with their relative contributions depending upon specific applications (e.g., performance enhancement, materials improvement, and functionalization, etc.). In fact, as we shall see in section 12.3, a “hybrid technology”, exploiting the advantageous attributes of both approaches, is on the horizon and, in some disciplines, being explored or already put to use.



## 2. Silicon vs Carbon: Similarities and Differences

Carbon and silicon are the two most important elements in the Periodic Table for obvious reasons. They occupy the central stage of the early rows of the Periodic Table by being the first and the second members of group IV (or group 14). It is ironic, however, that factors which make carbon unique in nature are also the factors that differentiate these two elements. We shall first describe six important factors (of relevance to the discussions in this review) that distinguish carbon from silicon, as well as the rest of the elements in the Periodic Table, followed by a discussion of the distinctions between silicon and carbon.

First, being a group IV member, carbon has four electrons and four valence orbitals. As such, it is capable of forming four two-center two-electron covalent bonds. Second, with carbon being more electronegative than hydrogen (Pauling's electronegativity,  $\chi = 2.55$  for C and 2.20 for H), the C–H bonds, unequivocally the most important bond in biology, are polarized as  $C^{\delta-}-H^{\delta+}$  with the partial negative charge residing on the carbon atom. Third, while C–H bonds are rather strong, carbon bonded to more electronegative atoms such as oxygen and halogens (except C–F bonds) are weaker and more reactive (note that C–H bonds have bond energies of 411 kJ/mol, whereas C–O and C–X bonds have bond energies of 357.7 and 485, 327.2, 285 kJ/mol, where X = F, Cl, and Br, respectively). Fourth, the small atomic size of carbon means efficient  $\pi-\pi$  overlap and the formation of stable double and triple bonds. The C–C, C=C, and C $\equiv$ C bond lengths are 1.54, 1.34, and 1.20 Å, with bond energies of 345.6, 602, and 835.1 kJ/mol, respectively. Fifth, the large energy difference between the valence s and p orbitals means a relatively large hybridization energy for carbon, which implies that carbon will “activate” one valence p orbital at a time (since hybridization causes energy), as required by the bonding situation, giving rise to sp, sp<sup>2</sup>, and sp<sup>3</sup> hybridizations, thereby forming triple, double, and single bonds, respectively. Sixth, since there are no energetically accessible d orbitals for carbon to expand its coordination (or valence shell), it makes the racemization of chiral carbon centers rather difficult.

Silicon differs from carbon, in terms of five of the six factors discussed above, as follows: (1) lower electronegativity; (2) kinetically more reactive; (3) larger atomic radius, and hence larger orbital size; (4) smaller energy difference between the s and the p orbitals, and hence lower hybridization energies; and (5) the availability of energetically low-lying d orbitals and the ability to expand its coordination sphere. These factors impact tremendously on the chemical and physical properties of silicon in comparison with that of carbon. They will be discussed briefly in this section and developed, albeit qualitatively, into bonding principles which can be used to rationalize many experimental observations described in latter sections. We shall now discuss each of these differences in detail.

The most important distinction between silicon and carbon is the difference in electronegativity ( $\chi$ ). In contrast to carbon, silicon ( $\chi = 1.90$ ) is less electronegative than hydrogen ( $\chi = 2.20$ ); hence, Si–H bonds are polarized in the opposite sense, as  $Si^{\delta+}-H^{\delta-}$ . This implies that nucleophilic attacks on silanes usually occur at the silicon centers. Second, Si–H bonds are significantly weaker than C–H bonds, as indicated by their respective bond energies (318 kJ/mol for Si–H vs 411 kJ/mol for C–H). Silanes are also much more reactive than the corresponding hydrocarbon analogues due to the

greater polarization caused by the larger disparity in the electronegativities of silicon vs its substituents. Indeed, the greatest bond polarization occurs when silicon is bonded to highly electronegative atoms such as oxygen and halogens (X), giving rise to kinetically labile Si–O and Si–X bonds, despite the fact that these latter bonds are very strong (with bond energies of 452 and 565, 381, and 310 kJ/mol for Si–O and Si–X bonds, where X = F, Cl, and Br, respectively). It is interesting to note the paradox that Si–O and Si–X bonds are thermodynamically stable on the one hand and kinetically reactive on the other, both due to the very same reason of large bond polarization (i.e., with high ionic characters). Third, the larger atomic size of silicon gives rise to longer Si–Si bonds of 2.35 Å and weaker Si–Si bonds with bond energy of 222 kJ/mol, in comparison to C–C bonds of 1.54 Å with bond energy of 345.6 kJ/mol. Furthermore, as a result of the poor  $\pi-\pi$  overlaps for silicon (smaller than those of carbon by roughly an order of magnitude), Si=Si bonds of 2.16 Å, with bond energy of 327 kJ/mol, are much weaker than C=C bonds of 1.34 Å with bond energy of 602 kJ/mol. As a result, Si=Si bonds are often nonplanar (folded and twisted). Fourth, the energy difference between the valence s and p orbitals for silicon is only half of the corresponding value for carbon (Si ( $E_{3p} - E_{3s} = 5.66$  eV) vs C ( $E_{2p} - E_{2s} = 10.60$  eV)). As a result, silicon tends to utilize all three of its valence p orbitals, resulting in sp<sup>3</sup> hybridization, in contrast to carbon which can “activate” one valence p orbital at a time to give sp, sp<sup>2</sup>, and sp<sup>3</sup> hybridizations. Finally, the energetically low-lying d or other virtual orbitals (such as the antibonding  $\sigma^*$  orbitals) allow silicon to expand its coordination sphere from four to five or six. While this attribute greatly enriches the chemistry of silicon, it is detrimental to biological systems which rely, among other things, on the stability of chiral centers. In other words, the expansion of coordination spheres, especially in the case of fluxional behavior in solution, can cause racemization of the chiral centers. This may be one of the reasons why nature chose carbon instead of silicon in building the biological world. The energetically accessible d,  $\pi^*$ , or  $\sigma^*$  orbitals of silicon also allow “back-bonding” to occur, with electron densities donated from the lone pair(s) of the bonded atom (substituent) back to the silicon virtual orbitals (thereby making them less basic) or the mixing of d,  $\pi$ , or  $\sigma$ -type orbitals. This bonding capability, which is not available to carbon, manifests itself in the reduced basicities of lone pairs of atoms (such as oxygen as in siloxanes and nitrogen as in silaxanes) attached to silicon. It is also one of the major causes of the nonplanar structures of silenes and disilenes (often folded and sometimes twisted, or both).

We should close this section by saying that it is the peculiar properties of silicon, and their seemingly paradoxical contrasts with carbon, that make silicon chemistry and materials most interesting and useful.

## 3. Silicon Nanowires vs Silicon Nanotubes: Why and Why Not?

Unlike carbon nanotubes, the analogous silicon nanotubes, based on rolled-up graphene-like sheets, are yet to be made, though several theoretical investigations suggesting their existence have appeared.<sup>37–43</sup> A closely related type of silicon nanostructure, described as crystalline silicon nanotubes, has recently been prepared.<sup>44–48</sup> However, these latter nanostructures, to be discussed later, are best considered as crystalline



silicon nanopipes or hollow crystalline silicon nanowires or nanorods.

On the basis of silicon's "inability" to adopt the  $sp^2$  coordination, Seifert et al.<sup>38</sup> argued that the existence of SiNTs is doubtful. Alternatively, these authors proposed that Si-based silicide and SiH nanotubes are theoretically stable and energetically viable, and could thus be considered as sources of SiNTs, particularly in view of the existence of many layered silicides. On the other hand, by applying density functional theory (DFT), Fagan et al.<sup>40</sup> investigated the similarities between silicon and carbon nanotubes. Their results showed that the electronic and structural properties of SiNTs are similar to those of CNTs; i.e., they may exhibit metallic or semiconductive behaviors, depending on the structure type (zigzag, armchair, or chiral) and the tube diameter. The strain energies of such structures have recently been described by Barnard and Russo.<sup>41</sup>

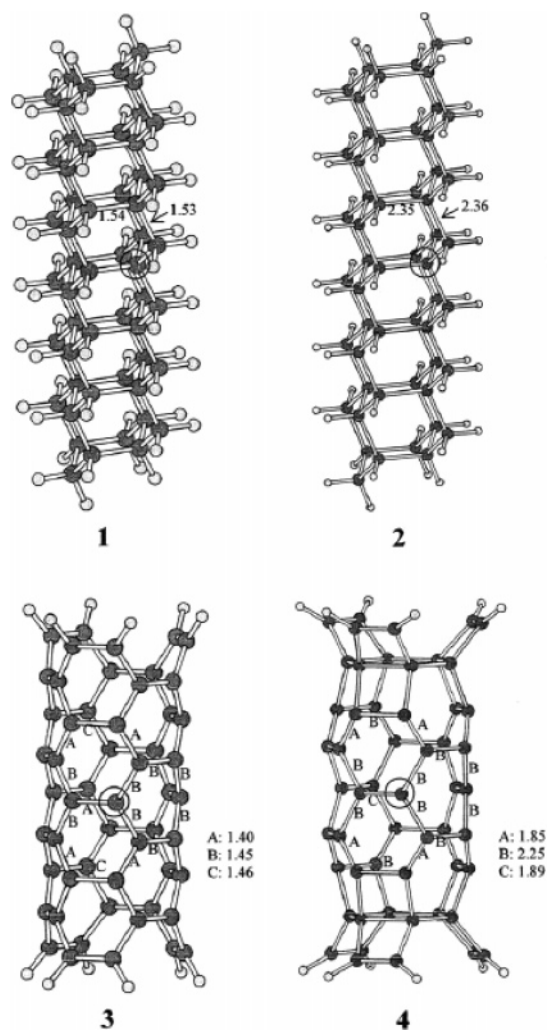
### 3.1. String-Bean-like Silicon Nanotube Structures

In a recent publication,<sup>42</sup> Zhang et al. compared the electronic structures of four systems: a diamond-structured carbon nanowire (CNW), a silicon nanowire (SiNW), a carbon nanotube (CNT), and a silicon nanotube (SiNT) in order to elucidate the differences in the structures and bonding between cubic (diamond-like) and tubular nanostructures of carbon and silicon with the hope of understanding the reason(s) for the hitherto unsuccessful synthesis of the silicon analogues of the CNTs.

Figure 1 shows the four model compounds studied in this work. They represent a diamond nanowire,  $C_{54}H_{60}$  (**1**), a silicon nanowire,  $Si_{54}H_{60}$  (**2**), a carbon nanotube,  $C_{54}H_{12}$  (**3**), and a silicon nanotube,  $Si_{54}H_{12}$  (**4**). The carbon nanotube selected here has an armchair (3,3) structure. It is one of the smallest carbon nanotubes reported recently.<sup>49–51</sup> Hydrogen atoms were added to saturate the dangling bonds. PM3 parametrization<sup>52</sup> of the MNDO semiempirical Hamiltonian<sup>53</sup> was used. The results were further confirmed by ab initio calculations.

For the geometrically optimized nanostructures **1–4**, there are general trends of bond length variations. As indicated in Figure 1, the C–C bonds in structure **1** are about 1.54 Å, as expected for single bonds. Similarly, the Si–Si bonds in structure **2** average about 2.35 Å expected for single bonds. In the CNT **3**, the C–C bond lengths alternate between 1.40 and 1.46 Å, indicating a relatively small degree of C=C vs C–C bond localization. In other words, the small bond length alternation of about 0.06 Å signifies that  $\pi$  delocalization is extensive in CNTs. SiNT such as **4** also shows similar bond length alternation (see Figure 1), but with a much larger variation of 0.40 Å. The shortest Si–Si bond length is only about 1.85 Å, while the longest is about 2.25 Å, showing a stronger tendency for bond localization (Si=Si vs Si–Si). As can be seen from Figure 1, CNT **3** has a smooth surface and a more-or-less uniform tube diameter. In contrast, SiNT **4** has a puckered (corrugated) structure which may be referred to as the "string-bean" distortion. It has a periodically varying diameter.

A detailed analysis of the total density of states revealed that tubular structures for silicon are, in general, less stable and tend to relax to the diamond-like structure with tetrahedral configuration, which allows for the largest extent of overlap of the  $sp^3$  hybridized orbitals. The results also suggest that SiNTs are less stable than the corresponding CNTs; the cause of which can be traced to the differences



**Figure 1.** Four cluster models for SiNTs and CNTs: a diamond nanowire  $C_{54}H_{60}$  (**1**), a SiNW  $Si_{54}H_{60}$  (**2**), a CNT  $C_{54}H_{12}$  (**3**), and a SiNT  $Si_{54}H_{12}$  (**4**). (Reprinted from ref 42, Copyright 2002, with permission from Elsevier.)



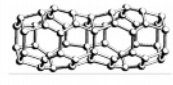

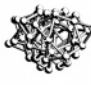
in the energetics and overlaps of the valence  $s$  and  $p$  orbitals of C vs Si discussed earlier. In particular, the poor  $\pi$ – $\pi$  overlap of silicon weakens the  $\pi$  delocalization and, under appropriate conditions, may lead to a puckered tubular structure as exemplified by the armchair structure **4**.

### 3.2. Gearlike Silicon Nanotube Structures

In a follow-up publication,<sup>43</sup> Zhang et al. explored the structural and energetic characteristics of different types (zigzag, armchair, and chiral) of SiNT structures by performing density-functional molecular dynamics simulations at various temperatures. A number of the findings were subsequently substantiated by ab initio Hartree–Fock (HF) or DFT calculations.

It was found that single-walled SiNTs can adopt a number of distorted tubular structures (see Table 1), representing respective local energy minima, depending on the theory used and the initial model adopted. In particular, "gearlike" structures containing alternating  $sp^3$ -like and  $sp^2$ -like silicon local configurations were found to be the dominant structural form for SiNTs via extensive density functional tight-binding molecular dynamics (DFTB–MD) simulations (followed by geometrical optimization using HF or DFT) at moderate temperatures (below 100 K). The gearlike structures of SiNTs

**Table 1. Degree of Distortion of Silicon Nanotubes as a Function of the Idealized Hybridizations of the Si–Si Bond, Producing Various Possible Structures (Reprinted with Permission from Ref 43. Copyright 2005 American Chemical Society.)**

Structure types	Smooth CNT-like tube	Gear-like puckering	String-bean- like distortion	Severe distortion	Collapsed tube
Degree of distortion	—————→				
Structural feature <sup>a</sup>					
Si-Si bond hybridization <sup>b</sup>	$sp^2$ - $sp^2$	$sp^2$ - $sp^3$	$sp^2$ - $sp^3$	$sp^3$ - $sp^3$	$sp^3$ - $sp^3$

deviate considerably from, and are energetically more stable than, the smooth-walled tubes (the silicon analogues of single-walled carbon nanotubes (SWCNTs)). The energetics and the structures of gearlike SiNTs are shown to depend primarily on the diameter of the tube, irrespective of the type (zigzag, armchair, or chiral). In contrast, the energy gap is very sensitive to both the diameter and the type of nanotube.

At 0 K, it was found that SiNTs deviate only slightly from the smooth-walled structures analogous to those of CNTs. However, as the temperature was raised to 10–30 K, considerable structural deformation could occur. Further annealing at higher temperatures eventually led to the collapse of many of the SiNTs. As a general rule, small-diameter zigzag ( $n, 0$ ) SiNTs (for  $n < 6$ ) easily collapse in the temperature range of 10–30 K, while SiNTs with larger diameters can withstand higher temperatures in the annealing process.

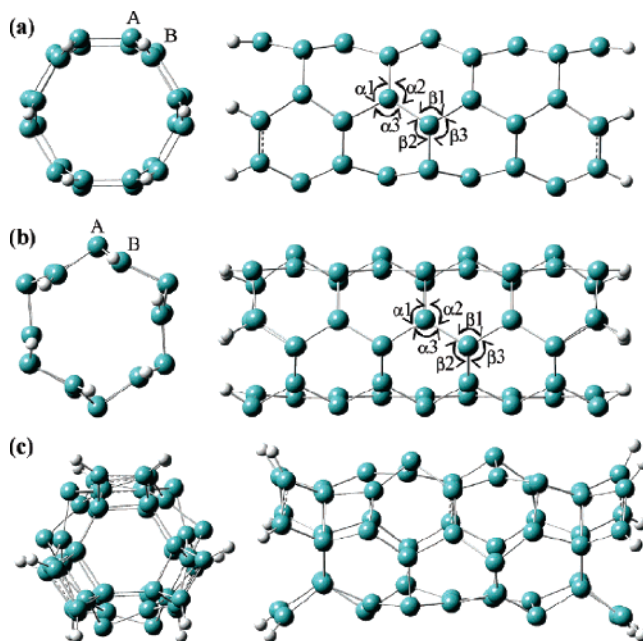
It was shown that the annealed SiNTs contain two alternating silicon sites “A” and “B.” Site A is close to tetrahedral, while site B is more-or-less trigonal planar, as indicated by the sums of bond angles,  $\Sigma\alpha$  and  $\Sigma\beta$ .  $\Sigma\alpha$  and  $\Sigma\beta$  designate the sums of the three angles around site A and site B silicon atoms (see Figure 2), respectively. Figure 3 shows the variation of  $\Sigma\alpha$  and  $\Sigma\beta$  as functions of the tube diameter. A sum close to the ideal value of  $3 \times 109.47^\circ = 328.4^\circ$  is taken here as an indication of a tetrahedral structure (with  $sp^3$ -like hybridization), whereas a sum close to the ideal value of  $3 \times 120^\circ = 360^\circ$  is indicative of a trigonal planar structure (with  $sp^2$ -like hybridization). It can be seen from Figure 3 that  $\Sigma\alpha$  and  $\Sigma\beta$  are generally independent of the type or chirality of the SiNTs. They are, however, highly dependent on the diameter of the tube.

Figure 4 shows the variation of cohesive energies of the relaxed gearlike SiNTs as a function of the diameter of the tube. It can be seen that the cohesive energy varies linearly with the inverse of the tube diameter, regardless of the type (zigzag, armchair, or chiral) of SiNT. The cohesive energy approaches asymptotically a value of about 4.77 eV per silicon atom as the diameter increases. A similar relationship between cohesive energy and tube diameter was also observed for CNTs.<sup>40</sup>

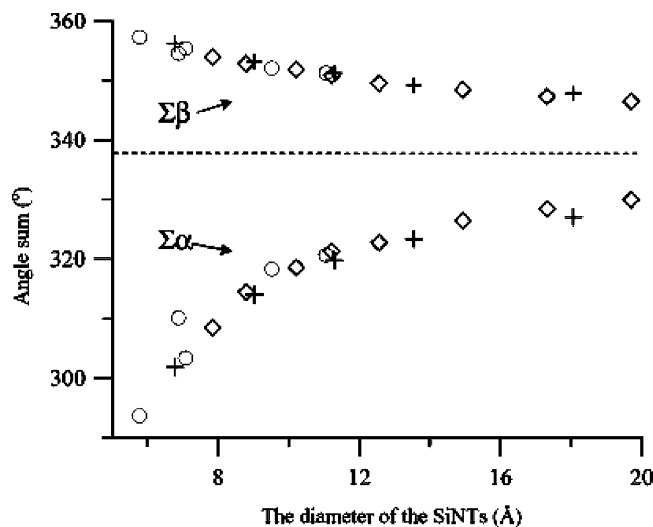
In sharp contrast, the calculated energy gaps (see Figure 5) seem to depend very much on the type or chirality of the

tube. They are all semiconductors with small band gaps (<1 eV), leveling off to fractions of an electronvolt at large diameters. Only those of the armchair ( $n,n$ ) SiNTs show a linear relation to the inverse of the diameter of the tube. For the purpose of comparison, SWCNTs can either be metallic or semiconducting. All armchair SWCNTs are metals; those with  $n - m = 3k$ , where  $k$  is a nonzero integer, are semiconductors with a small band gap; and all others are semiconductors with a band gap which is inversely proportional to the nanotube diameter.<sup>15,54</sup> With the limited set of zigzag SiNTs calculated, the  $n - m = 3k$  anomaly also seems to occur; i.e., the band gaps of zigzag ( $n,0$ ) SiNTs where  $n = 3k$  are abnormally small (cf. Figure 5).

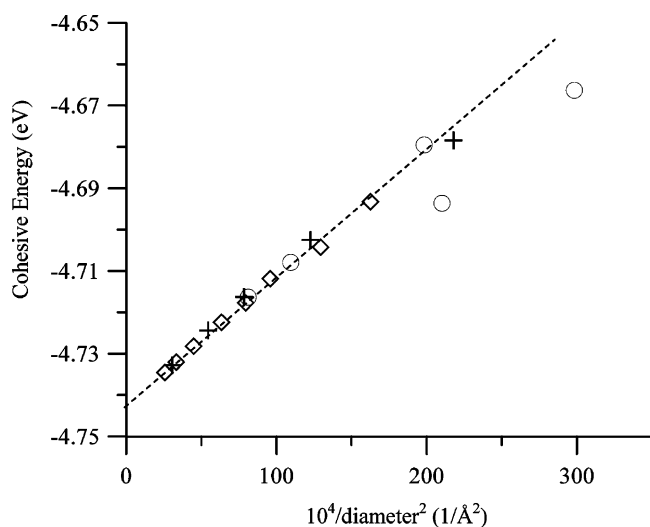
Table 1 shows schematically the structural features and the extents of distortion of the various possible structures of



**Figure 2.** Optimization of armchair (3,3) SiNT structures via ab initio calculations starting with (a) a smooth tube analogous to CNT, (b) gearlike configuration obtained by MD calculations, and (c) string-bean-like puckered configuration from PM3 calculations. (Reprinted with permission from ref 43. Copyright 2005 American Chemical Society.)

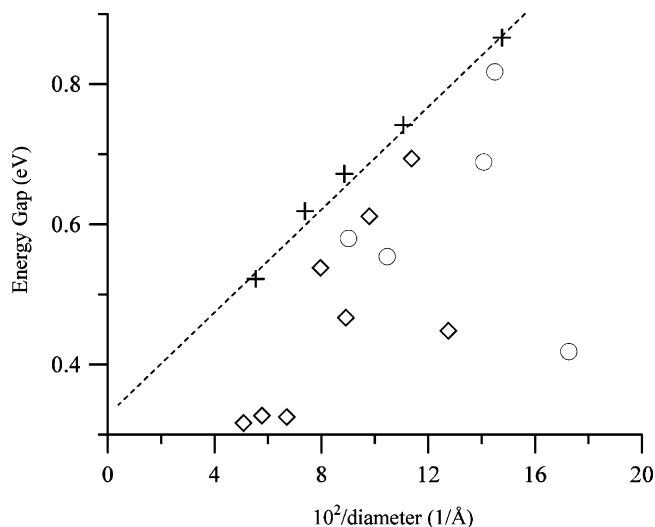


**Figure 3.** Sums of bond angles  $\Sigma\alpha$  ( $=\alpha_1 + \alpha_2 + \alpha_3$ ) and  $\Sigma\beta$  ( $=\beta_1 + \beta_2 + \beta_3$ ) vs the diameter of the SiNTs. The data points are “ $\diamond$ ” for zigzag ( $n,0$ ), “+” for armchair ( $n,n$ ), and “ $\circ$ ” for chiral ( $n,m$ ) SiNTs. (Reprinted with permission from ref 43. Copyright 2005 American Chemical Society.)



**Figure 4.** Cohesive energy vs  $10^4/\text{diameter}^2$  for the SiNTs. The data points are “ $\diamond$ ” for zigzag ( $n,0$ ), “+” for armchair ( $n,n$ ), and “ $\circ$ ” for chiral ( $n,m$ ) SiNTs. (Reprinted with permission from ref 43. Copyright 2005 American Chemical Society.)

SiNTs. The CNT-like structure is that of a smooth tubular shape and represents a local energy minimum for a given type of silicon nanotube. It contains mostly  $sp^2$ – $sp^2$  Si–Si bonding. The gearlike structure is that of a deformed tubular shape and represents an energetically more favorable local minimum. The wavelike deformation of the circumference of the cross-section gives rise to the gearlike shape. It is of good structural order containing mostly  $sp^2$ – $sp^3$  Si–Si bonding. The string-bean-like structure involves more distortion. The puckering is along the tube axis, containing mostly  $sp^2$ – $sp^3$  Si–Si bonding. Progressively more severe distortion results in the disruption of the tubular structure, though it may be energetically more favorable because of the increased number of  $sp^3$ – $sp^3$  Si–Si bonding. Final total collapse of the tube might occur when the distortion becomes so severe that the structure no longer looks like a tube but rather resembles that of amorphous  $sp^3$  silicon.



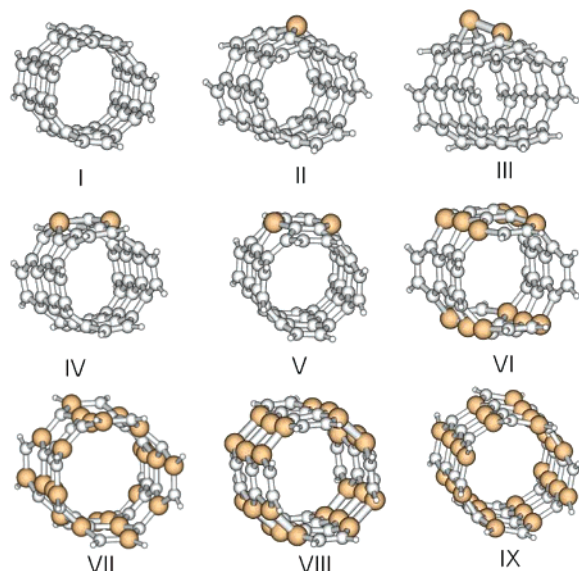
**Figure 5.** Energy gap vs  $10^2/\text{diameter}$  for the SiNTs. The data points are “ $\diamond$ ” for zigzag ( $n,0$ ), “+” for armchair ( $n,n$ ), and “ $\circ$ ” for chiral ( $n,m$ ) SiNTs. (Reprinted with permission from ref 43. Copyright 2005 American Chemical Society.)

### 3.3. Predictions on the Structures and Properties of Silicon Nanotubes

While the calculated structures of SiNTs may be sensitive to the method used, several predictions can be made. First, the weak  $\pi$ – $\pi$  overlap in Si=Si bonds, even in more-or-less planar structures, generally implies relatively weak silicon double bonds. Consequently, silenes and disilenes are usually synthesized with (and stabilized by) bulky ligands. They are often nonplanar, folded, and/or twisted to a varying degree. These attributes, carried over to SiNTs, would mean severe *structural distortion* and *thermodynamic instability*. Second, though the mode of distortions may take on a variety of forms, and vary from system to system, it will most likely involve a combination, or more appropriately, a compromise, between  $sp^3$ -like and  $sp^2$ -like local silicon configurations. Third, since the sum of the energies of two single Si–Si bonds is greater than that of a double Si=Si bond, there is a tendency for two Si=Si bonds to couple ( $[2 + 2]$  coupling), giving rise to four single bonds. This property will probably carry over to the SiNTs. In this context, the tendency of SiNTs to distort, and eventually collapse at high enough temperatures, may also be traced to the formation of Si–Si bonds in place of the Si=Si bonds. Obviously this tendency to convert  $sp^2$  to  $sp^3$ -hybridized silicon via  $[2 + 2]$  coupling becomes more pronounced between layers of silicon in multiwalled SiNTs. Finally, SiNTs, like molecular silicon compounds, will probably be more reactive than their CNT analogues in the sense that they are *kinetically labile*. Generally speaking, this kinetic lability is caused by the many reaction pathways with low activation energies available to silicon (in contrast to carbon) as a result of the smaller energy gap between HOMO and LUMO (as well as the energy difference between these frontier MOs and the Fermi level) and the availability and energetic accessibility of virtual d orbitals in the case of silicon.

It is well-known that disilenes have  $\pi \rightarrow \pi^*$  transitions with approximately half the energy of that of the carbon analogues. Because of this relatively small HOMO–LUMO gap (ca. 3 eV), disilenes oxidize at less positive potentials and reduce at less negative potentials than the corresponding alkenes. Also, disilenes are both better Lewis  $\pi$  bases and





**Figure 6.** DFT optimized geometries of finite-sized, single-walled silicon-carbon nanotubes (SiCNT) with various Si/C ratios (see text). (Reprinted with permission from ref 55. Copyright 2003 American Chemical Society.)

better Lewis  $\pi$  acids than the corresponding alkenes. We expect SiNTs to inherit most, if not all, of these attributes. For example, we expect SiNTs to exhibit interesting optical properties (due to the participation of energetically low-lying virtual d orbitals) and lower energy transitions (in comparison to the corresponding CNTs). They should also be easier to both oxidize and reduce and should behave as better  $\pi$  donors and better  $\pi$  acceptors, than their carbon analogues.

### 3.4. Crystalline Silicon Nanotubes

Though attempts to make bona fide CNT-like SiNTs have thus far been unsuccessful, the closely related tubelike silicon nanostructure, known as crystalline silicon nanotubes (cSiNTs) had been synthesized by several groups. This silicon nanostructure, however, is best described as crystalline silicon pipes or hollow crystalline silicon nanorods and will be discussed in section 6.5.<sup>44–48</sup>

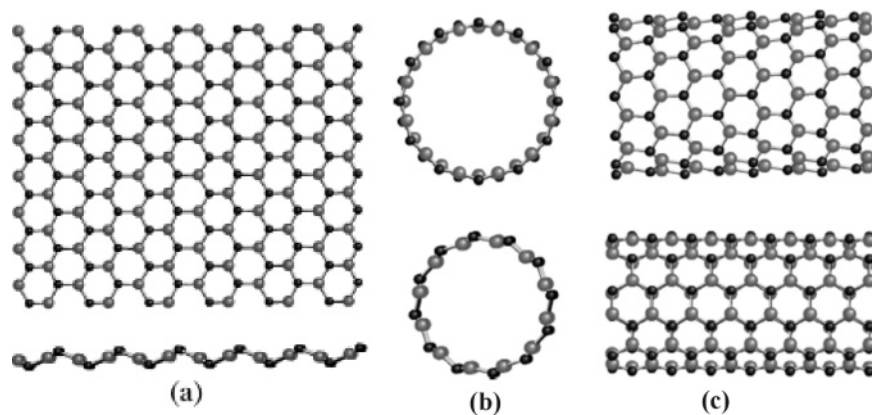
### 3.5. Theoretical Studies of SiCNT Structures

Despite the unsuccessful attempts to make bona fide SiNTs by many research groups, CNT-like silicon carbide nanotubes

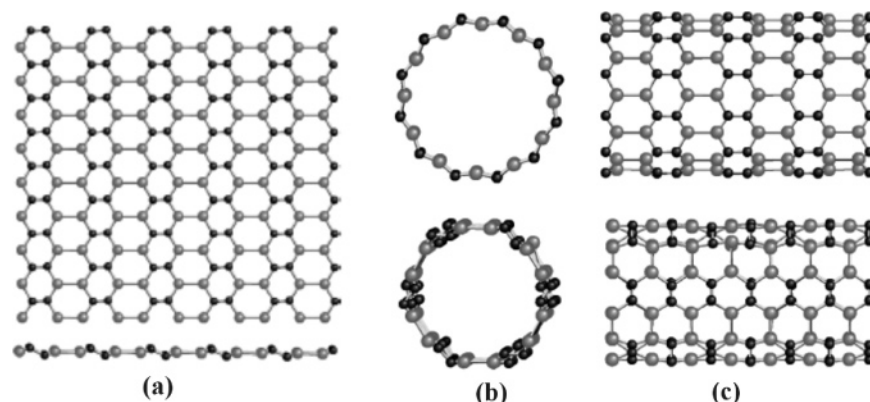
(SiCNTs) have been successfully synthesized and characterized. This topic will be discussed in section 8.3. Here we wish to discuss briefly two theoretical studies of SiCNTs. In one study, ab initio methods were used by Froudakis and co-workers<sup>55</sup> to study SiCNTs with different Si:C ratios, ranging from C-rich to Si-rich (Figure 6). It was found that SiCNTs gradually lose stability as the Si:C ratio increases. Nevertheless they remain stable until the ratio of 1:1; after which the Si-rich tubes collapse to nanowires or clusters with solid interiors. In another study,<sup>56</sup> the generalized tight-binding molecular-dynamics (GTBMD) scheme of Menon and Subbaswamy and ab initio methods were used to investigate structural and electronic properties of SiCNTs with Si:C ratios of 1:1. Two types of rolled-up graphene-sheet structures of SiCNTs were studied: type 1 involves alternate Si and C sites (Figure 7), whereas type 2 contains pairs of Si=Si and C=C bonds (Figure 8). Surface reconstruction, after relaxation, results in wavelike appearance for both structures, with the Si atoms situated in one plane and the C atoms located above and below the Si plane. However, the wavelike distortion is more severe for type 1 structures. It was found that type 1 structures are more stable than type 2 structures by 0.43 eV per SiC pair. These theoretical predictions are consistent with the experimental results (to be discussed later).

### 3.6. Theoretical Studies of Silicon Nanotubes with Encapsulated Metals

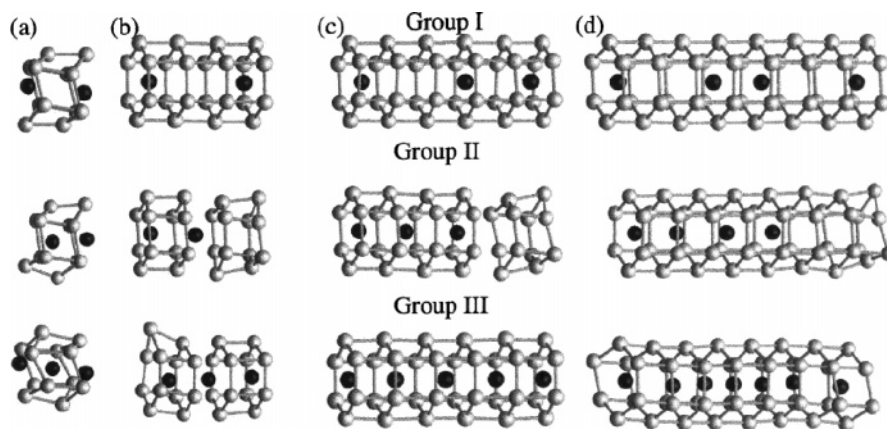
It is known that layered silicon systems exist in some silicides. For instance, in alkaline-earth metal silicides,<sup>57</sup> the silicon layers, formed by cyclohexane-like rings, are separated by metal ions. It is conceivable that the layered structure of silicon in these systems may be rolled up to form tubular structures analogous to the gearlike configurations described earlier. Indeed, using first-principle density functional calculations, Singh et al.<sup>58,59</sup> showed that hexagonal metallic silicon nanotubes can be stabilized by doping with Be or 3d transition metal atoms (Figure 9 and Figure 10). The resulting nanostructures are more stable than those formed from elemental silicon. Their electrical, magnetic, and optical properties can be modified by changing the metal atoms. Finite nanotubes doped with Fe and Mn have high local magnetic moments, whereas Co-doped nanotubes have low values and Ni-doped nanotubes are mostly nonmagnetic. The infinite  $\text{Si}_{24}\text{Fe}_4$  nanotube (Figure 11) is found to be ferro-



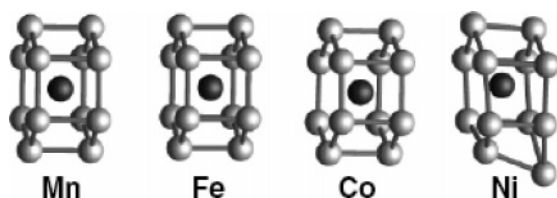
**Figure 7.** (a) Type-1 graphene sheets of SiC with a Si to C ratio of 1:1 obtained by GTBMD relaxation. The surface reconstruction results in wavelike appearance. The top and bottom panels in each of these figures show top and side views of the structures, respectively. In both structures Si atoms (colored gray) are all in a single plane, while C atoms (colored black) are displaced above and below this plane. (b) End views of single-wall SiC nanotubes of zigzag (top panel) and armchair (bottom panel) configurations. (c) Corresponding side views. (Reprinted with permission from ref 56 (<http://link.aps.org/abstract/PRB/v69/p115322>). Copyright 2004 by the American Physical Society.)



**Figure 8.** (a) Type-2 graphene sheets of SiC with a Si to C ratio of 1:1 obtained by GTBMD relaxation. (See caption for Figure 7a for color designations). (b) End views of single-wall SiC nanotubes of zigzag (top panel) and armchair (bottom panel) configurations. (c) Corresponding side views. (Reprinted with permission from ref 56 (<http://link.aps.org/abstract/PRB/v69/p115322>). Copyright 2004 by the American Physical Society.)



**Figure 9.** Finite Be-doped Si nanostructures: (a)  $\text{Si}_{12}\text{Be}_x$  ( $x = 2$  and  $3$ ), (b)  $\text{Si}_{24}\text{Be}_x$  ( $x = 2$  and  $3$ ), (c)  $\text{Si}_{36}\text{Be}_x$  ( $x = 3$  and  $5$ ), and (d)  $\text{Si}_{48}\text{Be}_x$  ( $x = 4$  and  $7$ ). Groups I and II represent structures with the same number of Si and Be atoms but different distributions of Be atoms, while the structures in group III have higher concentrations of Be atoms. (Reprinted with permission from ref 58. Copyright 2002 American Chemical Society.)



**Figure 10.** Lowest energy structures of the finite nanotubes with stoichiometry  $\text{Si}_{12}\text{M}$  ( $M = \text{Mn}, \text{Fe}, \text{Co},$  and  $\text{Ni}$ ). (Reprinted with permission from ref 59 (<http://link.aps.org/abstract/PRL/v91/p146802>). Copyright 2003 by the American Physical Society.)

magnetic with nearly the same local magnetic moment on each Fe atom as in bulk iron. Mn-doped nanotubes are antiferromagnetic, but a ferromagnetic state lies only 0.03 eV higher in energy with a gap in the majority spin bands near the Fermi energy.

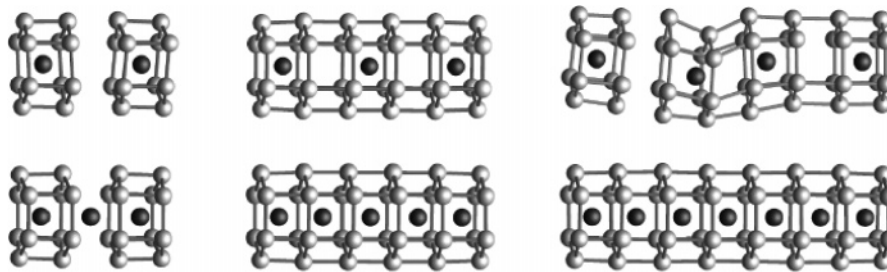
#### 4. Nanotechnologies: General Remarks

Nanotechnology is a revolution, not evolution, in science and technology. It distinguishes itself from all previous scientific and industrial revolutions in three major aspects. In fact, for the first time in human history, man can (1) change the fundamental properties (such as band gaps and luminescence) of matter as well as tailor make materials with desirable attributes; (2) observe and manipulate nanoscale objects (such as atoms and molecules); and (3) fabricate and

build single-nanowire/-nanotube single-electron/-photon nanodevices. The first characteristic is due to the so-called quantum-size effects whereby the properties of a material change with its size in the nanometer regime. The second is made possible by the invention of high-resolution transmission electron microscopy (TEM) and scanning probe microscopy (SPM, including scanning tunneling microscopy (STM) and atomic force microscopy (AFM)). The third is the result of the developments of various nanofabrication techniques (such as nanoimprint lithography using electron beams or X-rays) as well as due to a physical phenomenon known as “quantum confinement” in the nanorealm. There is no doubt that the nanorevolution will impact every aspect of human activities, not just in science and technology.

There are, in principle, two approaches to nanotechnology: the bottom-up strategy and the top-down approach. The bottom-up strategy attempts to build nanodevices from atomic or molecular components. The top-down approach seeks to fabricate nanodevices on silicon (or other semiconductors) chips directly using electron beam, “extreme ultraviolet,” or X-ray lithography.

The pros and cons of the bottom-up and top-down approaches to nanotechnology are matters of hot debate in the literature. It is widely held that the present top-down semiconductor technology has not exploited the physics and chemistry (e.g., quantum-size effects) of nanomaterials on the one hand and not taking advantage of the development



**Figure 11.** Structures of Fe-doped finite silicon nanotubes with stoichiometries  $\text{Si}_{24}\text{Fe}_2$ ,  $\text{Si}_{36}\text{Fe}_3$ ,  $\text{Si}_{48}\text{Fe}_4$ ,  $\text{Si}_{24}\text{Fe}_3$ ,  $\text{Si}_{36}\text{Fe}_5$ , and  $\text{Si}_{48}\text{Fe}_7$ . (Reprinted with permission from ref 59 (<http://link.aps.org/abstract/PRL/v91/p146802>). Copyright 2003 by the American Physical Society.)

of bottom-up nanotechnology on the other. Many reasons come to mind. First, nanomaterials and their properties in the nanorealm, especially at the interface, are not well-understood and/or still under investigation. Second, the fabrication techniques, both at the materials level and at the device stage, are not well-defined or fully developed. Third, connection to the macroworld remains a real problem. Finally, even if all these problems can be overcome, they are at present not mass producible and/or cost competitive enough to challenge the existing semiconductor technology. For a stand-alone bottom-up nanodevice to challenge the top-down nanodevice, it must overcome these hurdles and/or integrate into it.

While each approach has its advantages and disadvantages, it is our view that future development of nanotechnology will encompass both approaches with their relative contributions depending upon specific applications (and taking into account performance enhancement, materials improvement, and functionalization, etc.). In other words, application-specific nanodevices can be fabricated using a combination of the two approaches. For example, nanodevices could be made via the bottom-up strategy and assembled in situ (or “grown in place”) on a nanochip fabricated via the top-down lithographical techniques and interfaced to the macroworld. This *hybrid* nanotechnology allows the exploitation of the advantageous attributes of both approaches.

#### 4.1. Five Steps to Nanodevices in the Bottom-Up Approach

Similar to microelectronics, there are basically five steps in the bottom-up approach to nanotechnology. The first is to tailor *make* nanomaterials of desirable properties. The second is to etch (*clean*), prepare, or functionalize the surface for a particular application. The third is to precision *cut* or machine the nanomaterials into individual components. The fourth step is to *assemble* various components or elements into nanodevices. And finally, the last step is to link (*interconnect and integrate*) individual nanodevices together to form functional devices and connect to the microworld and eventually to the macroworld. We shall discuss each of these five steps in the following sections, with special emphasis on the first three.

### 5. Categorization of Nanomaterials: Terms and Symbols

In this review, we make use of a simple scheme, with special terms and symbols, to categorize the various types of low-dimensional nanomaterials. In fact, this scheme allows a systematization of the structural types of nanomaterials in general. Suffixes (following chemical symbols) such as ND, NC, and NS represent nanodots, nanocrystals, and nanoshells,

respectively, in 0-D whereas suffixes such as NW and NT designate nanowires and nanotubes, respectively, in 1-D. For example, SiND stands for silicon nanodot and AuNS represents gold nanoshell. Likewise, SiNW stands for silicon nanowire and CNT represents carbon nanotube. Single-walled and multiwalled nanotubes or nanooxions are designated by prefixes SW and MW, respectively. For example, SWCNT designates single-walled carbon nanotube while MWCNO means multiwalled carbon nanooxion.

Two-dimensional (2-D) materials are represented by chemical symbols without suffixes, but may be followed by the crystal orientation in parentheses. As an example, Si(111) signifies silicon (111) surface. Prefixes such as *a* and *c* may be used to indicate amorphous and crystalline materials, as exemplified by *a*-Si and *c*-Si respectively. Finally, intrinsic, p-, and n-type silicones are represented by i-Si, p-Si, and n-Si, respectively.

We may classify low-dimensional nanomaterials into six broad categories: namely, 0-D on 0-D, 0-D on 1-D, 1-D on 1-D, 0-D on 2-D, 1-D on 2-D, and 2-D on 2-D. Table 2 lists representative examples of nanomaterials discussed in Section 9, categorized in terms of their structures as denoted by these terms and symbols.

A number of symbols are employed in Table 2 to represent the composite nanomaterials. The symbol @ is used to represent inclusion of nanodots (ND) in nanoshells (NS), as designated by ND@NS, or nanocrystals (NC) in nanoshells (NS), as designated by NC@NS. For example, AuND@SiO<sub>2</sub>-NS indicates a core-shell structure of a gold nanodot encaged in a silica nanoshell.

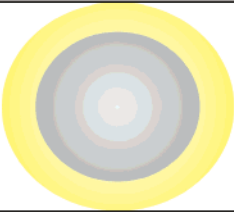


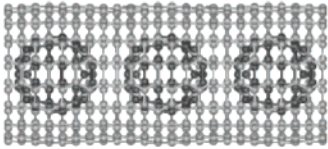
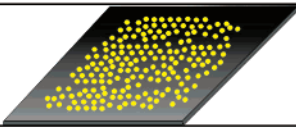

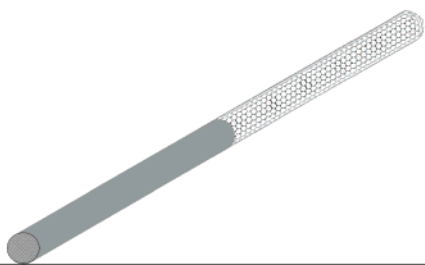

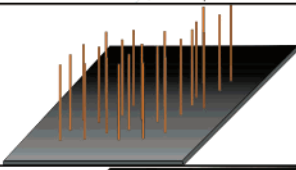

The symbol “÷” is used to designate the deposition of nanodots or nanoshells on the *outside* surfaces of nanowires or nanotubes. The former is exemplified by AuND÷SiNW, which indicates deposition of gold nanodots on a silicon nanowire surface. By the same token, the symbol “-” denotes 0-D nanodots deposited on a 2-D film or surface, as exemplified by NiND-Si(111), signifying the deposition of nickel nanodots on a Si(111) surface.

The symbol “C” is used to indicate “inclusion” 0-D in 1-D” composite nanomaterials. For example, ND<sub>C</sub>NW represents the dispersion of nanodots within a nanowire. One interesting example is the necklacelike silicon nanowire structure which constitutes crystalline Si nanodots (beads) immersed in an amorphous silica nanowire, designated as SiND<sub>C</sub>a-SiO<sub>2</sub>NW. Similarly, ND<sub>C</sub>NT may be used to signify the filling of a nanotube with nanodots. One example is SiND<sub>C</sub>CNT, which indicates filling of a carbon nanotube with silicon nanodots.

As we shall see in section 9, three classes of “1-D on 1-D” composite nanomaterials can be identified. The symbol ⊂ between two 1-D nanomaterials represents a “radial” heterostructure with one 1-D nanomaterial enwrapped in



Table 2. Terms and Symbols of Nanomaterials Classified in Terms of the Structures

	Symbols	Schematic	Examples
0D in 0D	@		AuND@SiO <sub>2</sub> NS
0D on 1D	÷		AuND÷SiNW
0D in 1D	⊂		SiND⊂ a-SiO <sub>2</sub> NW
	⊂		C <sub>60</sub> ⊂CNT
0D on 2D	⋅		AuND⋅Si
1D on 1D (radial heterostructure)	⊂		SiNW⊂CNT
1D on 1D (axial heterostructure)	-		SiNW-CNT
1D on 1D (Biaxial heterostructure)			SiNW SiO <sub>2</sub> NW
1D on 2D (perpendicular)	⊥		SiNW⊥Si
1D on 2D (parallel)			CNT  Si

another. For example, SiNW $\subset$ CNT indicates a SiNW enwrapped in a CNT. The corresponding “axial” heterostructure is represented by a “–” between two 1-D nanomaterials, as exemplified by SiNW–CNT which indicates the head-to-tail union of a SiNW and a CNT. And finally, biaxial nanowires are designated by the symbol “|” as illustrated in SiNW|ZnSNW, which represents side-by-side growth of Si and ZnS nanowires.

The “1-D on 2-D” composite nanomaterials are represented by “|” or “ $\perp$ ”, depending upon whether the 1-D nanomaterial is parallel or perpendicular to the 2-D surface. Examples are as follows: carbon nanotubes grown parallel to the silicon surface, CNT||Si, and silicon nanowires grown perpendicular to the silicon surface, SiNW $\perp$ Si.

Of course these simple symbols do not necessarily convey all the structural details of nanomaterials. For example, SiND $\subset$ CNT indicates neither the degree of filling of the CNT with the SiNDs, nor the crystallinity of the SiNDs, nor the layer structure of the CNT. Nevertheless, such information can easily be added if needed (e.g., cSiND-(0.15) $\subset$ SWCNT may be used to indicate a 15% filling of a single-walled carbon nanotube with crystalline silicon nanodots).

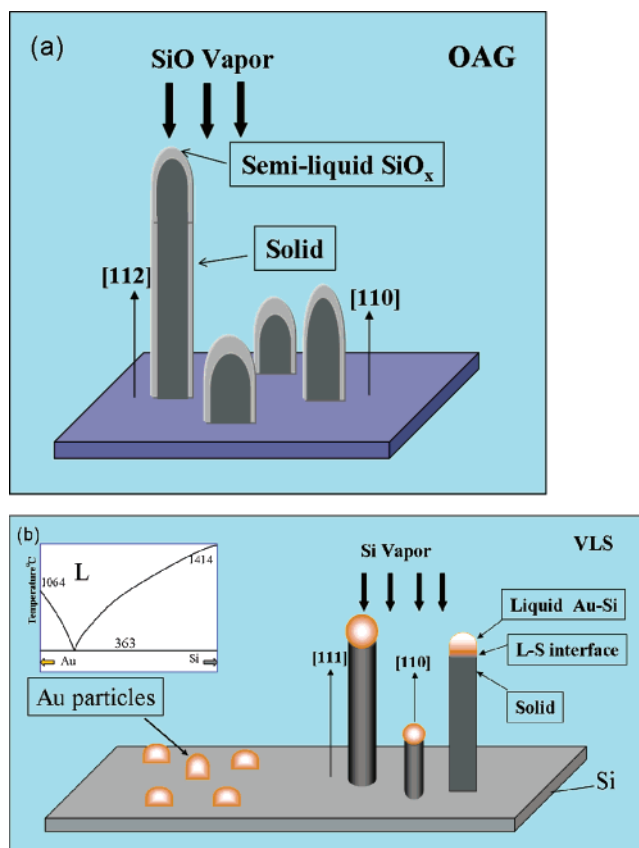
We shall make use of these symbols throughout this review.

## 6. Synthesis of Silicon Nanowires and Silicon Nanodots

Many bottom-up synthetic strategies have been developed to produce bulk quantities of SiNWs and SiNDs. They can be categorized into vapor-phase growth and solution-based syntheses. For the synthesis of 0-D SiNDs, readers are referred to an excellent review by Masala and Seshadri.<sup>60</sup>

For the synthesis of 1-D SiNWs, it is necessary to restrict the growth of silicon along one direction. A widely used technique is the so-called vapor–liquid–solid (VLS) growth.<sup>61</sup> Here a solid–liquid interface is introduced via a metal nanoparticle, serving as a catalyst, to limit the growth of silicon to occur only at the solid–liquid interface and hence promoting the growth in one dimension (i.e., the nanowire growth direction). Silicon from a gaseous source is “dissolved” in the liquid phase of the metal catalyst, in the form of a composite nanoparticle, forming a eutectic mixture. Oversaturated silicon subsequently crystallizes at the liquid–solid interface, promoting the one-dimensional growth in a continuous manner. Since this method involves three phases, the vapor phase of the silicon source, the liquid phase of the eutectic mixture droplet, and the solid phase of the nanowire, it is commonly referred to as the vapor–liquid–solid (VLS) growth. This method has been widely used to grow SiNWs.<sup>25,62</sup> The diameter of the resulting SiNWs can be controlled by the size of the metal catalyst. A variant of the VLS technique is the solution–liquid–solid (SLS) process, wherein the gaseous source is replaced by a solution source.<sup>27,63,64</sup>

Another commonly used technique is the oxide-assisted growth (OAG) via thermal evaporation of silicon suboxide or silicon powders mixed with silicon oxide.<sup>65–71</sup> In the OAG method, oxides, instead of metals, play an important role in inducing the nucleation and growth of nanowires. The major advantage of this technique is that no metal catalysts are needed; the latter can lead to the contamination, affecting the performance of nanowires in devices.

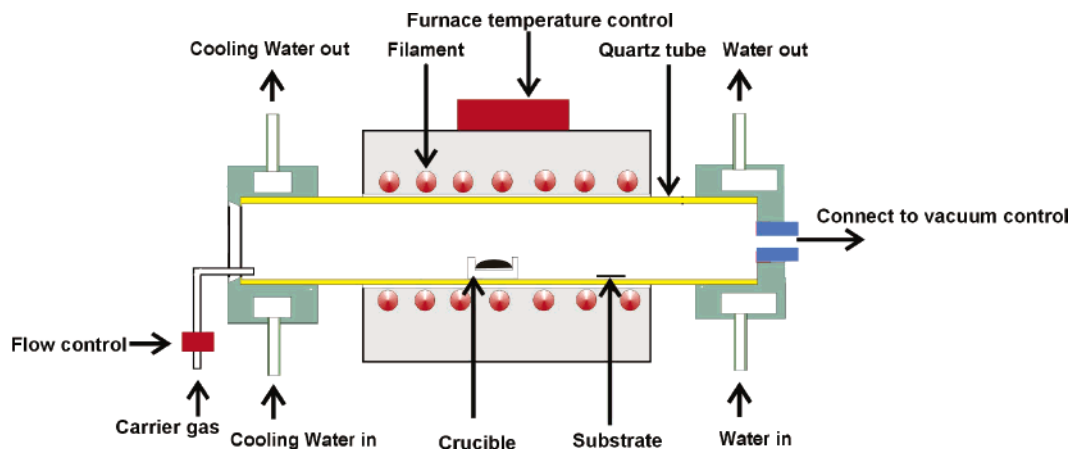


**Figure 12.** Schematic representations of the proposed mechanisms for (a) the OAG and (b) the VLS (inset: phase diagram of Au–Si for (a)) techniques widely used in SiNW growth. (Adapted with permission from ref 71. Copyright 2003 Wiley-VCH.)

A schematic diagrams of OAG and VLS growth are shown in Figure 12.<sup>71</sup> We shall describe both techniques, along with their advantages and disadvantages, in the next subsections. It should be mentioned here that both techniques produce homogeneous, monodispersed SiNWs with narrow size distributions (e.g.,  $20 \pm 2$  nm) and uniform diameters throughout the entire length ( $\sim 1 \mu\text{m}$  or longer) of nanowires.

### 6.1. Oxide-Assisted Growth Technique

The OAG technique is essentially a thermal evaporation technique. And, when laser is used as the energy source, it is called the “laser ablation” technique. Typical equipment used in the synthesis of silicon nanowires is depicted schematically in Figure 13. An alumina tube is mounted inside a tube furnace. Either pristine SiO powder or an equimolar mixture of silicon dioxide and silicon powders is placed at the center of the tube, the middle of the high-temperature zone of the furnace, which is the evaporation source. Silicon wafer or other substrates are placed at positions downstream from the carrier gas to collect the products. The tube is evacuated to a base pressure of  $10^{-2}$  Torr. A carrier gas of argon, mixed with 5% H<sub>2</sub>, is introduced at one end of the alumina tube with a flow rate of 50 sccm (standard cubic centimeters per minute) and a pressure of 500 Torr. The temperature of the furnace is gradually increased to 1130–1400 °C and kept at this temperature for the Si nanowire growth. Sublimed silicon monoxide disproportionates to produce silicon and silicon dioxide in the gas phase. The Si atoms collide with the carrier gas and, in the process, are cooled, to form silicon clusters that nucleate and



**Figure 13.** Schematic diagram of the thermal evaporation apparatus for SiNW growth via the OAG technique.

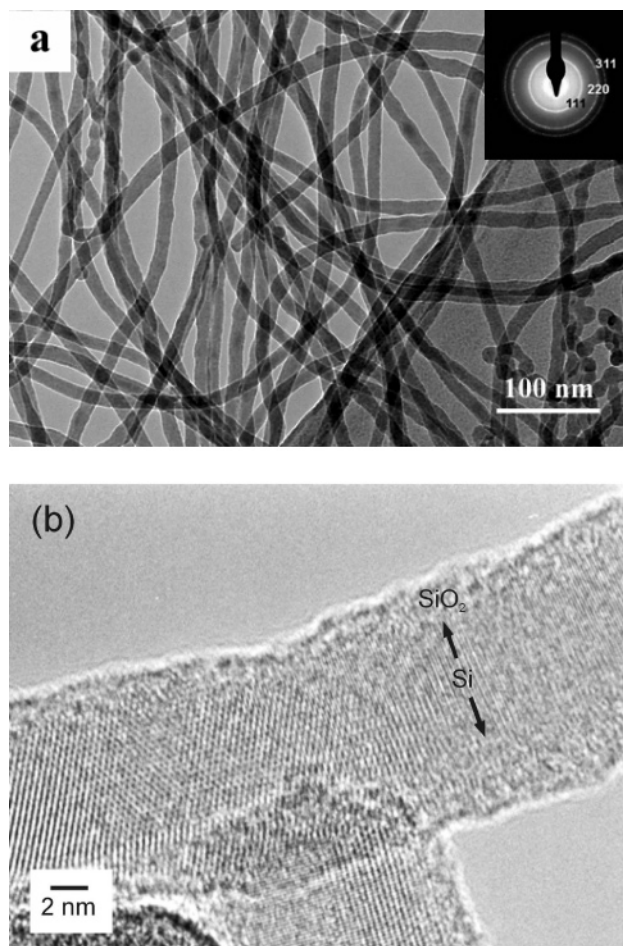
grow into nanowires and collect on the surfaces of the substrates. The nanowires thus formed comprise a crystalline silicon core and an oxide outer layer. The diameters of the silicon nanowires depend critically on the temperatures of the substrates. The temperatures at the substrate positions (where products are collected) are determined to be ranging from 900 to 850 °C, depending on their distances downstream from the evaporation source.

The SiNWs prepared by thermal evaporation technique are known to have a relatively thick oxide layer. Its presence has been associated with the preferred linear growth of the SiNWs. SiNWs prepared by this method are literally very long (micrometers), freestanding wires with a diameter of several nanometers to tens of nanometers. Each nanowire has a crystalline silicon core of approximately 15 nm in diameter and is sheathed with an amorphous oxide layer whose thickness is of one-quarter to one-third of the nominal diameter. Typical TEM images of SiNWs synthesized via OAG method are shown in Figure 14. The majority of the SiNWs produced via the evaporation technique generally grow along the (110) or (112) directions. As-prepared SiNWs are stable in air (under ambient conditions) for months. Apparently the crystalline silicon core is protected (passivated) by the amorphous oxide layer. Furthermore, under normal TEM imaging conditions, the oxide sheathing is relatively stable; though under prolonged intense e-beam irradiation, part of the oxide layer could be blown away or the entire SiNW could be “melted”.

The advantages of the thermal evaporation technique are as follows: (1) no need for metal catalysts; (2) uniform diameters. The main disadvantage is the lack of precise control of the diameters of the nanowires, though they can be controlled to a certain degree by varying the experimental conditions and/or the choice of the carrier gas.<sup>72</sup>

#### 6.1.1. Mechanism of Oxide-Assisted Growth: Theoretical Insights

The mechanism of the oxide-assisted growth of SiNWs had been explored by Zhang, and co-workers on the basis of DFT calculations of SiO clusters.<sup>73,74</sup> It was found by these researchers that for  $\text{Si}_n\text{O}_m$  clusters with  $m/(n+m)$  of less than 0.62 (hereafter referred to as “unsaturated clusters”), the tendency (as measured by the inverse of the HOMO–LUMO energy gap) to form Si–Si bonds is greater than that of forming Si–O or O–O bonds; and that such tendency increases with decreasing oxygen content  $m$ .<sup>74</sup> The term



**Figure 14.** (a) TEM image of as-prepared SiNWs by thermal evaporation. (b) HRTEM image of a single SiNW covered with an oxide layer (Reprinted with permission from ref 147. Copyright 2002 American Chemical Society.)

unsaturated clusters is taken here to mean  $\text{Si}_n\text{O}_m$  clusters containing coordinatively unsaturated silicon atoms with coordinations of less than four ( $\text{sp}^3$  hybridization). Furthermore, the HOMO comprises predominantly surface silicon orbitals, suggesting that surface silicon atoms are the reactive sites. As the  $(\text{SiO})_n$  cluster grows in size, Si–Si bonds begin to form at  $n = 5$  and, at  $n = 18$ , all silicon atoms are four-coordinate  $\text{sp}^3$  hybridized.<sup>73</sup> On the basis of these results, it was conjectured that two unsaturated clusters can be fused together via Si–Si bond formation, with concomitant re-



construction and migration of some of the oxygen atoms to the surface.

Experimentally, it is known that in the oxide-assisted growth, the maximum yield is obtained when SiO powder or an equal molar mixture of Si and SiO<sub>2</sub> is used as the source.<sup>65</sup> Furthermore, little or no SiNWs can be obtained with pure Si or SiO<sub>2</sub> as the source. These observations suggest that silicon monoxide clusters play an important role in the nucleation and growth of the SiNWs.

On the basis of these theoretical results, Zhang, Lee, and Lifshitz proposed the following mechanism for the oxide-assisted growth of SiNWs. Initially, (SiO)<sub>n</sub> clusters are formed in the gas phase from the silicon and oxygen atoms evaporated from the source via collisions with the carrier gas. These gaseous (SiO)<sub>n</sub> clusters are carried to, and anchored on, the substrate. The anchored (SiO)<sub>n</sub> clusters serve as nucleation sites. With their surface silicon atoms, containing “dangling bonds,” exposed to the vapor, these unsaturated clusters can “absorb” additional (SiO)<sub>n</sub> clusters to form larger clusters. At about  $n = 5$ , Si–Si bonds begin to form. And at the cluster size of approximately  $n = 18$ , a silicon core resembling bulk silicon begins to take shape. In the process, some of the oxygen atoms will be expelled and migrate to the perimeter, forming a chemically inert SiO<sub>2</sub> sheath. The oxygen diffusion length depends on the temperature and the crystal orientation of the Si core. Ultimately, crystalline SiNWs with a specific crystallographic orientation and an amorphous silicon oxide sheath are formed. The growth direction of the nanowires depends critically on the surface free energies of the crystal faces at the interface. The highly reactive (SiO)<sub>n</sub>-like tip of the nanowires serves as the “collector” for (i.e., capturing) the incoming vapor-phase (SiO)<sub>n</sub> clusters, promoting the axial growth of the crystalline Si core, while the inert SiO<sub>2</sub> layer in the outer perimeter restricts the lateral growth of the nanowire, resulting in the 1-D growth of SiNWs.

## 6.2. Vapor–Liquid–Solid Method

The VLS method for growth of nanowires relies on the dissolution of gaseous reactants into nanosized liquid droplets of a metal catalyst, followed by nucleation and growth of single-crystalline rods in one direction, thereby forming the nanowires. The one-dimensional growth is induced and directed by the liquid droplets, whose sizes remain essentially unchanged during the entire growth process. Hence, each liquid droplet serves as a virtual template to restrict the lateral growth of an individual wire. Metal nanoparticles of Au, Fe, and Ti, etc., have been employed as the metal catalysts in the growth of SiNWs.<sup>25,62,75–78</sup> Gold is commonly used in SiNW growth because of its inertness and its ability in forming relatively low-temperature eutectics with Si at 363 °C. The phase diagram of the Au–Si eutectic is shown in the inset of Figure 12b. It should be emphasized that, though often referred to as “catalysts”, the metal nanoparticles play more of the role as “initiator” and “director” for the one-dimensional growth of the nanowires.

The advantage of the VLS process is that the diameter of the nanowire can be controlled by the size of catalyst nanoparticles. Recently, Wu et al. reported that single-crystal silicon nanowires with diameters approaching molecular dimensions and a small diameter distribution can be synthesized using a well-defined gold nanocluster as catalyst.<sup>75</sup> Little or no visible amorphous oxide outer layer was observed.

A variant of the VLS growth is the so-called SLS method. The SLS method, as applied to the growth of SiNWs, uses high-temperature supercritical fluids (in place of the vapor phase) and organic-monolayer-protected gold nanocrystals as seed particles (in place of the metal catalysts).<sup>27,63,64</sup> Bulk quantities of defect-free SiNWs with nearly uniform diameters in the range of 4–5 nm can be grown to a length of several micrometers with this approach. Alkanethiol-coated gold nanocrystals (2.5 nm in diameter) were used as seeds to direct one-dimensional Si crystallization in a solvent heated and pressurized above its critical point. The orientation of the Si nanowires produced with this method can also be controlled with the reaction pressure.<sup>22</sup>

## 6.3. Growth Habits of Silicon Nanowires

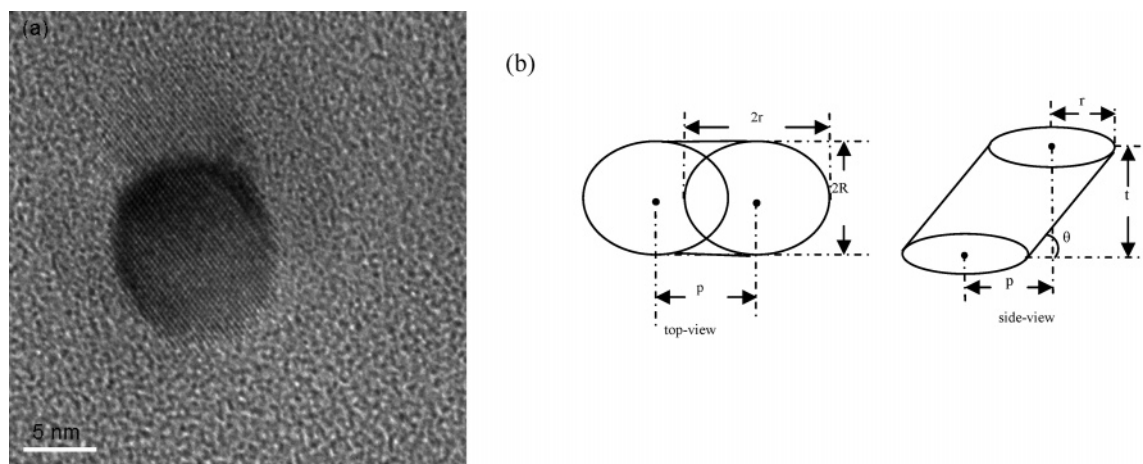
The growth direction, the shape of the cross-section, and the internal atomic structure (including twinning or other stacking faults, if any) of single nanowires can be determined by the microtome technique widely used in the preparation of transmission electron microscopy specimens of biological samples.<sup>75,79</sup> Using this technique, it was demonstrated that both the coaxial structure of vertical cross-section of normal SiNWs and the horizontal cross-section of SiNWs can be obtained and examined under TEM.<sup>79</sup>

Another important aspect of the microtome technique lies in the fact that it allows direct visualization of the cross-sections of silicon or other nanowires or nanotubes. The direct observation under high-resolution transmission electron microscopy (HRTEM) of the cross-sections of nanowires is critical in the determination of the orientation and behavior of the growth of these nanowires as well as their internal structures and atomic arrangements. This information is crucial in the understanding of their properties in the nanorealm (e.g., quantum size effects) and, ultimately, in the construction of nanodevices.

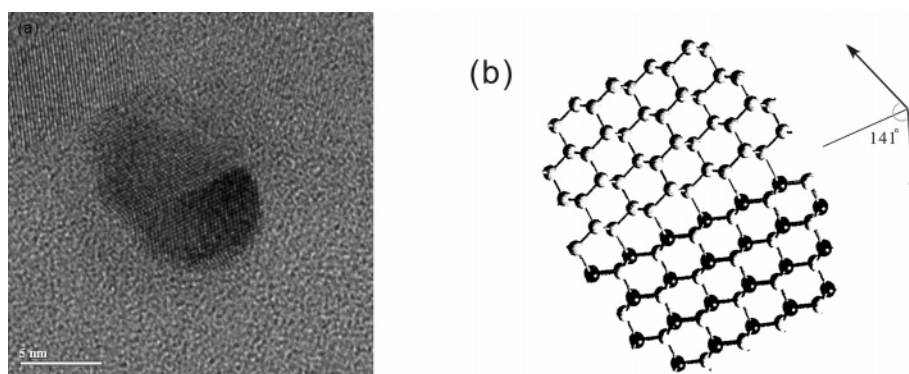
### 6.3.1. Silicon Nanowires Prepared by Oxide Assisted Growth

SiNWs prepared by the OAG technique generally grow along the [110] or [112] direction and, less frequently, in the [100] or [111] direction. Figure 15a shows a typical HRTEM image of the vertical cross-section of a SiNW grown by the OAG method. The silicon atomic-resolution image allows the determination of the growth direction of the SiNW to be the (110) direction with the perpendicular (111) planes (with  $d$  spacings of 3.1 Å for Si(111)) meeting at the expected angle of 109.5°. Figure 16a depicts the HRTEM of the cross-section of a twinned SiNW. It is obvious that this particular SiNW is twinned with the two twinning (111) planes meeting at an angle of 140°. A structure model of the twinning mechanism is portrayed in Figure 16b, showing the mirror images of two twin (111) planes meeting at the theoretical angle of 141° at the twin boundary (111) plane.

A totally different technique, namely, the polishing and ion milling method, has been used by Li et al. to prepare a cross-section sample of SiNWs prepared by OAG.<sup>80</sup> TEM results show that the growth axes of SiNWs prepared by the OAG method are predominantly along  $\langle 112 \rangle$  and  $\langle 110 \rangle$  directions, occasionally along the  $\langle 001 \rangle$  direction, but rarely along the  $\langle 111 \rangle$  direction. Wires with different growth directions are associated with different diameters and various cross-sectional shapes as categorized in Figure 17. The



**Figure 15.** (a) HRTEM image of the cross-section of a SiNW. Note the dark and light ellipses of the top and bottom cross-sections. (b) Schematic representations of the top (left) and side (right) views. (Reprinted with permission from ref 79. Copyright 2003 American Chemical Society.)



**Figure 16.** (a) HRTEM image of the cross-section of a SiNW with two twinning (111) planes meeting at the angle of  $140^\circ$ . (b) Structure model of the twinning in a. (Reprinted with permission from ref 79. Copyright 2003 American Chemical Society.)

growth direction of SiNWs has been rationalized in terms of the relative surface energies of different crystallographic planes.

### 6.3.2. Silicon Nanowires Prepared by VLS Growth

The growth direction of SiNWs prepared by the VLS process has a strong diameter dependence, with the small-diameter NWs growing primarily along the  $\langle 110 \rangle$  direction and the larger diameter NWs growing along the  $\langle 111 \rangle$  direction.<sup>75</sup> A cross-sectional image, depicted in Figure 18, of a 3.8-nm SiNW prepared by VLS process confirms the growth axis to be the  $\langle 110 \rangle$  direction and reveals a hexagonal cross-section with well-developed facets. An analysis of the lattice-resolved image shows that these facets correspond to the low-free-energy (111) and (100) planes, which is consistent with the equilibrium shape (Figure 18d) predicted by a Wulff construction. The measured  $d$  spacings are 3.1 Å for the (111) plane and 2.7 Å for the (200) plane, as expected.

## 6.4. Rational Growth Controls

The rational control of the growth process of nanomaterials in general, and of SiNWs in particular, is a key step in the future development of the bottom-up strategy in nanotechnology. Needless to say the physical and chemical properties of SiNWs depend critically on their diameter, crystal orientation, and dopant composition and concentration. Positioned growth of SiNWs and direct growth of SiNWs network on prefabricated silicon wafers will benefit the

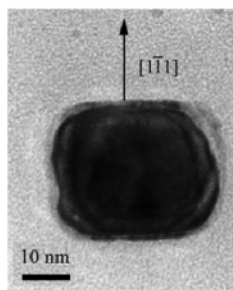
assembly and integration of SiNW-based nanodevices onto the existing silicon microtechnology. In this section, we shall review some of the strategies developed to date with regard to the diameter and orientation controls of the growth of SiNWs, to controlled doping during and after growth, and to the positioning of the SiNWs at the designated sites and connecting them to predetermined network during growth. Obviously these strategies may also be applied to other one-dimensional nanomaterials.

### 6.4.1. Diameter Control

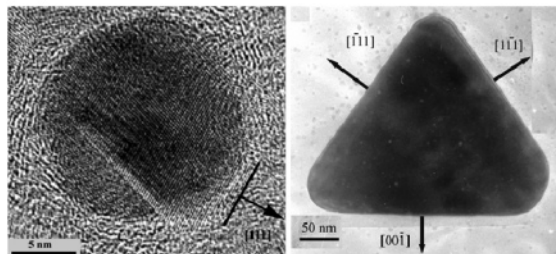
There are many ways to control the diameters of SiNWs during growth: via the use of catalysts or templates, carrier gas, reaction temperature, or combinations thereof.

In the VLS process, the diameter of the resulting SiNWs depends critically on the size of metal catalyst particles. Thus, one can obtain SiNWs with a desirable diameter by selecting catalyst nanoparticles with a suitable size. The monodisperse SiNWs were synthesized by exploiting well-defined Au nanoclusters as catalysts for one-dimensional growth via a VLS mechanism (Figure 19).<sup>62</sup> The SiNWs grown from 5, 10, 20, and 30 nm nanocluster catalysts had mean diameters of 6, 12, 20, and 31 nm, respectively (Figure 20). Obviously the diameter distribution of the SiNWs prepared by this method is determined by the spread of the sizes of the metal catalysts. As mentioned earlier, Wu et al. recently reported that single-crystal silicon nanowires with diameters approaching molecular dimensions and a small diameter distribution can be synthesized using well-defined gold

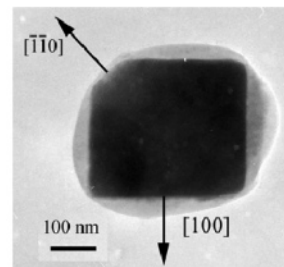


(a)  $[112]$ 

circular (15nm) to rounded rectangle (30nm)

(b)  $[110]$ 

circular (15nm) rounded triangle (300nm)

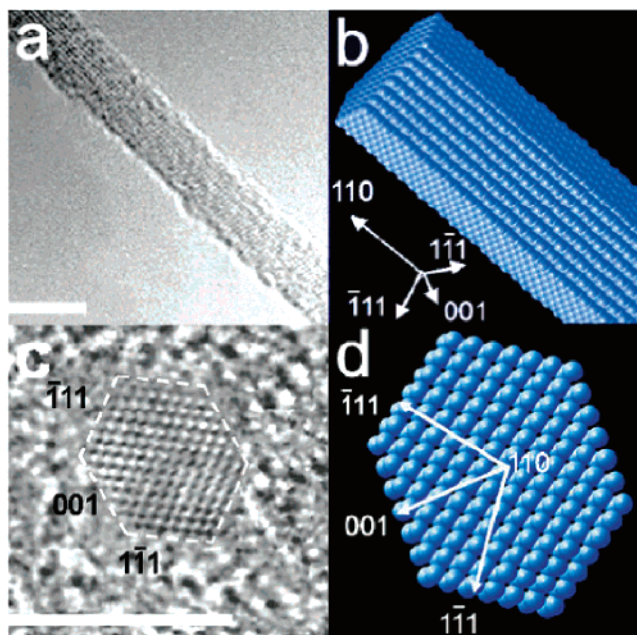
(c)  $[001]$ 

truncated rectangle (350nm)

**Figure 17.** (a) Cross-sectional HTREM image of a small-sized SiNW grown along  $[112]$ . (b) Cross-sectional TEM images of a small- and a large-sized SiNW grown along  $[110]$ . (c) Cross-sectional TEM image of a SiNW grown along  $[001]$  (Adapted with permission from ref 80. Copyright 2003 Wiley-VCH.)

nanocluster as catalyst.<sup>75</sup> As mentioned earlier, the growth direction has a strong diameter dependence, with the smallest diameter NWs growing primarily along  $\langle 110 \rangle$  and the larger NWs growing along  $\langle 111 \rangle$ .

In the OAG growth, the diameters of the SiNWs can be controlled by the carrier gas used in the growth process.<sup>72</sup> SiNWs with the diameter distributions peaking at 13, 9.5, and 6 nm have been obtained using He, Ar (5% H<sub>2</sub>), and N<sub>2</sub>, respectively, as carrier gases. This is shown in Figure 21. The exact effect of the carrier gas on, and the detailed mechanism of, the growth process is presently unclear. Nevertheless, the carrier gas atoms are expected to affect the formation and transport of the silicon nanoclusters and the phase separation process at the growth front of the SiNWs. The substrate temperature (i.e., growth temperature) also affects the diameter and shape of the SiNWs in the OAG growth. For example, in one study,<sup>81</sup> the average diameters of SiNWs were determined to be 200, 80, and 50 nm for substrate temperatures of 1190, 1160, and 1130 °C, respectively. Furthermore, while the first two types of nanowires (200 and 80 nm in diameter) resemble long straight rods,



**Figure 18.** TEM images of a 3.8 nm SiNWs grown along the  $\langle 110 \rangle$  direction: (a) side view; (c) HRTEM cross-sectional image. These images are compared with the equilibrium shapes predicted by Wulff construction: (b) side view; (d) cross-section view. The scale bars are 5 nm. (Reprinted with permission from ref 75. Copyright 2004 American Chemical Society.)

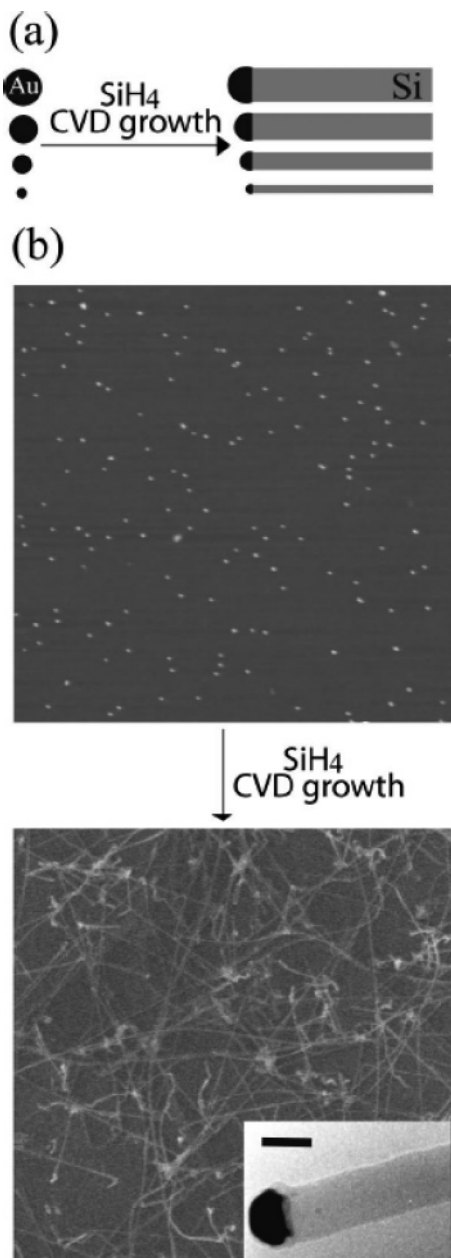
the third one has a tadpolelike shape and appears to be broken into short Si rods. The head of the tadpoles is crystalline silicon, while the tail of the tadpoles is amorphous silicon oxide.

We shall now turn to the use of templates or molds to control the diameters of nanowires or nanotubes. Generally speaking, templates can be categorized into two broad classes: *concave*- and *convex*-types. Concave-type templates are porous materials with cavities or channels for the SiNWs to grow within, whereas convex-type molds are templates for the SiNWs to grow on the outside. Each of these two types can further be categorized into inert vs sacrificial templates. We shall discuss a few examples of various types of templates. It is obvious that these classification schemes or concepts are also applicable to the growth of other nanomaterials.

#### 6.4.1.1. Anodized Aluminum Oxide as Templates.

Porous templates can be used not only to control the diameter of SiNWs but also to obtain ordered SiNW arrays. As an example, ordered single-crystal SiNW arrays had been synthesized by pyrolysis of silane on Au particles deposited (via the VLS method) within hexagonal close-packed nanochannel alumina (NCA) templates called anodized aluminum oxide.<sup>82,83</sup> A schematic of nanowire fabrication process is shown in Figure 22. The SiNWs produced by this fabrication technique have several important features. The pore diameter, length, and density in the NCA templates can be controlled by varying adjustable parameters such as the anodizing voltage, electrolyte composition, temperature, and the time of anodization. The diameter and length of the nanowires depend on the pore diameter and the growth time, respectively. Figure 23 shows typical histograms of the measured SiNW diameters and corresponding SEM images of the nanowires after VLS growth of nanowires within the NCA membrane (Figure 23a) and protruding from the tip surface of the membrane (Figure 23b). For this particular



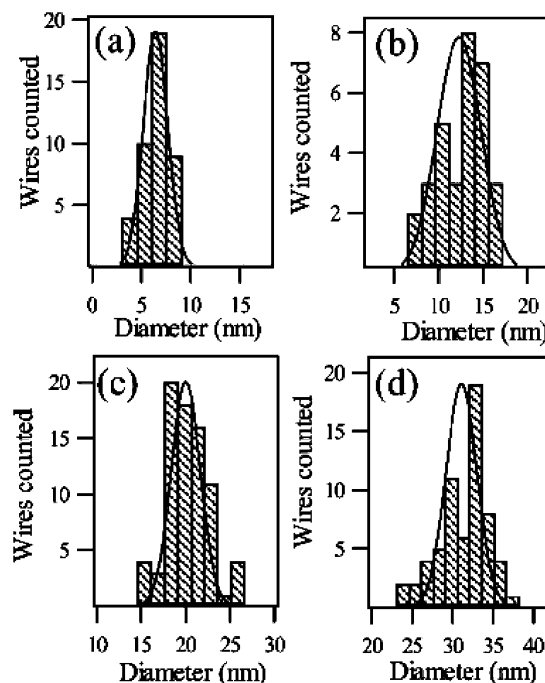


**Figure 19.** (a) Schematic representation of size-controlled synthesis of SiNWs from Au nanoclusters. (b) AFM image of 10 nm Au nanoclusters dispersed on the substrate (top). FESEM image of SiNWs grown from the 10 nm nanoclusters (bottom). The inset in the bottom image is a TEM micrograph of a 20.6 nm diameter SiNW with a Au catalyst at the end. The scale bar is 20 nm. (Reprinted with permission from ref 62. Copyright 2001 American Institute of Physics.)

sample, the average pore diameter of the membrane was  $136 \pm 27$  nm. The average SiNW diameter was  $138 \pm 13$  nm for wires grown within the membrane, which matches closely to the pore diameter of the membrane. The average diameter of the SiNWs protruding from the top surface of the membrane was  $158 \pm 9$  nm, substantially larger than the size of the membrane pores.

Other applications and/or strategies using AAO as templates (e.g., “template replication” method) will be described in sections 6.5.3 and 9.5.5.2.

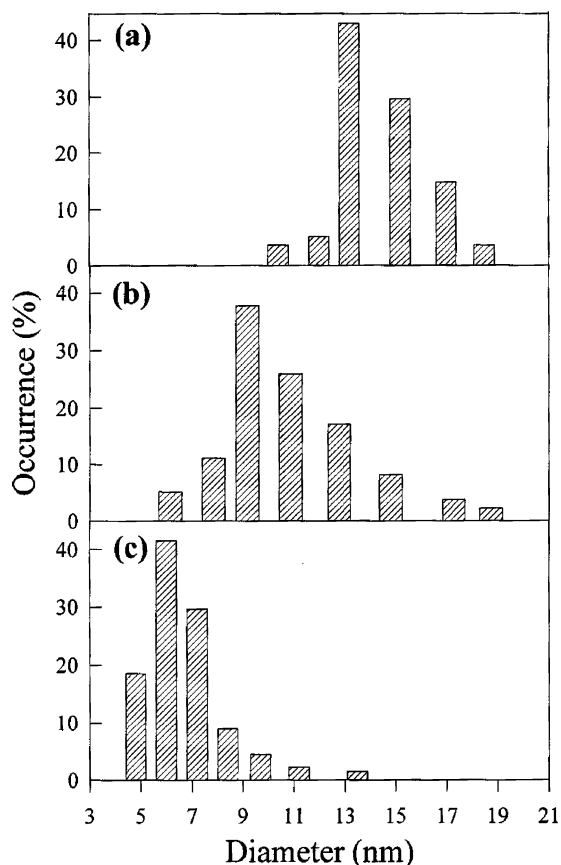
**6.4.1.2. Silica as Templates.** In another study, SiNWs were synthesized within the 5 nm diameter pores of mesoporous silica using a supercritical fluid solution-phase



**Figure 20.** Histograms of SiNW diameters grown from 5, 10, 20, and 30 nm diameter Au nanoclusters. The smooth curves show a Gaussian fit of the nanowire distributions. The calculated NW diameters include the oxide layers. (Reprinted with permission from ref 62. Copyright 2001 American Institute of Physics.)

approach. Mesoporous silica, formed by the hydrolysis of tetramethoxysilane in the presence of a triblock copolymer surfactant, was employed for the nucleation and growth of silicon.<sup>84,85</sup> The silica matrix provides a means of producing a high density of stable, well-ordered arrays of SiNWs in a low dielectric medium.

**6.4.1.3. Zeolites as Quasi-Templates.** It has been demonstrated that zeolite can be used as a sacrificial template to grow very fine and uniform SiNWs via the disproportionation reaction of SiO by thermal evaporation (the OAG technique).<sup>48,86</sup> The diameter of the Si core of the resulting SiNWs ranges from 1 to 5 nm with an average of 3 nm. The single-crystalline silicon core is sheathed by a thick and uniform amorphous oxide layer of 20–40 nm in diameter. Figure 24a is an overview of the SEM image of the SiNWs. A large quantity of SiNWs can be found on the surface of the zeolite pallet. In the zoom-in image (Figure 24b), it is seen that the SiNWs were attached to the surface of the zeolite pallet. Energy dispersive X-ray spectroscopy (EDX) results show that SiNWs are composed of mainly Si, O, and a small amount of Al. The small amount of Al came from zeolite and provides strong evidence for the growth mechanism proposed by the authors.<sup>48,86</sup> Figure 25 shows the TEM image of a single SiNW. These Si cores are very fine and uniform in diameter throughout the entire length ( $\sim 1 \mu\text{m}$  or longer) of each wire. The central Si core measures 1.3 nm in diameter with a relatively thick SiO<sub>2</sub> outer layer of 20 nm in diameter. Assuming a Si–Si bond length of 0.235 nm, this fine nanowire of 1.3 nm in diameter contains only six to seven silicon atoms across the short dimension. This is one of the finest SiNWs synthesized to date. The inset of Figure 25 shows a HRTEM image of the same SiNW. It confirms that the core is crystalline silicon with  $3.1 \text{ \AA}$   $d$  spacing.



**Figure 21.** Histograms (size distribution in terms of diameter) for SiNWs synthesized by laser ablation using different carrying gases: (a) He, (b) Ar (5% H<sub>2</sub>), and (c) N<sub>2</sub>. (Reprinted with permission from ref 72. Copyright 1999 American Institute of Physics.)

#### 6.4.2. Orientation Control

Controlling the crystal orientation of SiNWs in the growth process is important for many applications. Many physical and chemical properties, such as optical, electronic transport, and surface properties, depend on the crystal orientation of SiNWs. In fact, the growth direction is determined by the crystal orientation of SiNWs in the growth process. In either VLS or OAG method, it has been observed that growth orientation correlates with the diameter of SiNWs. In the VLS process, the SiNWs with small diameters tend to grow primarily along  $\langle 110 \rangle$ , whereas SiNWs with larger diameters tend to grow along  $\langle 111 \rangle$  as depicted in Figure 26.<sup>75</sup> In the OAG method, SiNWs predominantly grow along  $\langle 112 \rangle$  and  $\langle 110 \rangle$  directions and occasionally along the  $\langle 001 \rangle$  direction (but rarely along the  $\langle 111 \rangle$  direction), as shown in Figure 27.<sup>71</sup> The growth orientation of SiNWs produced via the SLS method can be controlled by the reaction pressure.<sup>27</sup> Nanowires formed at low pressure (200 bar) exhibit a preponderance of  $\langle 100 \rangle$  growth direction, whereas those synthesized at high pressure (270 bar) grow almost exclusively along the  $\langle 110 \rangle$  direction. By applying the conventional epitaxial crystal growth technique to the VLS process, it is possible to achieve precise orientation control during the SiNWs growth. This so-called vapor–liquid–solid epitaxy (VLSE) technique is particularly powerful in controlled synthesis of nanowire arrays. In VLS process, large-diameter SiNWs prefer to grow along the  $\langle 111 \rangle$  direction. If a Si(111) wafer is used as a substrate, SiNWs will grow epitaxially and vertically on the substrate to form a nanowire array.<sup>87,88</sup> The

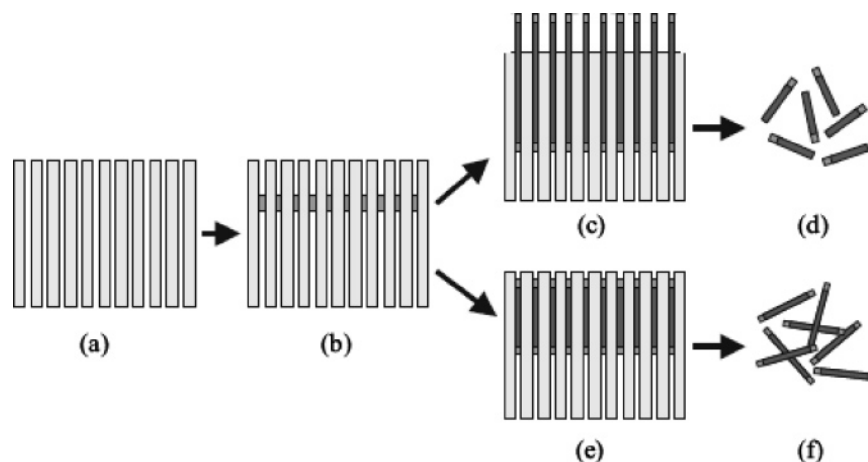
orientation-controlled growth of SiNW arrays on silicon (100), (111), and (110) substrates have been demonstrated. The axes of as-synthesized SiNWs lie along the  $[111]$  direction. Furthermore, the SiNWs are oriented perpendicular to one set of the crystal planes of the substrate. As a result, the orientation of the SiNW array can be controlled by the crystal orientation of the substrate.<sup>89</sup> These well-aligned SiNW arrays form ordered networks on the substrate, and their orthographic projections on (100), (111), and (110) substrates form rectangular patterns, triangular networks, and parallel straight lines, respectively, as portrayed in Figure 28.

#### 6.4.3. Position Control

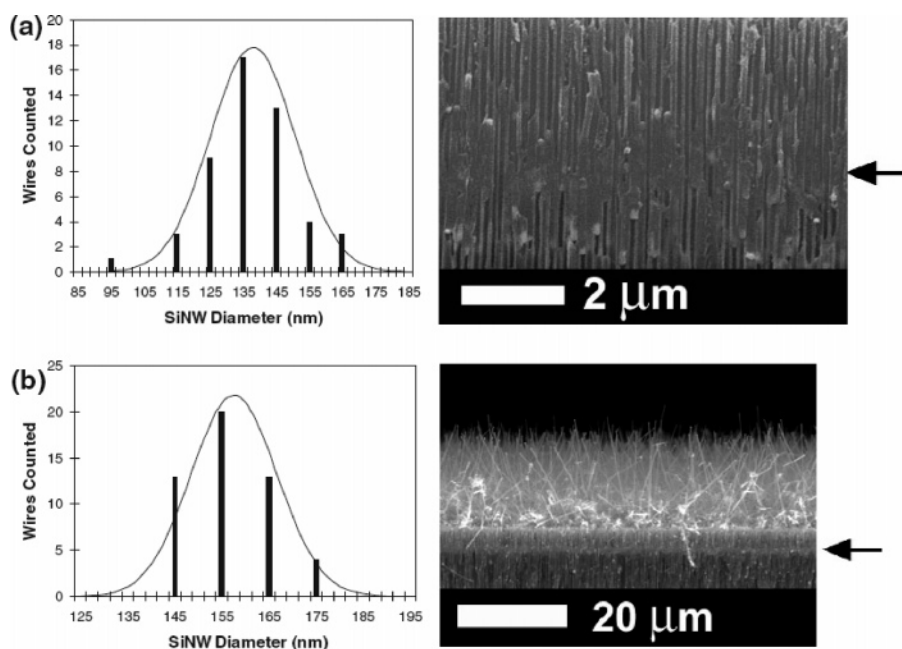
Precisely controlled growth of SiNWs on desirable sites is very important in the bottom-up strategy in fabricating nanoelectronic or nanophotonic devices. In the VLS method, the positions of SiNWs can be controlled by the initial positions of metal clusters or thin films as the catalyst. Various lithographical techniques have been used to create patterns of metal thin film for the SiNW growth. For example, SiNWs with diameters of 10–60 nm can be grown on iron-patterned silicon substrates. The patterning was done with 5 nm thick iron film by e-beam evaporation through a shadow mask. SiNWs are grown only within the patterned iron squares on the substrates (Figure 29).<sup>76</sup> In another example, nanosphere lithography method was found to be a useful lithographic tool for fabricating regularly arranged gold islands in the nanometer range which served as catalysts for the growth of SiNWs (Figure 30).<sup>90</sup> The ordered arrays of vertically aligned silicon nanowires were grown by molecular beam epitaxy growth using prepatterned arrays of gold droplets on Si(111) substrates.

Recently, Yang and co-workers reported the use of galvanic displacement processes to selectively deposit Au nanoclusters onto prepatterned Si surfaces for the growth of vertically and laterally aligned Si nanowire arrays.<sup>91</sup> The key advantage of this approach is that the metal deposition occurs selectively on Si surfaces and not on other surfaces such as silicon dioxide and silicon nitride (commonly used masks in microfabrication). Water-in-oil microemulsions were employed in the galvanic displacement process to control the size of the Au clusters, which in turn control the size of the nanowires synthesized by the VLS method. Figure 31 shows laterally aligned Si nanowire arrays grown on Si pillars with (111)-exposed sidewalls fabricated on (110) silicon-oxide-insulator (SOI) substrates. The diameters of the nanowires retain a good correlation with the  $R$  parameter of the microemulsions used to deposit Au clusters on the Si pillars. In addition, the nanowires only grow on the Si sidewalls and are absent on both the top and bottom surfaces of the sample, due to the selectivity of the galvanic displacement process.

In another study, Wang et al. exploited a multistep nanocluster-catalyzed VLS process to grow branched and hyperbranched SiNWs by depositing Au nanoclusters on prefabricated SiNWs backbone.<sup>92</sup> Figure 32 shows a scheme of the growth process of the branched and hyperbranched SiNWs. First, a SiNW of specific diameter and composition, serving as the backbone, is prepared by Au nanocluster-mediated VLS growth using silane as the reactant. Second, Au nanocluster catalysts of defined diameter are deposited onto the SiNW backbone from solution, and then first-order branches are grown by the VLS process. Third, the branch



**Figure 22.** Schematic representation of silicon nanowire fabrication process: (a) cross-section view of nanoporous alumina membrane, (b) electrodeposition of Au within pores, (c) VLS growth of SiNWs protruding out of the membrane surface, (d) removal of the SiNWs by mechanical agitation, (e) VLS growth of SiNWs within the membrane, and (f) removal of the SiNWs by wet etching of the membrane. (Reprinted with permission from ref 83. Copyright 2005 Wiley-VCH.)



**Figure 23.** Histograms of SiNW diameters and the corresponding SEM images of nanowires grown (a) entirely within membrane and (b) protruding out of the top surface of the membrane. The arrows indicate the initial position of Au within the membrane. (Reprinted with permission from ref 83. Copyright 2005 Wiley-VCH.)

growth steps can be repeated many times to yield higher order or hyperbranched SiNW structures. Typical SEM images of branched Si nanowire structures are depicted in Figure 33.

**6.4.3.1. “Grown-in-Place” Approach.** A “grown-in-place” approach,<sup>93,94</sup> which combines the VLS method with lithographically fabricated, nanochannel templates, was explored to produce Si nanowires and nanoribbons of controlled size, shape, orientation, and positioning in pre-determined device architectures. This technique will be discussed in detail in section 10.3.

#### 6.4.4. Composition Control

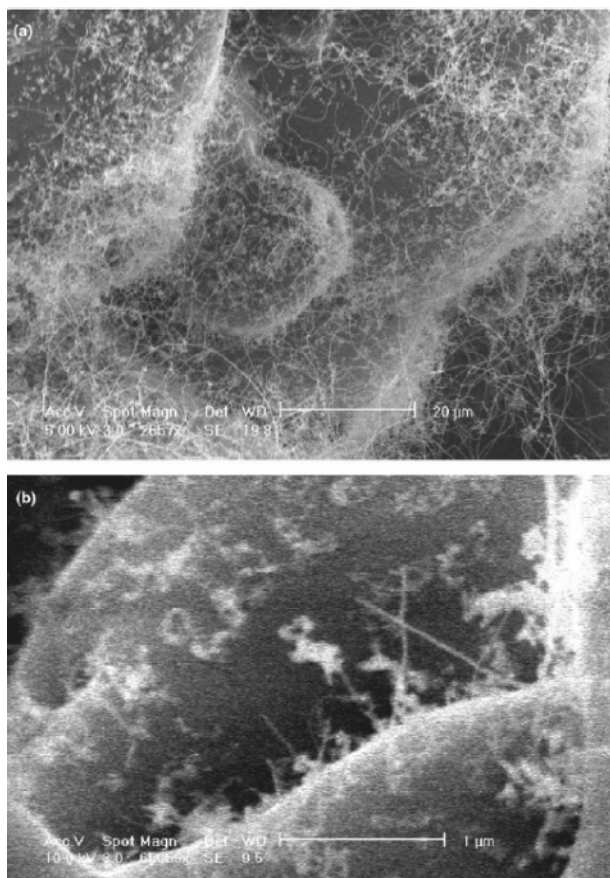
Obviously the performance of a nanodevice fabricated with a particular nanowire depends critically on its composition. Here the word “composition” is taken to imply both the relative concentrations of the constituents and their distribution profiles within the nanowire. Composition control can

be asserted during or after growth. Changing the reactants and/or the substrate during growth is the most direct way to control the composition of the resulting nanowires. Post-growth reactions (e.g., induced by a high-temperature treatment) between the constituents of the nanowire or between the constituents of the nanowire and the substrate or the template can sometimes change the composition of the nanowires as well. We will see many examples of these control strategies in later sections.

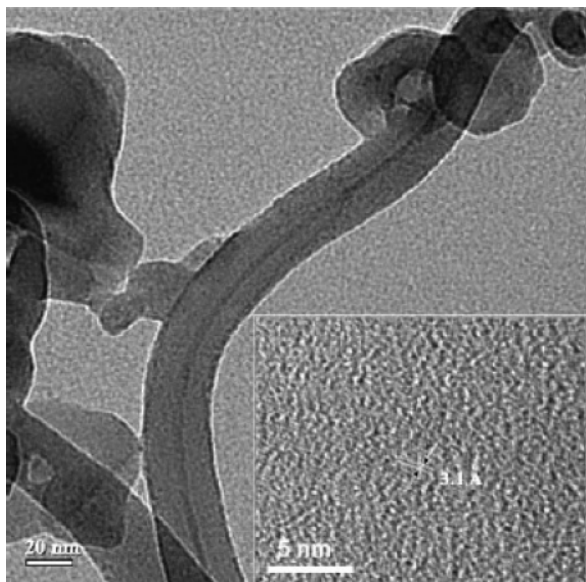
Other ways of composition control, commonly used in the semiconductor industry, are sputtering, implantation, doping, etc. Doping can be done during or after growth of the nanomaterial, as we shall discuss next.

**6.4.4.1. Doping of SiNWs.** Doping of SiNWs can be achieved in two ways: in-situ doping (doping during the growth process) and postdoping (doping after growth through an implantation and annealing process). Single-crystal n-type and p-type silicon nanowires have been prepared by in-situ



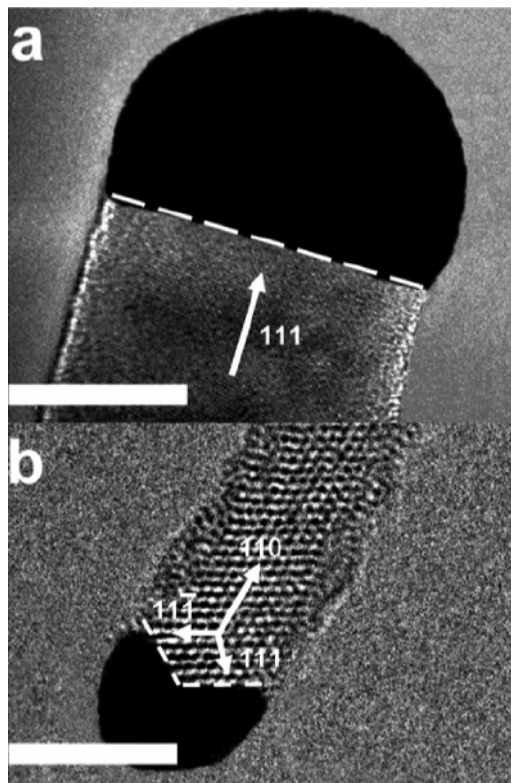


**Figure 24.** (a) A typical SEM image of the SiNWs synthesized with zeolite Y as quasi template. (b) Zoom-in image of a. (Reprinted with permission from ref 48. Copyright 2003 American Chemical Society.)

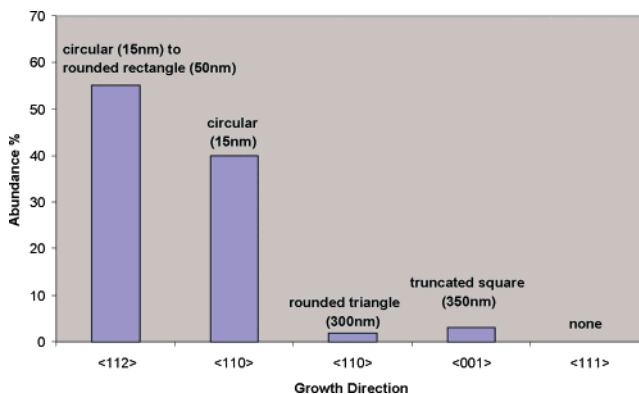


**Figure 25.** TEM image of a typical single SiNW with a Si core diameter of 3 nm covered with a SiO<sub>2</sub> layer of 28 nm. The inset is the HRTEM image of the same SiNW. (Reprinted with permission from ref 48. Copyright 2003 American Chemical Society.)

doping and characterized by electrical transport measurements.<sup>28,95–102</sup> Laser-assisted VLS growth was used to introduce either boron or phosphorus dopants during the vapor-phase growth of SiNWs.<sup>95–99</sup> Gaseous compounds such as diborane, trimethylboron, and phosphine, etc., have



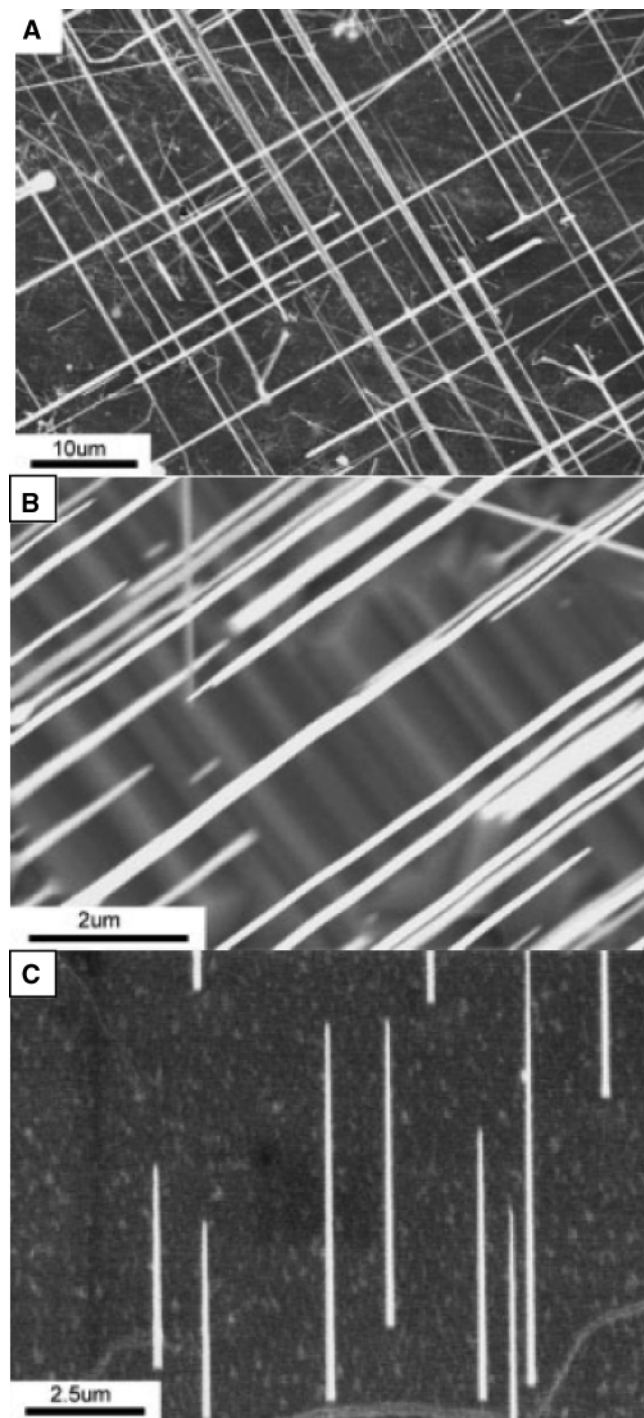
**Figure 26.** (a) HRTEM image of the catalyst alloy/NW interface of a SiNW with a  $\langle 111 \rangle$  growth axis. Scale bar, 20 nm. (b) HRTEM image of a catalyst alloy/NW interface of a SiNW with a  $\langle 110 \rangle$  growth axis. Scale bar = 5 nm. (Reprinted with permission from ref 75. Copyright 2004 American Chemical Society.)



**Figure 27.** Distribution of shapes, sizes, and growth directions of SiNWs synthesized by OAG technique. (Adapted with permission from ref 71. Copyright 2003 Wiley-VCH.)

also been used as dopants in a gas-phase VLS-CVD (CVD = chemical vapor deposition) approach in which silane (SiH<sub>4</sub>) or silicon tetrachloride, etc., is used as Si source.<sup>100,101</sup> Compared to solid dopants, the doping level can be controlled easily by tuning the concentration (flow rate) of the gas dopant(s) in the gas-phase silicon source. In other studies, metals such as Zn, Au,<sup>28,102</sup> and Li<sup>103</sup> have been doped into Si nanowires in order to change the electronic transport properties and morphology of the Si nanowires.

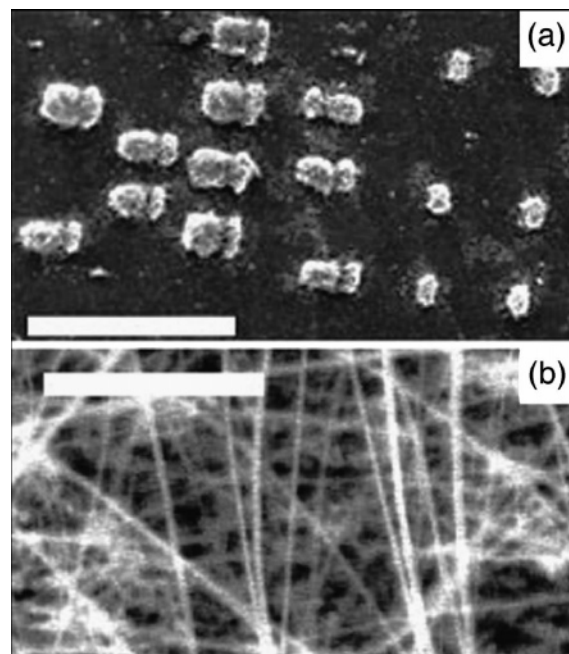
Two-terminal, gate-dependent measurements made on individual boron-doped and phosphorus-doped SiNWs showed that these materials behave as p-type and n-type materials, respectively.<sup>95</sup> In addition, these studies show that it is



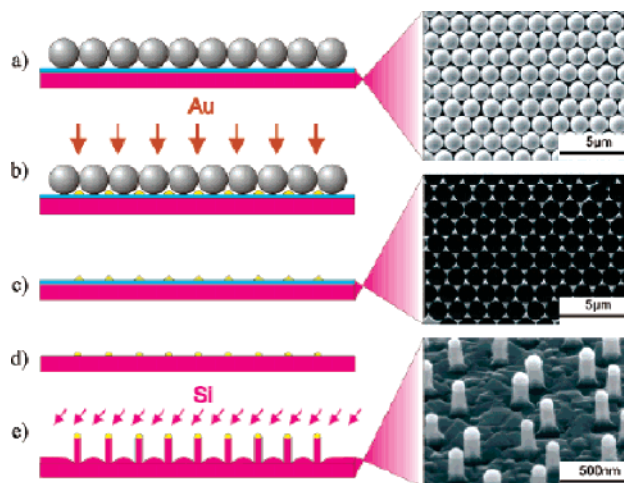
**Figure 28.** SEM images of SiNW arrays grown on (A) Si (100) substrate, (B) Si (110) substrate, and (C) Si (111) substrate. (Reprinted with permission from ref 89. Copyright 2005 Wiley-VCH.)

possible to incorporate high dopant concentrations in the SiNWs to approach the metallic regime.

The doping process can also be done after Si nanowire growth. In one example, n-type Bi-doped SiNWs were fabricated by allowing bismuth vapor to diffuse into the SiNWs after the growth of SiNWs in a sealed evacuated ( $10^{-6}$ – $10^{-7}$  Torr) quartz tube at 1000 °C.<sup>104</sup> The doping concentrations depend on the oxide sheath thickness. The postdoping has the advantages such as appropriate choice of the vapor-phase dopants and selective patterning of the doped SiNWs.



**Figure 29.** SEM images of silicon nanowires on the silicon substrate. (a) Image at low magnification. The white rectangles are silicon nanowires grown on previous iron patterns. The other area remains blank. (b) Top view of the silicon nanowires on one iron pattern at high magnification (bar = 1 μm). The diameters of the SiNWs are generally below 60 nm. (Reprinted with permission from ref 76. Copyright 2000 American Institute of Physics.)

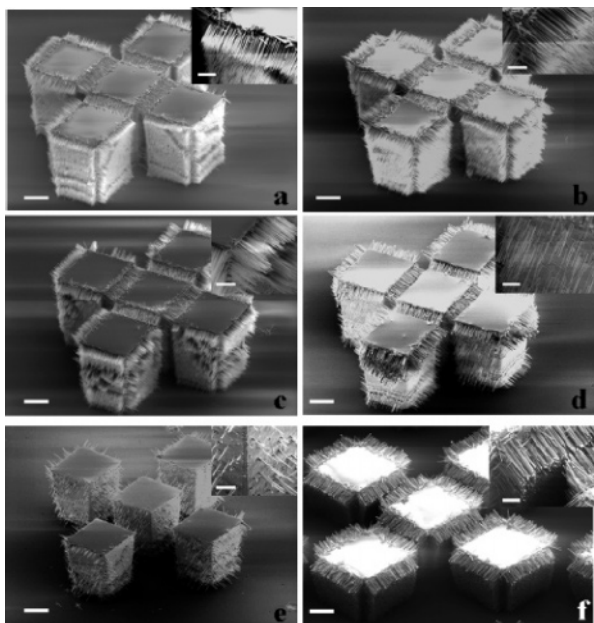


**Figure 30.** (Left) Steps of Si nanowire fabrication using nanosphere lithography: (a) deposition of a mask of polystyrene particles on a Si(111) substrate covered by a 2 nm thick oxide layer (blue), (b) deposition of gold by thermal evaporation, (c) removal of the spheres, (d) thermal annealing and cleaning step to remove the oxide layer, and (e) Si deposition and growth of nanowires by MBE. (Right) The corresponding SEM micrographs of wafers (from step a to step e): regular monolayer mask and structured gold layer made using 1320 nm polystyrene particles. The Si nanowires were grown with gold templates produced with 600 nm polystyrene particles. (Reprinted with permission from ref 90. Copyright 2005 American Chemical Society.)

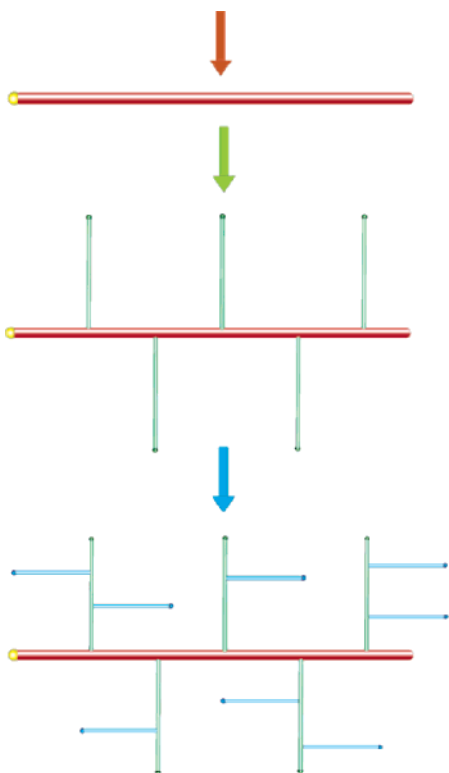
### 6.5. Preparation of Crystalline Silicon Nanotubes via Various Templates

As discussed earlier, while carbon nanotubes are relatively easy to make, the corresponding silicon nanotubes, based on rolled-up graphite-like sheets, are yet to be synthesized. Crystalline silicon nanotubes, designated as cSiNTs, though,



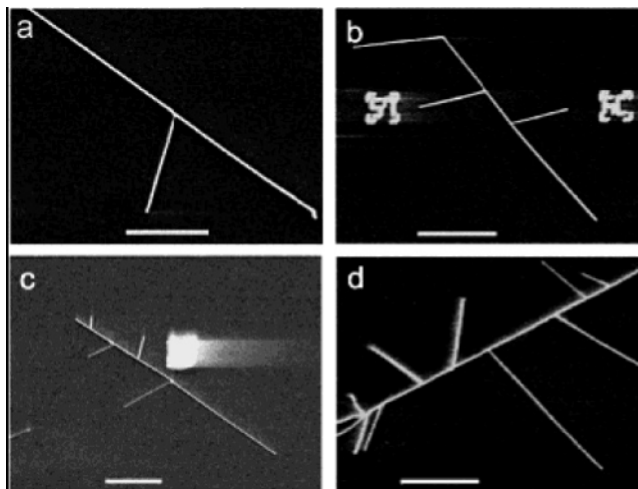


**Figure 31.** Laterally aligned Si nanowire arrays grown on Si pillars bounded by (111) sidewalls fabricated on (110) SOI substrates. Bar = 20  $\mu\text{m}$ . The insets are close-ups of each image; bar = 2  $\mu\text{m}$ . The  $R$  parameter of the microemulsion used in the galvanic displacement process was 16 (a), 25 (b), 50 (c), 100 (d), and 200 (e), respectively. Au clusters were deposited from water-based solution in f. (Reprinted with permission from ref 91. Copyright 2005 American Chemical Society.)



**Figure 32.** Schematic representation of the multistep syntheses of branched and hyperbranched NW structures. Red, green, and blue arrows/colors signify the growth of the backbone, first generation, and second generation NWs, respectively. (Reprinted with permission from ref 92. Copyright 2004 American Chemical Society.)

have been prepared by several groups. The latter are, in reality, hollow SiNWs.



**Figure 33.** SEM images of the branched structures of SiNWs prepared following deposition of gold nanoclusters from (a) 1:20, (b) 1:8, (c) 1:3, and (d) 1:1 diluted stock solutions and subsequent growth. Bars = 1  $\mu\text{m}$ . (Reprinted with permission from ref 92. Copyright 2004 American Chemical Society.)

Besides being an interesting nanostructure, crystalline silicon nanotubes may open up new and exciting possibilities for making different kinds of nanosized heterostructures by filling the inside (hollow) space with one type of nanomaterial and/or by decorating the outside surfaces of the nanotubes with yet another type of nanomaterial to produce integrated nanodevices. Such possibilities have been well-demonstrated for CNTs.

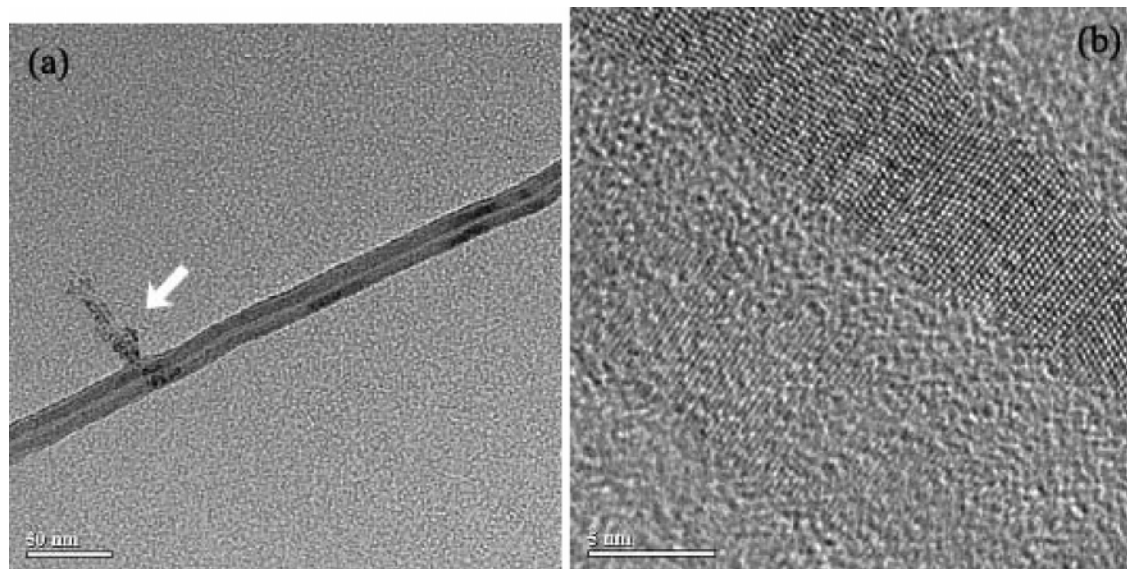
We shall describe several examples of recently prepared cSiNTs.

#### 6.5.1. $\text{SiO}_2\text{NW}\subset\text{cSiNT}$ : Crystalline Silicon Nanotubes Filled with Silica

It was discussed earlier in section 6.4.1.3 that zeolites can be used as a sacrificial template to grow very fine and uniform silicon nanostructures. In fact, three distinct types of composite nanowires and nanotubes of (crystalline) silicon and (amorphous) silica<sup>48,86</sup> were grown on zeolite Y via disproportionation of SiO by thermal evaporation: **1**, a silicon nanowire *inside* a silica nanotube; **2**, a silicon nanotube *outside* a silica nanowire; and **3**, a *side-by-side* growth of a biaxial silicon–silica nanowire structure. The first type had been described earlier. Here we discuss the second type,  $\text{SiO}_2\text{NW}\subset\text{cSiNT}$ , which can be described as a crystalline silicon nanotube filled with amorphous silica (a silicon nanotube *outside* a silica nanowire). The third type will be described in a later section.

Typical TEM images of  $\text{SiO}_2\text{NW}\subset\text{cSiNT}$  are shown in Figure 34. This morphology represents a new silicon nanotubular structure, distinctly different from the conventional rolled-up graphene-sheet structures epitomized by the CNTs. In this context, it is best described as a hollow crystalline silicon nanowire or nanorod. The particular cSiNT portrayed in Figure 34 has an inner diameter of 3 nm and an outer diameter of 15 nm. The crystalline silicon walls have a thickness of about 6 nm on each side. The crystal lattices on the two sides of the tube are almost parallel (within  $10^\circ$  in most cases). The distinctive features of these cSiNTs are as follows: (1) single-crystalline tube walls; (2) uniform inner and outer tube diameters throughout the length of the nanotube; and (3) the tube interior being filled with silica.





**Figure 34.** (a) TEM of a crystalline silicon nanotube, cSiNT. (b) Corresponding HRTEM image (Reprinted with permission from ref 48. Copyright 2003 American Chemical Society.)

Furthermore, this method is rather simple and requires no catalysts.

### 6.5.2. Using AAO as Templates

Independent works by several other groups to produce cSiNTs are worth mentioning. For example, Sha et al.<sup>44</sup> produced a somewhat different pcSiNT structure with the tube wall being made of polycrystalline (pc) silicon interlaced with amorphous silicon. These latter pcSiNTs were prepared by chemical vapor deposition using a nanochannel Al<sub>2</sub>O<sub>3</sub> substrate (i.e., the AAO membrane) as template. In this case, the channels were presputtered with gold which served as a catalyst for the VLS growth of the pcSiNTs (along with SiNWs) inside the AAO nanochannels. Jeong et al.<sup>45</sup> also reported the growth of polycrystalline or amorphous SiNTs, with thick SiO<sub>2</sub> sheaths, by molecular beam epitaxy on top of the protruding pore edges of the AAO membrane, but without metal catalysts.

### 6.5.3. "Template Replication" Technique

Another interesting strategy to produce cSiNT using AAO is the so-called "template replication" method from which highly ordered cSiNT arrays can be prepared.<sup>46</sup> The method, demonstrated schematically in Figure 87 (*vide infra*), involves a combination of a multistep template replication (with NiO cores inside AAO nanochannels) technique and the CVD (using silane) approach. By dissolving away the NiO cores and the AAO templates, cSiNTs of uniform diameters, lengths, and wall thicknesses can be obtained (see Figure 35).

### 6.5.4. Using ZnS Nanowires as Templates

Recently, Hu et al.<sup>47</sup> demonstrated an epitaxial casting technique in producing cSiNTs using ZnS nanowires as templates. In the template-based growth of the crystalline Si tubular nanostructures, ZnSNW@cSiNT core-shell nanowires were initially obtained by epitaxial growth of Si shell layer on ZnS nanowires as templates (see section 9.3.2.1, ZnSNW@cSiNT), in which the shell is a Si thin layer and the core is a ZnS nanowire. The ZnS nanowire templates were subsequently removed from the ZnSNW@cSiNT core-

shell nanowires with HCl solution which resulted in the formation of the crystalline Si tubular nanostructures, cSiNTs. Some nanotubes have one closed end (Figure 36a), while others are open-ended (Figure 36c). The high-resolution TEM image of a crystalline tubular nanostructure shows that the (111) fringes with a *d* spacing of about 0.31 nm are aligned perpendicular to the longitudinal direction of the tube, suggesting a [111] growth orientation of the single-crystalline Si tubular domains.

## 7. Surface Treatments: Etching of Silicon Nanowires

As discussed previously, the silicon oxide layer of the as-prepared SiNWs or SiNDs serves as a protective layer, rendering the as-prepared SiNWs relatively inert. The inertness of the as-prepared SiNWs is unfavorable for most applications of SiNWs in nanotechnology. Further fabrication and/or processing require removal of the oxide layer.

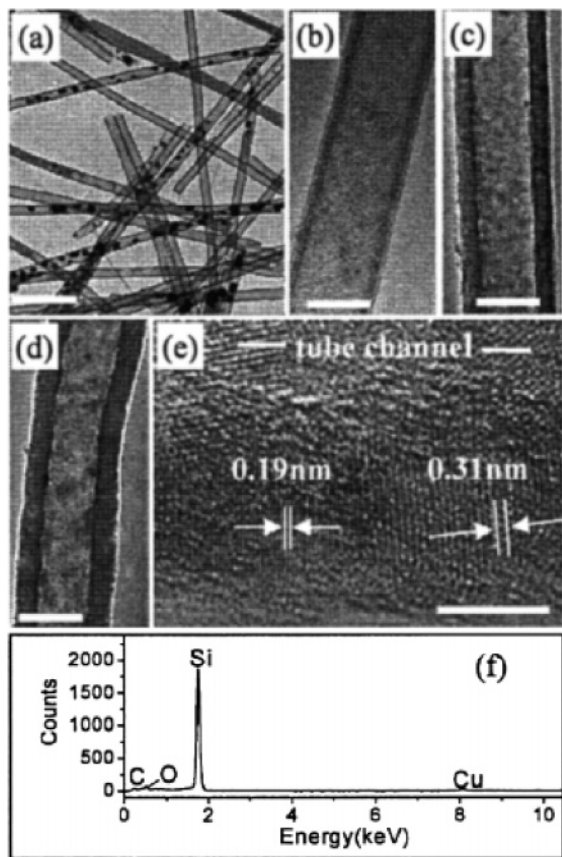
The most widely used technique for removing silicon oxide from the silicon surface is by etching with dilute hydrofluoric acid. It is known from studies of 2-D Si wafer that, after HF treatment, the silicon surfaces are hydrogen-passivated. It is thus of importance to investigate the etching behavior of SiNWs and the stabilities and properties of the resulting SiNWs after etching.

### 7.1. Surface Speciation of Etched SiNWs

During the past decade there have been numerous studies on hydrogen-terminated Si surfaces of bulk silicon materials.<sup>105-111</sup> Species such as SiH, SiH<sub>2</sub>, and SiH<sub>3</sub> have been observed on HF-treated surfaces of Si by high-resolution electron energy loss spectroscopy (HREELS),<sup>105,106</sup> infrared spectroscopy (IRS),<sup>109-117</sup> scanning tunneling microscopy,<sup>118,119</sup> and low-energy electron diffraction (LEED),<sup>120,121</sup> etc. Here we discuss Fourier-transform infrared spectroscopy (FTIR) and STM probes of etched SiNWs.

#### 7.1.1. FTIR Probe of Etching

Attenuated total reflection (ATR) Fourier-transform infrared spectroscopy has recently been used to characterize

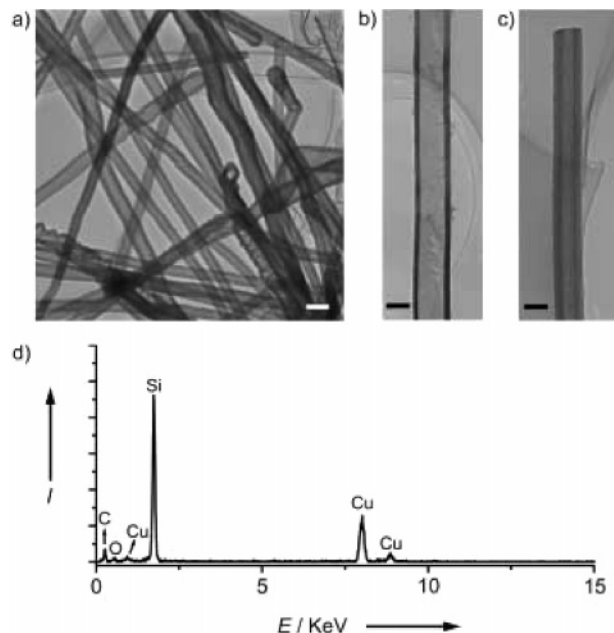


**Figure 35.** TEM image of crystalline silicon nanotube, cSiNTs: (a) cSiNTs and (b–d) the individual SiNT with different wall thicknesses. Scale bar: (a) 250 and (b–d) 50 nm. (e) High-resolution TEM image of the cSiNT. Bar = 5 nm. (f) EDS spectrum taken from an individual cSiNT. (Reprinted with permission from ref 46. Copyright 2005 American Institute of Physics.)

the surface species on oxide-free SiNWs after etching with aqueous HF solution.<sup>122</sup> Figure 37 shows the ATR-FTIR spectra in the range of 700–4000  $\text{cm}^{-1}$  obtained from (a) as-prepared SiNWs and (b) HF-etched SiNWs. In the spectrum of as-prepared SiNWs (Figure 37a), only Si–O vibrations at  $\sim 1050$  and  $\sim 800$   $\text{cm}^{-1}$  were observed. The strong absorption near 1050  $\text{cm}^{-1}$  is due to the in-plane stretching vibration involving the Si–O–Si moiety. The absorption at about 800  $\text{cm}^{-1}$  is due to in-plane bending vibration involving the same moiety. Upon etching with a dilute (5%) aqueous HF solution, new absorption bands attributable to Si–H<sub>x</sub> (2000–2200  $\text{cm}^{-1}$ , and  $\sim 900$   $\text{cm}^{-1}$ ) and CH<sub>x</sub> (2800–3000  $\text{cm}^{-1}$  due to organic impurities) were observed in the spectrum, while the Si–O absorption bands virtually disappeared (Figure 37b).

Figure 38 shows the vibrational spectra of HF-etched SiNWs in the frequency range of the Si–H stretching vibrations. Three broad overlapping bands, labeled as M, D, and T, can be observed. In accordance with the FTIR results of Si(111) and Si(100) wafers,<sup>107–111</sup> the M, D, and T bands were assigned to the monohydride (SiH), the dihydride (SiH<sub>2</sub>), and the trihydride (SiH<sub>3</sub>), respectively. These bands are composed of several unresolved peaks due to different chemical adstructures. Detailed assignments of these peaks, labeled M1, M2, M3, D1, D2, and T (also three or more unresolved peaks), can be found in the literature.<sup>107–111,122</sup>

To specify the adstructures, it is necessary to differentiate between isolated vs interacting vibrational modes of silicon hydrides in the IR spectra. This was accomplished by a



**Figure 36.** (a) TEM image of cSiNTs. Scale bar: 200 nm. (b) TEM image displaying a cSiNT with a thin wall. (c) TEM image displaying the open end of a cSiNT. Scale bars in b and c: 100 nm. (d) EDS spectrum taken from an individual Si tubular nanostructure. (Reprinted with permission from ref 47. Copyright 2004 Wiley-VCH.)

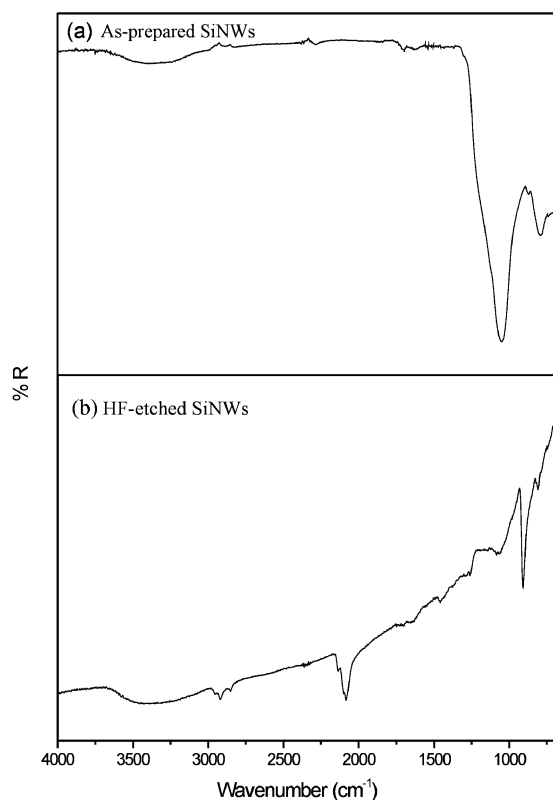
deuterated experiment described in ref 122. Suffice it to say here that the shapes of the envelopes of the SiH<sub>x</sub> and the SiD<sub>x</sub> peaks are rather similar and the ratios of the corresponding Si–H:Si–D stretching frequencies average about 1.38, which agrees with the expected theoretical ratio of 1.39 calculated on the basis of the (reduced) mass ratio of 2:1 for D vs H.

### 7.1.2. Scanning Tunneling Microscopic Observations

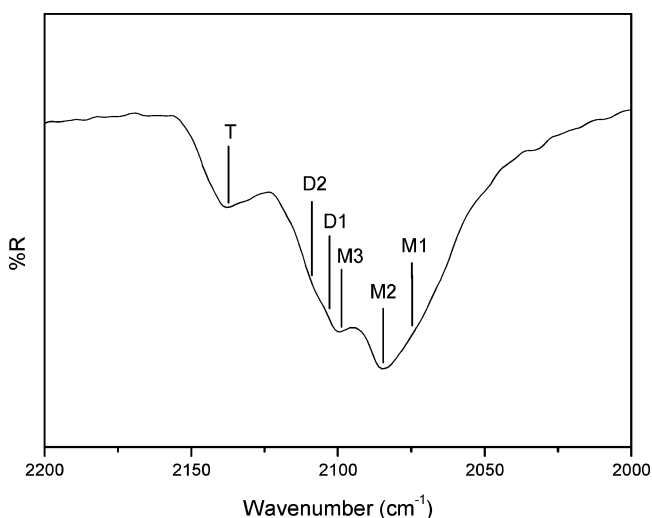
Direct observation of the arrangement of surface species on etched SiNWs is provided by STM, which revealed atomically resolved images as portrayed in Figure 39.<sup>123</sup> These images were interpreted as hydrogen-terminated Si-(111)-(1 × 1) and Si(001)-(1 × 1) surfaces corresponding to SiH<sub>3</sub> on Si(111) and SiH<sub>2</sub> on Si(001), respectively. We shall discuss these interesting STM results further in section 11.2.

## 7.2. Etched SiNWs: Why H-Terminated?

Chemical cleaning of silicon wafers play an important role in the manufacture of integrated circuits in the semiconductor industry. The so-called RCA cleaning procedure<sup>124</sup> has three major steps: (1) “organic clean” with a H<sub>2</sub>O<sub>2</sub>–NH<sub>4</sub>OH solution; (2) “oxide strip” with a dilute HF solution; and (3) “ionic clean” with a H<sub>2</sub>O<sub>2</sub>–HCl solution. In the second step, the oxides on the silicon surfaces are removed by dipping the silicon wafers into a HF solution.<sup>107–109</sup> This technique for oxide removal has recently been shown to be also applicable in the postgrowth treatment of silicon nanowires.<sup>122,123</sup> The etched silicon surfaces were found to be passivated by H instead of F for both silicon wafer<sup>107–109</sup> and silicon nanowires.<sup>122,123</sup> This is puzzling since a Si–F bond is almost twice as strong as a Si–H bond (bond energies: 5.7 vs 3.1 eV<sup>125</sup>). Because of the high electronegativity of F, one might have expected that silicon surfaces are F-terminated in the final step of the oxide removal.



**Figure 37.** ATR-FTIR spectra of (a) as-prepared SiNWs and (b) HF-etched SiNWs. (Reprinted with permission from ref 122. Copyright 2003 American Chemical Society.)



**Figure 38.** ATR-FTIR spectrum of HF-etched SiNWs in the range of 2000–2200  $\text{cm}^{-1}$ . (Reprinted with permission from ref 122. Copyright 2003 American Chemical Society.)

Attempts have been made to elucidate the phenomenon in various theoretical and experimental studies.<sup>126–132</sup> For example, Trucks et al.<sup>126</sup> proposed a mechanism of hydrogen passivation of silicon surfaces based on a transition-state theory, by considering the hydrogen fluoride molecule as the main reactive species attacking the Si surfaces. On the basis of the assumption that the Si–F bonds polarize the silicon back-bonds (the underlying layer) due to their highly ionic nature, this polarization was thought to facilitate the insertion of HF into the Si–Si bond, leading to fluorination of the surface silicon and hydrogenation of the underlying (second) layer silicon.

In an independent study, Zhang et al., proposed a “fluorination-induced back-bond weakening” rationale for the hydrogen termination based on extensive DFT calculations.<sup>133</sup> As the surface silicons are bonded with fluorine, the bonds between surface silicon atoms and the silicon atoms underneath are significantly weakened due to the high electronegativity of fluorine and the extraordinary strength of Si–F bonds. The weakened Si–Si back-bonds facilitate the reaction between the HF molecule and the Si surface, thereby peeling off the surface layer, leaving behind a hydrogen-terminated Si surface.

Two reaction pathways, or modes of attack, were proposed. As illustrated in Figure 40a, if there are three F atoms attached to a surface Si atom, the  $\text{SiF}_3$  strongly polarize and weaken the Si1–Si2 bond underneath and enhance the reactivity of the silicon back-bonds. The highly polar HF molecule attacks the “polar” Si–Si bond involving the  $\text{SiF}_3$ . The negatively charged F atom from the HF molecule will attack the positively charged Si1, and the positively charged H atom from the HF molecule will attack the negatively charged Si2, thereby abstracting the  $\text{SiF}_3$  moiety from the surface and resulting in a H-terminated surface. This reaction pathway may be termed “dipole–dipole” interaction. If the surface silicon is bonded with a single F atom, an alternative reaction pathway involving an “insertion-type” interaction is more appropriate, as depicted in Figure 40b. Here the F atom of the incoming HF molecule eventually attaches itself to the more positively charged Si1 and H to the remaining unsaturated Si2, leading to the hydrogenation of the silicon surface.

The reaction kinetics was also studied. Transition-state (activation energy) calculations modeled by various cluster structures in order to simulate the possible reaction pathways also suggest that H-terminated surfaces are more favorable than F-terminated surfaces. Details can be found in the literature (cf. ref 133).

### 7.3. Stabilities of SiNWs

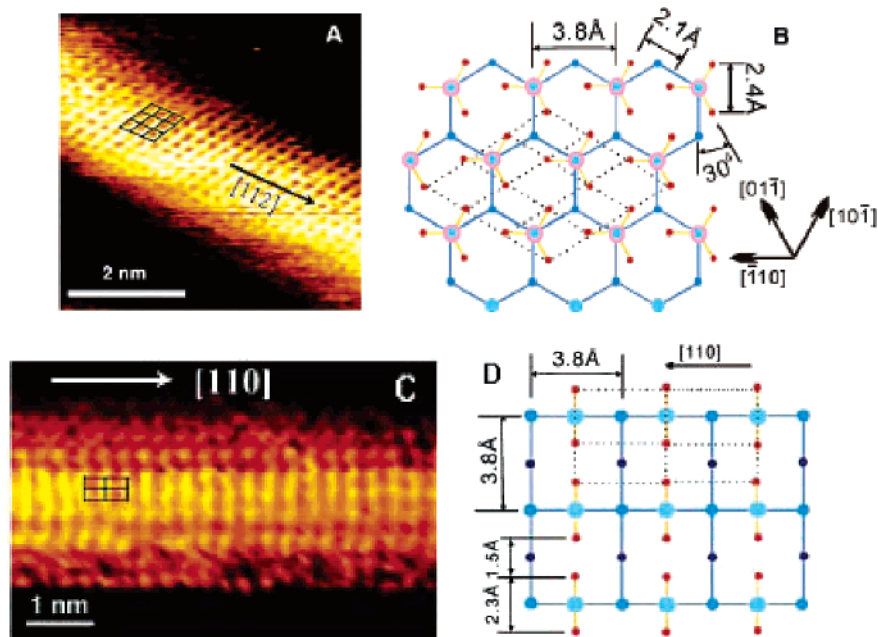
The thermal stability of the hydrogen-passivated surfaces of SiNWs was investigated by Sun et al., using FTIR spectroscopy.<sup>122</sup> It was found that hydrogen desorption due to the trihydrides occurred at  $\sim 550$  K and that due to the dihydrides occurred at  $\sim 650$  K. At or above 750 K, all silicon hydride species began to desorb from the surfaces of SiNWs. At around 850 K, the SiNW surfaces were practically free of all silicon hydride species.

The stabilities/reactivities of HF-etched SiNWs in air and in water were also studied. Hydrogen-passivated surfaces of SiNWs showed good stability in air (under ambient conditions) but relatively poor stability in water,<sup>122</sup> in comparison with the silicon wafer. The difference in the stabilities of hydrogen-passivated SiNWs in air vs in water may be associated with the hydroxide ion (albeit very low concentration in neutral solutions) in water and oxygen in air (vide infra), since it is known that hydroxide ions and oxygen can attack the silicon surface.

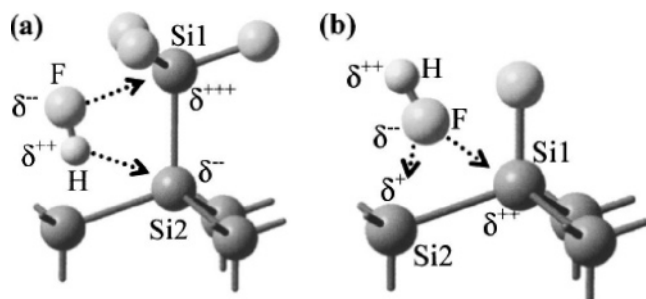
### 7.4. Etching SiNWs with HF and $\text{NH}_4\text{F}$

In a series of papers, Chen et al. reported a systematic study of the etching behavior and the surface speciation of SiNWs in various HF and  $\text{NH}_4\text{F}$  etching solutions.<sup>134,135</sup> Specifically, the concentration and pH dependences of the etching time, or the “stability”, of SiNWs in these solutions





**Figure 39.** STM images and theoretical views of (a, top panels) a SiNW with a Si (111) facet and (b, bottom panels) a SiNW with a Si (001) facet. (A) Constant-current STM image of the Si (111) facet of a SiNW on an HOPG substrate. The wire's axis is along the [112] direction. (B) Theoretical representation of SiH<sub>3</sub> on Si (111) viewed along the [111] direction. Red and large blue circles represent the H atoms and Si atoms in the SiH<sub>3</sub> moieties, respectively. Small blue circles represent Si (111) atoms in the layer below. (C) Constant-current STM image of the Si (001) facet of a SiNW on an HOPG substrate. The wire's axis is along the [110] direction. (D) Theoretical representation of the SiH<sub>2</sub> on Si (001). (From ref 123 (<http://www.sciencemag.org>). Reprinted with permission from AAAS.)

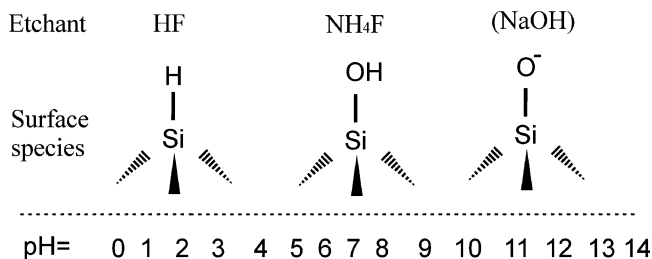


**Figure 40.** Schematic diagrams of (a) dipole-dipole interaction and (b) insertion-type interaction. (Reprinted with permission from ref 133 (<http://link.aps.org/abstract/PRB/v69/p125319>). Copyright 2004 by the American Physical Society.)

were investigated. It was concluded that NH<sub>4</sub>F is an efficient etchant for SiNWs and that SiNWs are stable only in relatively narrow pH ranges in these solutions. When SiNWs are etched with HF, the stability range is pH = 1–2, where the surface moieties are Si–H<sub>x</sub> species ( $x = 1-3$ ) and, at high HF concentrations, the H-terminated Si surfaces are covered with (passivated by) HF or HF-related molecules through H-bonding. When SiNWs are etched with NH<sub>4</sub>F, the stability range is pH = 12–14 (NaOH added for high pH values) where the surface moieties are mainly Si–(O<sup>−</sup>)<sub>x</sub> species ( $x = 1-3$ ) and, at high NH<sub>4</sub>F concentrations, the negatively charged Si surfaces are stabilized (passivated) by NH<sub>4</sub><sup>+</sup> ions via ionic bonding. These features, termed “double passivation” model, are represented schematically in Scheme 1, using monosubstituted surface silicon as examples, respectively. The same principles apply to di- and trisubstituted surface speciations.

To better understand the etching behaviors, ATR-FTIR spectroscopy was used to characterize the surface species on the SiNWs. It was found that, while etching SiNWs with HF gives rise to Si–H<sub>x</sub> surface species, no Si–H<sub>x</sub> species were observed when SiNWs were etched with NH<sub>4</sub>F. This

#### Scheme 1. Schematic Representations of Different Surface Species on SiNW Surfaces in Various HF–NH<sub>4</sub>F Solutions with Different pH Values



is to be contrasted with the Si wafer results in which etching with either HF or NH<sub>4</sub>F produces Si–H<sub>x</sub> species on the surface. This difference suggests that the Si–H<sub>x</sub> surface species produced in NH<sub>4</sub>F solutions are so unstable that they are hydrolyzed readily at pH > 4. Efforts were made to rationalize the strikingly different etching behaviors using HF vs NH<sub>4</sub>F as etchants, in terms of their concentration and pH dependences via the double passivation model described above.

#### 7.5. Similarities and Differences in Etching Behavior between 1-D and 2-D Silicon

While there are many similarities between 1- and 2-D Si systems, there are also striking differences in their etching behaviors. In both cases, variables such as the concentration and the pH value of the etching solutions and the oxidizing power (and its anisotropy, if any) of the etchant, along with experimental parameters such as the etching time and the dissolved oxygen (in air), all play important roles in determining the etching behavior, the resulting surface speciation, and the quality (smoothness, definition) of the surfaces.

First and foremost, as discussed earlier, ATR-FTIR measurements showed that, while etching SiNWs with HF

gave rise to Si–H<sub>x</sub> surface species, no Si–H<sub>x</sub> species were observed when SiNWs were etched with NH<sub>4</sub>F. The former is in line with the 2-D results. The latter, however, is at odds with the corresponding results reported for the 2-D Si wafers, where etching with NH<sub>4</sub>F produces Si–H<sub>x</sub> species on the surface. Indeed, etching Si wafers with HF, NH<sub>4</sub>F, or HF buffered with NH<sub>4</sub>F (BHF) all give rise to H-terminated silicon surfaces. It is believed that the nanoscale dimensions of SiNWs may have contributed to the rapid hydrolysis of the surface Si–H<sub>x</sub> species (to give Si–(OH)<sub>x</sub> or Si–(O<sup>–</sup>)<sub>x</sub>), especially at neutral or high pH values and in the presence of oxygen.

Second, as discussed earlier, SiNWs are stable only in relatively narrow pH ranges in the respective etching solutions (pH = 1–2 for HF and 12–14 for NH<sub>4</sub>F). These results differ from those of 2-D Si wafers and can be rationalized in terms of the double passivation model.

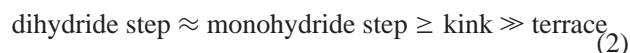
There are many studies regarding the pH dependence of the etching of Si wafers in various etching solutions. For example, Jakob and Chabal<sup>110</sup> first reported that the Si(111) surface etched in low pH (<5) HF-containing solutions exhibited a rough morphology, whereas those etched in high-pH (~6.6) HF-containing solutions gave rise to “atomically smooth” surfaces.<sup>108,137</sup> Under similar conditions, however, etching of Si(100) surfaces generally produces rougher surfaces. It is generally believed that the close-packing structure of the terminal hydrides on the Si(111) surfaces contributes to the smoothness of the surface by hindering the attacks by the etchants.

Third, the effect of oxygen on the etching behavior of 1-D SiNWs in different etching solutions is rather interesting. In acidic (HF) etching solutions, the etching curves (as a function of etchant concentration) are unaffected by oxygen. In neutral or basic (NH<sub>4</sub>F) solutions, oxygen greatly accelerates the etching process. These observations may be related to the dramatic changes in surface morphologies of 2-D silicon wafers upon etching in oxygen-containing vs oxygen-free etchants. For 2-D Si wafers, for example, Garcia et al.<sup>136</sup> reported that Si(111) surfaces etched in buffered HF solution (BHF) containing oxygen are much rougher than those etched in oxygen-free BHF (both of pH ~ 4.7). This effect was interpreted by these authors via a model involving kinetic competition between oxygen-induced and etchant-induced oxidation reactions, summarized below.

Previous morphological studies have shown that OH<sup>–</sup> is a highly *anisotropic* oxidant with the following site-specific rate of attack:



On the other hand, O<sub>2</sub> is an *isotropic* oxidant with the following site-specific rate of attack:



According to these authors, the etched surface morphology reflects the kinetic competition between these two oxidants. In low-pH solutions, the etch morphology is rough since O<sub>2</sub> oxidation dominates and the etching is isotropic. In high-pH solutions, the etching is dominated by OH<sup>–</sup> and the etch morphology is primarily determined by the anisotropy of the etchant (OH<sup>–</sup>). Since the rates of attacks of kinks and steps by OH<sup>–</sup> are much faster than that of the terraces, they are preferentially etched away. Thus, defect-free, almost perfect

“atomically flat surfaces” of Si(111), passivated with Si–H<sub>x</sub> species, can be obtained by etching with NH<sub>4</sub>F (which has a pH of 7.8).<sup>108,110,137</sup>

For 1-D SiNWs, the distinction between the isotropic (such as O<sub>2</sub>) and the anisotropic (such as OH<sup>–</sup>) etchants disappeared due to their nanoscale dimensions. Thus, SiNWs are etched away easily in solutions with pH values ranging from 3 to 10. In acidic HF solutions with pH of 1 to 2, however, protection by HF impedes oxidation by O<sub>2</sub>, whereas, in basic NH<sub>4</sub>F solutions of pH = 12–14, passivation by the ammonium ions again slows down the etching process. This is, in essence, the double passivation model.<sup>134,135</sup>

Fourth, while NH<sub>4</sub>F is a *slow* etchant for Si(111) surfaces in the 2-D system, it is an *efficient* etchant for the 1-D SiNWs grown from SiO, which also have predominantly Si(111) faces, again due to the nanoscale dimension of SiNWs.

Finally we shall close this section by demonstrating that, while etching behavior of silicon depends on many factors, the interplay between these effects (such as the pH of the etchant, the crystal orientation of Si wafer, and oxygen) may be exploited to produce smooth Si surfaces. For example, while Si(100) surfaces tend to give rough surfaces after etching by HF solutions with pH values of 4–7, a recent report by Schmidt et al.<sup>138</sup> showed that, in fairly acidic (pH ~ 0.5) solutions such as HF:H<sub>2</sub>SO<sub>4</sub>, etching of Si(100) surfaces can also produce smooth surfaces as well. This latter observation may be related to the etching behavior of SiNWs in acidic HF solutions discussed earlier. Here the effect of oxygen on the etching curve was minimal (almost nonexistent) at low pH (<1) values. Apparently the double passivation of the silicon surfaces by HF under acidic conditions protects the surfaces from attack by oxygen (oxidation) for both 1-D and 2-D Si systems.

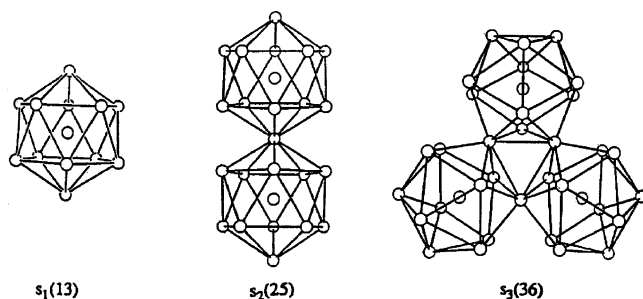
## 8. Silicon Nanowires as Platforms and Templates

In this section, we shall discuss the use of low-dimensional silicon-based nanomaterials as platforms, templates, and molds in creating other composite nanomaterials, which may or may not contain silicon. Role reversal, with other materials such as CNTs, zeolites, AAO as templates, can also afford a wide variety of silicon-based nanomaterials. In both cases, it involves reactions on the surfaces of the templates, or, in essence, doing chemistry at the interfaces between the substrates and the templates in the nanorealm.

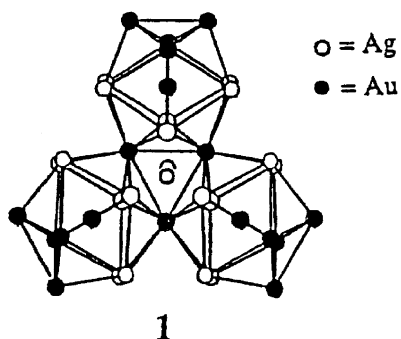
### 8.1. AuAgND/SiNW: Reductive Growth of Ligated Metal Nanodots on SiNWs

In an attempt to deposit structurally well-defined metal clusters, which may be considered as zero-dimensional “nanodots,” on one-dimensional semiconducting silicon “nanowires,” heterogeneous reaction between the nanosized polyicosahedral metal (PIMs) clusters<sup>139–146</sup> and HF-etched silicon nanowires was studied. The metal frameworks of these nanosized Au–Ag clusters can be described as vertex-sharing polyicosahedra. They grow in solution via a “cluster of clusters” growth pathway, giving rise to a well-defined growth sequence, from a single icosahedron with 13 atoms (*s*<sub>1</sub>(13)) to an icosahedron of 13 icosahedra with 127 atoms (*s*<sub>13</sub>(127)). These metal clusters are protected from spontaneous aggregation by organic ligands such as triphenylphosphine. The early members of the vertex-sharing polyicosahedral mixed-metal clusters are portrayed in Scheme 2. These ligand-protected nanosized metal particles are of interest in

## Scheme 2

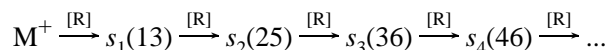


## Scheme 3



that they exhibit quantum-size effects with properties highly dependent upon the size, shape, structure, and composition of the metal core.<sup>139–146</sup>

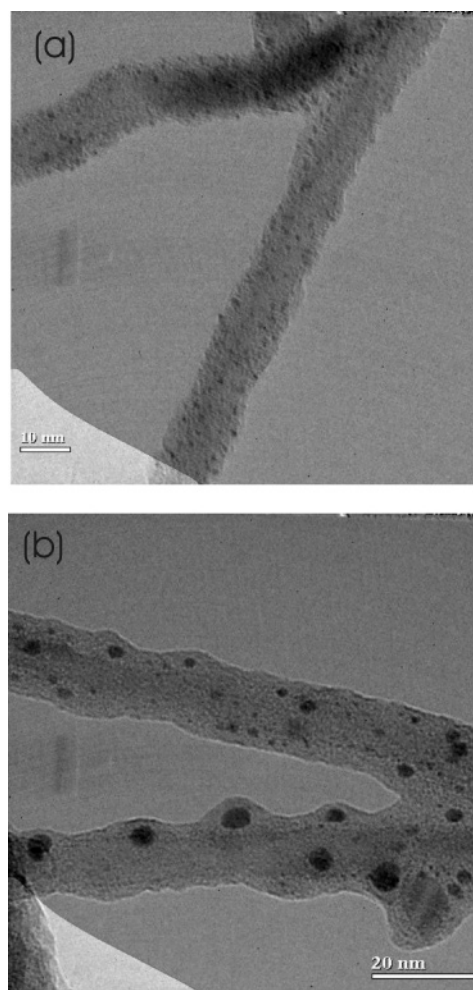
As reported in ref 147, the heterogeneous reduction causes a progressive growth of the metal clusters, in a way similar to the homogeneous reductive cluster growth observed in solution.<sup>139–146</sup> In the latter case, progressive reductive condensation of the metal clusters caused by chemical reducing agent [R] is a spontaneous but stepwise agglomeration process of a smaller cluster building block (in this case, an icosahedral cluster unit) as follows (cf. Scheme 2):



Here  $M^+$  denotes monocationic Au(I) or Ag(I) complexes and [R] represents reducing agents such as  $\text{NaBH}_4$ . In this process, instead of adding one atom at a time, the cluster “grows” by adding one icosahedron at a time, giving rise to the vertex-sharing polyicosahedral growth sequence via spontaneous self-assembly.

In ref 147, it was reported that reductive cluster growth of a triicosahedral cluster,  $(\text{Ph}_3\text{P})_{12}\text{Au}_{18}\text{Ag}_{20}\text{Cl}_{14}$  (**1**), depicted in Scheme 3, can occur on the surface of the hydrogen-passivated SiNWs. Cluster **1** is a vertex-sharing triicosahedral cluster with 18 gold and 20 silver atoms, encapsulated within a ligand shell containing 12  $\text{Ph}_3\text{P}$  ligands and 14 chloride ligands. The metal core measures  $1 \times 1.5 \times 1.5 \text{ nm}^3$  and has an oblate shape. The heterogeneous reaction was followed by high-resolution transmission electron microscopy.

The TEM images of the products from the reaction of the HF-etched SiNWs with a solution containing cluster **1** are shown in Figure 41. It was found that the original cluster (**1**) was reduced to clusters of larger sizes by the SiNWs within minutes. Concomitantly surface Si atoms were re-oxidized to silicon oxide. On the basis of the time sequence (by quenching the reaction at 5 min intervals) of the HRTEM images, the following general observations can be made. At the beginning, the metal clusters were chemisorbed (an-

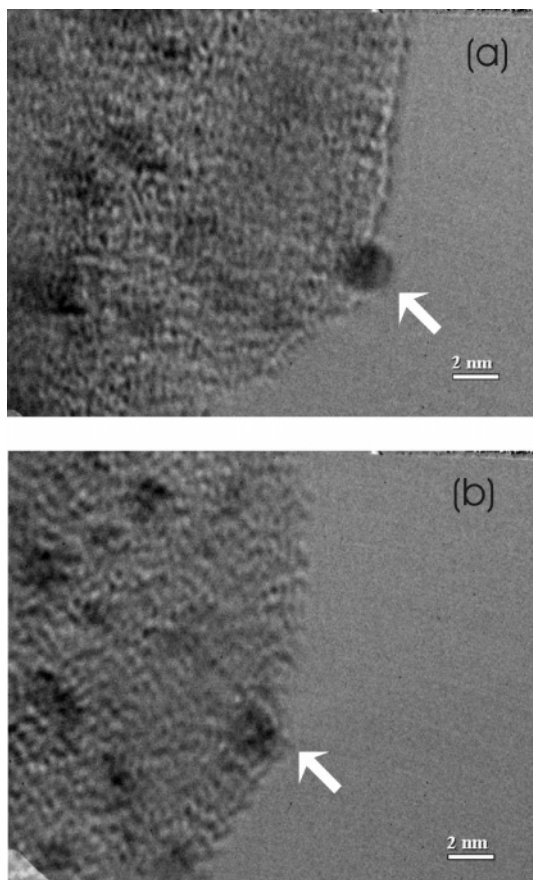


**Figure 41.** TEM image of the reduced AuAg cluster (**1**) on silicon nanowires: (a) at the beginning of the reaction; (b) after about 30 min. (Reprinted with permission from ref 147. Copyright 2002 American Chemical Society.)

chored) to the SiNW surface (Figure 41a). As the reaction progressed, the anchored metal clusters were reduced by the  $\text{SiH}_x$  (where  $x = 1, 2, 3$ ) and/or Si atoms on the SiNW surfaces and grew to form larger clusters on the SiNW surface. After about 30 min, metal clusters of different sizes, ranging from 1 to 7 nm in diameter, were observed on the SiNW surface (Figure 41b). In solution, larger metal clusters of 7–25 nm in diameter, as indicated by TEM, were obtained. Metal particles of sizes greater than about 5 nm in diameter are bulklike with the face-centered cubic structure (fcc), as indicated by electron diffraction (not shown). As the metal clusters grew to larger particle sizes (approximately 7–25 nm in diameter), they tended to separate from the SiNW surfaces. And finally, after about an hour, aggregates of these colloidal particles were formed and precipitated from the solution. As a result, the color of the solution turned from dark cherry red at the beginning to light red in about 30 min, and eventually to almost colorless after about an hour. A plausible mechanism for the heterogeneous reductive cluster growth of the Au–Ag cluster **1** on the surfaces of SiNWs can be found in ref 147.

Two interesting phenomena, the “sinking cluster” and the “cluster fusion” processes, were observed during the TEM observation of the reaction products. It was found that some metal clusters attached on the SiNW surface were sinking into the amorphous oxide layer under TEM observation. Parts





**Figure 42.** TEM image of the “sinking cluster” process: (a) at the beginning of the TEM observation; (b) after about 1 min. (Reprinted with permission from ref 147. Copyright 2002 American Chemical Society.)

a and b of Figure 42 are two snap shots of the sinking process of a cluster of approximately 2 nm in diameter (indicated by an arrow in Figure 42a). Under the intense electron, the throbbing cluster, while barely attached to the SiNW surface, sank beneath the surface of the oxide layer. And, after about 1 min, it was completely submerged in the oxide layer (Figure 42b). It was believed that the ligands played a role in the cluster “sinking” process. In other words, under intense electron beam irradiation, some of the phosphine and/or chloride ligands on the cluster were lost and the cluster became coordinatively unsaturated. The oxide ions in the silicon oxide layer became the replacement ligands, thereby stabilizing the cluster.

Another interesting phenomenon observed here is the “fusion” or “aggregation” of metal clusters (see Figure 5 of ref 147). It was found that clusters can travel a distance more than 10 times its size and fuse or link together to form larger clusters or aggregates, respectively. Since the rates of both the sinking and the aggregation processes appear to increase with increasing electron fluxes, it was suggested that electron irradiation, rather than thermal effects, provides the driving force for these processes.<sup>147</sup>

## 8.2. SiNW<sub>C</sub>CNT and SiNW<sub>C</sub>HCNT: Syntheses of Carbon and Hydrocarbon Nanostructures on SiNW (as Templates)

In this section, we shall discuss a special class of composite nanomaterials based on SiNWs and CNTs or HCNTs, where

HCNTs refers to a new type of hydrocarbon nanotubes. Specifically, SiNWs sheathed by CNTs or HCNTs, as represented by SiNW<sub>C</sub>CNT and SiNW<sub>C</sub>HCNT, respectively, can be prepared by ultrasonication of HF-etched SiNWs in common organic solvents. Further sonication causes demolding of the products, giving rise to the conventional CNTs and/or the new HCNTs. Depending upon the sonication time as well as other experimental conditions, a hybrid composite nanomaterial CNT/HCNT, with or without SiNW inside, can also be found. We shall discuss these interesting nanomaterials next.

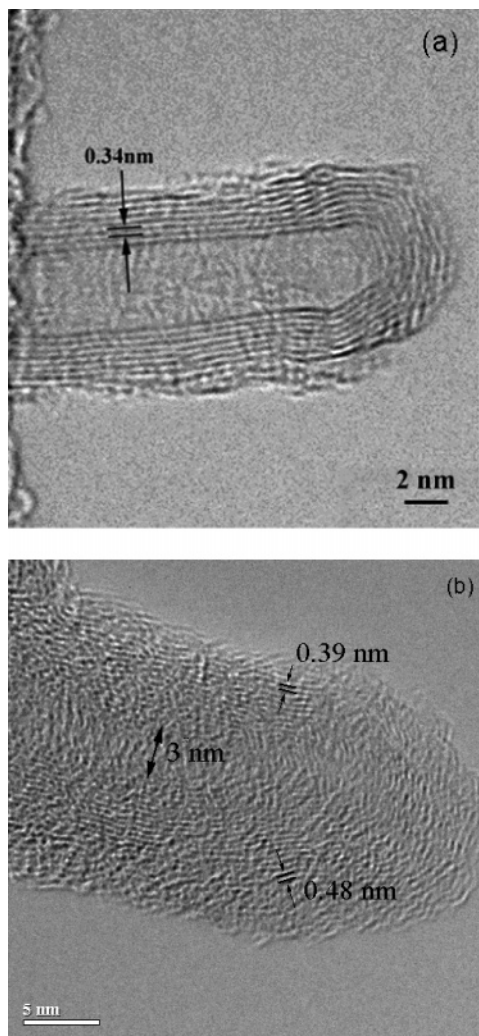
### 8.2.1. CNT(O)s vs HCNT(O)s via Sonochemical Reactions Using SiNWs as Molds

First we shall describe the synthesis of HCNTs, along with the conventional CNTs, using SiNWs as templates.<sup>148,149</sup> Conventional carbon nanotubes and nanofibers (CNOs) can be produced by such diverse techniques as arc discharge,<sup>4</sup> laser ablation,<sup>14</sup> CVD,<sup>150</sup> electron beam irradiation, and high-temperature annealing,<sup>151,152</sup> etc. Generally speaking, these carbon nanostructures can only be produced under such severe conditions as high temperature, high vacuum, high voltage arc discharge, or high-energy electron irradiation. Many of these preparative methods require specialized equipment (such as lasers and CVD) and metal catalysts. Recently, however, a simple sonochemical solution method, using SiNWs as templates, to produce carbon nanostructures under mild ambient conditions (room temperature and atmospheric pressure) and without metal catalysts have been reported.<sup>148,149</sup> These carbon nanotubes and nanofibers, termed HCNTs and HCNOs, have interlayer spacings ranging from 3.4 to 5.9 Å. Since many common organic solvents can be used, this simple method provides a new synthetic route to a wide variety of carbon and hydrocarbon nanomaterials.

These nanostructures exhibit a wide variety of shapes and forms, the most common ones being multiwalled hydrocarbon nanotubes. Most of these carbon nanostructures have a closed cap at one end and without encapsulated metal catalysts. Figure 43a depicts a typical CNT which has an inner diameter of 4 nm. The interlayer spacing is 3.4 Å, a distinctive signature of CNT. The HRTEM image of a typical hydrocarbon nanotube (HCNT) is shown in Figure 43b. This multiwalled HCNT has an outer diameter of 18 nm and an inner diameter of 3 nm. Unlike the conventional CNTs, HCNTs have wavy layers and interlayer spacings of 3.9–4.8 Å.

### 8.2.2. SiNW<sub>C</sub>HCNT and SiNW<sub>C</sub>CNT

It is believed that the SiNWs serve as templates in the formation of these nanostructures. Indeed, both SiNW<sub>C</sub>HCNT and SiNW<sub>C</sub>CNT were observed, along with the final product HCNTs and CNTs, in the ultrasonication process. This is evidenced by the “caught-in-the-act” HRTEM picture shown in Figure 44a. Here, a HCNT of about 4 nm in diameter and 65 nm in length was found to connect the tip of one SiNW (A) to the body of another SiNW (B). The SiNWs have diameters of about 30 nm. The EELS results, taken from the area between A and B, revealed that it is comprised purely of carbon. The HRTEM image in Figure 44b, taken from area A in Figure 44a, showed that this new type of HCNT has an interlayer spacing of 4.2 Å, emanating from the tip of SiNW A. This seven-layered HCNT (or a total of 14 layers) is connected to SiNW B as shown in Figure 44c, taken from area B in Figure 44a.



**Figure 43.** (a) High-resolution TEM (HRTEM) image of a typical CNT with interlayer spacing of 3.4 Å and 8 walls. (b) HRTEM image of a typical HCNT with inner and outer diameters of 3 and 18 nm, respectively. (Reprinted with permission from ref 149. Copyright 2005 American Chemical Society.)

Figure 45 shows the TEM element mapping results which confirm the chemical compositions of the SiNW (the template, silicon mapping, Figure 45b) and the HCNT (the product, carbon mapping, Figure 45c).

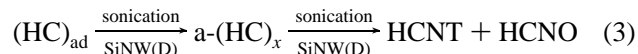
### 8.2.3. Templating Effect and Formation Pathway(s)

Ultrasonication is believed to play an important role in the formation of these HCNTs/HCNOs. In other words, chemical transformations on the surfaces of the SiNWs occur in the acoustic cavitation of ultrasound which can achieve a local heating of up to 5200 K in temperature with lifetimes of  $<1 \mu\text{s}$ .<sup>153</sup> In fact, sonication not only promotes the heterogeneous reaction between the  $\text{SiH}_x$  moieties on the SiNW surfaces and the organic molecules in solution to form the different types/shapes of carbon and hydrocarbon nanostructures but also causes the extrusion (or demolding) of the products (see Figures 44a and 45a).

On the surfaces of the SiNWs, the chemisorbed organic solvent molecules react with the  $\text{SiH}_x$  moieties, and, under the local heating condition of the ultrasonication process, result in the elimination of the substituents of the solvent molecules. In the case of chlorinated solvents, the reaction between the Si–H and C–Cl bonds results in dehydrochlori-

nation, giving rise to CH units which subsequently polymerize to form the hydrogenated graphene sheets<sup>154</sup> that wrap around the SiNWs (templating effect).

While these heterogeneous reactions may be rather complicated, they may be represented as



Here  $(\text{HC})_{\text{ad}}$  denotes the adsorbed hydrocarbon fragments on the surfaces of the SiNWs or silicon nanodots (hereafter referred to collectively as SiNW(D)s after the removal of the substituents (e.g., dehydrochlorination), and  $\text{a}-(\text{HC})_x$  represents the polymerized amorphous hydrocarbons. These hydrocarbon polymer fragments may resemble hydrogenated amorphous carbon (a-C:H) on the one hand and hydrogenated graphite on the other. The joining of the hydrogenated graphite fragments eventually forms wavy layers of HCNT(O)s.

Further ultrasonication also causes the SiNWs to shed off the HCNT(O)s, refreshing the SiNW surfaces for further reactions. The extruded HCNTs or HCNOs usually collapse to form different types of solid or hollow tubes or onions, depending on the types and frames of silicon nanostructures. One example of the collapsed HCNT as it extrudes from a SiNW is depicted in Figure 44b.

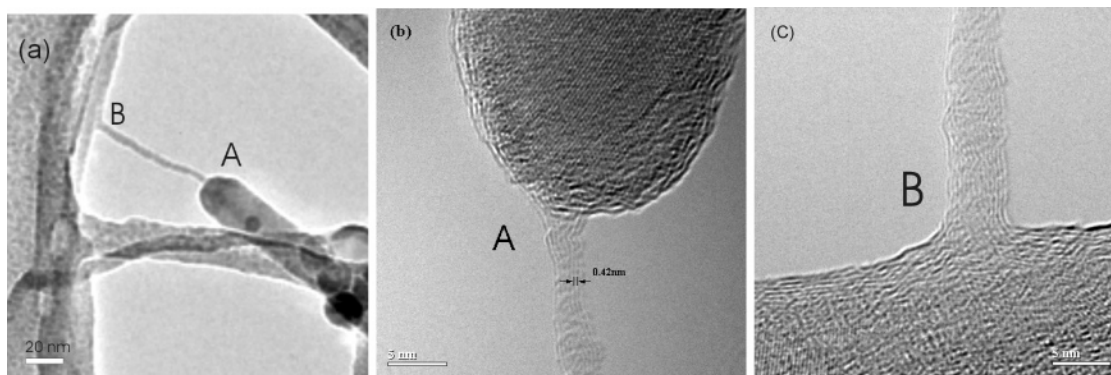
Upon prolonged ultrasonication (5 min), the HCNT(O)s, with interlayer spacings greater than 3.4 Å, can be converted to the conventional CNT(O)s, with interlayer spacings of 3.4 Å, as represented in eq 4. Apparently these transformations involve dehydrogenation reactions (which may be catalyzed by the SiNW(D) templates), followed by the annealing process.



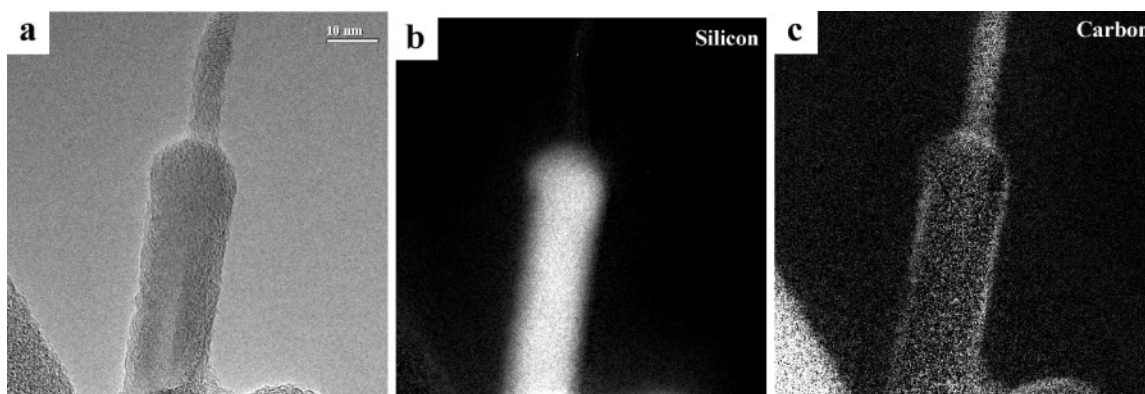
The nucleation and growth mechanism described above for the HCNT(O)s and CNT(O)s on SiNWs may be compared with the formation and growth of conventional carbon nanotubes. For example, nucleation and growth mechanisms of carbon nanotubes from polyene rings,<sup>155</sup> from two parallel carbon sheets via thermal activation,<sup>156</sup> or from a semifullerene nucleus,<sup>157</sup> as well as on a nanoparticle catalyst via a carbon precipitation process have been proposed.<sup>158,159</sup> In particular, carbon nanotube growth associated with metal particle catalysts has been proposed to occur by either a “root growth”<sup>160</sup> process, in which the nanotube base interfaces directly with the metal nanoparticles, or a “folded growth” mode,<sup>161</sup> in which the carbon shell that forms the nanotube wraps around the nanoparticles leading to the curved graphitic layers that extrude from the nanoparticle surface. In this context, the sonochemical growth of hydrocarbon or carbon nanotubes/onions on SiNWs reported here resembles more of the folded growth mode.

It is believed that these new structures of HCNTs/HCNOs are formed by networks of chair-form cyclohexane-like hexagonal structure, similar to that of partially hydrogenated graphite on the one extreme and that of amorphous hydrocarbon (a-C:H) on the other. Morphologically, they are similar to the conventional CNTs or CNOs except that C–H bonds have been inserted between layers, thereby converting curved  $\text{sp}^2$  sheets into puckered  $\text{sp}^3$  planes or combinations thereof. The more C–H bonds being inserted, the larger will be the interlayer spacings. The interlayer spacing also depends on the degree of packing between adjacent layers.





**Figure 44.** (a) TEM image of a HCNT connecting the tip of a SiNW (A) to the body of another SiNW (B). (b) HREM image taken from area "A" in a. (c) HRTEM image taken from area "B" in a. (Reprinted with permission from ref 148. Copyright 2002 American Chemical Society.)

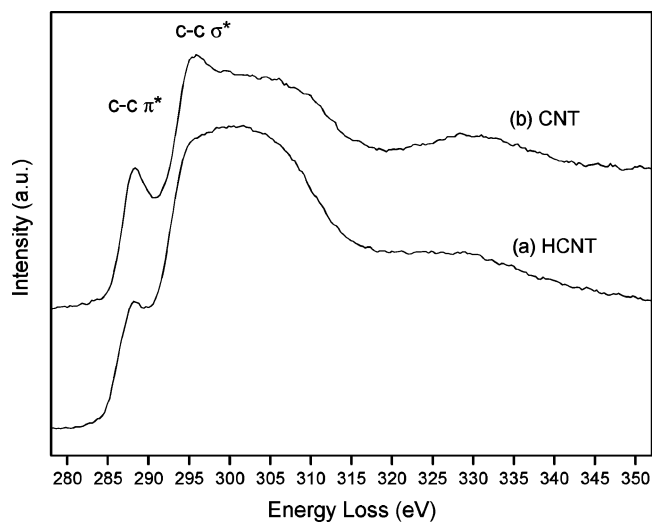


**Figure 45.** Caught-in-the-act: (a) TEM image of the extrusion of a multilayer HCNT from an oxide-removed SiNW. The elemental mapping images are as follows: (b) silicon mapping; (c) carbon mapping. (Reprinted with permission from ref 149 Copyright 2005 American Chemical Society.)

The characteristics of HCNT(O)s, which distinguish them from the conventional CNT(O)s, are as follows: (1) HCNT(O)s have wavy layers or shells; (2) their large and variable interlayer spacings range from 3.4 to 5.9 Å; (3) they easily shrink or buckle or can be damaged or broken by intense electron beam; (4) they are partially hydrogenated, the degree of hydrogenation decreasing with the sonication time; (5) they are free of metal or other catalysts; and (6) prolonged ultrasonication can convert HCNT(O) into CNT(O)s.

Spectroscopic data are consistent with the TEM observations and the proposed structural models for these carbon and hydrocarbon nanomaterials. For example, *single-tube* EELS results of individual new HCNT (curve a) and the normal CNT (curve b), shown in Figure 46, are consistent with this notion. The main difference between the new HCNT and the conventional CNT is that HCNT exhibits less  $sp^2$  bonds and more disordered  $sp^3$  bonds than that in CNT as evidenced by the edge ratio  $\sigma^*(C-C)/\pi^*(C=C)$  of approximately 1 for the conventional CNT but 1.5 for the new HCNT. This observation is consistent with the (partial) hydrogenation of the  $C=C$  bonds.

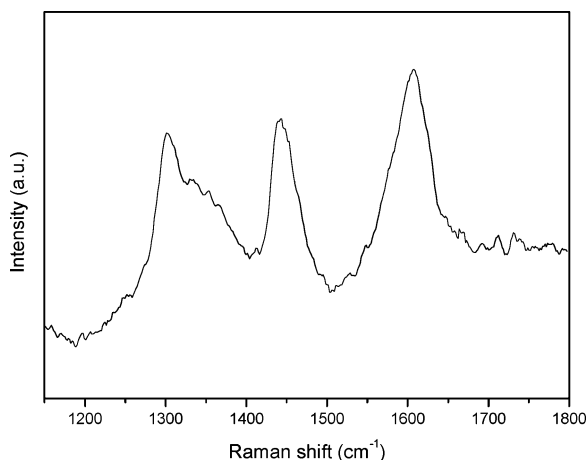
The Raman spectra of the products are also consistent with the structural model. The intense peaks at 517 and 960  $cm^{-1}$  can be ascribed to the scattering of the first-order optical phonon and the overtone of TO (L) of Si in SiNWs, respectively. More importantly, in the range of 1100–1800  $cm^{-1}$ , there were three weak peaks at 1300, 1450, and 1600  $cm^{-1}$ , depicted in Figure 47. The peak at 1300  $cm^{-1}$  can be assigned to  $sp^3$  (C–C single bond), whereas that at 1600  $cm^{-1}$  to  $sp^2$  (C=C double bond) stretching frequencies of the HCNT(O)s. The peak at 1450  $cm^{-1}$  is rather unusual



**Figure 46.** Comparison of the EELS of an individual hydrocarbon nanotube (HCNT) (curve a) with that of a normal carbon nanotube (CNT) (curve b). (Reprinted with permission from ref 148. Copyright 2002 American Chemical Society.)

and may be tentatively assigned to a carbon–carbon stretching frequency corresponding to a bond order of approximately 1.5. We note that these bands are very different from those observed for conventional CNTs, which has a strong peak at 1580  $cm^{-1}$  ( $sp^2$ ), the so-called G-band tangential mode, and a much weaker peak at 1348  $cm^{-1}$  ( $sp^3$ ), the so-called D-band related to the disordered graphite and/or amorphous carbon. For comparison, the characteristic Raman peak of diamond occurs at 1332  $cm^{-1}$  which may be taken





**Figure 47.** Raman spectra of hydrocarbon nanostructures (HCNTs). (Reprinted with permission from ref 149. Copyright 2005 American Chemical Society.)

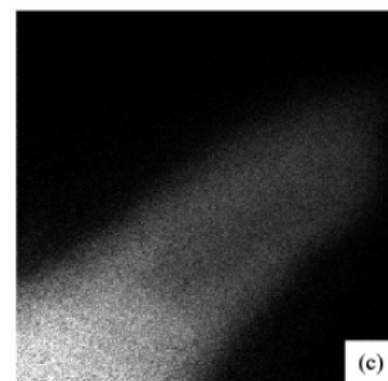
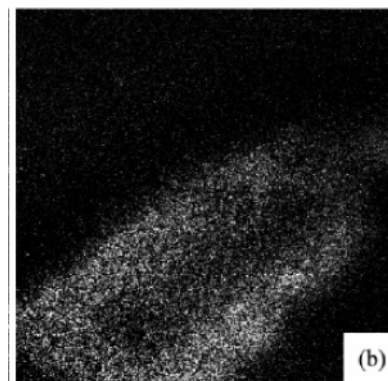
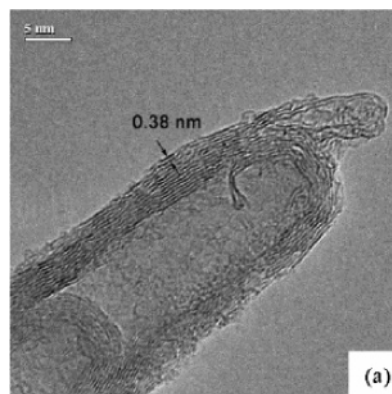
as the bench mark for the  $sp^3$  C–C single-bond stretching frequency.

Other related reports of the synthesis of CNTs and CNOs are worth mentioning.<sup>162–165</sup> One is a recent report of the synthesis of single-walled carbon nanotubes on the surface of the silica powder in *p*-xylene under sonication conditions.<sup>164</sup> This method is similar to that using SiNWs as molds just described; however, it requires ferrocene as the precursor of Fe catalyst and silica powder as the nucleation site. Two reports on the synthesis of CNTs<sup>162</sup> and CNOs<sup>163</sup> by arc discharge (using graphite electrodes) in water at room temperature have also appeared. Finally, Lee and co-workers produced CNT-encapsulated crystalline SiNWs by a hot filament chemical vapor deposition (HFCVD) method.<sup>165</sup> At  $\sim 900$  °C, carbon multilayers were formed on the surface of carbonized SiNWs. However, at a higher reaction temperature ( $\sim 1000$  °C), the silicon core reacted with carbon and transformed into a  $\beta$ -SiC core. Carbon shells formed on the SiC core were not as uniform as those on the Si core. As the substrate temperature increased further to 1100 °C, featherlike carbon sheets sprouting from the surface of the nanowires were formed. At an even higher deposition temperature (1300 °C), a mixture of carbon flakes with  $\beta$ -SiC nanowires was obtained.

### 8.3. CNT $\subset$ SiCNT: Synthesis of SiCNTs using CNTs as Reactive Templates

Among the various semiconducting materials, silicon carbide possesses unique physical and electronic properties which make it a suitable material for the fabrication of electronic devices for high-temperature, high-power, and high-frequency applications.<sup>166</sup> One-dimensional SiC nanostructures may exhibit unique properties due to quantum-size effects, making them useful materials in nanotechnology and nanoscale engineering. In this subsection, we shall describe the synthesis of SiCNT using CNT as a reactive template, thereby producing a new composite heterostructure of CNT $\subset$ SiCNT.<sup>167</sup>

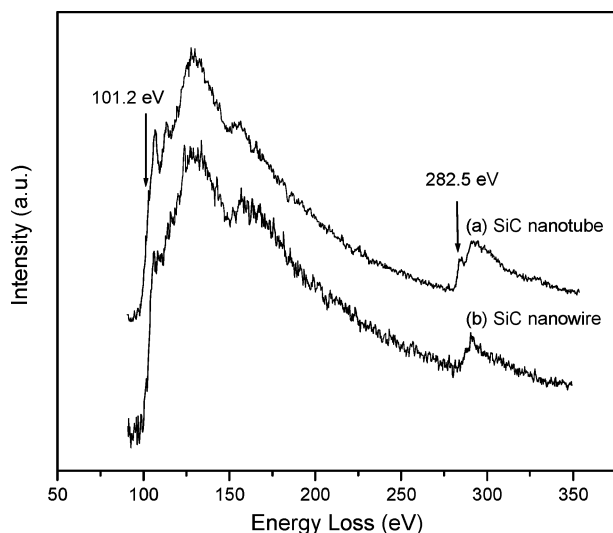
In ref 167, the growth of one-dimensional nanostructures of SiC was observed in the reaction between silicon (produced by disproportionation of SiO) and carbon nanotubes (as templates) in a tube furnace (at about 935 °C). The original goal was to synthesize SiNTs (see section 3) using CNTs as molds. Instead, three types of interesting SiC nanostructures were obtained. The first type is the silicon



**Figure 48.** (a) HRTEM image of a SiC nanotube structure with 3.8 Å interlayer spacings. Panels b and c are Si and C element mappings of the SiC nanotube in a, respectively. (Reprinted with permission from ref 167. Copyright 2002 American Chemical Society.)

carbide nanowires with 2.5 Å spacing of the {111} planes of  $\beta$ -SiC with the cubic zinc blende structure. These nanomaterials are similar to those produced by Pan et al.<sup>168</sup> The second nanostructure obtained was the biaxial nanowires of silicon carbide–silicon oxide (see Figure 3a,b of ref 167). A similar biaxial structure had been observed by Wang et al.<sup>169</sup> The biaxial SiC|SiO<sub>x</sub> nanowires consist of two side-by-side subnanowires of  $\beta$ -SiC and silica to be described in section 9.3.3.1.

A third type of nanostructure may be described as CNT $\subset$ SiCNT. A typical image is shown in Figure 48a. Element mappings (Figure 48b,c) showed the multiwalled tube structures to be composed of Si and C with the interior being CNTs and the exterior being SiCNTs. Furthermore, the interlayer spacings of the exterior multiwalled SiCNTs are significantly larger than those of 3.4 Å normally observed for the interior multiwalled CNTs (see Figure 48a).<sup>167</sup>



**Figure 49.** EELS spectra of (a) a single SiC nanotube and (b) a single SiC nanowire. Both were found in the B3 sample. (Reprinted with permission from ref 167. Copyright 2002 American Chemical Society.)

It is known that, at a sufficiently high temperature ( $T > 800$  °C), Si can react with C to form silicon carbide.<sup>170</sup> At the experimental temperature of 935 °C, Si and C react to form SiC. The transformation of carbon nanotube to a silicon carbide nanotube is controlled by the diffusion of Si to the SiC/C interface. However, since the Si diffusion rate through bulk SiC is extremely slow in the temperature range of 800–1000 °C, a steady supply of Si atoms from the disproportionation of SiO must therefore be transported primarily via surface diffusion.<sup>171</sup> This is consistent with the observation that the SiCNTs were formed layer by layer, from outside in, via diffusion of Si atoms into the multiwalled carbon nanotube.<sup>167</sup>

The EELS spectrum (curve a in Figure 49) of a single multiwalled SiCNT shows that the Si  $L_{3,2}$ -edge shifts to a higher energy at 101.2 eV (from 99.3 eV of pure silicon) and the C K-edge shifts to a low energy at 282.5 eV (from 284 eV of pure carbon), indicating a strong chemical bonding between Si and C. This is to be expected on the basis of the fact that carbon is more electronegative than silicon. The EELS of SiCNT is contrasted with the EELS of  $\beta$ -SiC nanowire (curve b in Figure 49). With the exception of the preedge peaks, the two EELS spectra are rather similar. The strong preedge absorption peaks of both the Si and the C EELS of SiCNT (curve a of Figure 49) are indicative of the  $\pi$  bonding between Si and C (compare with curve b of Figure 49 for  $\beta$ -SiC).

The observed multiwalled SiC nanotube is a new polytype (allotrope) of SiC, with interlayer spacings, ranging from 3.5 to 4.5 Å, distinctly different from those of the amorphous SiC or any of the common crystalline SiC phases (such as the cubic (3C), hexagonal (4H, 6H), or rhombohedral (15R) structures, etc).<sup>166</sup> It was also proposed that the structure of these new SiC nanotubes is similar to that of carbon nanotubes with silicon atoms substituting half of the carbon atoms in the curved hexagonal graphite tubular structure.

#### 8.4. Formation of Gold Nanocables on SiNWs: SiNW<sub>C</sub>AuNT

The potential applications of SiNWs in interconnection and as basic components in future mesoscopic electronic and

optoelectronic devices raise the issues of electrical conductivity of SiNWs and the patterning of electrical (ohmic) contacts to SiNWs. Although SiNWs can be mass-produced, it is difficult to increase the electrical conductivity of SiNWs during the growth process. A number of strategies have been developed in order to provide ohmic contacts to SiNWs, including deposition of Ag particles on SiNWs by chemical methods,<sup>172,173</sup> or formation of metal silicide layers on SiNWs.<sup>174</sup> A simple and effective technique to fabricate a metal thin film on the surface of SiNWs, or SiNWs wrapped with Au cable (SiNW<sub>C</sub>AuNT), was reported.<sup>175</sup>

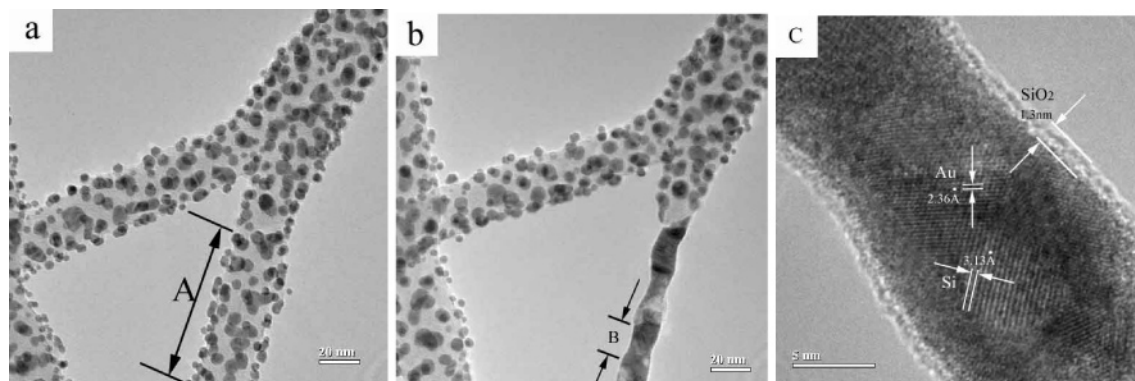
In Figure 50a, gold nanoparticles, with an average diameter of 5 nm, were deposited onto the silicon oxide surfaces of the SiNWs via argon-ion sputtering. Most, if not all, of the Au particles were crystalline with distinct facets. Some of the Au nanoparticles, however, aggregated to form larger fused clusters. The region marked “A” was annealed by the electron beam in the TEM. It can be seen that all Au particles in this region were transformed into a metallic layer covering the surface of the SiNW as depicted in Figure 50b. The diameter of the annealed region was reduced about 50% in comparison to region “B” in Figure 50b, a HRTEM image shows an Au film covering the SiNW which is in turn covered by a SiO<sub>2</sub> layer of about 1 nm, as shown in Figure 50c. Judging from the lattice parameters (d-spacings), the Au film and some bared (uncovered) Si spots can be found on the SiNW surfaces as shown in Figure 50(c).

Parts a–d of Figure 51 depict the snapshots and the time sequence of the Au film formation process. In Figure 51a, a polyhedral Au nanoparticle, about 5 nm in diameter, was attached to the surface of a SiNW. Part of this Au nanoparticle was covered by SiO<sub>2</sub> (serving as ligands). In Figure 51b, the attached SiO<sub>2</sub> ligand began to disappear, and the Au nanoparticle started to sink into the SiO<sub>2</sub> layer of SiNW. In Figure 51c, half of the Au nanoparticle merged with the existing Au film layer. In Figure 51d, the entire Au nanoparticle disappeared and integrated with the existing Au film layer. It is interesting to note that, in the process (Figure 51b–d), the Au nanocrystal rotated and reoriented to match the lattice orientation of the existing Au film layer.

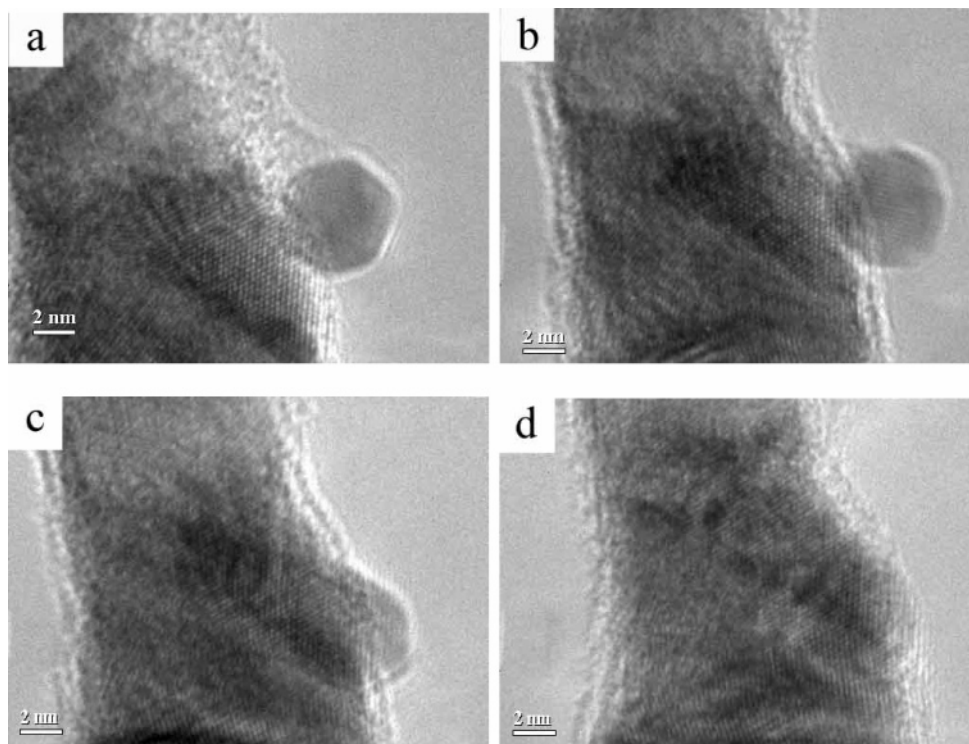
In the second part of the study, SiNWs with the oxide layer removed (by HF etching) were coated with Au nanoparticles and annealed by an electron beam in the same fashion. The results are similar. The reader is referred to ref 175 for details.

##### 8.4.1. Formation of AuNW<sub>C</sub>SiO<sub>2</sub>NT: SiNWs as Sacrificial Templates

When the heterostructures SiNW<sub>C</sub>AuNT (Au nanocable wrapped around SiNWs), as described in the previous section, were furnace annealed at  $\sim 880$  °C and  $10^{-2}$  Torr, uniform crystalline AuNWs were formed in the core of the nanowire, with the SiNWs being oxidized to SiO<sub>2</sub> concomitantly.<sup>176</sup> Figure 52 shows TEM images of an AuNW inside a SiO<sub>x</sub> sheath. The resulting heterostructure may be designated as AuNW<sub>C</sub>SiO<sub>2</sub>NT. The formation of AuNWs is due to the softening of SiNWs upon oxidation and the enhanced Au diffusion at elevated temperatures. The SiO<sub>2</sub> overlayer on AuNWs can be readily removed by HF etching to expose the AuNWs. Thus, the furnace annealing of Au-coated SiNWs offers a simple method of synthesizing very thin crystalline Au nanowires.



**Figure 50.** (a) Au nanoparticles, with an average diameter of 5 nm, are randomly attached to the surface silicon oxide layer of the SiNWs. (b) The region marked “A” in a was annealed by the electron beam in the TEM. It can be seen that all Au particles in this region transformed into a metallic layer covering the surface of the SiNW. (c) HRTEM image of region “B” in b shows an Au film covering the SiNW, which is in turn covered by a SiO<sub>2</sub> layer of about 1 nm. (Reprinted with permission from ref 175. Copyright 2002 American Chemical Society.)



**Figure 51.** (a) Polyhedral Au nanoparticle, about 5 nm in diameter, was attached to the surface of a SiNW. (b) The Au nanoparticle started to sink into the SiO<sub>2</sub> layer of SiNW. (c) Half of the Au nanoparticle merged with the existing Au layer. (d) The entire Au nanoparticle disappeared and integrated with the existing Au layer. (Reprinted with permission from ref 175. Copyright 2002 American Chemical Society.)

## 9. Silicon-Based Low-Dimensional Nanomaterials

In this section, we shall provide a systematic review of the syntheses and structures of various silicon-based low-dimensional nanomaterials with special emphasis on building a wide materials base for future nanotechnological applications. Specifically, we shall focus our attention on  $n$ -D on  $m$ -D silicon-based composite nanomaterials where  $n, m \leq 2$ .

Since there are many excellent reviews dealing with 0-D on 0-D and 2-D on 2-D, these topics will only be touched upon briefly.

### 9.1. 0-D on 0-D

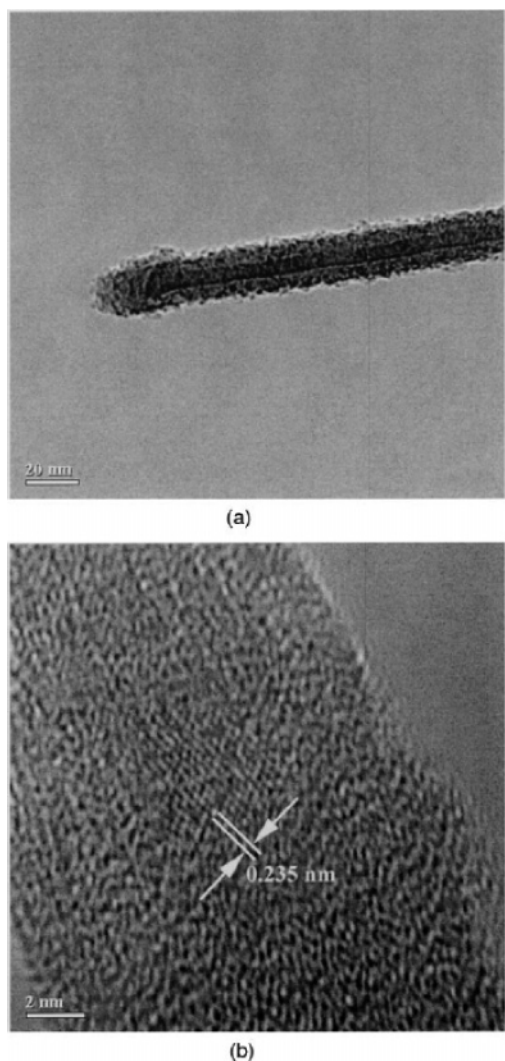
Composite nanomaterials based on 0-D Si nanodots (or nanocrystals, or quantum dots) have attracted considerable interests in microelectronics, optoelectronics, photonics, and

hybrid composite materials.<sup>177–190</sup> There are two major morphologies in SiND-based composite nanomaterials: those involving free-standing SiND structures and those in which SiNDs exist in solid solution (as in SiO<sub>x</sub> matrix,  $x \leq 2$ )<sup>191,192</sup> or as part of a solid network (as in porous Si).<sup>193–196</sup> The latter can also be categorized as 0-D in 2D. Almost all the free-standing SiNDs have to be stabilized or functionalized by an oxide, a ligand, or a self-assembled molecular outer layer, resulting in the formation of a core–shell structure. Many excellent reviews<sup>188,189,192–199</sup> are available for 0-D SiND-based composites, specifically those involving SiNDs/SiO<sub>x</sub> matrix and porous Si. We will briefly discuss some interesting SiNDs core–shell structures and silica-based core–shell heterostructures in the following sections.

#### 9.1.1. Silicon-Based Core–Shell Heterostructures

The most common SiND core–shell structures are formed by surface modification and/or functionalization of SiNDs





**Figure 52.** (a) TEM image of AuNW inside a  $\text{SiO}_x$  sheath formed by annealing the Au-coated SiNW at  $880\text{ }^\circ\text{C}$  for 1 h at  $10^{-2}$  Torr, and (b) the corresponding HRTEM image showing the Au core. (Reprinted with permission from ref 176. Copyright 2004 American Institute of Physics.)

during the synthesis process or postprocess.<sup>200–204</sup> The outer layers may be oxide, metal, or molecules, etc., depending on the surface reactions and treatment methods used.<sup>200–204</sup> One example is the (silicon core)–(gold shell) structures  $\text{SiND@AuNS}$ .

It is also possible to fabricate the reverse core–shell structure in which alkyl (R) terminated Si is the outer shell layer with the core being another material such as Ge, or  $\text{GeND@Si-RNS}$ .<sup>205</sup> This reverse core–shell material was synthesized via a solution synthesis route. The reaction of  $\text{SiCl}_4$  with  $\text{Mg}_2\text{Ge}$  in tri(ethylene glycol) dimethyl ether (triglyme) produces nanometer-sized  $\text{GeND@Si-CINS}$  crystallites with a chloride passivated surface. Further reaction with alkyllithium provides a stable surface terminated with alkyl groups. The resulting crystalline particles (average 5.8 nm in diameter) can be suspended in organic solvent, such as hexane or cyclohexane, or isolated as a powder. The termination with alkyls protects the Si surface from oxidation and allows these Ge nanoparticles to be soluble in a variety of organic solvents, thus making them amenable for polymer blends in device applications.

If 30%  $\text{H}_2\text{O}_2$  was added to the  $\text{GeND@Si-CINS}$  colloid solution,  $\text{GeND@SiO}_2\text{NS}$  structures can be obtained. The

$\text{SiO}_2$  termination provides a different surface modification that allows one to probe the photoluminescence (PL) of these nanoparticles with different surfaces. The  $\text{SiO}_2$  termination also provides an alternate surface that can be further modified to make more complex arrays of nanoparticles attached to surfaces or polymers.

### 9.1.2. Silica-Based Core–Shell Heterostructures

Silica ( $\text{SiO}_2$ ) can be a good “core” as well as a good “shell” material in the fabrication of 0-D core–shell heterostructures. The use of silica as a coating (shell) material has a long tradition in colloid science.<sup>187</sup> One reason is the good stability of silica colloids (especially in aqueous media), though other reasons such as easy control of the deposition process (and the shell thickness), processability, chemical inertness, controllable porosity, and optical transparency, etc., are also attractive features. All these properties make silica an ideal, low-cost material to tailor surface properties, while basically maintaining the physical integrity of the underlying core material. Different core materials such as metals (e.g.,  $\text{AuND@SiO}_2\text{NS}$ ,  $\text{AgND@SiO}_2\text{NS}$ ,  $\text{FeND@SiO}_2\text{NS}$ ), metal oxide (e.g.,  $\text{Fe}_3\text{O}_4\text{ND@SiO}_2\text{NS}$ ), and semiconductor (e.g.,  $\text{CdSND@SiO}_2\text{NS}$ ,  $\text{CdTeND@SiO}_2\text{NS}$ ) have been coated with silica to form core–shell nanoparticles.

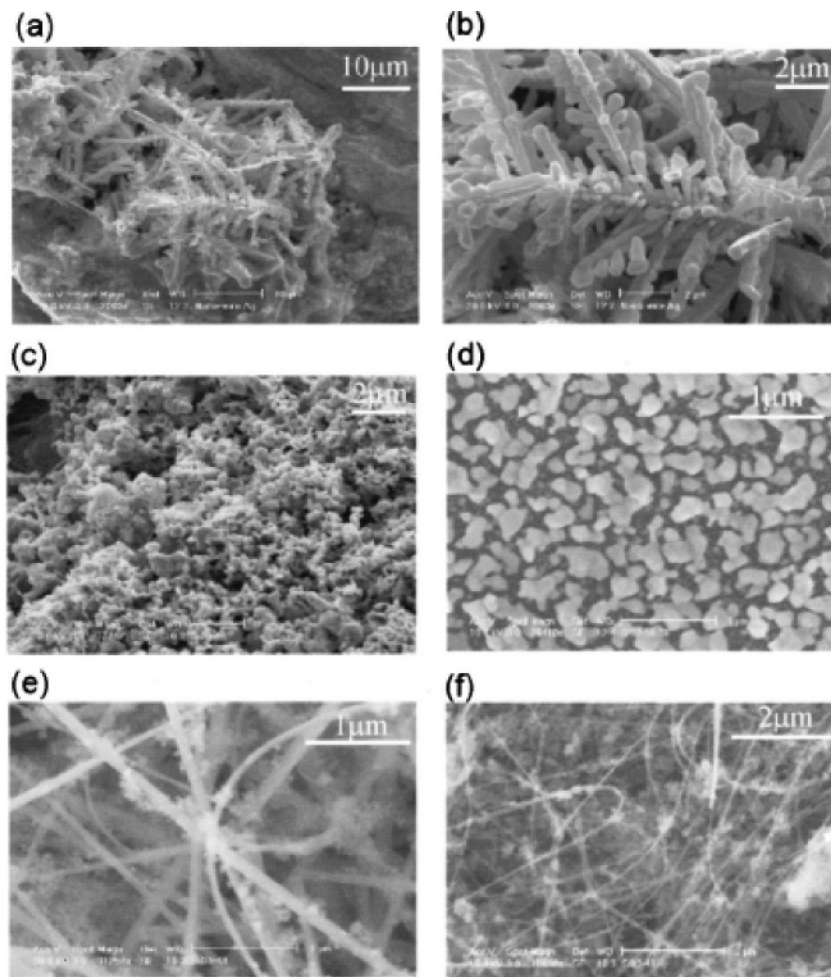
Hollow nanospheres can also be coated with silica. This gives rise to hollow multishell heterostructures. For example, silica-coated gold hollow nanospheres (designated here as  $\text{AuNS@SiO}_2\text{NS}$ ) with tunable interior-cavity sizes had been fabricated by a two-step reaction scheme.<sup>206</sup> First, uniform gold hollow nanospheres with tunable interior-cavity sizes were fabricated by using Co nanoparticles as sacrificial templates and varying the stoichiometric ratio of starting material  $\text{HAuCl}_4$  over the reductants. Then the hollow gold nanospheres were coated with amorphous silica by using the Stöber method.<sup>206</sup> The surface plasmon resonance peak corresponding to the hollow gold nanospheres shifted over a region of more than 100 nm in wavelength due to the change in shell thickness.

Another interesting example is the silica-coated carbon nanoion heterostructure  $\text{CNO@SiO}_2\text{NS}$ . This core–shell nanostructure was synthesized via a slow reaction (days) of  $\text{AuND@SiO}_2\text{NS}$  of 15 nm in diameter with  $\text{CCl}_4$  (as solvent).<sup>207</sup> The silica covering of  $\text{AuND@SiO}_2\text{NS}$  is porous in nature, and the gold core is accessible for halocarbons. It is believed that confinement of carbon formed within the nanoshells forces its conversion to onions. The halocarbon mineralization process is catalytic in nature, producing more carbon per metal ion removed. This appears to bring carbon atoms together, leading to the formation of the onions.

Silica is also a good nanodot core material. For example, silica nanospheres can be used as templates for metal shell deposition to form  $\text{SiO}_2\text{ND@MNS}$  structures. Metals (M) such as Au, Ag can be deposited on silica nanospheres via either metal ion or colloid reduction in solution,<sup>208–219</sup> or via thermal evaporation techniques.<sup>220,221</sup> The silica core supported metal shell structures are good candidates for plasmon resonances investigation. Noble metal nanoshells (e.g., Au, Ag) exhibit a strong, plasmon-derived optical resonance, typically shifted to much longer wavelengths than the plasmon resonance of the corresponding solid metal nanospheres.

### 9.1.3. Core–Multishell Heterostructures

In principle,  $\text{MND@SiO}_2\text{NS}$  or  $\text{SiO}_2\text{ND@MNS}$  structure can further be coated by metal or silica, respectively, via



**Figure 53.** SEM images of different silver structures formed in (a) 0.1, (b) 0.1 (zoomed-in image), (c)  $1.0 \times 10^{-2}$ , (d)  $1.0 \times 10^{-3}$ , (e)  $1.0 \times 10^{-4}$ , (f)  $1.0 \times 10^{-6}$  M silver nitrate solutions. (Reprinted with permission from ref 172. Copyright 2001 American Institute of Physics.)

the synthetic strategies described above to form core–multishell heterostructures. For example, a  $\text{SiO}_2@AuNS@SiO_2$  multishell heterostructure had been fabricated, starting with the  $\text{SiO}_2@AuNS$  structure.<sup>222</sup> The outer silica layer provides greatly enhanced thermal stability of the nanoparticle, raising its melting temperature by  $300^\circ$  relative to uncoated nanoshells.

Core–multishell heterostructures of general formulas  $ND@NS1@NS2@NS3\dots$  can in principle be made sequentially with different kinds of materials, giving rise to a wide variety of interesting 0-D nanostructures.

## 9.2. 0-D on 1-D

Zero-dimensional nanodots or nanoshells can be deposited on the outside or the inside of one-dimensional nanowires or nanotubes. In the following subsections, the word “nanodots” is taken to mean either solid nanodots, hollow nanoshells, or composite core–shell nanostructures discussed in the previous sections.

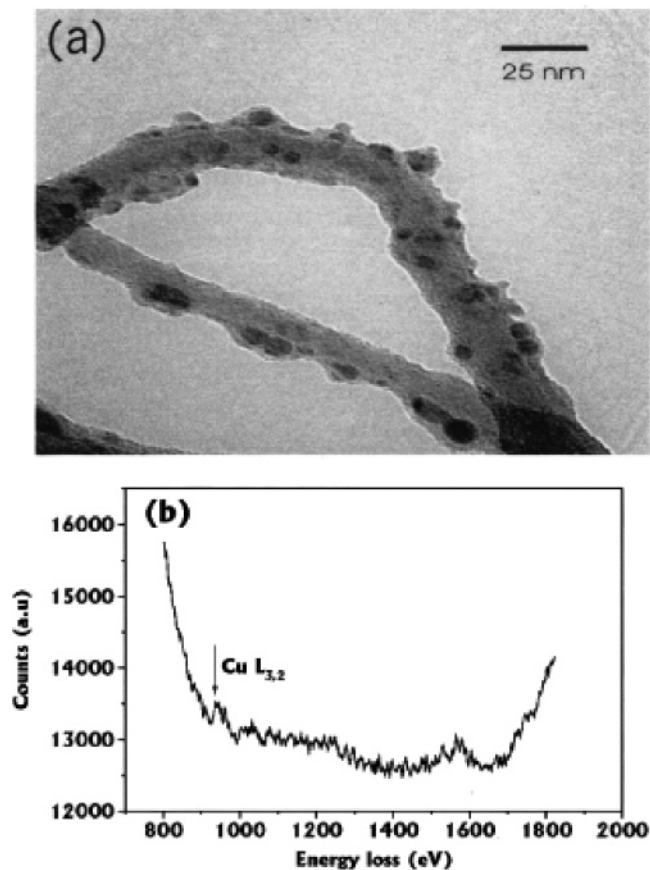
### 9.2.1. Nanodots on Nanowires: $ND\text{-}NW$

HF-etched SiNWs exhibit moderately high reactivity in solution as a reducing agent. The reductive growth of nanosized Au–Ag clusters on HF-etched SiNWs in organic solvents have already been discussed.<sup>147</sup> HF-etched SiNWs can also reduce a number of metal ions such as silver, copper, palladium, and rhodium in aqueous solution to produce metal nanoparticles on the surfaces of SiNWs at room temperature,

with concomitant reoxidation of the SiNW surface.<sup>172,173,223</sup> By varying the concentration of the metal ions in solution, nanostructures of these metals with different shapes and sizes can be produced. These reactions provide a simple method to fabricate zero-dimensional metal nanoparticles on one-dimensional silicon nanowires. We shall describe a few examples next.

**9.2.1.1  $AgND\text{-}SiNW$ .** The reductive deposition of Ag on HF-etched SiNW surfaces produced a wide variety of morphologies as depicted in Figure 53.<sup>172</sup> It can be seen that the size and morphology of the silver metal particles range from small clusters to dendrite with increasing concentration of  $AgNO_3$ . These variations can be understood in terms of mass transport of silver ions across the electrical double layers of the surfaces of SiNWs.

Upon immersion into the  $AgNO_3$  solution, the local concentration of the surface silicon atoms in the volume around the nanowires can be assumed to be in excess of that of the Ag ions. In fact, at the concentration of  $1 \times 10^{-4}$  M, 1 mL of the solution contains  $10^{16}$  ions, corresponding to approximately a monolayer coverage on a  $1 \text{ cm}^2$  surface of the nanowires. The redox reaction will thus be controlled by the concentration of the Ag ions (mass action). In high-concentration solutions, a large quantity of Ag ions in the vicinity of the wires was reduced and aggregated as dendrites. In low-concentration solutions, however, silver clusters or aggregates of clusters were deposited on the surfaces of SiNWs.



**Figure 54.** (a) TEM image of the SiNWs treated with a  $1.0 \times 10^{-3}$  M copper sulfate solution. (b) Corresponding EELS spectrum of the SiNWs shown in a. (Reprinted with permission from ref 172. Copyright 2001 American Institute of Physics.)

**9.2.1.2 CuND÷SiNW.** When HF-etched SiNWs were immersed in  $1.0 \times 10^{-2}$  and  $1.0 \times 10^{-3}$  M copper sulfate solutions, brown metallic copper formed on the SiNWs was clearly visible at high concentration ( $1.0 \times 10^{-2}$  M). The product from the reaction of HF-etched SiNWs and the  $1.0 \times 10^{-3}$  M copper sulfate are shown in Figure 54a. The corresponding EELS spectrum is shown in Figure 54b, where the Cu  $L_{3,2}$ -edge at 931.1 and 951.0 eV can be clearly identified. The prominent feature just below 1600 eV has been interpreted as the XAFS of the Cu L-edge.

**9.2.1.3 PdND÷SiNW, RhND÷SiNW.** The palladium and rhodium nanoparticles (<10 nm in diameter) have also been produced on the hydrogen passivated surfaces of SiNWs.<sup>223</sup> Figure 55a shows the SEM image of Pd nanoparticles aggregated on SiNWs from reductive deposition of Pd(II) ions in a  $1.0 \times 10^{-3}$  M solution on SiNW surfaces. High magnification, Figure 55b, revealed a distribution of aggregates varying from tens of nanometers to hundreds of nanometers. The TEM images of Pd nanoparticles on SiNWs from the  $1.0 \times 10^{-4}$  M Pd(II) solution are shown in Figure 56a. The sizes of most of the Pd nanoparticles are smaller than 5 nm. The HRTEM image shown in Figure 56b reveals the fcc structure of these Pd nanoparticles with lattice spacing of 2.2 Å. They are either attached to the SiNWs or immersed in the amorphous SiO<sub>2</sub>. Similar results were obtained for Rh. No Pd and Rh nanoparticles larger than 10 nm were found to attach to the SiNW surface. Apparently as the metal nanoparticles grow to a larger size (>10 nm in diameter), they tend to separate from the SiNW surfaces.

The morphologies of Pd and Rh nanoparticles formed on the SiNW surfaces, as revealed by HRTEM, are rather interesting. Roughly speaking, there are two types of nanoparticles: the larger ones (4–10 nm in diameter) are generally round-shaped and have a thin amorphous oxide sheathing, whereas the smaller ones (<4 nm in diameter) are often faceted and without the oxide sheathing. Figure 57a depicts a typical round-shaped Rh nanoparticle with an 8 nm diameter attached to a SiNW surface. Some of these nanoparticles were partially or completely surrounded by a silicon oxide layer. In this regard, the oxides served as the ligands, stabilizing the metal nanoparticles on the SiNW surfaces. As a result, these nanoparticles showed good stabilities under HRTEM observation.

Many of the smaller nanoparticles (<5 nm) exhibit well-defined facets, suggesting a high-frequency polyhedral structure as illustrated by the HRTEM image of such an Rh particle shown in Figure 57b. The Rh nanoparticle appears to be an individual polyhedron of about 3.5 nm in diameter. Both Rh and Pd nanoparticles exhibited fcc lattice structure without the amorphous oxide layer. This type of nanoparticles, with little or no oxide sheathing, showed poor stability under intense TEM electron beam bombardment. It was found that some metal nanoparticles on the SiNW surface eventually detached from the SiNW surface or sank into the amorphous oxide layer during TEM observation. These observations are similar to those discussed earlier for the ligated Au–Ag alloy nanoparticles on SiNW surfaces.<sup>147</sup>

Other shapes or morphologies of the nanoparticles or aggregates of nanoparticles have also been observed.

**9.2.1.4. AuAgND÷SiNW.** Au–Ag nanodots deposited on silicon nanowires, AuAgND÷SiNW, via reductive growth of structurally well-defined phosphine-ligated gold–silver clusters on HF-etched SiNWs, have been discussed in section 8.1.<sup>147</sup>

## 9.2.2. Nanodots in Nanowires: ND<sub>C</sub>NW

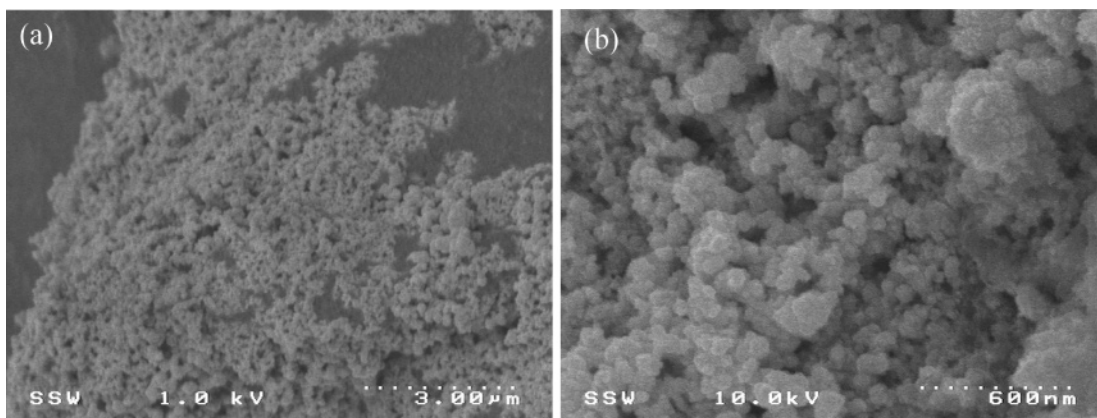
We shall now describe a few examples of nanodots immersed in nanowires.

**9.2.2.1. SiND<sub>C</sub>SiO<sub>2</sub>NW (Necklacelike Chains).** The necklace- or chainlike SiNWs have been synthesized by alternating the pressure of the carrier gas in the OAG growth process.<sup>224</sup> The necklacelike SiND<sub>C</sub>SiO<sub>2</sub>NW nanostructure may be described as a chain of crystalline Si nanoparticles immersed in an amorphous silicon oxide nanowire.

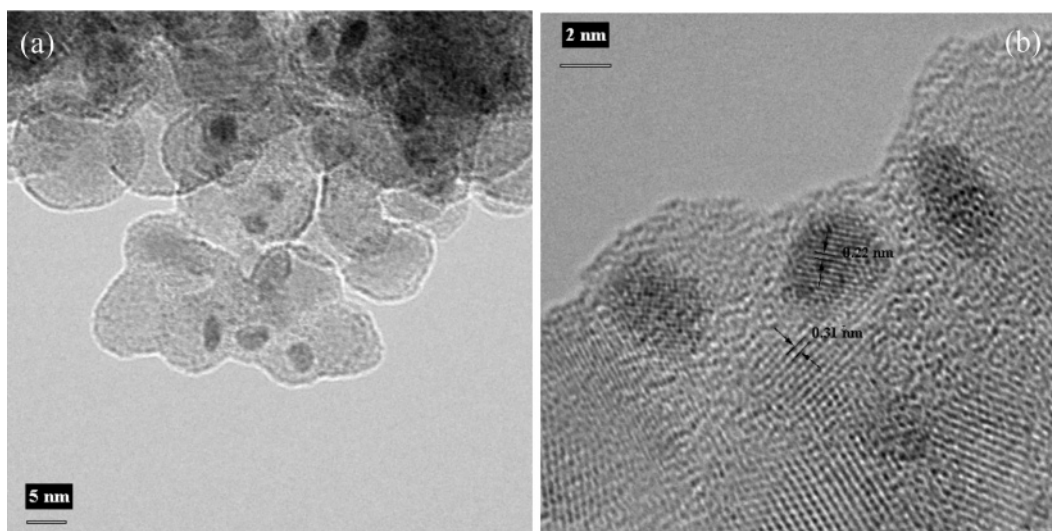
The necklacelike SiND<sub>C</sub>SiO<sub>2</sub>NW nanostructures are sometimes referred to in the literature as “chainlike SiNWs”. They are often observed as byproducts in the fabrication of normal SiNWs by both laser ablation<sup>225</sup> and thermal evaporation methods.<sup>81</sup> A bulk quantity of Si nanosphere chains can also be prepared by annealing normal SiNWs at high temperature via a spheroidization mechanism<sup>81,226</sup> or by heating a gold-coated silicon substrate via an extension of the vapor–liquid–solid mechanism.<sup>227</sup>

Figure 58 shows a typical TEM image of the necklacelike SiND<sub>C</sub>SiO<sub>2</sub>NWs. The nanoparticles have an average diameter of 16 nm and are connected by ~20 nm long oxide wires. The HRTEM images are depicted in Figure 59. The nanoparticles are single crystalline silicon nanodots as confirmed by electron diffraction. The outer shells of the nanoparticles and connecting wires are amorphous silicon oxide. It is interesting to note that the silicon nanoparticles in the chainlike SiNWs exhibit a variety of shapes. In addition to the commonly observed spherical shape, shown

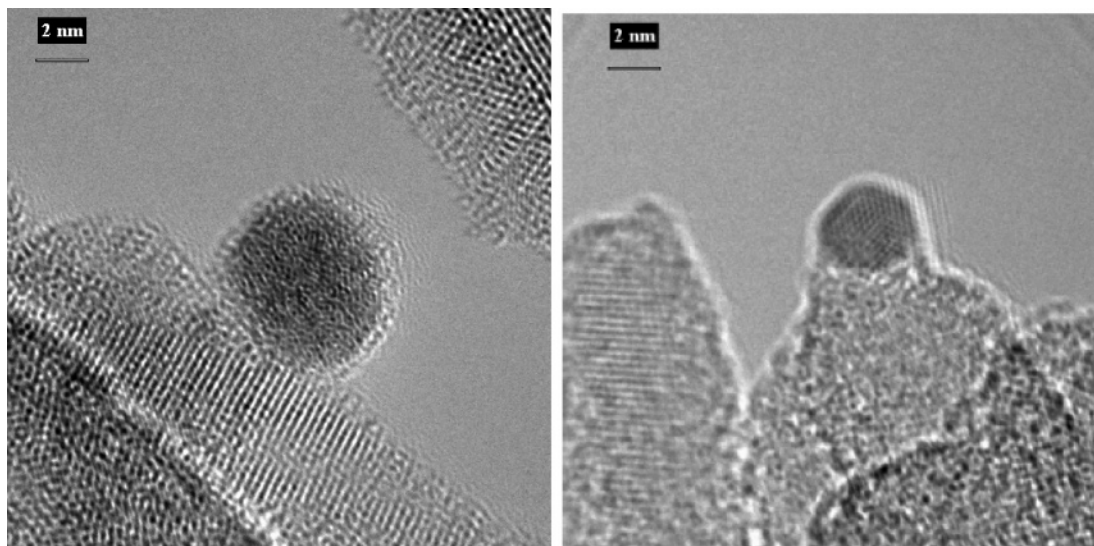




**Figure 55.** (a) SEM image showing metallic Pd nanoparticle aggregates from the reductive deposition of Pd onto the surfaces of SiNWs in a  $1.0 \times 10^{-3}$  M Pd(II) solution. (b) High magnification of SEM image of a. (Reprinted with permission from ref 223. Copyright 2004 American Chemical Society.)



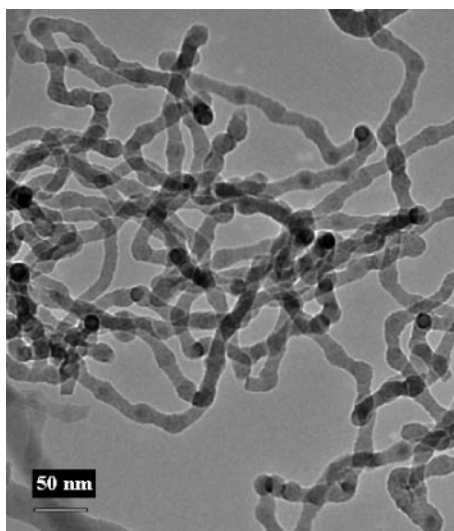
**Figure 56.** (a) TEM image of Pd nanoparticles on SiNWs formed in a  $1.0 \times 10^{-4}$  M Pd(II) solution. (b) HRTEM image of the Pd nanoparticles in a. (Reprinted with permission from ref 223. Copyright 2004 American Chemical Society.)



**Figure 57.** HRTEM image of (a) a round Rh nanoparticle of 8 nm in diameter on the surface of a SiNW and (b) a near perfect individual polyhedral Rh nanoparticle of about 3.5 nm in diameter on SiNW surface. (Reprinted with permission from ref 223. Copyright 2004 American Chemical Society.)

in Figure 59a, rectangular and triangular shapes are also observed, as shown in Figure 59b,c, respectively. From the HRTEM images, it can be determined that the Si nanopar-

ticles exhibit (111) crystal planes with a 3.1 Å  $d$ -spacing. In a cross-sectional study of the nanowires,<sup>79</sup> the horizontal cross-section of a chainlike SiNW was obtained and it was



**Figure 58.** Typical TEM image of the necklace- or chainlike SiNWs. (Reprinted with permission from ref 224. Copyright 2004 American Institute of Physics.)

found that some nanoparticles, measuring 16–20 nm in diameter, exhibited polyhedral shapes such as hexagons and octagons in the cross-sectional view. While it is believed that fluctuations of the chamber pressure in the OAG growth process contribute to the formation of these nanostructures, the detailed mechanism remains unclear and awaits further investigation.

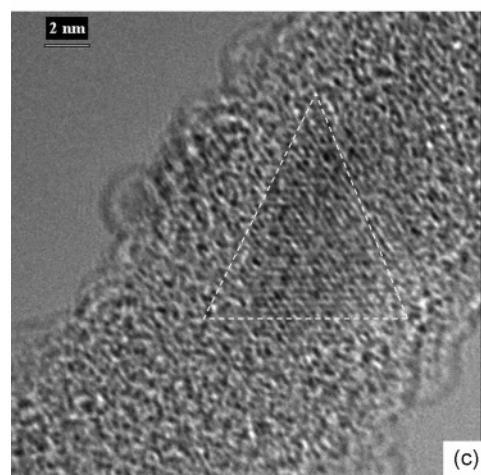
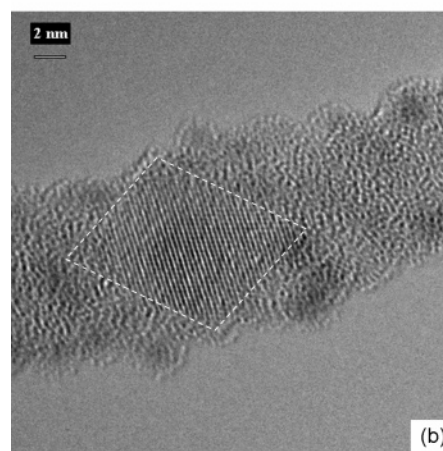
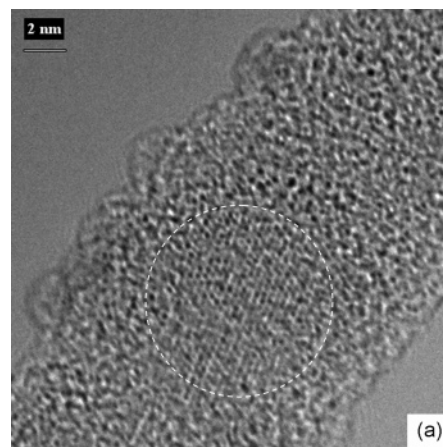
**9.2.2.2. CuSiND<sub>C</sub>SiNW.** Copper silicide nanocrystals embedded in a silicon nanowire, CuSiND<sub>C</sub>SiNW, were obtained by laser ablation of Si/metal mixture targets at 1200 °C in an argon gas flow.<sup>228</sup> Consistent with the bulk-phase properties, copper was found to have a high solubility in silicon nanowires. The copper atoms react with silicon to form copper silicide, which precipitates as nanocrystals within the nanowires. The copper silicide nanocrystals are spherical in shape and embedded in the silicon nanowire as depicted in Figure 60. The diameters of the nanocrystals tend to increase with increasing diameter of the host nanowire.

### 9.2.3. Nanodots on Nanotubes: ND÷NT

The discovery of carbon nanotubes opens up new and exciting possibilities for making different kinds of nanosized heterostructures by filling the inside hollow space with other elements (nanodots in nanotubes, designated as ND<sub>CNT</sub>)<sup>229,230</sup> or by decorating the outside surfaces of the nanotubes (nanodots on nanotubes, designated as ND÷NT).<sup>231–233</sup> One example of the latter is the attachment of CdSe nanoparticles on the surface of CNTs, designated as CdSe÷CNT.<sup>233</sup> Further examples can be found in the literature. We shall now discuss the filling of CNTs in the following sections (sections 9.2.4 and 9.2.5).

### 9.2.4. Nanodots in Nanotubes: ND<sub>CNT</sub>

Confinement of molecules (nanodots or nanoshells) within the cavities (channels) of nanotubes can result in distortion of the shape of the molecules as well as perturbation of bond lengths and/or angles. These changes can be caused by geometrical constraints (shape matching) and/or interactions between the molecules (guests) and the interior (host) of the nanotubes (guest–guest and guest–host interactions). The nature of these interactions could range from weak van der Waals or hydrogen bond interactions to rather strong  $\pi$ – $\pi$



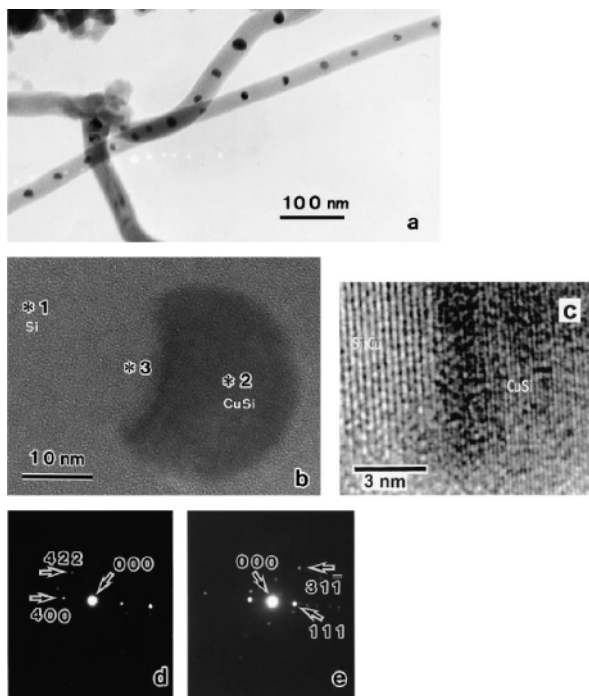
**Figure 59.** HRTEM images of the chainlike SiNWs with (a) spherical Si nanoparticles, (b) rectangular Si nanoparticles, and (c) triangular Si nanoparticles. (Reprinted with permission from ref 224. Copyright 2004 American Institute of Physics.)

or ionic interactions. These confinement effects, coupled with the positions and orientations of molecules inside the cavities of the nanotubes could, in some cases, lower the activation energy of some reactions (thereby facilitating the kinetics) and, in others, favor the formation of one isomer (whose shape conforms better to the nanotube cavity) over others (thereby defying thermodynamics).

We shall now discuss a few examples of nanodots (ND) or nanoshells (NS) in nanotubes (ND<sub>CNT</sub> or NS<sub>CNT</sub>).

**9.2.4.1. SiND<sub>C</sub>MWCNT.** Recently a simple approach was developed to introduce ex-situ synthesized silicon nano-



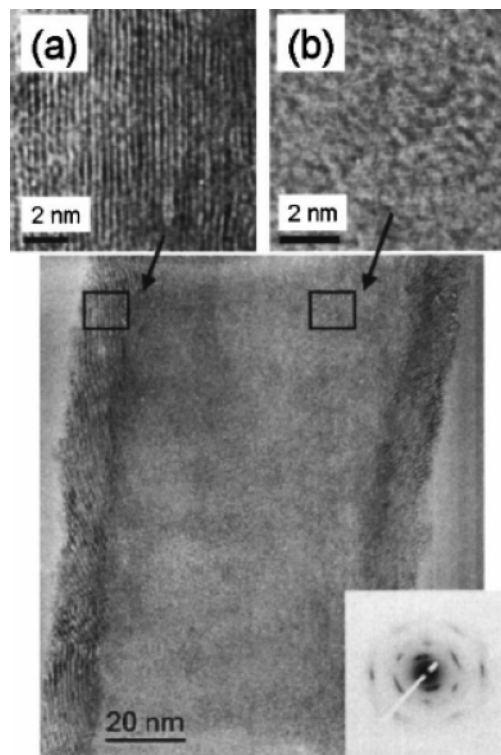


**Figure 60.** (a) TEM image of the composite structures of the silicon nanowires and the metal silicide nanocrystals. (b) HRTEM image of a metal silicide nanoparticle. Snow marks indicate the sites where electron beam diffractions and EDX were probed. (c) HRTEM image of a part of the metal nanoparticle and its interface with the silicon nanowire. The lattice spacing at the interface is about 0.31 nm, corresponding to that of the (111) planes of Si. The lattice distance at the site of the particle is about 0.20 nm. (d) SAED patterns taken at the nanoparticle (site 2 in b). (e) SAED patterns probed at the interface (site 3 in b). (Reprinted from ref 228, Copyright 2001, with permission from Elsevier.)

crystals, either dispersed in organic solvents such as methanol or embedded in SiO<sub>2</sub>-based spin-on-glass (SOG) solutions, into multiwalled carbon nanotubes at room temperature and atmospheric pressure.<sup>234</sup> It is known that opened MWCNTs exhibit strong capillary effect and can be wetted and filled by substances having low surface tensions. Theoretical calculations suggested (see ref 16 in the original paper) that any liquid having a surface tension below 200 mN/m will spontaneously enter the channels of CNTs under ambient conditions. This rules out most of the molten semiconductors and heavy metals. In contrast, water and organic solvents will easily enter and fill the CNT channels.

Figure 61 shows the TEM images of SiNDs that were dispersed in methanol via sonication and introduced into MWCNT channels through the capillary effect. The ends of the MWCNTs were opened by thermal annealing in an oxygen atmosphere at 580 °C. The MWCNTs have an average inner diameter of 40 nm. The darker dot images, having diameters of 3–10 nm, within the CNT channels correspond to the embedded crystalline SiNDs, as confirmed by the high-resolution TEM images and electron diffractions shown in Figure 61a,b.

**9.2.4.2. Nanocluster<math>C\_{CNT}</math>.** Nanoclusters such as cubic octasiloxane, H<sub>8</sub>Si<sub>8</sub>O<sub>12</sub>, and icosahedral *o*-carborane, C<sub>2</sub>B<sub>10</sub>H<sub>12</sub>, had been incorporated into CNTs. The former is a cubic cluster with eight silicon atoms at the corners, bridged by twelve oxygen atoms on the edges, of the cube. Each silicon atom is bonded to a hydrogen atom. In the nanotubes (SWCNTs or DWCNTs), the octasiloxane clusters exhibit a large degree of disorder. The Si–H stretching frequency is



**Figure 61.** Plan-view HRTEM image of an open MWCNT with diameter 40 nm filled with a SiNDs/methanol solution: (a) HRTEM image of a small section of MWCNTs where the graphitic walls appear as dark fringes. (b) TEM image of the hollow part of the tube with SiND particles. The distance between atomic columns of 0.20 nm corresponds to silicon (220) *d* spacing. The inset indicates the corresponding selected area electron diffraction (SAED) pattern. (Reprinted with permission from ref 234. Copyright 2006 American Institute of Physics.)

red-shifted by 15 cm<sup>-1</sup> and significantly broadened. These observations can be interpreted as being caused by the interactions between the Si–H bonds of the cluster with the interior wall of the CNT.<sup>235</sup> In contrast, the icosahedral *o*-carborane forms an ordered zigzag chain in SWCNTs.<sup>236</sup>

**9.2.4.3. Nanoshells in Nanotubes: NS<math>C\_{CNT}</math>.** The structures and dynamics of carbon nanotubes filled with fullerenes can be found in the excellent review by Khlobystov et al.<sup>237</sup> Here we provide a brief account of the important experimental observations and theoretical investigations to date.

The filling of carbon nanotubes with fullerenes was discovered accidentally when both were produced simultaneously by the pulsed laser vaporization technique.<sup>238</sup> Carbon nanotubes filled with fullerenes are called “peapods”. The  $\pi$ – $\pi$  interactions between the fullerene surface and the interior of a nanotube,<sup>238</sup> both consisting of curved graphitic sheets, had been estimated to amount to ca. 3 eV per C<sub>60</sub> molecule. This represents a 50% increase over the cohesive energy of fcc fullerene crystals.<sup>239</sup> Good shape matching and the effective  $\pi$ – $\pi$  interactions suggest that the encapsulation of fullerenes in SWCNTs should be spontaneous and irreversible, provided the nanotube diameter is at least 0.6 nm larger than that of the fullerenes (to allow for the thickness of the  $\pi$  orbitals, i.e., 2  $\times$  0.34 nm).

**9.2.4.3.1. C<sub>60</sub><math>C\_{CNT}</math> and C<sub>70</sub><math>C\_{CNT}</math>.** The packing arrangement of nanoshells in nanotubes depends not only on the internal diameter of the nanotubes but also the size and shape of the nanoshells. It has been determined theoretically that there are ten possible arrangements for fullerenes in CNTs,<sup>240,241</sup> ranging from a linear array to a zigzag config-



uration to a two-molecule layer structure, as the diameter of the nanotube increases. For example,  $C_{60}$  molecules form a linear array for (10,10)CNTs (diameter  $d = 1.36$  nm) but a zigzag chain for (11,11)CNTs ( $d = 1.49$  nm). The threshold diameter for the linear to zigzag phase transition seems to occur at  $d = 1.45$  nm. Interestingly, the situation is different for the ellipsoidal-shaped  $C_{70}$  molecules. In (10,10)CNTs, the  $C_{70}$  molecules adopt a longitudinal orientation, with the long molecular axis parallel to the nanotube axis, whereas in (11,11)CNTs, they adopt a transverse orientation, with the long molecular axis parallel to the nanotube axis. Here the molecular orientations are obviously dictated by fullerene–nanotube interactions rather than fullerene–fullerene interactions, in addition to the diameter of the nanotube.

Theoretical calculations<sup>242</sup> suggested that the ordering of the fullerene molecules in CNTs depends not only on the filling factor and the diameters of the nanotubes (electronic and size effects) but also on the temperature. For example, an ordered zigzag phase of  $C_{60}$  in (15,15)CNT undergoes a phase transition (melting) to a disordered state at 75 K.

**9.2.4.3.2.  $Ce@C_{82}C_{80}$  and  $La_2@C_{80}C_{82}$  SWCNT.** Endohedral fullerenes such as  $Ce@C_{82}$ <sup>243</sup> and  $La_2@C_{80}$ <sup>244</sup> have also been inserted into SWCNTs. Interesting molecular motions were observed under HRTEM imaging.

### 9.2.5. CNT and cSiNTs as Nano-Test-Tubes/Nanoreactors

Carbon nanotubes (CNTs) and crystalline silicon nanotubes (cSiNTs) can be used as nanosized test tubes or reactors. The interior walls of CNTs are curved graphene sheets, whereas those of the cSiNTs are curved silicon or silicon oxide surfaces. These distinct surfaces should have different effects on chemical reactions inside the nanotubes. They may also catalyze different types of reactions. Here we discuss two types of reactions inside CNTs: fullerene oligomerization/polymerizations and formation of ionic crystals.

**9.2.5.1. Fullerene Reactions Inside CNTs.** The reactions of fullerene and nonfullerene molecules encapsulated in carbon nanotubes have been reviewed in ref 237. Instead of using high temperatures and common organic solvents in filling CNTs, it was found that supercritical  $CO_2$ , with the critical point just above room temperature, acts as an efficient medium for transporting molecules into the nanotube cavities.<sup>245</sup> Once inside, the reactions can be induced by light, heat, or electrical potential, etc.

It is important to note that the confinement effects discussed in section 9.2.4 can affect chemical reactions within nanotubes in two ways. In some cases, it may lower the activation energies of some reactions (kinetic effect), while, in others, it may favor the formation of one isomer (which conforms better to the nanotube cavity) over other isomers (thermodynamic effect). For example, fullerene epoxide,  $C_{60}O$ , can be inserted into SWCNTs and heated to produce a linear polymer  $(C_{60}O)_n$  in SWCNT wherein the  $C_{60}O$  molecules are bonded in a head-to-tail fashion.<sup>246</sup> In contrast, a randomly disordered polymeric structure was obtained when bulk  $C_{60}O$  crystals were heated to 260 °C. Yet another beautiful example is the formation of the thermodynamically disfavored linear trimer  $C_{60}OC_{60}OC_{60}$  in SWCNT when SWCNTs are filled with an appropriate mixture of  $C_{60}$  and  $C_{60}O$ . The bent isomer is preferentially formed in solution instead.

**9.2.5.2. Formation of Nano Ionic Crystals Inside CNTs.** The formation of nanosized ionic crystalline rods within SWCNTs have been reviewed by Sloan et al.<sup>247</sup> The well-defined nanotube channels of precise diameters allow atomi-

cally regulated growth of ionic crystals. Deviations from the corresponding bulk structures were observed, including lower coordinations and lattice distortions. The first reported example is a  $2 \times 2$  KI linear crystal formed within a SWCNT of 1.4 nm in diameter. As expected, the coordinations reduce from the bulk values of 6:6 to 4:4. It is interesting that the (200) spacing along the tube axis of  $\sim 0.35$  nm is similar to that of the bulk, but expanded to  $\sim 0.4$  nm across the capillary.<sup>248</sup> Larger  $3 \times 3$  KI crystals have also been formed in SWCNTs with a larger diameter (1.6 nm).<sup>249</sup> The  $3 \times 3$  KI crystal shows three separate coordinations of 6:6, 5:5, and 4:4 for the center, face, and corner ...I–K–I–K... rows, respectively, along the SWCNT axis. Similar slight lattice distortions were also observed.

Eutectic silver halide systems<sup>250</sup> and metal oxides such as  $Sb_2O_3$ <sup>251</sup> have also been incorporated into SWCNTs.

**9.2.5.3. Clusterization Inside CNTs.** Electron-beam irradiation of  $ZrCl_4$  (1-D chainlike structure with bridging halides) inside a SWCNT causes elimination of  $Cl_2$  and the formation of clusters of different lengths (2–4 nm).<sup>252</sup>

### 9.2.6. CNTs and cSiNTs as Nanotemplates/Nanomolds

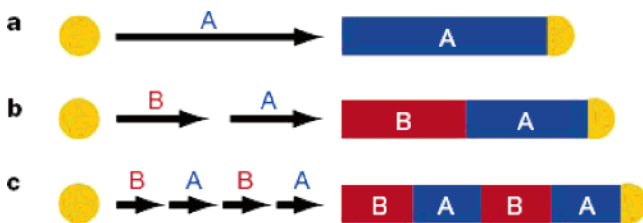
We have already discussed the use of CNT templates or molds in the fabrication of low-dimensional silicon composite nanomaterials in earlier sections. In a sense, these composite nanomaterials may also be considered as CNTs decorated on the outside with nanodots or nanoshells, giving rise to 0-D on 1-D heterostructures ND÷CNT or NS÷CNT, or wrapped with other nanotubes, CNT÷CNT, giving rise to 1-D on 1-D heterostructures. The former heterostructures had been discussed in section 9.2.3. The latter will be discussed in detail in section 9.3.2.

In choosing a template or a mold, it is important to bear in mind that it can either be inert, reactive, or sacrificial. For example, silicon carbide,<sup>167,168, 253</sup> gallium nitride nanowires,<sup>254</sup> Si–B–C–N nanocables,<sup>255</sup> heterostructures of carbon nanotubes and carbide nanorods,<sup>170</sup> and SiC–SiO<sub>x</sub> biaxial nanowires<sup>169</sup> have recently been synthesized using carbon nanotubes as molds. These CNT-template-directed fabrication methods are highly promising due to the morphological integrity of carbon nanotubes which spatially confine the reactions to the contours of the nanotubes. The net result is the formation of one-dimensional products with diameters, lengths, and orientation similar to that of the carbon nanotube templates. However, sometimes reactions can occur between the template and the product, as in the case of the synthesis of SiCNTs using CNTs as reactive templates.<sup>167</sup> In this case, biaxial nanowires of silicon carbide–silicon oxide, designated as SiCNW|SiO<sub>2</sub>NW, were also obtained, indicating that the CNTs also function as sacrificial templates.<sup>167</sup>

By the same token, cSiNTs can also be used as templates or molds in the fabrication of other nano-heterostructures.

## 9.3. 1-D on 1-D

Generally speaking, 1-D on 1-D nanostructures can be categorized into three broad classes: axial, radial, and multiaxial heterostructures. Heterostructures can be made during the growth process or by treatments after growth. Postgrowth treatment can be accomplished either by physical processes (e.g., coating) or by chemical means (e.g., surface reactions). The growth of axial heterostructures is usually achieved by using a single growth mechanism that can be easily switched between different precursor materials during the growth process. Radial heterostructures, on the other



**Figure 62.** Axial heterostructural growth of nanowire superlattices. (a) A nanocluster catalyst (shown gold) nucleates and directs one-dimensional semiconductor nanowire (blue) growth with the catalyst remaining at the terminus of the nanowire. (b) Upon completion of the first growth step, a different material (red) can be grown from the end of the nanowire. (c) Repetition of steps a and b leads to a compositional superlattice within a single nanowire. (Reprinted by permission from Macmillan Publishers Ltd. (ref 256, <http://www.nature.com>), copyright 2002.)

hand, can be fabricated by coating the 1-D nanostructures with a conformal layer of a second material. We shall discuss each of these distinct types of composite nanostructures in the following subsections.

### 9.3.1. Axial Heterostructures

**9.3.1.1. Binary Axial Heterostructures.** Binary axial heterostructures are designated here as A–B, where A and B can be nanowires or nanotubes of the same material but with different dopants, as exemplified by p-SiNW–n-SiNW, or of different materials, as exemplified by SiNW–CNT. A or B, or both, can be multicomponent composite materials of insulators, semiconductors, metals, etc. A and B can also be repeated in a single wire to fabricate infinite, periodic axial heterostructures. For example, if A and B represent nanowire and nanotube, respectively, then the  $-(A-B)_n-$  heterostructure can be  $-(NW-NW)_n-$ ,  $-(NW-NT)_n-$ ,  $-(NT-NT)_n-$ , etc. In short, the possibilities are endless. Finally, the arrangement can either be ordered, modulated, or random. Some representative examples are discussed below.

**9.3.1.1.1. p-SiNW–n-SiNW.** The p–n homojunctions are the basis of planar silicon field effect transistor (FET) technology and many semiconductor devices. Intrawire p–n junction diodes can be fabricated within individual silicon nanowires by direct addition of gas-phase dopants during the growth process. This creates the *axial* heterostructures comprising p- and n-type semiconductors. Figure 62 shows a scheme of growth process of A–B semiconductor nanowire axial heterostructures. One example is the homojunction p-SiNW–n-SiNW.<sup>256</sup> To switch dopants during the growth of the SiNWs, the dopant flow was turned off and the reactor evacuated and refilled with silane flow before switching on the alternate dopant. Typical growth conditions were a temperature of 450 °C, a pressure of 10 Torr, and silane flow rates of 3 sccm.

Rectifying behavior was observed in two-terminal electrical measurements, which can be attributed to the formation of a nanoscale p–n junction within a single nanowire. The abrupt transition in carrier type and the resulting built-in potential barrier was revealed by simultaneous conductivity and atomic force microscopy measurements.

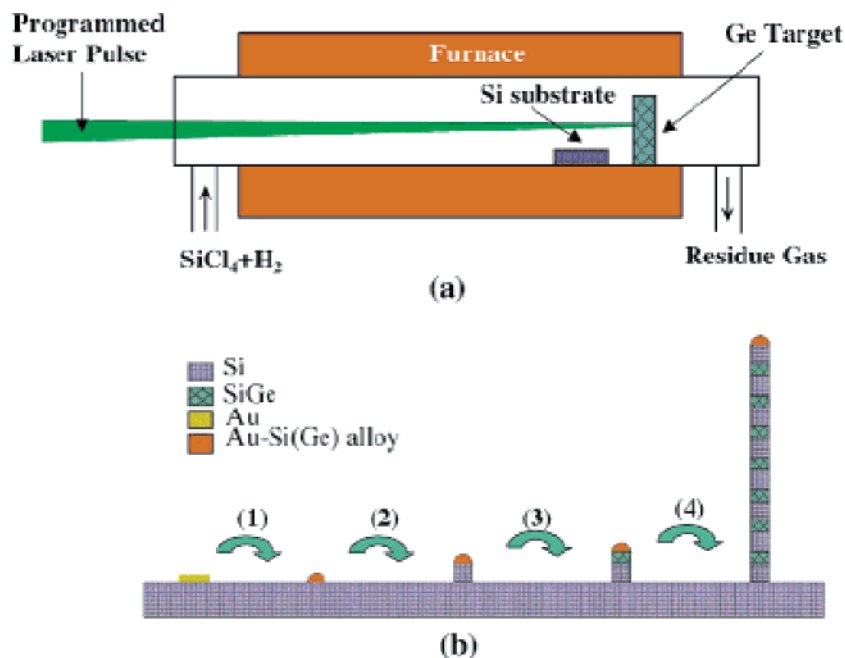
**9.3.1.1.2. SiNW–SiGeNW.** Recently, Wu et al. reported a hybrid pulsed laser ablation/chemical vapor deposition (PLA-CVD) method for the synthesis of semiconductor nanowires with axial heterostructures.<sup>257</sup> The laser ablation process generates a programmable pulsed vapor source that enables the nanowire growth in a block-by-block fashion with a well-

defined, modulated compositional profile along the wire axis. Schematic illustration of the experimental setup and the block-by-block nanowire growth process are shown in Figure 63. Single-crystalline nanowires with axial SiNW–SiGeNW superlattice structure, depicted in Figure 64, have been successfully synthesized. The SiNW–SiGeNW superlattice growth is based on the VLS mechanism with Au as catalyst, and a gas mixture of H<sub>2</sub> and SiCl<sub>4</sub> was continuously introduced into the reaction tube for continuous growth of SiNWs. Ge vapor was generated in pulsed form through the laser ablation of a pure Ge target. The reaction temperature typically ranged from 850 to 950 °C. By periodically turning the laser on and off, SiNW–SiGeNW superlattice can be formed in a block-by-block fashion. This particular growth process may be likened to the living polymerization synthesis of block copolymer.

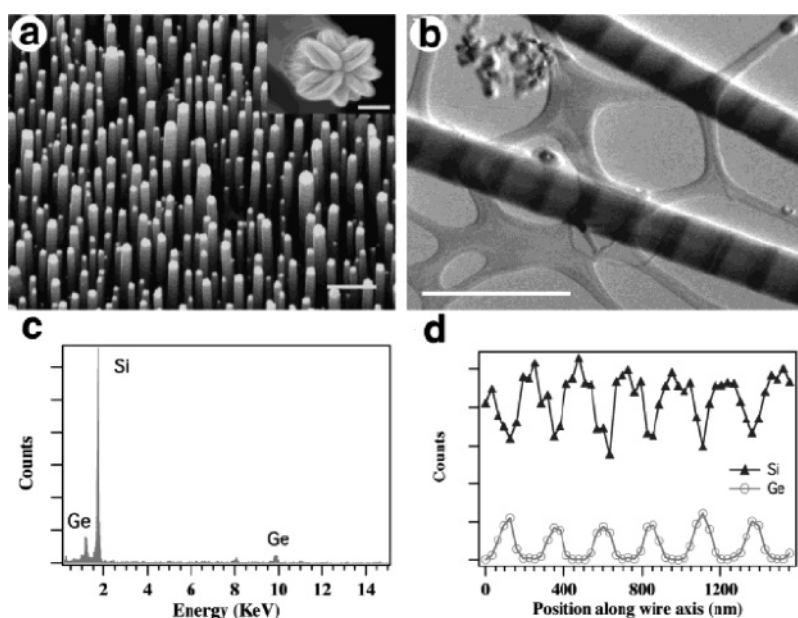
**9.3.1.1.3. SiNW–NiSiNW.** Recently Lieber and co-workers<sup>258</sup> demonstrated that NiSi nanowires can be prepared from single-crystal Si nanowires by deposition of nickel metal film onto the surfaces of the SiNWs followed by a solid-state reaction at 550 °C to form NiSi, and the removal of the residual metal by wet etching. This approach can be modified to transform selective segments of single-crystal silicon nanowires to produce SiNW–NiSiNW heterostructures with well-defined superlattices (Figure 65a). TEM images (Figure 65c) show a periodic variation in contrast that is consistent with NiSi (dark) and Si (light) materials within the heterostructure. It is clear that this approach enables spatially controlled transformation of silicon to metallic NiSi heterostructures. Interestingly, a detailed examination of the SiNW–NiSiNW heterostructure by high-resolution TEM (Figure 65d) reveals that the transformation yields an atomically abrupt interface (irrespective of any axial diffusion).

**9.3.1.1.4. SiNW–CNT vs CNT–SiNW.** A controlled, catalytic growth of metal–semiconductor junctions between carbon nanotubes and silicon nanowires was reported by Lieber and co-workers.<sup>259</sup> Two approaches were used to prepare the nanotube–nanowire junctions, CNTs growing from the SiNW end (SiNW–CNT) and SiNW growing from the CNT end (CNT–SiNW) as shown schematically in Figure 66. In the former, a common Fe-based (Fe/Au) catalyst was used to grow CNTs from the ends of SiNWs. The catalyst is naturally localized at the ends of the SiNWs after their growth and thus can be used to direct the growth of CNTs using a hydrocarbon reactant such as ethylene at 600 °C. Electron diffraction and high-resolution imaging reveal that the SiNWs remain crystalline after CNT growth (Figure 67). Two types of junctions can be produced from the SiNW ends. As depicted in Figure 66a, the CNT may form a sharp junction with the SiNW, with the metal nanocluster being excluded (top), or the metal catalyst may remain at the junction between the CNT and SiNW (bottom). The former is the majority product. Because MWCNTs are typically metallic, these sharp SiNW–CNT nanojunctions exhibit behavior typical of metal–semiconductor (M–S) junctions.

For the growth of CNT–SiNW junction, CNT was first attached to sharpened Pt/Ir scanned probe microscopy tips, and then a gold nanoparticle was electrodeposited onto the CNT free ends. SiNWs were grown from the CNT tip ends by using silane as the silicon source (Figure 68). As portrayed schematically in Figure 66b, the SiNW forms a sharp junction with the CNT, with the metal nanocluster attached to the



**Figure 63.** Schematic illustration of the experimental setup (a) and vapor–liquid–solid sequential nanowire growth mechanism (b). Panel b shows different stages of the block-by-block nanowire growth process: (1) alloying process between Au thin film and Si species in substrate/vapor; (2) growth of pure Si block when the laser is off (only Si species deposit into the alloy droplet); (3) growth of SiGe alloy block when the laser is on (both Si and Ge species deposit into the liquid droplet); (4) growth of Si/SiGe superlattice structure by turning on and off the laser beam periodically. (Reprinted with permission from ref 257. Copyright 2002 American Chemical Society.)



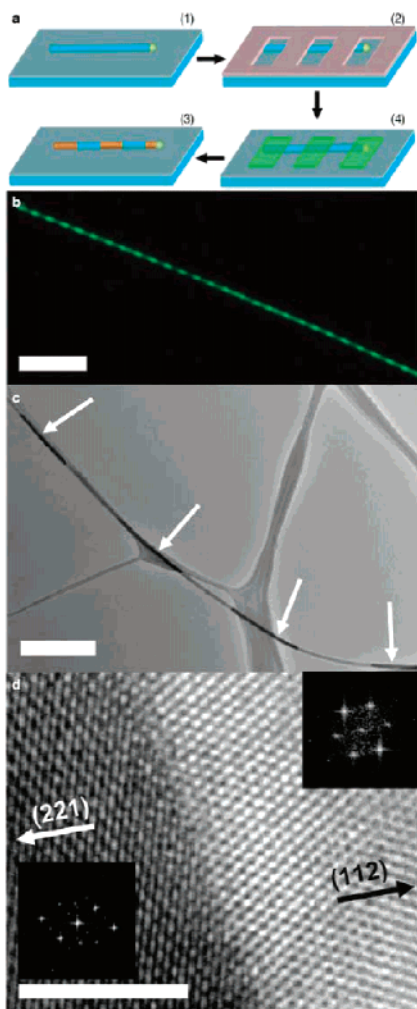
**Figure 64.** Axial heterostructural growth of Si–SiGeNWs: (a) SEM image of the heterostructured nanowire array on Si (111) substrate. Bar = 1  $\mu\text{m}$ . The inset shows the tip of one nanowire. Bar = 100 nm. (b) STEM image of two nanowires in bright-field mode. The scale bar is 500 nm. (c) EDS spectrum of the Ge-rich region on Si–SiGe superlattice nanowires. (d) Line profile of EDS signal from Si and Ge components along the nanowire growth axis. (Reprinted with permission from ref 257. Copyright 2002 American Chemical Society.)

free end of the SiNW. The preference for growth with Au catalyst at the SiNW free end, instead of at the CNT–SiNW junction, reflects the more favorable energetics of NT–Si versus NT–liquid Au–Si interfaces. A typical field emission SEM (FESEM) image of a CNT–SiNW junction (Figure 68b) shows roughly equal 5 nm straight segments of CNT and SiNW. TEM and FESEM images showed that the nanotube and SiNW can be either on-axis or off-axis. Current–voltage ( $I$ – $V$ ) measurements on CNT–SiNW junctions with only the SiNW in contact with the Ga–In liquid exhibit rectifying behavior typified by the results for two

independent junctions. This rectifying behavior is characteristic of an M–S Schottky diode device.

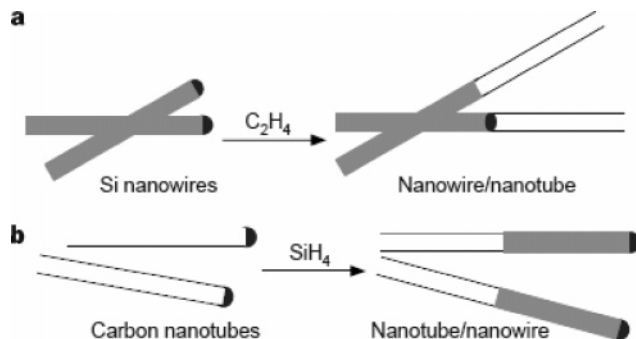
**9.3.1.1.5. SiCNR–SWCNT, SiCND–SWCNT.** A method based on a controlled solid–solid reaction was used by Iijima and co-workers to fabricate heterostructures between single-walled carbon nanotubes (SWCNTs) and nanorods or particles of silicon carbide.<sup>170</sup> The SiCNR–SWCNT junctions have crystalline interfaces with a nanometer-scale area defined by the cross-section of a SWCNT bundle or of a single nanotube. The method is based on a direct solid–solid reaction: C (nanotubes) + M (solid)  $\rightarrow$  MC (solid),



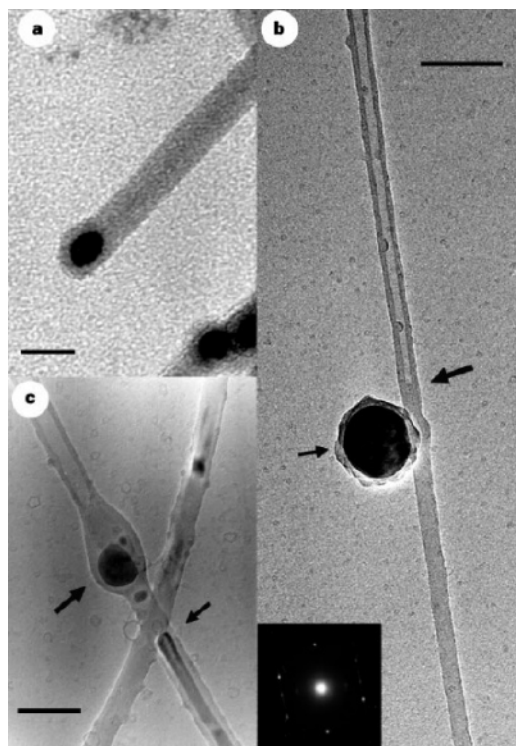


**Figure 65.** Fabrication and structural characterization of NiSi–Si nanowire heterostructures and superlattices. (a) Fabrication of NiSi–Si nanowire heterostructures and superlattices. (1) Si nanowires (blue) dispersed on a substrate are (2) coated with photoresist (gray) and lithographically patterned, (3) selectively coated with Ni metal (green) to a total thickness comparable to the Si nanowire diameter, and (4) reacted at 550 °C to form NiSi, resulting in NiSi–Si nanowires. (b) Dark-field optical image of a single NiSi–Si nanowire heterostructure. The bright green segments correspond to silicon and the dark segments to NiSi. Bar = 10  $\mu\text{m}$ . (c) TEM image of a NiSi–Si nanowire. The bright segments of the nanowire correspond to silicon, and the dark segments correspond to NiSi. Bar = 1  $\mu\text{m}$ . (d) High-resolution TEM image of the junction between NiSi and Si showing an atomically abrupt interface. Insets: two-dimensional Fourier transforms of the image depicting the [110] and [111] zone axes of NiSi and Si, respectively. Bar = 5 nm. (Reprinted by permission from Macmillan Publishers Ltd. (ref 258, <http://www.nature.com>), copyright 2004.)

where M is either Si or a transition metal (shown schematically in Figure 69). The carbide initially forms at the C/M interface once a sufficient temperature is reached for the reaction to occur ( $T > 800$  °C). The continuous transformation of the SWCNTs to carbide is controlled by the diffusion of M to the C–MC interface. However, the self-diffusion rate through bulk SiC or transition metal carbide is extremely slow in the temperature range of interest ( $800$  °C  $< T < 1000$  °C). A continuous supply of Si or metal atoms is therefore transported primarily via surface diffusion. This is consistent with the known formation of SiC films on the surface of Si. Figure 70 shows SiC nanorods and SWCNT bundles (or a single SWCNT) connected by the nanorods.

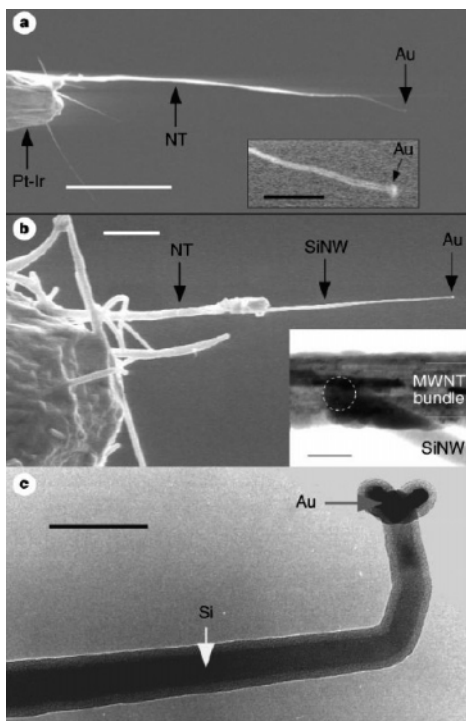


**Figure 66.** Fabrication of NT–NW junctions. (a) SiNWs (gray) grown by a catalytic process terminate in nanocluster catalysts (black). This catalyst is used to direct the growth of CNTs (black lines) from ethylene. The catalyst can be excluded or remain at the NT/SiNW junction. (b) Catalyst nanoclusters (black) are deposited on CNT ends and then used to direct the growth of SiNWs. In this case, the catalyst is on the SiNW free end and the NT/SiNW junction is clean. The CNTs are multiwalled. (Reprinted by permission from Macmillan Publishers Ltd. (ref 259, <http://www.nature.com>), copyright 1999.)



**Figure 67.** SiNW–CNT junctions grown from SiNWs with a common Fe–Au catalyst. (a) TEM image of SiNW produced with a  $\text{Fe}_{0.9}\text{Au}_{0.1}$  catalyst. The 15 nm diameter NW terminates in a Fe–Au nanocluster that appears as a dark, solid sphere. (b) The large black arrow highlights the junction position. The small arrow indicates a metal catalyst cluster that was probably excluded from the junction during growth. The inset is an electron diffraction showing that the SiNW maintains its crystalline structure after CNT growth. (c) The larger arrow highlights the junction region that contains a metal nanocluster. The contrast variation highlighted by the smaller arrow corresponds to SiNW. The scale bars in a–c are 20, 50 and 50 nm, respectively. (Reprinted by permission from Macmillan Publishers Ltd. (ref 259, <http://www.nature.com>), copyright 1999.)

**9.3.1.1.6. MetalNW–SiNW: InNW–SiNW.** The end-to-end In–Si nanowires have been synthesized by simultaneous thermal evaporation of In and SiO powders.<sup>260</sup> Figure 71 shows a typical TEM image of an In–Si nanowire heterostructure. InNW–SiNWs are uniformly sheathed with amor-



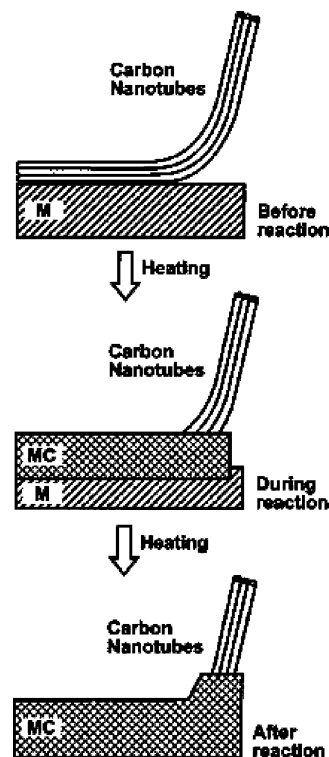
**Figure 68.** CNT–SiNW junctions grown from NT tips with a Au catalyst. (a) FESEM images of a CNT with an electrodeposited Au nanocluster at the free end. The CNT is attached to a Pt–Ir STM tip with micromanipulators. Inset, high-magnification view of the Au nanocluster at the CNT end. The white and black scale bars correspond to 5  $\mu\text{m}$  and 500 nm, respectively. (b) FESEM image of the CNT–SiNW junction grown from a nanotube tip. The large structure at the left is the Pt–Ir tip. Bar = 2  $\mu\text{m}$ . Inset, TEM image of a CNT–SiNW junction. The junction, which is indicated by the dashed white circle, is located at the back of the MWNT bundle and seems clean. Bar = 50 nm. (c) TEM image of the tip of the nanowire in b. The nanowire consists of a crystalline core and an amorphous Si/SiO<sub>x</sub> coating with an Au nanocluster at the SiNW free end. Bar = 50 nm. (Reprinted by permission from Macmillan Publishers Ltd. (ref 259, <http://www.nature.com>), copyright 1999.)

phous silica. Within a junction, the In and Si segments are crystallographically oriented with respect to each other. The In branch of a given junction, confined within the silica nanotube, displays a thermal expansion similar to that of bulk metallic In which opens prospects for the design of a unique temperature-driven switch and/or sensor within a metal–semiconductor electronic device.

**9.3.1.2. Ternary and Higher-Order Axial Heterostructures.** Ternary (designated here as A–B–C) or higher order axial heterostructures can also be made. Here A, B, and C can be nanowires or nanotubes of the same material but with different dopants, as exemplified by i-SiNW–n-SiNW–p-SiNW, or of different materials, as exemplified by SiNW–CNT–ZnSNW. Furthermore, any or all of the components A, B, and C can be either a binary or a ternary, etc., composite material of insulators, semiconductors, metals, or any combination thereof.

### 9.3.2. Radial Heterostructures

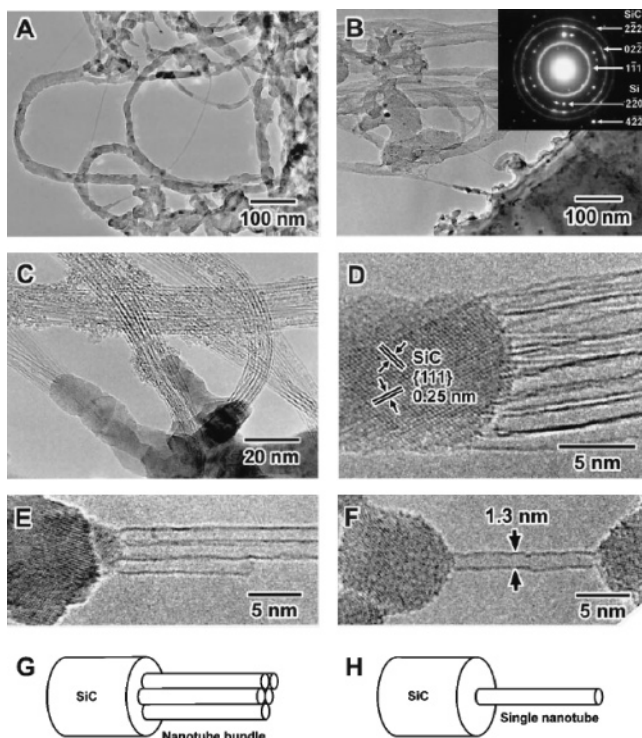
Radial heterostructures are designated in this review as A⊂B, where A and B can be nanowires or nanotubes of the same material but with different dopants or of different materials. Each of the components A and B can be made of a single material, or of binary or ternary, etc., composite materials, of insulators, semiconductors, metals, or combina-



**Figure 69.** Schematic illustration of the method for fabricating nanotube–carbide axial heterostructures by means of a solid–solid reaction. The top drawing shows a partial contact between the solid reactant (Si or transition metals) and carbon nanotubes. The middle drawing shows the formation of carbide (MC) near the point of contact by diffusive reaction during heating. The bottom drawing shows the growth of a nanorod and the formation of a nanojunction. (From ref 170 (<http://www.sciencemag.org>). Reprinted with permission from AAAS.)

tions thereof. This review focuses on SiNWs enwrapped in nanotubes that are made of insulating, semiconducting, or metallic materials. The role, however, could also be reversed, with nanowires or nanotubes of other insulating, semiconducting, or metallic materials encased in nanocylinders or nanotubes of SiNWs. For example, nanodevices based on p- or n-type SiNWs encased in nanotubes of dielectric materials such as SiO<sub>2</sub>NTs, of semiconducting materials such as CNTs, or of metals such as AuNTs can be envisioned. In a sense, these are the coaxial cables in the nanorealm. These composite 1-D on 1-D radial heterostructures will play a major role in building the materials base for future nanotechnology. In the following subsections, we shall describe some representative examples of radial heterostructures, namely, SiNW⊂SiO<sub>2</sub>NT, SiNW⊂CNT, SiNW⊂HCNT, CNT⊂SiCNT, SiNW⊂AuNT, SiO<sub>2</sub>NW⊂cSiNT, AuNW⊂SiO<sub>2</sub>NT, SiNW⊂CdSeNT, and ZnS⊂cSiNT etc.

It is apparent that the synthesis of radial nanowire⊂nanotube core–shell heterostructures relies on the control of radial versus axial growth. Figure 72 shows a scheme of core–shell nanowires growth process by chemical vapor deposition method.<sup>263</sup> In the CVD technique, radial growth is achieved by altering conditions to favor homogeneous vapor-phase deposition on the nanowire surface, thereby driving conformal shell growth (Figure 72c). In a sense, the core serves as the template for the shell growth (vide supra). Subsequent introduction of different reactants and/or dopants produces multiple shell structures of varying composition or dopant concentrations, though epitaxial growth of these shells sometimes requires matching of lattice structures.



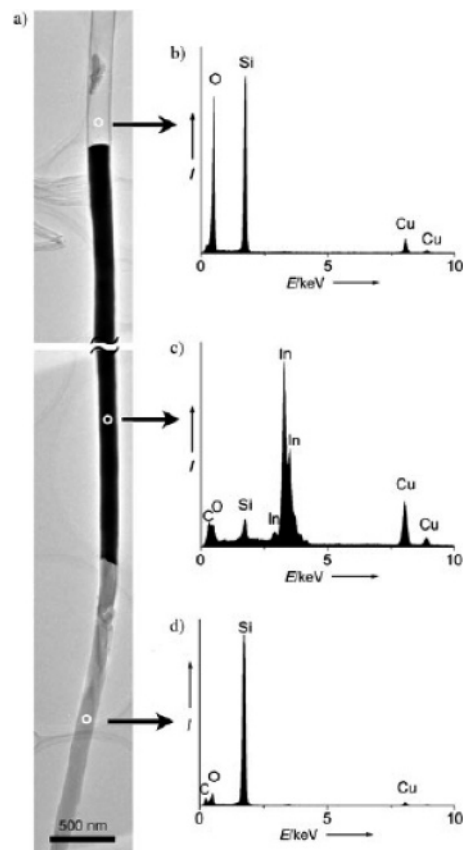
**Figure 70.** Axial heterostructural growth of SiCNW-SWCNTs: (A) TEM image showing SiC nanorods and SWCNT bundles connected by the nanorods. (B) TEM image showing SWCNTs far from the Si substrate (top, left) and the reacted substrate (bottom, right) after heating. The inset shows an electron diffraction pattern taken from the reacted substrate. (C and D) High-resolution TEM images showing heterostructures between SWCNT bundles and SiC nanorods. Interfaces (E) between SiC and a bundle consisting of five SWCNTs and (F) between SiC and a single SWCNT. Panels G and H are models of the heterostructures shown in E and F, respectively. (From ref 170 (<http://www.sciencemag.org>). Reprinted with permission from AAAS.)

**9.3.2.1. Binary Radial Heterostructures: Core-Shell Nanowire/Nanocable Structures.** We shall now discuss a number of examples of radial core-shell heterostructures.

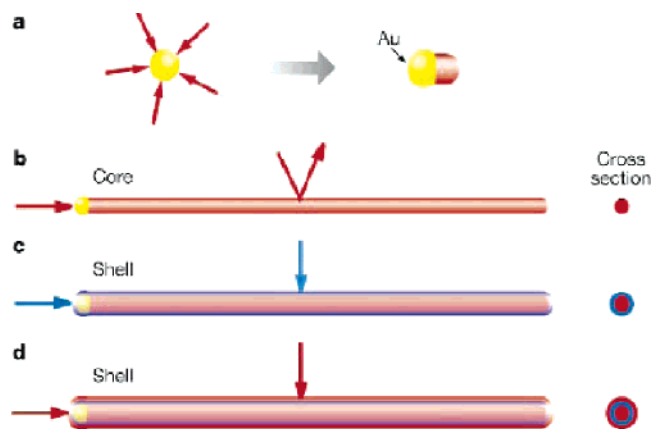
**9.3.2.1.1. SiNW<sub>C</sub>-a-SiO<sub>2</sub>NT.** As prepared SiNWs are known to have a relatively thick amorphous oxide layer sheathing and hence may be considered as SiNW<sub>C</sub>-a-SiO<sub>2</sub>-NT. As described earlier, SiNWs prepared by the oxide assisted growth method are long (micrometers), freestanding wires with a diameter of several nanometers to tens of nanometers. Each wire has a crystalline silicon core of approximately 15 nm in diameter and is coated with an amorphous oxide layer whose thickness is one-quarter to one-third of the nominal diameter.

**9.3.2.1.2. GeNW<sub>C</sub>-a-SiO<sub>2</sub>NT.** GeNW<sub>C</sub>-a-SiO<sub>2</sub>NT nanocables have been prepared by Lee and co-workers via simple thermal evaporation of SiO and Ge powders in an alumina tube with Ar premixed with 5% H<sub>2</sub> as the carrier gases.<sup>261</sup> The nanocables have a diameter of 60–150 nm and a length of several tens of micrometers. The outer shell of the nanocable consists of amorphous SiO<sub>2</sub>, and the inner core is single crystalline Ge (Figure 73). The spherical Ge particle at the tip, which acts as a catalyst, and the SiO<sub>2</sub> shell and tail suggest the growth of the nanocables by a combination of oxide assisted and VLS growth processes. The composition and morphology of the resulting nanocables are determined by the relative supplies of the Ge and SiO<sub>x</sub> vapors.

**9.3.2.1.3. SiNW<sub>C</sub>CNT, SiNW<sub>C</sub>HCNT.** An interesting class of composite nanomaterials based on SiNWs and CNTs and



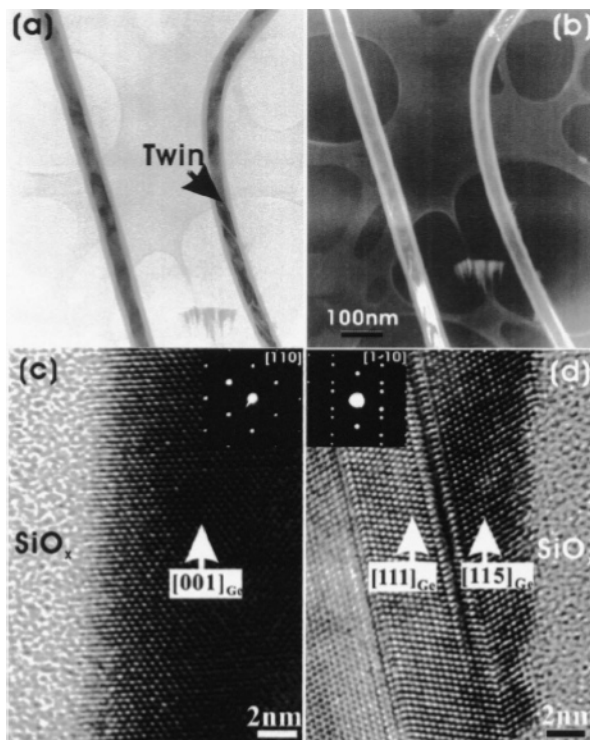
**Figure 71.** (a) TEM image of a typical In-Si nanowire heterojunction; (b-d) respective EDS spectra taken from the regions indicated with the white circles on the nanowire image in part a. (Reprinted with permission from ref 260. Copyright 2005 Wiley-VCH.)



**Figure 72.** Radial heterostructural growth of core-shell nanowires by chemical vapor deposition. (a) Gaseous reactants (red) catalytically decompose on the surface of a gold nanocluster leading to nucleation and directed nanowire growth. (b) One-dimensional growth is maintained as reactant decomposition on the gold catalyst is strongly preferred. (c) Synthetic conditions are altered to induce homogeneous reactant decomposition on the nanowire surface, leading to a thin, uniform shell (blue). (d) Multiple shells can be grown by repeated modulation of reactants. (Reprinted by permission from Macmillan Publishers Ltd. (ref 263, <http://www.nature.com>), copyright 2002.)

HCNTs, as exemplified by SiNW<sub>C</sub>CNT and SiNW<sub>C</sub>HCNT, respectively, has been discussed in section 8.2. Here HCNTs refers to a new type of hydrocarbon nanotubes, and the radial heterostructures may be described as SiNWs sheathed by multiwalled CNTs or HCNTs.





**Figure 73.** (a) Bright-field image and (b) dark-field image of two radial heterostructural GeNW $\subset$ SiO $_2$ NT nanocables; HRTEM image and electron diffraction pattern of (c) straight (single crystalline) and (d) curved (twin) nanocables in a and b, respectively. (Reprinted with permission from ref 261. Copyright 2003 American Institute of Physics.)

**9.3.2.1.4. CNT $\subset$ SiCNT.** A composite radial heterostructure of multiwalled CNT $\subset$ SiCNT, involving a new SiC nanotube structure, had been prepared using CNT as template, as discussed in section 8.3.<sup>167</sup>

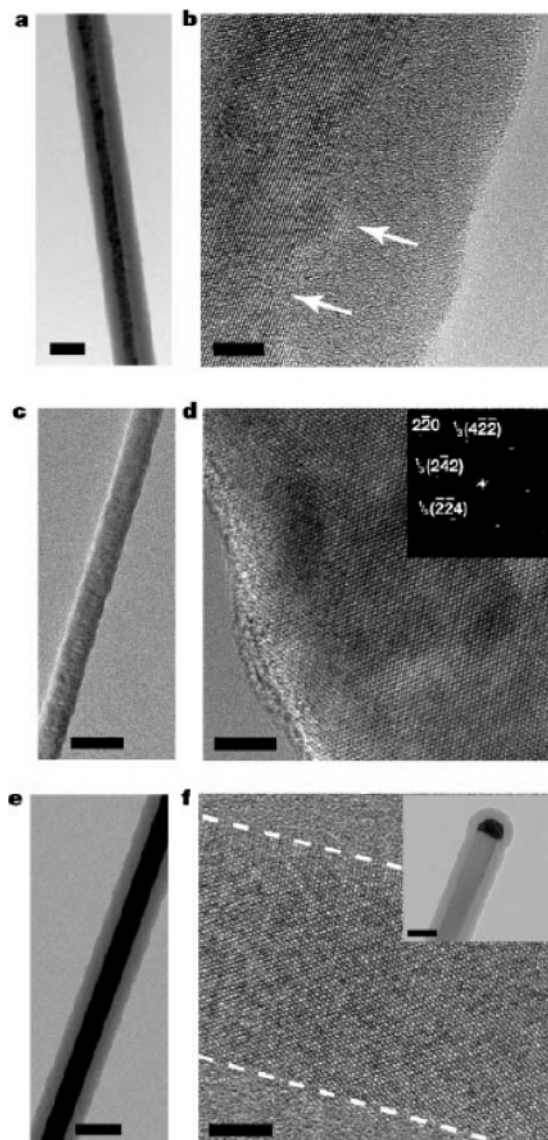
**9.3.2.1.5. SiNW $\subset$ pcSiCNT.** Using an ion beam deposition technique, Lee and co-workers produced a thin coating layer of cubic silicon carbide ( $\beta$ -SiC) via the reaction of silicon nanowires with methane and hydrogen.<sup>262</sup> HRTEM images showed that silicon oxide shells originally cladding the as-grown SiNW were removed and replaced by a thin layer of nanosized polycrystals of  $\beta$ -SiC, giving rise to SiNW $\subset$ pcSiCNT. The PL of the SiC-coated SiNW, SiNW $\subset$ pcSiCNT, increases by almost a factor of 3 after SiC coating.

**9.3.2.1.6. SiNW $\subset$ NiNT.** As discussed earlier, in the preparation of NiSi nanowires,<sup>258</sup> Lieber and co-workers deposited metallic nickel onto SiNWs as the first step. The resulting coaxial nanocable may be represented by SiNW $\subset$ NiNT.

**9.3.2.1.7. SiNW $\subset$ AuNT.** A simple and effective technique to fabricate a metal thin film on the surface of SiNWs, or SiNWs wrapped with Au cable (SiNW $\subset$ AuNT), was described in section 8.4.<sup>175</sup>

**9.3.2.1.8. AuNW $\subset$ SiO $_2$ NT.** When the radial heterostructures SiNW $\subset$ AuNT (Au nanocable wrapped around SiNWs), as described in the section 8.4, are furnace annealed at  $\sim$ 880  $^{\circ}$ C and  $10^{-2}$  Torr, uniform crystalline AuNWs were formed with the SiNWs being oxidized to SiO $_2$  concomitantly, as described in section 8.4.1.<sup>176</sup>

**9.3.2.1.9. SiO $_2$ NW $\subset$ cSiNT.** As discussed in section 6.5.1, zeolite can be used as a reactive template to fabricate a crystalline silicon nanotube filled with amorphous silica (a silica nanowire within a crystalline silicon nanotube, designated as SiO $_2$ NW $\subset$ cSiNT) via disproportionation reaction of SiO by thermal evaporation.

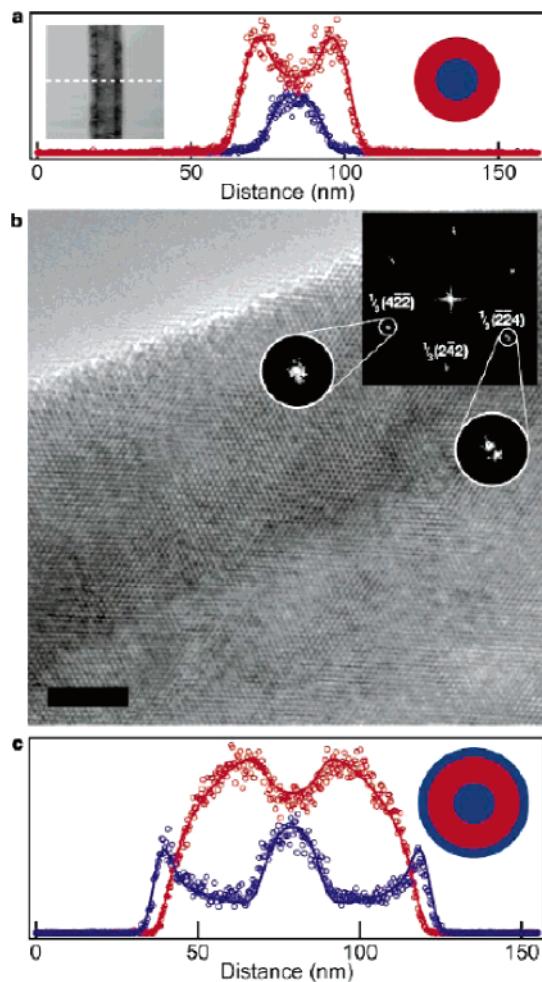


**Figure 74.** Radial heterostructures: Si-Si homoepitaxial core-shell nanowires. (a, b) Diffraction contrast and high-resolution TEM images, respectively, of an unannealed intrinsic silicon core and p-type silicon shell nanowire grown at 450  $^{\circ}$ C. See text for details. Scale bars are 50 and 5 nm, respectively. (c, d) TEM images of an i-SiNW $\subset$ p-SiNT core-shell nanowire annealed at 600  $^{\circ}$ C. Inset, two-dimensional Fourier transforms of the image depicting the [111] zone axis of the single-crystal nanowire. (e, f), TEM images of an i-SiNW $\subset$ SiO $_2$ NT $\subset$ p-SiNT nanowire. The oxide layer is too thin ( $<$ 1 nm) to be seen. Inset, TEM image of p-Si coating the nanowire and the Au nanocluster tip. Bar = 50 nm. (Reprinted by permission from Macmillan Publishers Ltd. (ref 263, <http://www.nature.com>), copyright 2002.)

**9.3.2.1.10. NiONW $\subset$ cSiNT.** NiONW $\subset$ cSiNT was also discussed earlier in section 6.5.3.

**9.3.2.1.11. ZnSNW $\subset$ cSiNT.** ZnSNW $\subset$ cSiNT was discussed in section 6.5.4 and will be discussed again in section 9.3.2.1.17.

**9.3.2.1.12. i-SiNW $\subset$ p-SiNT.** Homoepitaxial Si-Si core-shell nanowires, designated here as i-SiNW $\subset$ p-SiNT, have been grown by CVD using silane as the silicon source (Figure 74).<sup>263</sup> Intrinsic silicon nanowire (i-SiNW) cores were first prepared by gold nanocluster directed axial growth, and then boron-doped (p-type) silicon (p-Si) shells were grown by homogeneous CVD. The shell thickness was directly proportional to the growth time. Radial shell growth can be



**Figure 75.** Radial heterostructures of  $\text{SiNW}_{\text{c}}\text{GeNT}$  and  $\text{SiNW}_{\text{c}}\text{GeNT}_{\text{c}}\text{SiNT}$  core-shell nanowires. (a) Elemental mapping cross-section indicating a 21 nm diameter Si core (blue circles), 10 nm Ge shell (red circles), and a 1 nm interface. Inset: TEM image of the corresponding  $\text{Si}_{\text{c}}\text{Ge}$  core-shell nanowire. The white dashed line indicates the mapping cross-section. (b) HRTEM image of a representative crystalline nanowire core and shell from the same synthesis as the wire in a. Bar = 5 nm. Inset: Two-dimensional Fourier transform of the real-space image showing the [111] zone axis. See text for details. (c) Cross-sectional elemental mapping of a double-shell structure with an intrinsic Si core (diameter, 20 nm), intrinsic Ge inner shell (thickness, 30 nm), and p-type silicon outer shell (4 nm),  $\text{i-Si}_{\text{c}}\text{i-Ge}_{\text{c}}\text{p-Si}$ . Si is in blue, and Ge is in red. (Reprinted by permission from Macmillan Publishers Ltd. (ref 263, <http://www.nature.com>), copyright 2002.)

“turned-on” by the addition of diborane, which acts as a p-type dopant. TEM images of the product, designated as  $\text{i-SiNW}_{\text{c}}\text{ap-SiNT}$  (the prefix “a” stands for amorphous), shows a uniform core-shell structure consisting of a crystalline Si core and an amorphous p-type Si shell (Figure 74a). TEM images also show crystalline faceting at the core-shell interface (Figure 74b).

When the  $\text{i-SiNW}_{\text{c}}\text{ap-SiNT}$  core-shell nanowires prepared as described above were annealed in situ at 600 °C, TEM images of the resulting annealed samples exhibited no diffraction contrast between the core and shell (Figure 74c). Lattice-resolved images and electron diffraction data further showed that the amorphous p-type Si shell crystallized to yield a single-crystal structure (Figure 74d), i.e., giving rise to  $\text{i-SiNW}_{\text{c}}\text{cp-SiNT}$ .

**9.3.2.1.13.  $\text{p-SiNW}_{\text{c}}\text{GeNT}$ .** Controls of Si-Ge core-shell nanowire heterostructures could be used to explore a

variety of fundamental phenomena and new device concepts. To this end, Ge deposition on Si nanowire cores, or  $\text{p-SiNW}_{\text{c}}\text{GeNT}$  nanowires, had been fabricated by Lieber and co-workers. TEM images and composition mapping (Figure 75a) revealed a Si-Ge core-shell structure with a sharp (<1 nm) interface and a crystalline Ge shell (Figure 75b). The diffraction data are consistent with coherently strained epitaxial overgrowth (inset of Figure 75b): that is, a single diffraction peak is observed along the axial direction, which indicates compressively strained Ge and tensile-strained Si. Two peaks, which can be indexed to the Ge (5.657 Å) and Si (5.431 Å) lattice constants, are also observed in the radial direction and indicate relaxation normal to the interface.<sup>264</sup>

**9.3.2.1.14.  $\text{i-GeNW}_{\text{c}}\text{p-SiNT}$ .** The inverse of the nanostructure described in the previous section, namely,  $\text{GeNW}_{\text{c}}\text{p-SiNT}$ , can also be fabricated. Single-crystal Ge nanowires were grown by gold nanocluster directed VLS method, followed by radial growth of the boron-doped p-Si shells by CVD. Bright-field TEM images (Figure 76a) revealed a core-shell structure that is consistent with Ge-core (dark) and Si-shell (light) structure, as confirmed by elemental mapping (Figure 76b,c). HRTEM images of  $\text{i-GeNW}_{\text{c}}\text{p-SiNT}$  core-shell nanowires showed a crystalline Ge core and predominantly amorphous Si shell; hence, they are best designated as  $\text{i-GeNW}_{\text{c}}\text{ap-SiNT}$  (Figure 76d). The Ge-Si interface width is believed to be <1 nm on the basis of cross-sectional elemental mapping. The amorphous Si shell can be crystallized following in-situ thermal annealing at 600 °C, giving rise to  $\text{i-GeNW}_{\text{c}}\text{cp-SiNT}$  (Figure 76f).

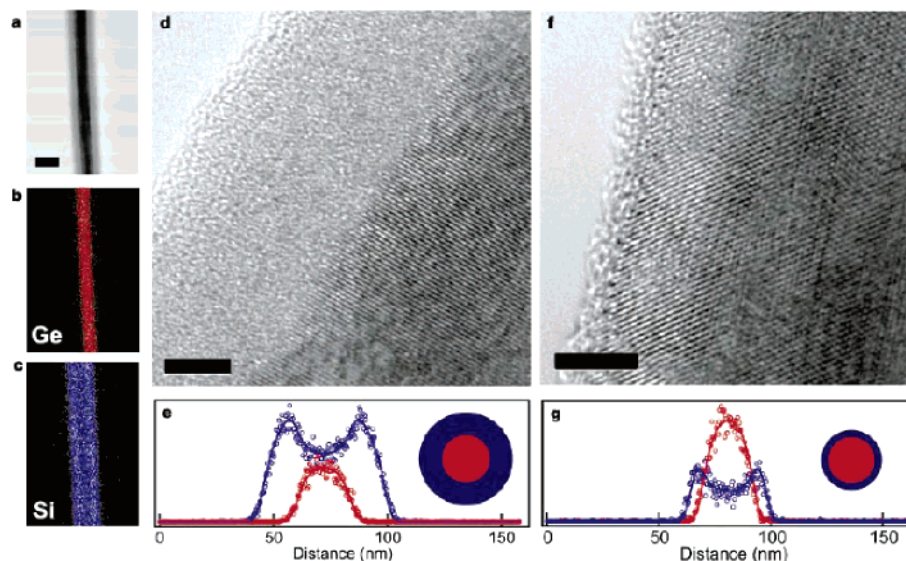
**9.3.2.1.15.  $\text{SiNW}_{\text{c}}\text{Er-SiNW}$ .** The synthesis of silicon nanowires containing erbium in a discrete layered structure has been reported.<sup>265</sup> These nanowires are prepared by pyrolysis of silane and a volatile erbium complex on a gold catalyst surface. The relative size of the wire and sample crystallinity are affected by the timing in which erbium is introduced into the reactant stream. Structural analyses by electron microscopies and X-ray dispersive measurements revealed that the Er is enriched on the surfaces of the nanowires (Figure 77). After a high-temperature vacuum annealing, the characteristic near-IR photoluminescence associated with  $\text{Er}^{3+}$  transitions was obtained.

**9.3.2.1.16.  $\text{SiNW}_{\text{c}}\text{CdSeNT}$ .** The coaxial core-shell  $\text{SiNW}_{\text{c}}\text{CdSeNT}$  nanocables have been fabricated via a simple one-step thermal evaporation process.<sup>266</sup> Both the silicon core and the CdSe sheath are single crystalline. Oxygen is present at both the Si/CdSe interfaces and the outer surfaces of the nanocables. Since both the Si and the CdSe surfaces are oxidized, this constitutes a semiconductor-(s)/insulator multishell nanocable configuration.

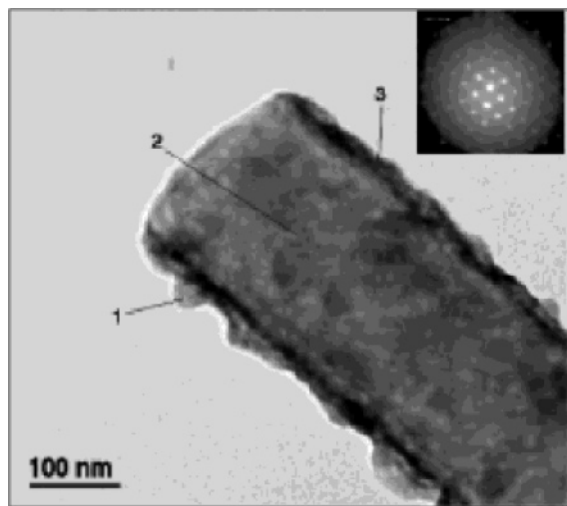
**9.3.2.1.17.  $\text{ZnSNW}_{\text{c}}\text{cSiNT}$ .** The “inverse” of the nanostructure described in the previous section can also be made. It is known that diamond-like cubic Si and zinc blende ZnS have similar crystal structures and very close lattice constants ( $\text{ZnS}$ ,  $a = 0.5431$  nm;  $\text{Si}$ ,  $a = 0.5420$  nm). This lattice matching allows the growth of ZnS thin films on Si substrates. In a recent report by Hu et al.<sup>47</sup> zinc blende ZnS nanowires were used as one-dimensional templates for epitaxial growth of thin monocrystalline Si shells, giving rise to  $\text{ZnSNW}_{\text{c}}\text{cSiNT}$  core-shell nanocables with outer diameters of about 60–180 nm, wall thicknesses of about 20–60 nm, and lengths of several micrometers (Figure 78).

As described in section 6.5.4, this nano-heterostructure,  $\text{ZnSNW}_{\text{c}}\text{cSiNT}$ , can be used to prepare crystalline SiNTs





**Figure 76.** Radial heterostructures of GeNW/SiNT core-shell nanowires. (a) Bright-field image of an unannealed GeNW/SiNT core-shell nanowire with an amorphous p-Si shell. Bar = 50 nm. (b, c) Scanning TEM elemental maps of Ge (red) and Si (blue) concentrations, respectively, in the nanowire of a. (d) HRTEM image of a representative nanowire from the same synthesis as the wire in a–c. Bar = 5 nm. (e) Elemental mapping cross-section showing the Ge (red circles) and Si (blue circles) concentrations. (f) HRTEM image of annealed GeNW/SiNT core-shell nanowire exhibiting a crystalline p-Si shell. Bar = 5 nm. (g) Elemental mapping cross-section gives a 5 nm shell thickness with a sharp interface consistent with the TEM image, suggesting that the Ge and Si do not interdiffuse substantially during the annealing process. (Reprinted by permission from Macmillan Publishers Ltd. (ref 263, <http://www.nature.com>), copyright 2002.)



**Figure 77.** Typical TEM image of a surface Er enriched Si nanowire. Inset: SAED pattern from the center of the wire. EDX analysis for the marked three areas: The center of the wire is Si rich (96%) (area 2) with a dark rim which is Er rich. On the surface of the wire, however, there are two different regions; one relatively smoother area with an appreciably larger erbium concentration (~12%) (area 3), along with nodules emanating from the “stalk” that have a higher erbium concentration (53%) (area 1). (Reprinted with permission from ref 265. Copyright 2002 American Chemical Society.)

by chemical removal of the ZnS nanowire cores with HCl.

**9.3.2.2. Ternary or Higher-Order Radial Heterostructures: Core–Multishell Nanowire Structures.** It is obvious that more complex core–multishell nanostructures can also be fabricated by the same strategy. Examples include the ternary radial heterostructures i-SiNW/SiO<sub>2</sub>NT/p-SiNT (Figure 74e,f) and i-SiNW/c-GeNT/c-SiNT (Figure 75c) core–shell–shell structures made by Lieber and co-workers,<sup>263</sup> SiNW/SiO<sub>2</sub>NT/c-C by Lee and co-workers,<sup>267</sup> and SiNW/SiO<sub>2</sub>NT/c-Er<sub>2</sub>Si<sub>2</sub>O<sub>7</sub>NT by Choi et al. recently.<sup>268</sup>

### 9.3.3. Biaxial, Triaxial, Tetraaxial, and Higher-Order Heterostructures

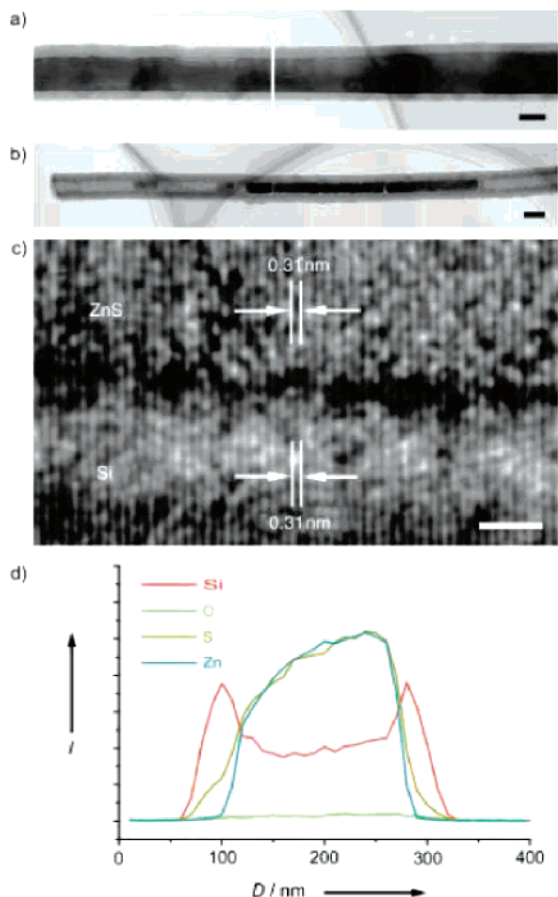
Side-by-side growth of two, three, and four nanowires produces bi-, tri-, and tetraaxial heterostructures, represented by A|B, A|B|C, and A|B|C|D, respectively. As in the case of axial or radial heterostructures, the components A–D can be nanowires (or nanotubes) of the same material but with different dopants or of different materials. Furthermore, they can be multicomponent composite materials of insulators, semiconductors, or metals, or combinations thereof. Examples are given in the following subsections.

**9.3.3.1. Biaxial Nanowires.** *9.3.3.1.1. SiNW/SiO<sub>2</sub>NW.* As discussed in section 6.4.1, one peculiar type of nanostructure obtained using zeolite as quasi template is the biaxial silicon–silica nanowire structure with the *side-by-side* growth of silicon and silica,<sup>48</sup> which may be designated as SiNW/SiO<sub>2</sub>NW. One such nanowire is portrayed in Figure 79. This particular biaxial nanowire has an overall diameter of 10 nm with half of the wire (5 nm) being crystalline silicon and the other half (5 nm) being amorphous silica. The biaxial Si/SiO<sub>2</sub> nanowires also come in different sizes and shapes.

*9.3.3.1.2. SiCNW/SiO<sub>2</sub>NW.* As described earlier in section 8.3, biaxial nanowires of silicon carbide–silicon oxide, designated as SiCNW/SiO<sub>2</sub>NW, can be obtained via the reaction of silicon (produced by disproportionation reaction of SiO) with multiwalled carbon nanotubes (as templates) at 935 °C.<sup>167</sup> A similar biaxial structure was observed by Wang et al. using a different method.<sup>169</sup> The biaxial SiC–SiO<sub>x</sub> nanowires consist of two side-by-side subnanowires of β-SiC and silica, which can be simply referred to as a composite nanowire.

*9.3.3.1.3. SiNW/ZnSNW, SiNW/ZnSeNW.* Epitaxial semiconducting heterostructures, for example, side-by-side SiNW/ZnSNW and SiNW/ZnSeNW biaxial nanowires, can be grown via a simple two-stage thermal evaporation of mixed SiO and SiO and ZnS and ZnSe powders under a precise temperature control.<sup>269,270</sup> Each nanowire had a





**Figure 78.** (a) TEM image of a segment of a ZnSNW@SiNT core-shell nanocable. (b) TEM image showing the residual segments of the ZnS nanowire template in the open-ended Si nanotube after treatment of the ZnSNW@SiNT nanocables with HCl solution. Scale bars in a and b: 100 nm. (c) HRTEM image taken from the interfacial domain between the Si shell and ZnS core of a ZnSNW@SiNT core/shell nanowire, revealing an epitaxial relationship between the Si shell and the ZnS core. Bar = 2 nm. (d) Line-scanning (indicated by a white line in a) elemental mapping displaying Si, Zn, and S spatial elemental distribution profiles across the ZnSNW@SiNT core-shell interface. (Reprinted with permission from ref 47. Copyright 2004 Wiley-VCH.)

uniform diameter of 40–120 nm and length ranging from several to several tens of micrometers. Sub-nanowires of Si, ZnS, and ZnSe within them had diameters of 20–50, 40–60, and 20–50 nm, respectively (Figures 80 and 81). It was proposed that the Si nanowires formed via disproportionation of SiO to Si in the first evaporation stage and then served as one-dimensional nanoscale substrates (or templates) for an epitaxial growth of ZnS or ZnSe nanowires in subsequent thermal evaporation of ZnS or ZnSe. This simple method may be useful for the synthesis of other biaxial heterostructures containing Si and II–VI or III–V semiconducting composite materials.

The optical property (nanoscale cathodoluminescence) of these new structures was also investigated.

**9.3.3.2. Triaxial Heterostructures.** *9.3.3.2.1. ZnSNW|SiNW|ZnSNW.* Sandwichlike ZnSNW|SiNW|ZnSNW triaxial nanowires can also be grown from the two-stage thermal evaporation method detailed in the last paragraph (Figure 82).

**9.3.3.3. Tetraaxial and Higher Order Heterostructures.** Likewise tetraaxial or higher order multiparallel nanowires can in principle be fabricated.

## 9.4. 0-D on 2-D

### 9.4.1. Solid Nanodots on Silicon Wafer

**9.4.1.1. Quantum Dots on Si Wafer.** A wide variety of quantum dots such as Si, Ge, Au, Ni, CdSe, and CdS, etc., have been grown on 2-D Si wafers epitaxially or assembled on Si substrates by taking advantage of surface features such as surface reconstruction, atomic steps, and phase boundaries of reconstructed domains, as well as via self-assembled monolayer (SAM).<sup>271–274</sup> Examples are as follows: SiND–Si, AuND–Si, AgND–Si, AuND–Si, GeND–Si, GaAsND–Si, CdSND–Si, CdSeND–Si, and NiSeND–S, etc. Most of these quantum dots are solid nanoparticles, many are faceted crystallites, some are round shaped, yet others are faceted particles with rounded boundaries. Many excellent reviews are available regarding the fabrication, properties, and applications of these nanomaterials. We shall discuss a few representative examples here.

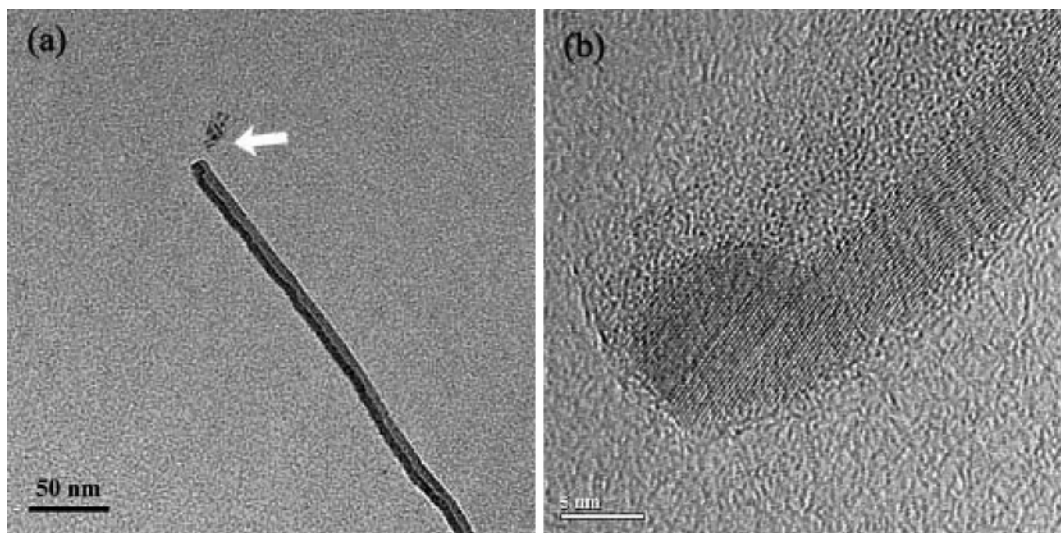
The control of the heteroepitaxial growth of Ge on Si surfaces is important in the fabrication of electronic and optical devices in Si technology. The morphology of Ge grown on Si surface depends on the orientation of the Si surface and the Ge coverage.<sup>275</sup> When the Ge coverage is low, pyramidal islands<sup>276</sup> are formed. As the coverage increases, larger islands called “domes” with many facets become predominant.<sup>277,278</sup> On Si(111) surfaces, coherent island growth is not a commonly observed mode. However, surface structure control strategies have been developed in order to achieve formation of island patterns. For example, Ge quantum dot networks on Si(111) surfaces can be fabricated by depositing an amorphous Ge layer, 1 nm thick, on step-controlled Si(111) surfaces and then annealed.<sup>279,280</sup> During the annealing process, excess Ge beyond a critical coverage formed islands. The average size of the Ge islands can be controlled by the coverage of deposited Ge and the annealing temperature, but island uniformity remains uncontrolled.

The metal or semiconductor nanoparticles can also be fabricated on organosilane monolayers self-assembled on silicon surfaces<sup>281,282</sup> via an approach which combines surface self-assembly with the so-called “constructive nanolithography.” The latter is a nanoelectrochemical patterning process that utilizes electrical pulses delivered by a conductive AFM tip for the nondestructive nanometer-scale inscription of chemical information (in the form of local chemical modification) on the top surfaces of certain highly ordered, long-tail organosilane monolayers self-assembled on silicon. Tip-induced oxidation of surface-exposed vinyl and methyl groups to hydroxyl-containing functions was achieved, followed by the reduction of Ag or CdS nanoparticles on the monolayers.

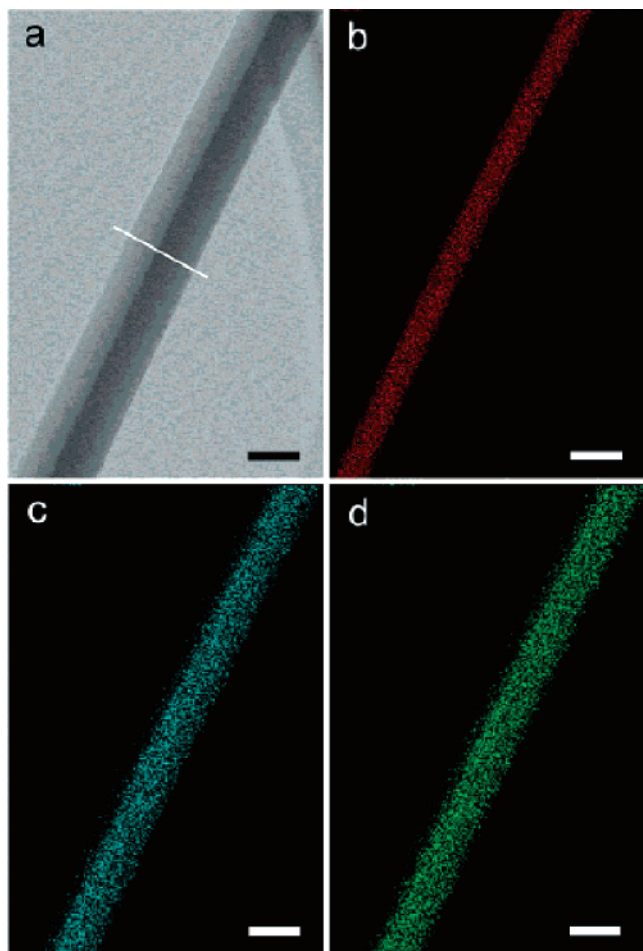
### 9.4.2. Hollow Nanospheres on Silicon Wafer

Hollow nanospheres such as C<sub>60</sub> can be deposited on Si surfaces as we shall discuss next.

**9.4.2.1. Fullerenes on Si wafer: C<sub>60</sub>–Si.** A number of experimental studies have been carried out to determine the nature of the bonding between the C<sub>60</sub> molecules and the Si surface. Some workers in this field have obtained results which imply that the molecules are physisorbed,<sup>283–285</sup> while the results of others suggested chemisorption.<sup>286–290</sup> Again, the reader is referred to the literature for more information regarding this class of nanomaterials. Only a brief discussion is given here.



**Figure 79.** (a) TEM of a biaxial Si|SiO<sub>2</sub> nanowire. (b) Corresponding HRTEM image. (Reprinted with permission from ref 48. Copyright 2003 American Chemical Society.)



**Figure 80.** (a) TEM image depicting a Si (light) and ZnS (dark) subnanowire sides within a SiNW|ZnSNW biaxial nanowire. (b–d) Si, Zn, and S elemental mappings demonstrating a well-defined compositional profile and an abrupt interface. All scale bars in a–d are 50 nm. (Reprinted with permission from ref 269. Copyright 2003 American Chemical Society.)

The interaction between C<sub>60</sub> molecules and Si surfaces was recently probed by near-edge X-ray absorption fine structure (NEXAFS); the results indicated a coverage dependence.<sup>291</sup> The NEXAFS spectra of 1.0 monolayer (ML) C<sub>60</sub> films adsorbed on Si(001)-(2 × 1) and Si(111)-(7 × 7) surfaces

showed the same spectral profile as those of C<sub>60</sub> solids. It was concluded that 75% of C<sub>60</sub> molecules are physisorbed and 25% are chemisorbed at 1.0 ML. At 0.25 ML, the C<sub>60</sub> molecules are chemisorbed. The character of the chemisorption is covalent. Furthermore, the temperature-dependent interaction between C<sub>60</sub> molecules and Si(001)-(2 × 1)<sup>292</sup> and Si(111)-(7 × 7)<sup>293</sup> surfaces at 1.0 ML coverage have been investigated using NEXAFS. At 300 K, the NEXAFS spectrum revealed that the interactions between a C<sub>60</sub> film and both Si surfaces are mainly van der Waals in nature. Annealing at 500 K, however, induced a strong covalent interaction between the C<sub>60</sub> molecules and the silicon substrates.

## 9.5. 1-D on 2-D

### 9.5.1. Nanowires Parallel to Silicon Wafer: NW||Si

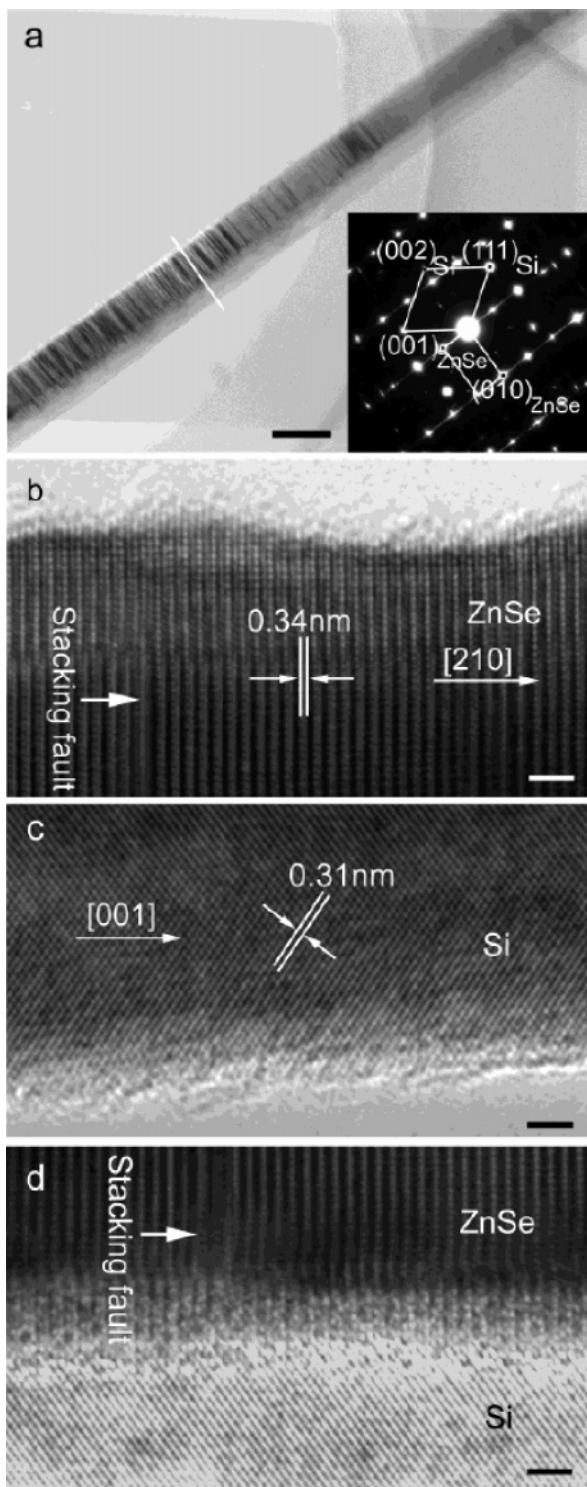
**9.5.1.1. MetalNW||Si.** The self-organized formation of metal or semimetal atom chains (or nanowires) on 2-D Si surface with different surface configurations have been well-studied by STM. In,<sup>294,295</sup> Bi,<sup>296</sup> Al,<sup>297</sup> Ga,<sup>298</sup> and Ag,<sup>299</sup> etc., wires have been self-assembled on Si surfaces by taking advantage of surface features such as surface reconstruction, atomic steps, and phase boundaries of reconstructed domains. Besides imaging, they can also be manipulated by STM as well.

**9.5.1.2. SiNW||Si.** It is also possible to lay SiNWs and other nanowires on pre-designed Si wafer to fabricate NW-based nanoelectronics such as FETs. Several intergration methods have been used to achieve these fabrications, as we will discuss later (section 12).

### 9.5.2. Nanowires Perpendicular to Silicon Wafer: NW⊥Si

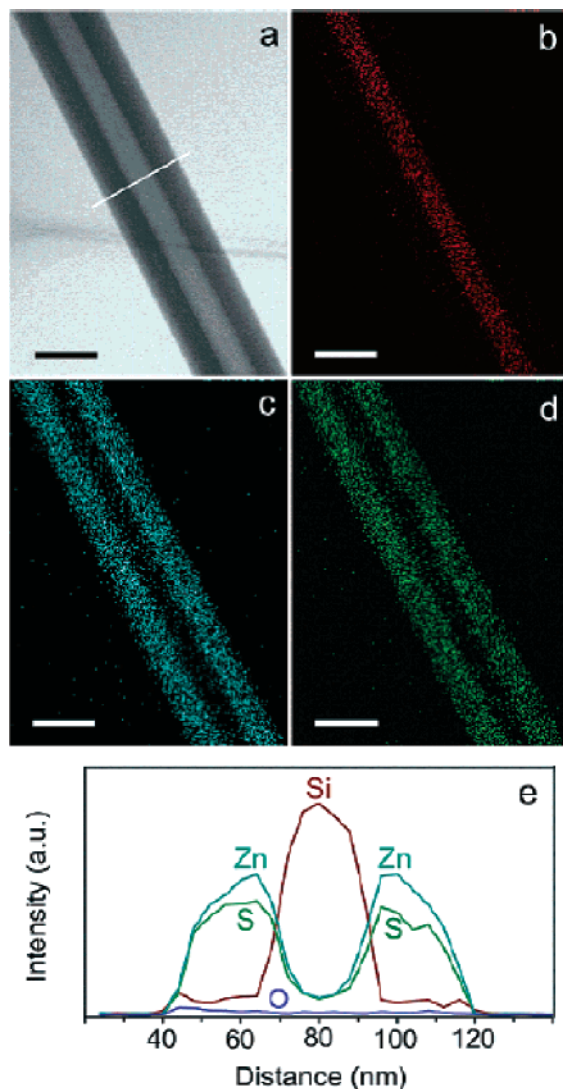
**9.5.2.1. SiNW⊥Si.** The vapor–liquid–solid epitaxy technique is particularly useful in the controlled synthesis of nanowire arrays on prefabricated 2-D Si wafer. In the VLS process, it is known that large-diameter SiNWs prefer to grow along the ⟨111⟩ direction. If a Si (111) wafer is used as a substrate, SiNWs will grow epitaxially and vertically on the substrate to form a nanowire array.<sup>87,88</sup> Figure 83 shows SEM images of SiNWs grown vertically on Si(111) substrate from 50, 30, and 20 nm (nominally) Au colloids (as catalysts).





**Figure 81.** (a) High-magnification TEM image of a straight side-to-side Si|ZnSe biaxial nanowire. An ED pattern (inset) taken from the Si|ZnSe interface area. Bar = 50 nm. (b) HRTEM image of the ZnSe subnanowire growing along the [210] direction. (c) HRTEM image of the Si subnanowire growing along [001] (d) HRTEM image taken from a Si|ZnSe interface domain, revealing a thin intermediate layer between the Si and ZnSe subnanowires. All scale bars in b–d are 2 nm. (Reprinted with permission from ref 269. Copyright 2003 American Chemical Society.)

Recently a new assembly method of 1-D SiNWs perpendicular to a 2-D Si surface was reported.<sup>300</sup> Needlelike structures of jagged SiNWs on the surface of Si wafer are formed after deep reactive ion etching.

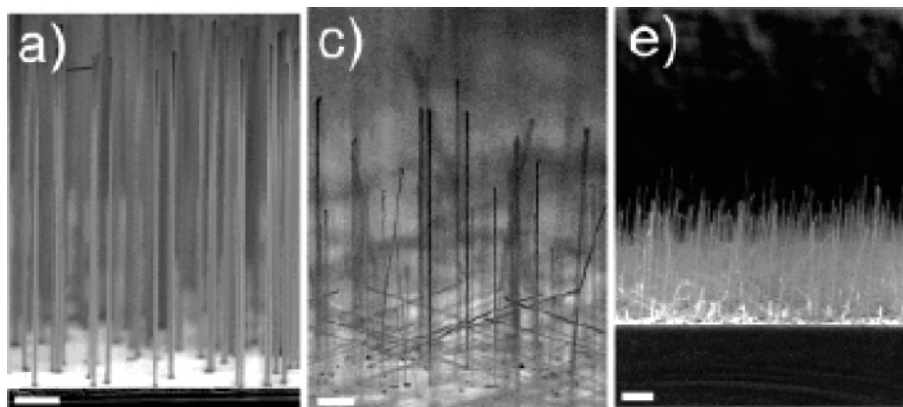


**Figure 82.** (a) High-magnification TEM image depicting two separated ZnS (dark) subnanowires and one central Si (light) subnanowire within a sandwichlike ZnSNW|SiNW|ZnSNW triaxial nanowire. (b–d) Si, Zn, and S elemental mappings, respectively, revealing a three-layer sandwichlike geometry with well-defined compositional profiles. All scale bars in a–d are 50 nm. (e) Line-scanning (indicated by a line in a) elemental mapping of Si, Zn, and S elemental profiles across the sandwichlike ZnSNW|SiNW|ZnSNW triaxial nanowire. (Reprinted with permission from ref 269. Copyright 2003 American Chemical Society.)

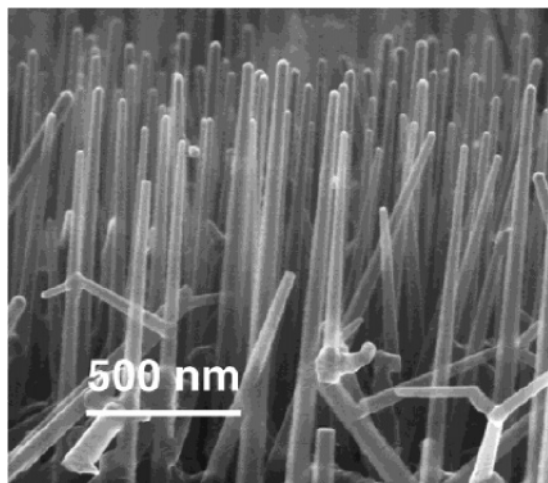
**9.5.2.2. GeNW⊥Si.** Au-catalyzed Ge nanowires had been grown on Si(001) and Si(111) by chemical vapor deposition over the temperature range of 320–380 °C by the VLS process.<sup>301</sup> At the optimum temperature near 320 °C, scanning electron microscopy (Figure 84) showed that many of the nanowires grow epitaxially along the ⟨111⟩ direction of the Si substrate. Au-containing nanoparticles were found at the tips of the nanowires.

**9.5.2.3. (III–V)NW⊥Si.** III–V semiconductor nanowires (GaP, InP, GaAs, GaAsP, and GaAsP) can also be grown epitaxially on Si substrates with perfect epitaxial nucleation of oriented III–V nanowires.<sup>302</sup> The vertical GaP, GaAs, and InP nanowires grown on Si (111) substrates are shown in Figure 85 and Figure 86. Efficient room-temperature generation of light (luminescence) on silicon is demonstrated by the incorporation of double heterostructure segments in such nanowires.





**Figure 83.** (a, c, e) Cross-sectional images of SiNWs grown on Si(111), designated as SiNW $\perp$ Si, from 50, 30, and 20 nm (nominally) Au colloids, respectively. Bar = 1  $\mu$ m. (Reprinted with permission from ref 88. Copyright 2005 American Chemical Society.)



**Figure 84.** Scanning electron micrograph of Au-catalyzed Ge nanowires grown on nominal Si(111), GeNW $\perp$ Si, showing the near vertical orientation of many of the nanowires. (Reprinted with permission from ref 301. Copyright 2004 American Chemical Society.)

### 9.5.3. Nanotubes Parallel to Silicon Wafer: NT $\parallel$ Si

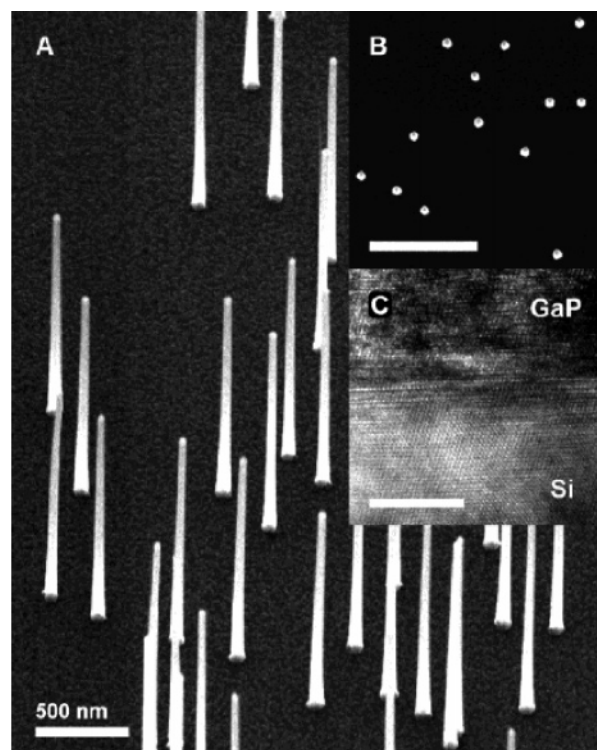
**9.5.3.1. CNT $\parallel$ Si.** CNTs had been laid on pre-designed Si wafer to fabricate CNT-based nanoelectronics such as FETs. Several integration methods have been used to achieve these fabrications, as we shall discuss in a later section (section 12).

### 9.5.4. Nanotubes Perpendicular to Silicon Wafer: NT $\perp$ Si

**9.5.4.1. CNT $\perp$ Si.** CNTs can also be grown perpendicular to 2-D Si wafers, either by employing mesoporous silica as template<sup>303</sup> or by orienting the silicon surface lattices.<sup>304</sup> In addition, CNTs can be self-oriented on patterned porous silicon or plain silicon substrates by a catalytic CVD growth method.<sup>305</sup>

### 9.5.5. 1-D in 2-D: 1-D $\subset$ 2-D

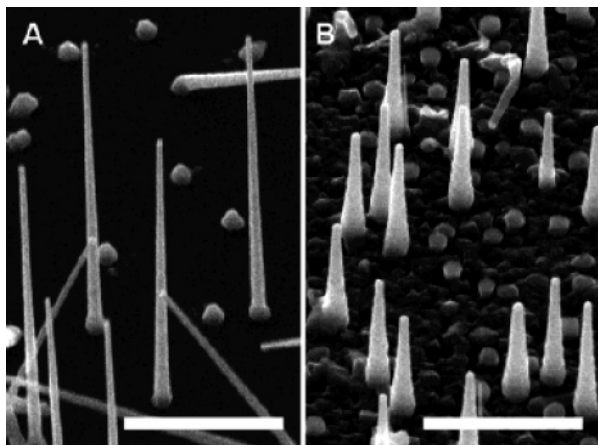
In this section, we shall describe some Si-containing composite nanomaterials based on 1-D nanowires or nanotubes embedded in 2-D nanochannels of membranes. As discussed earlier, hexagonal nanochannel arrays of the so-called anodic aluminum oxide membrane with uniform nanosized pores can be prepared by a potentiostatic anodization process. AAO membranes are widely used as templates or molds in the fabrication of highly ordered arrays of 1-D nanowires or nanotubes.



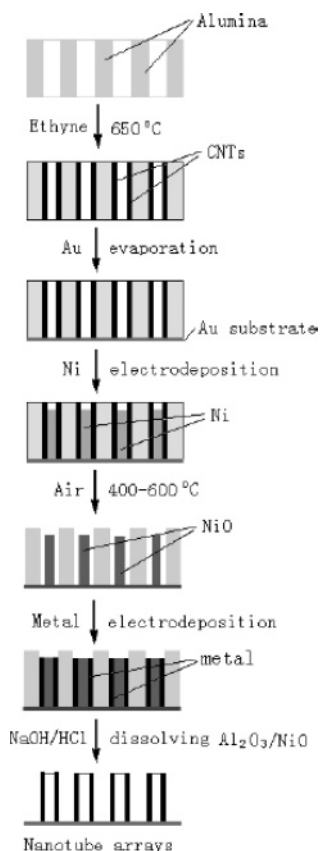
**Figure 85.** Perpendicular growth of GaP nanowires on Si(111), GaP $\perp$ Si. (A) A 45° tilt SEM micrograph of GaP nanowires growing vertically from the Si(111) surface. (B) Top view of the same sample showing the perfection in the vertical alignment. Bar = 1  $\mu$ m. (C) HRTEM image of the Si substrate–GaP nanowire interface. Bar = 10 nm. (Reprinted with permission from ref 302. Copyright 2004 American Chemical Society.)

**9.5.5.1. SiNW $\subset$ AAO, CNT $\subset$ AAO; (III–V)NW $\subset$ AAO, NiNW $\subset$ AAO.** Silicon nanowires embedded in AAO membrane, represented by SiNW $\subset$ AAO, can be prepared by the VLS technique using metal catalysts predeposited within the AAO channels. Nanowires or nanotubes of predetermined diameters of a wide variety of semiconducting, metallic, or insulating materials can also be deposited within the highly ordered arrays of nanochannels of AAO membranes of various pore sizes. Examples are: CNT $\subset$ AAO; (III–V)NW $\subset$ AAO such as GaAsNWs $\subset$ AAO; metals such as NiNW $\subset$ AAO; etc.

**9.5.5.2. cSiNT $\subset$ AAO, NiNW $\subset$ CNT $\subset$ AAO.** Recently, a multistep “template replication” method has been developed by Xu and co-workers in order to fabricate uniform metal nanotube arrays using AAO as templates.<sup>306</sup> Figure 87 shows

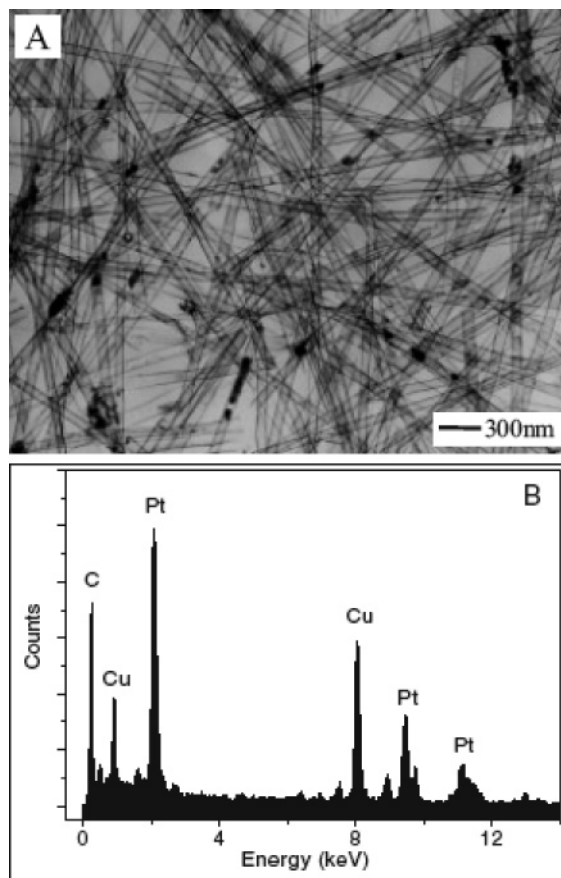


**Figure 86.** SEM images of vertical (A) GaAs nanowires and (B) InP nanowires grown on a Si(111) substrate, giving rise to GaAs $\perp$ Si and InP $\perp$ Si, respectively. Tilt, 45°; bar = 1  $\mu$ m. (Reprinted with permission from ref 302. Copyright 2004 American Chemical Society.)



**Figure 87.** Flow chart of the multistep “template replication” technique for preparing uniform nanotube arrays. Though shown here for metals, this method is also applicable to other materials (e.g., cSiNTs, see section 6.5.3). (Reprinted with permission from ref 306. Copyright 2004 Wiley-VCH.)

a flow chart of the multistep template replication process for preparing uniform metal nanotube arrays. Figure 88 shows a TEM image and EDX spectrum of a Pt nanotube sample prepared by this process. One application of this particular technique is the fabrication of crystalline silicon nanotubes, cSiNTs, as discussed in section 6.5.3.<sup>46</sup> The first step is the deposition of CNTs onto the interior walls of the AAO templated by pyrolytic decomposition of ethyne in Ar atmosphere. The nickel metal was electrodeposited into the pores of the CNT $\perp$ AAO membranes to form a coaxial



**Figure 88.** (A) TEM image of the as-prepared metal nanotubes. (B) EDS spectrum of the metal nanotubes shown in A. (Reprinted with permission from ref 306. Copyright 2004 Wiley-VCH.)

nanocable structure of NiNW $\perp$ CNT $\perp$ AAO. These NiNW $\perp$ CNT $\perp$ AAO membranes were heated in air at 400 °C, causing the oxidation of nickel to NiO, and at higher temperatures (600 °C) the decomposition (incineration) of the CNT shells, leaving NiO nanowires in the channels, NiONWs $\perp$ AAO. Here, instead of electrodeposition of metals as in the preparation of metal nanotubes, silane was introduced (after evacuation) in a stream of argon gas and the reaction temperature kept at 600 °C to cause the growth of crystalline silicon nanotubes, cSiNT. The arrays of multishell structures can be represented by NiONWs $\perp$ CcSiNT $\perp$ AAO. Here the outer diameter of the resulting cSiNT is limited by the pore size of the AAO membrane, and the inner diameter is determined by the diameter of the NiONW template, with the wall thickness being the difference of the two diameters. Finally, the NiO cores and the AAO membranes can be chemically removed with NaOH followed by HCl to yield highly ordered arrays of cSiNTs.

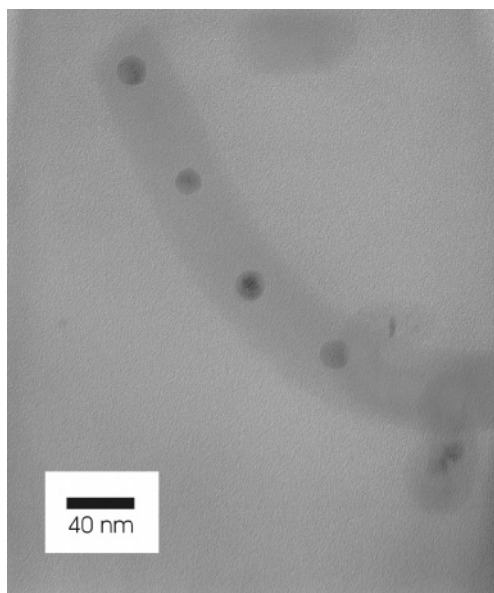
It is interesting to note that the composite nanostructures NiNW $\perp$ CNT $\perp$ AAO, NiONW $\perp$ metalNT $\perp$ AAO, and NiONW $\perp$ CcSiNT $\perp$ AAO may be regarded as 1-D $\perp$ 1-D $\perp$ 2-D.

## 9.6. 2-D on 2-D

### 9.6.1. Quantum Wells

Two-dimensional on 2-D structures are commonly referred to as quantum wells. Quantum wells have been well-studied. The reader is referred to many excellent reviews in the literature.<sup>307–312</sup> Only a brief discussion is warranted here.

Si/Si<sub>1-x</sub>Ge<sub>x</sub> heterostructures<sup>307–310</sup> have attracted much interest in recent years because silicon-based heterostructures



**Figure 89.** TEM image of horizontal cross-section of a necklacelike silicon nanowire with silicon nanoparticles immersed in an amorphous silicon dioxide nanowire. (Reprinted with permission from ref 79. Copyright 2003 American Chemical Society.)

can significantly enhance the performance level of contemporary Si devices without sacrificing the essential compatibility with standard Si technologies. Epitaxially smooth Si/SiGe quantum wells and heterostructures were fabricated and extensively characterized in the past decade with the main goal of producing highly conducting electronic channels for improved field effect transistor structures.<sup>313</sup> Si/Si<sub>1-x</sub>Ge<sub>x</sub> heterostructures have been synthesized by self-assembling and self-ordering during heteroepitaxy growth of silicon-germanium alloys on single-crystal silicon substrates. The most important deposition techniques to fabricate Si/Si<sub>1-x</sub>Ge<sub>x</sub> heterostructures are molecular beam epitaxy (MBE) and CVD, though new powerful techniques such as atomic layer deposition (ALD) have been developed.<sup>314</sup>

The photoluminescence (PL) from Si quantum well structure is another attractive property.<sup>312,315</sup> For example, PL has been observed from Si single quantum well structures,<sup>315</sup> consisting of either an amorphous or a crystalline Si layer of 3 nm in thickness, embedded between silicon nitride layers. These structures were grown by plasma-enhanced CVD on Si substrates. After crystallization of the originally amorphous Si layers and passivation by hydrogen, strongly polarized PL was observed in the entire visible region. In contrast, a reference structure without the 3 nm silicon layer, but otherwise identical, shows PL in the red and infrared only. It was concluded that the PL in the blue and green part of the spectrum comes from recombination via Si quantum well states, while the red and infrared PL are due to states at the interface between crystalline Si and silicon nitride.

## 10. Nanomachining, Nanomanipulating, and Nanoassembling Techniques

Fabrication of nanomaterials of precise dimensions and well-defined shapes poses a real challenge in nanotechnology. To construct a nanodevice, one must be able to control the sizes and shapes of materials and to manipulate and assemble the components at the nanometer level. In this section, we describe a number of strategies or ways to produce nano-

structures of precise dimensions and well-defined shapes and to manipulate or assemble them in a controllable manner in the nanorealm.

### 10.1. Nanomachining Crystalline Silicon Nanowires into Nanodots and Nanorods

A simple and convenient method,<sup>79</sup> using the well-established microtome technique widely used in the preparation of biological microscope samples, was recently developed to precision-cut silicon nanowires into nanodots (SiNDs) or nanorods (SiNRs) of well-defined sizes and shapes. It is obvious that if nanodots or nanorods can be cut reproducibly from an oriented nanowire, a wide range of identical nanostructures of well-defined sizes and shapes can be produced.

This nanomachining technique also allows TEM observation of the cross-sections of nanowires. Figure 15a shows the HRTEM image of the vertical cross-section of a SiNW. The solid-wire nature, the elliptical shape, and the perfect single crystalline structure of the cross-section can be observed. The Si atomic-resolution image allows determination of the growth direction of the SiNW to be the (110) direction with the perpendicular (111) planes ( $d$ -spacing = 3.15 Å) meeting at the expected angle of 109.5°. Other growth orientations such as (112) and (111) have also been obtained. In fact, as discussed earlier, (110) and (112) growth orientations are quite common with SiNWs prepared from the SiO thermal evaporation technique, while (111) growth is more common with the laser ablation method.

From the HRTEM image, three parameters can be deduced:  $R$ , the radius of the Si core (which is also the short (minor) radius of the elliptical image of the cross-section);  $r$ , the long (major) radius of the ellipse; and  $p$ , the distance between the centers of the two ellipses (see Figure 15b). On the basis of these parameters, the thickness  $t$  and the inclination angle  $\theta$  of the nanocylinder can be calculated. For this particular nanocylinder, the diameter measured  $2R = 10.6$  nm with the other parameters being  $2r = 12.4$  nm,  $t = 9.4$  nm, and  $\theta = 32^\circ$ .

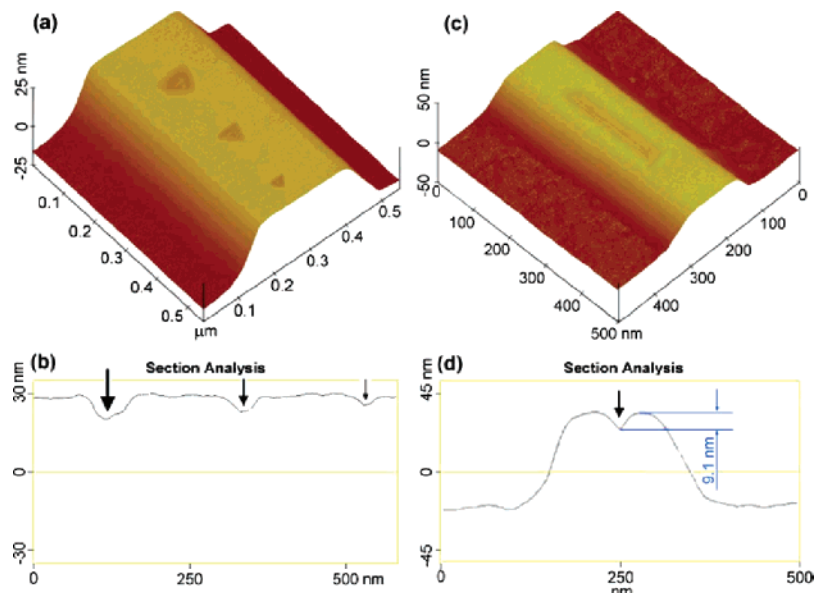
This technique also reveals twinning of SiNDs and SiNWs, as exemplified by the cross-section of a twinned SiNW shown in Figure 16. The diameter of this particular twinned nanocylinder measured  $2R = 8.2$  nm. On the basis of the measured  $R$ ,  $r$ , and  $p$ ,  $t$  was calculated to be 9.4 nm and  $\theta$  to be 20°. The fact that this nanocylinder was composed of two half-cylinders of single crystalline silicon is rather amazing.

Other sizes and shapes of nanodots and nanorods can likewise be cut and measured from their HRTEM images.

In addition to regular SiNWs, some necklacelike silicon nanowires can also be sectioned. These latter SiNWs were formed by silicon nanoparticles which are connected by a continuous outer layer of silicon dioxide.<sup>224</sup> One example is the horizontal cross-section of a chainlike SiNW depicted in Figure 89. The silicon nanodots, measuring 16–20 nm in diameter, were immersed in an amorphous silicon oxide nanowire of 48 nm in diameter, giving rise to the necklacelike structure.

The same technique can also be applied to other nanowires, nanotubes, nanoribbons, and multiaxial nanowires, as well as more complex low-dimensional composite nanomaterials.





**Figure 90.** (a) AFM image of an array of nanoindentations fabricated on the top surface of a ZnS nanobelt. The indentations are created with a diamond AFM tip at loads of 18.9, 15.2, and 11.4  $\mu\text{N}$ , respectively, and imaged with the same tip in situ. (b) Cross-sectional view ( $z$  scan) of indentation depths of successively deeper dents. (c) AFM image of a nanochannel fabricated by dragging the AFM diamond dip along the nanobelt. (d) Cross-sectional ( $z$  scan) profile of the nanochannel. (Reprinted with permission from ref 323. Copyright 2005 American Institute of Physics.)

## 10.2. Nanomanipulating Using Scanning Probe Microscopy and Lasers

### 10.2.1. Nanomanipulating Using SPMs and SEM

Nanoscale objects can be manipulated by using scanning probe microscopes, including scanning tunneling microscope, atomic force microscope, or variants thereof. Although SPMs are normally used for imaging, they can also be used to manipulate nanoscale objects as small as atoms.<sup>316</sup> While STMs are limited to electrically conducting surfaces, AFMs can image insulators under ambient conditions. Many excellent reviews are available regarding nanomanipulating by STMs and AFMs.<sup>317–321</sup>

The drawback of SPMs technique is the lack of visual feedback of the manipulation process in real time. The integration of AFMs into scanning electron microscopies can overcome this drawback. Operating the AFM in the chamber of an SEM allows visual feedback from the SEM which can be used for the manipulation.<sup>322</sup>

Likewise other devices can be integrated into SEM or SPM to perform functions such as for nanopositioning, nanomanipulation, and microgripping, etc.<sup>322</sup> One example is the nanoindenter integrated with an atomic force microscope<sup>323</sup> which has been shown to be a powerful machining tool for cutting precise-length nanowires or nanobelts and for manipulating the pre-cut wires. Its utility in cutting grooves and fabricating dents (or periodic arrays of dents) in ZnS nanobelts was also demonstrated (Figure 90). This approach allows the direct mechanical machining of nanodevices that are supported on a substrate without the inherent complications of e beam or photolithography.

Yet another example is the nanopatterning of nanosquares and nanodots of nickel using atomic force microscopy for nanomachining in combination with a lift-off process.<sup>324</sup> With the use of nickel nanodots as catalysts, single silica nanowires with a uniform diameter of 20 nm have been grown.

### 10.2.2. Nanomanipulating Using Lasers

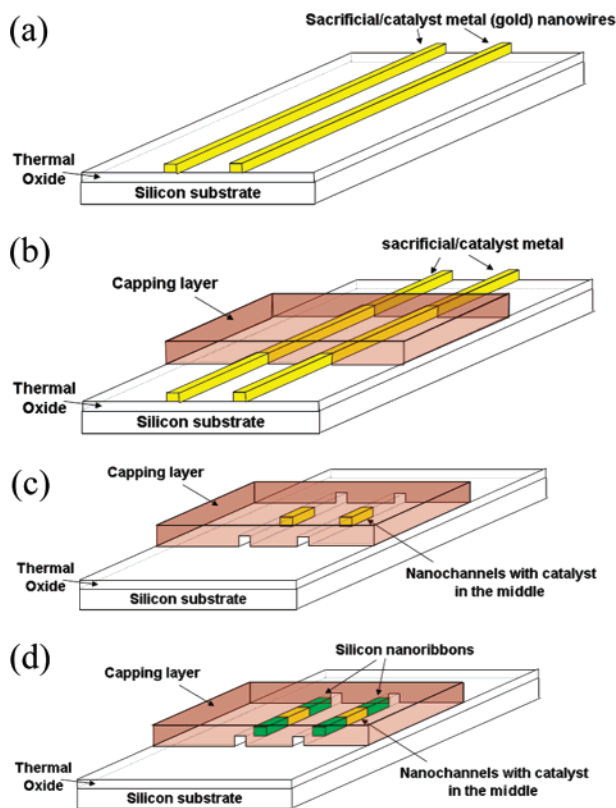
The optical forces are ideally suited for manipulating mesoscopic systems. Many of the powerful optical manipu-

lation techniques are derived from single-beam optical traps known as optical tweezers.<sup>325</sup> An optical tweezer uses forces exerted by a strongly focused beam of light to trap small objects.<sup>326–328</sup> Although the theory behind optical tweezers is still being developed, small objects develop an electric dipole moment in response to light's electric field. Optical tweezers can trap objects as small as 5 nm<sup>329,330</sup> and can exert forces exceeding 100 pN<sup>331–333</sup> with resolutions as fine as 100 aN,<sup>334–336</sup> ideal for manipulating. The reader is referred to an excellent review on optical tweezers by Grier.<sup>325</sup>

## 10.3. “Grown-in-Place” Approach

The grown-in-place approach<sup>93,94</sup> was recently developed to produce SiNWs and/or Si nanoribbons of controlled size, shape, and orientation. This technique was briefly discussed in section 6.4.3.1. In ref 93, the VLS growth mechanism and lithographically fabricated nanochannel templates were combined to control the size, shape, orientation, and positioning of the Si nanowires and ribbons in predetermined device architectures. Figure 91 is the flow chart of the fabrication technique. The growth nanochannels were horizontally arrayed and became a permanent part of the device structure. Contacts and interconnects, as well as device encapsulation, can be built into the templates as well (Figure 92). As another example, He et al.<sup>94</sup> employed a similar method to grow Si nanowires laterally in microtrenches that were prefabricated on silicon-on-insulator (SOI) wafers via vapor–liquid–solid epitaxial growth (Figure 93). After a growing nanowire impinges on the opposite sidewall, an electrical or thermal connection will be automatically made, with the bridging Si nanowire being the active device unit, the Si pads confining the trench as the electrodes, and the underlying SiO<sub>2</sub> layer acting as the insulator/dielectric barrier.

Compared to the “pick and place” approach, the grown-in-place strategy has the distinct advantage of allowing integration of nanomaterials growth into device fabrication, i.e., growing nanowire/ribbon in place and fabricating devices directly onto integrated circuits.



**Figure 91.** “Grown-in-place” approach for the fabrication of self-assembling/positioning Si nanowires/nanoribbons using nanochannel templates. (a) Sacrificial/catalyst metal (Au) lines defined by e beam lithography and lift-off. (b) Deposition and patterning of the capping layer. (c) Partial etching of the sacrificial metal to form the nanochannels with catalyst in the middle. (d) Si nanowire/nanoribbon growth by the VLS mechanism. (Reprinted with permission from ref 93. Copyright 2004 American Chemical Society.)

#### 10.4. Langmuir–Blodgett Technique

Langmuir–Blodgett (LB) technique<sup>337–340</sup> has been used to assemble nanowires to form high-density arrays. As an example, Figure 94 shows a schematic process for the use of LB technique to assemble nanowires. For nanotechnology applications, how to address individual elements in a high-density arrays and how to achieve precise layer-to-layer registration for vertical integration are just two of the many challenges lying ahead.

#### 10.5. Electrical Field Directed Assembly

Applied electric fields (E-fields) can be used to attract and align NWs due to their highly anisotropic structures and large polarizabilities. One example is shown in Figure 95.<sup>341</sup> Here an electric field was used to position individual NWs at specific positions with controlled orientation. E-field directed assembly of NWs between an array of electrodes is illustrated in Figure 95C which shows that, by applying an electric field, individual NWs can be positioned to bridge pairs of diametrically opposite electrodes to form a parallel array. Furthermore, by changing the direction of the applied electric field with sequential NW solutions, the alignment can be carried out in a layer-by-layer fashion to produce crossed NW junctions (Figure 95D).

#### 10.6. Microfluidics Assembly

Lieber and his co-workers have developed a fluidic flow directed assembly method<sup>342</sup> to align and assemble nano-

wires. Using this technique, NWs (or NTs) can be aligned by passing a suspension of NW solution through microfluidic channel structures. Figure 96 shows a schematic process of microfluidic assembly method to assemble nanowires. In this case, the microfluidic channel structure was formed between a poly(dimethylsiloxane) (PDMS) mold and a flat substrate. Parallel and crossed NW arrays can be created using single (Figure 96A) and sequential crossed (Figure 96B) flows, respectively, in the assembly process.

#### 10.7. Other Techniques

Many new and powerful techniques for nanofabrication have been developed in recent years. Examples are nanoimprint lithography (NIL),<sup>343–345</sup> step-and-flash imprint lithography (SFIL),<sup>346–348</sup> scanning probe lithography (SPL),<sup>349–352</sup> edge lithography,<sup>353–360</sup> and atomic layer deposition (ALD),<sup>314</sup> etc. These new approaches for nanofabrication are pushing the boundaries of nanoscience and technology, some are even close to reaching the limits of the laws of physics. For example, NIL can mold a variety of polymeric materials and pattern features as small as  $\sim 5$  nm<sup>361,362</sup> and aspect ratios of up to  $\sim 20$  (height-to-width).<sup>363</sup>

Compared to conventional techniques of photolithography and scanning beam (or maskless) lithography (e.g., electron beam and focused ion beam lithography), these new techniques have been classified “unconventional” nanofabrication techniques. These techniques create opportunities for fabrication at the nanometer level and over large areas and thus offer competition in nanofabrication where cost and materials make photolithography difficult.<sup>364</sup> The reader is referred to several excellent reviews in the literature (see, for example, Gates et al.<sup>364,365</sup> and Bratton et al.<sup>366</sup>).

The combination of different techniques, conventional or unconventional, can create new methods for nanofabrication. One example is the use of templates fabricated by top-down methods to direct the bottom-up assembly of components—in essence, combining top-down and bottom-up strategies. We will discuss the latter in section 12. Here we shall illustrate such strategy with two examples.

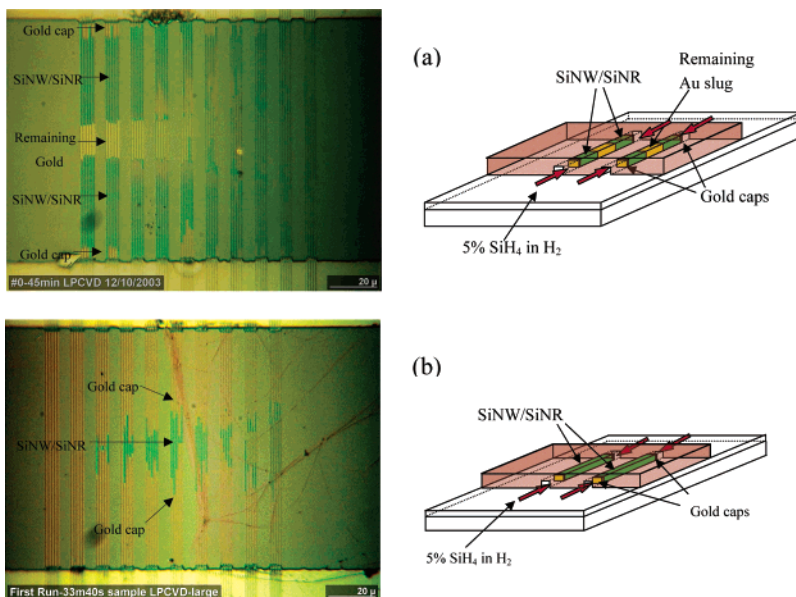
A simple technique to form a variety of three-dimensional structures in silicon was reported.<sup>367</sup> The process comprises two steps: lithography and electrochemical etching (LEE). The LEE process is a promising nanomachining tool useful for fabricating high-aspect-ratio structures such as walls, tubes, and pillars, etc.

Choi et al. reported a new nanomachining strategy<sup>368</sup> for the fabrication of arrayed colloidal particles with well-ordered nanometric holes of 3- or 4-fold symmetry by anisotropic reactive ion (plasma) etching (RIE) of self-organized layers of colloidal spheres.

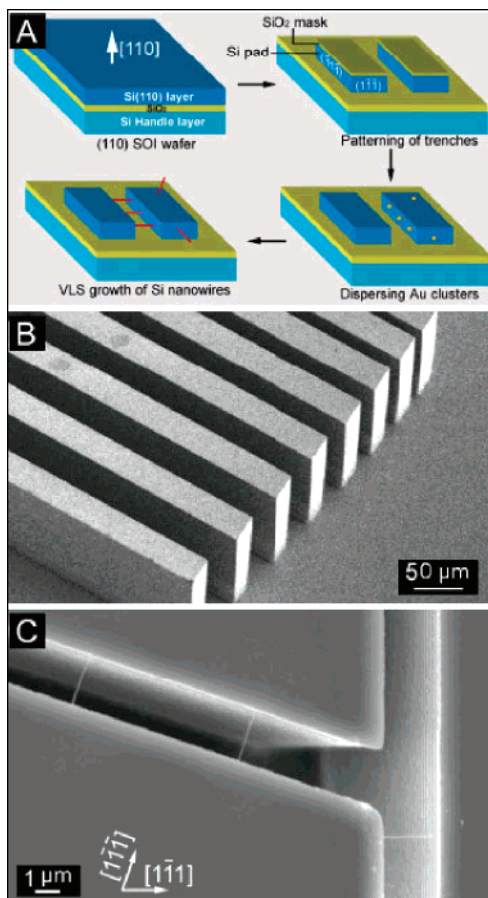
#### 11. Quantum-Size Effects

Nanostructures such as nanodots (0-D), nanowires (1-D), and quantum wells (2-D), as well as composite nanostructures ( $n$ -D on  $m$ -D) described in this review, exhibit quantum confinement effects when their dimensions are reduced to below 10 nm.

Silicon is without doubt the most important electronic material, the basic building material for the semiconductor industry, and the workhorse for micro- and nanotechnologies. However, since silicon is not a direct band gap semiconductor, it is generally not considered a good photonic material, though this view is gradually changing, primarily due to

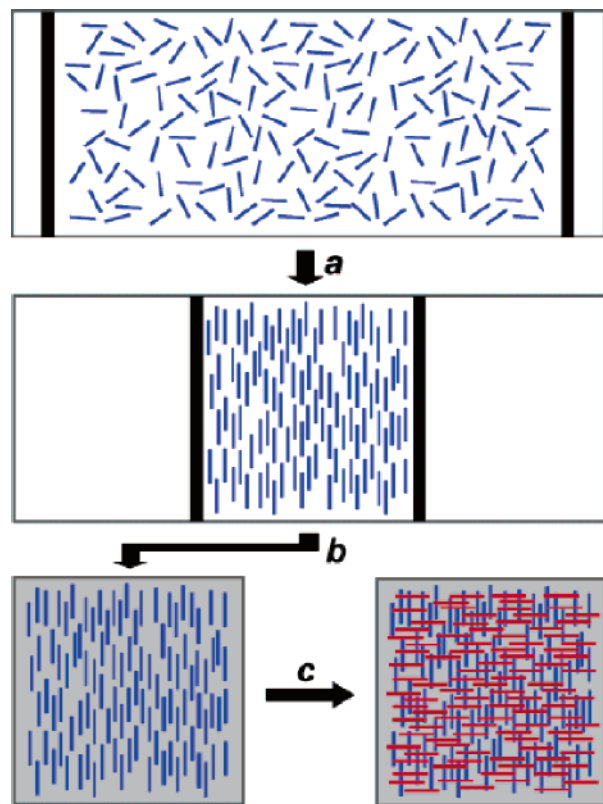


**Figure 92.** Optical microscope images and corresponding schematics for SiNW/Rs grown inside nanochannel templates by the grown-in-place VLS approach. Growth patterns are shown for (a) the long Au slug case and (b) the short Au slug case. (Reprinted with permission from ref 93. Copyright 2004 American Chemical Society.)



**Figure 93.** Growth of Si nanowire bridges in microfabricated trenches. (A) Schematic illustration of the formation of the Si nanowire bridge between two vertical Si{111} surfaces on (110)-oriented SOI wafers. (B) SEM image of a group of parallel trenches formed on an SOI wafer. (C) SEM image of nanowire bridges grown in the microtrenches. (Reprinted with permission from ref 94. Copyright 2005 Wiley-VCH.)

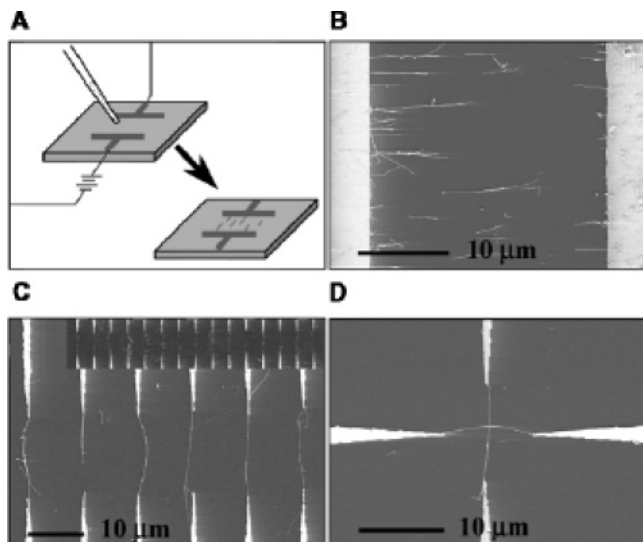
many recent discoveries and advances in nanomaterials and nanotechnologies (especially nanophotonics) involving silicon. For one, all the quantum-confined Si systems, such as



**Figure 94.** NWs (blue lines) in a monolayer of surfactant at the air-water interface are (a) compressed on a Langmuir-Blodgett trough to a specified pitch. (b) The aligned NWs are transferred to the surface of a substrate to make a uniform parallel array. (c) Crossed NW structures are formed by uniform transfer of a second layer of aligned parallel NWs (red lines) perpendicular to the first layer (blue lines). (Reprinted with permission from ref 337. Copyright 2003 American Chemical Society.)

porous silicon,<sup>369,370</sup> single Si nanocrystallites,<sup>371–373</sup> Si/SiO<sub>2</sub> quantum wells,<sup>374</sup> and SiNWs,<sup>375–378</sup> exhibit enhanced photoluminescence in the visible as well as band gap opening in the nanorealm.





**Figure 95.** Electric field directed assembly of NWs. (A) Schematic view of E-field alignment. (B) Parallel array of NWs aligned between two parallel electrodes. (C) Spatially positioned parallel array of NWs obtained following E-field assembly. The top inset shows 15 pairs of parallel electrodes with individual NWs bridging each diametrically opposed electrode pair. (D) Crossed NW junction obtained using layer-by-layer alignment with the E-field applied in orthogonal directions in the two assembly steps. (Reprinted with permission from Macmillan Publishers Ltd. (ref 341, <http://www.nature.com>), copyright 2001.)

SiNWs in the quantum confinement regime, in particular, may play a key role as interconnects and functional components in future nanosized electronic and optical devices (see section 12.5). It has been suggested that semiconductor wires finer than 100 nm in diameter can be used for developing 1-D quantum-wire high-speed field effect transistors and light-emitting devices with extremely low power consumption.

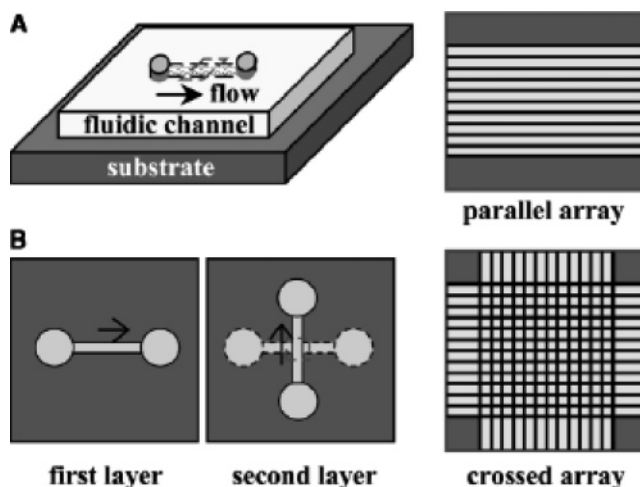
We will discuss photoluminescence and band opening of SiNWs and SiNDs in this section.

## 11.1. Photoluminescence

Photoluminescence is emission of light when a pair of electron and hole, created by absorption of a photon, recombine in a material. Photoluminescence differs from electroluminescence in that the electron–hole pair is excited by light absorption rather than by applying a voltage. In general, the wavelength of the luminescence is longer than that of the light being absorbed because part of the energy is lost to other nonradiative processes.

When silicon is irradiated with a visible light, it emits radiation only weakly in the infrared region. In other words, silicon does not emit light efficiently. This is because the radiative recombination of the electron–hole pair is very slow in silicon due to the fact that silicon is an “indirect band gap” semiconductor which means that momentum is not conserved in the recombination process. Hence bulk silicon has traditionally been considered not a good photonic material.

This view was changed when Leigh Canham, in 1990, discovered that silicon can be turned into an efficient light emitter when etched by electrochemical or other means to form a spongelike material known as “porous silicon”, which comprises an array of nanosized filaments containing SiNDs and SiNWs. Porous silicon, when illuminated with an ultraviolet light, will emit red, yellow, green, and blue lights,



**Figure 96.** Fluid flow directed assembly of NWs. (A) A channel is formed when a trench structure is brought in contact with a flat substrate. Nanowire assembly is carried out by flowing a NW suspension through the channel at a controlled rate and for a set duration. Parallel arrays of NWs are observed in the flow direction on the substrate when the trench structure is removed. (B) Crossed NW arrays can be obtained by changing the flow direction sequentially in a layer-by-layer assembly process. (From ref 342 (<http://www.sciencemag.org>). Reprinted with permission from AAAS.)

depending upon the degree of etching. We shall discuss the photoluminescence, as well as the electroluminescence properties of porous silicon, SiNDs, and SiNWs in section 12.5.2 (Nanophotonics)

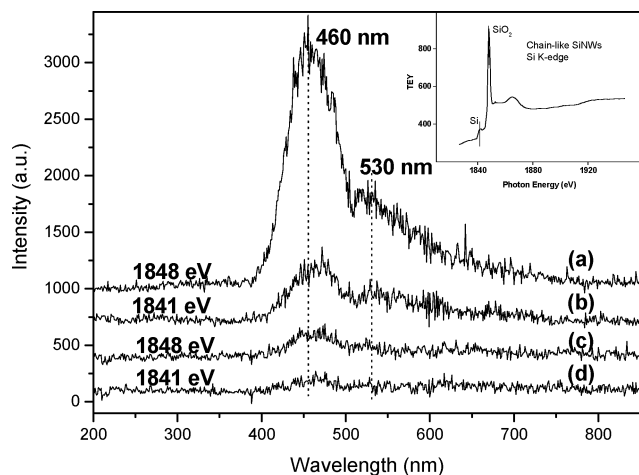
### 11.1.1. 0-D on 0-D: $\text{SiND}_C\text{SiO}_2\text{ND}$

There is a vast literature on the photoluminescence of porous silicon and silicon nanocrystallites. The reader is referred to the many excellent reviews<sup>193–196,379–382</sup> in the literature.

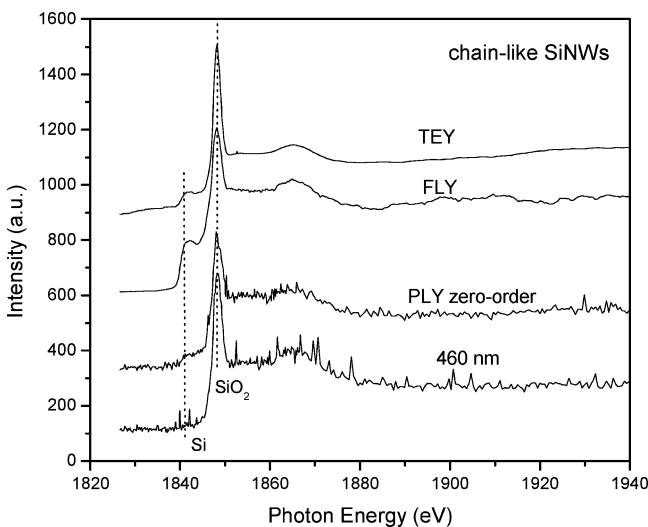
### 11.1.2. 0-D in 1-D: Chainlike $\text{SiND}_C\text{SiO}_2\text{NW}$

We shall discuss here the photoluminescence of necklace- or chainlike silicon nanowires (SiNWs),  $\text{SiND}_C\text{SiO}_2\text{NW}$ , which may be described as a chain of crystalline Si nanoparticles immersed in an amorphous silicon oxide wire.

X-ray excited optical luminescence (XEOL) has been used by Sham and co-workers to study SiNWs.<sup>224,375,376</sup> The XEOL technique monitors the optical response of a light-emitting material by tuning the X-ray energy to a specific excitation channel (often at the X-ray absorption edge of an element of interest) and monitoring the luminescence with an optical monochromator (typically in the range of 200–900 nm). The relative quantum yield of the luminescence depends strongly on the site and chemical environment of the absorbing atom. The luminescence may be due to excitons (i.e., recombination of a hole in the valence band and an electron in the conduction band) or defects. The photoluminescence yield (PLY) can in turn be used to record X-ray absorption fine structure (XAFS) that provides structural information for the absorption site responsible for the luminescence. By combining the XEOL and PLY spectra, one can obtain the structural dependence of the luminescence. The XEOL of the necklacelike SiNWs is compared with that of the normal SiNWs in Figure 97. The excitation photon energies were at the Si K-edge (1841 eV) and  $\text{SiO}_2$  resonance position (1848 eV). Two emission bands in the blue and green regions, with maxima at 460 (2.7 eV) and 530 nm (2.34 eV),



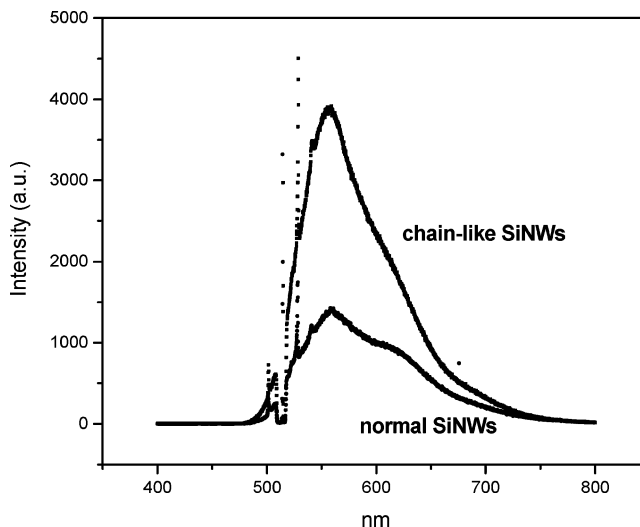
**Figure 97.** XEOL of the chainlike SiNWs (curves a, b) compared to the normal SiNWs (curves c, d) excited with photon energies at Si K-edge (1841 eV) and SiO<sub>2</sub> resonance position (1848 eV). (Reprinted with permission from ref 224. Copyright 2004 American Institute of Physics.)



**Figure 98.** PLY at the Si K-edge XAFS of the chainlike SiNW sample monitored with total (zero-order) and wavelength-selected (460 nm) luminescence. TEY and FLY are also shown. (Reprinted with permission from ref 224. Copyright 2004 American Institute of Physics.)

respectively, were observed. It can be seen that the neck-lacelike SiNWs exhibited much stronger emission intensities than that of the normal SiNWs. The intensities of the two peaks increased remarkably, especially in the chainlike SiNWs when the K-edge channel of silicon oxide was turned on at 1847.5 eV. The peak at 460 nm (2.7 eV) is similar to the results observed in the silica nanowires<sup>383</sup> and can be attributed to the neutral oxygen vacancy in the oxide, while the peak at 530 nm (2.34 eV) may arise (primarily) from the small Si crystallites embedded in the SiNW (due to the quantum-size effects exhibited by small nanosized Si crystallites<sup>372,384,385</sup> or from defects surrounding the silicon nanoparticles.<sup>376</sup>

Figure 98 shows the PLY at the Si K-edge XAFS of the chainlike SiNW sample monitored with total (zero order) and wavelength-selected (460 nm) luminescence. The total electron yield (TEY) and fluorescence yield (FLY) are also shown. Both PLY spectra show spectral features similar to those observed in TEY and FLY spectra except for the intensity of the elemental Si whiteline (~1841 eV) which



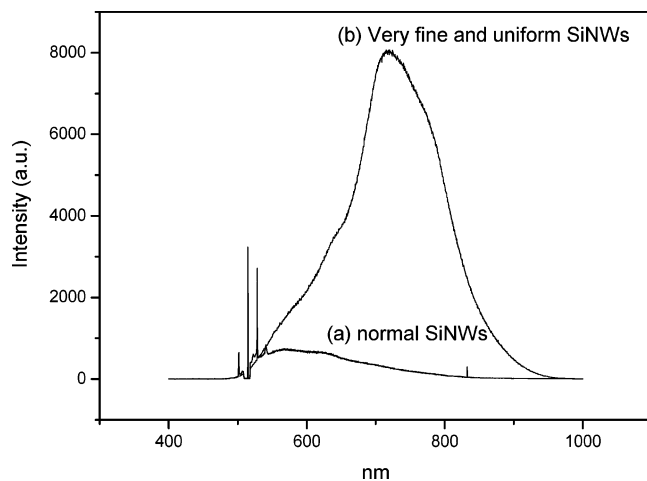
**Figure 99.** Photoluminescence spectra of chainlike and normal SiNWs excited at 514 nm with an argon ion laser. (Reprinted with permission from ref 224. Copyright 2004 American Institute of Physics.)

decreases noticeably in the zero-order PLY and nearly disappears at the 460 nm (2.7 eV) PLY. Since TEY is surface sensitive while FLY and PLY are bulk sensitive, this observation indicates that the total luminescence (zero-order PLY) arises mainly from silicon oxide, as expected from Figure 97. The disappearance of the elemental Si whiteline and an enhanced oxide feature in the 460 nm PLY show that the luminescence at 460 nm (2.7 eV) originates primarily from silicon oxide. The weaker luminescence at 530 nm and the difference in the intensities of the elemental Si K-edge whiteline between the zero-order and 460 nm PLY are consistent with the notion that the 530 nm peak originates primarily from the quantum-confined Si crystallites. Another evidence for the oxide dominant luminescence in chainlike SiNWs comes from XEOL recorded after the complete removal of silicon oxide by HF solution. After HF-etching, no luminescence can be observed in either chainlike SiNWs or normal 1-D SiNWs (vide infra) under the same experimental conditions.

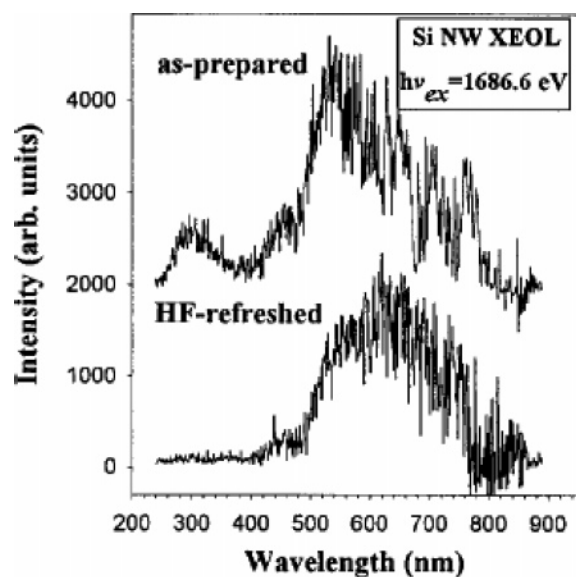
Finally, the PL spectra of the chainlike and normal SiNWs excited at 514.5 nm with an argon ion laser are shown in Figure 99. The PL spectral features for both samples are similar except for the much stronger emission in the chainlike SiNW. A strong PL peak around 560 nm with a broad shoulder at 620 nm was obtained for the chainlike SiNW sample. These PL peaks can be attributed to defects in silicon oxide and/or interface between silicon oxide and silicon nanoparticles.

### 11.1.3. 1-D in 1-D: Ultrafine SiNW<sub>C</sub>SiO<sub>2</sub>NT

It has been shown in ref 48 that ultrafine SiNWs (1–5 nm in diameter) exhibit very intense (at least 1 order of magnitude higher) luminescence in the PL measurement (Figure 100, curve b).<sup>48</sup> The PL peak centers around 720 nm. Very weak PL intensity was obtained from normal SiNW samples of 20–50 nm in diameter (Figure 100, curve a). The PL peak centers at around 600 nm. The strong PL intensity of 1-D SiNWs sheathed with an oxide layer, designated as SiNW<sub>C</sub>SiO<sub>2</sub>NT, may be attributed to the quantum-size effect of ultrafine Si core (<5 nm in diameter)<sup>123</sup> and/or with impurities within the nanowires or the silicon–(silicon oxide) interface states.<sup>48,86</sup>



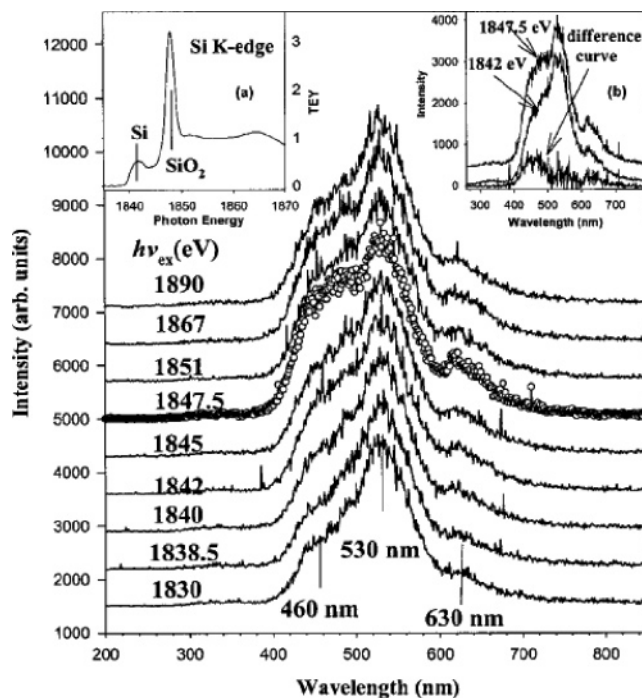
**Figure 100.** Photoluminescence spectra from (a) normal SiNWs of 20–50 nm in diameter and (b) very fine and uniform SiNWs of 1–5 nm in diameters synthesized with zeolites. (Reprinted with permission from ref 48. Copyright 2003 American Chemical Society.)



**Figure 101.** X-ray excited optical luminescence (XEOL) of a Si nanowire specimen (26 nm in diameter), before and after HF treatment, using an Al  $K\alpha$  X-ray source. It exhibits luminescence in the UV and visible regions. The short-wavelength peaks ( $\sim 300$  and  $\sim 450$  nm) diminish after HF treatment, while the 530 nm peak and longer wavelength emission remain. (Reprinted with permission from ref 375. Copyright 2001 American Institute of Physics.)

#### 11.1.4. Silicon Nanowires

An XEOL spectrum of a single as-prepared nanowire of 26 nm in diameter, excited using an Al  $K\alpha$  X-ray source, clearly shows luminescence in both UV and visible regions (Figure 101).<sup>375</sup> Upon HF etching, the luminescence at the shorter wavelengths (295 and 460 nm) diminishes but those at  $\sim 530$  nm and longer wavelengths remain. This result indicates that as-prepared SiNWs contain small unoxidized Si nanocrystallites that contribute to the luminescence (a quantum confinement effect). The short-wavelength luminescence probably originates from the presence of the oxide layer. XEOL of SiNW with excitations at the silicon K- and  $L_{3,2}$ -edges by synchrotron radiation exhibits several luminescence bands at  $\sim 460$ ,  $\sim 530$ , and  $\sim 630$  nm (Figure 102).<sup>376</sup> These luminescence bands are broad and are sensitive to the Si 1s excitation channel (Si versus SiO<sub>2</sub>



**Figure 102.** Normalized XEOL of SiNW (nominal diameter  $\sim 13$  nm and oxide layer  $\sim 4$  nm) excited at photon energy across the Si K edge. The TEY XANES and the difference curve between the luminescence of the SiO<sub>2</sub> and the Si white line excitation channel are shown in insets (a) and (b), respectively. The baselines have been shifted vertically for clarity. (Reprinted with permission from ref 376. (<http://link.aps.org/abstract/PRB/v70/p045313>). Copyright 2004 by the American Physical Society.)

whiteline). These chemical- and morphology-dependent luminescences had been attributed to factors such as the emission from the oxide layer, the quantum-confined silicon nanowires, and the silicon–(silicon oxide) interface, respectively.<sup>376</sup>

## 11.2. Band Gaps

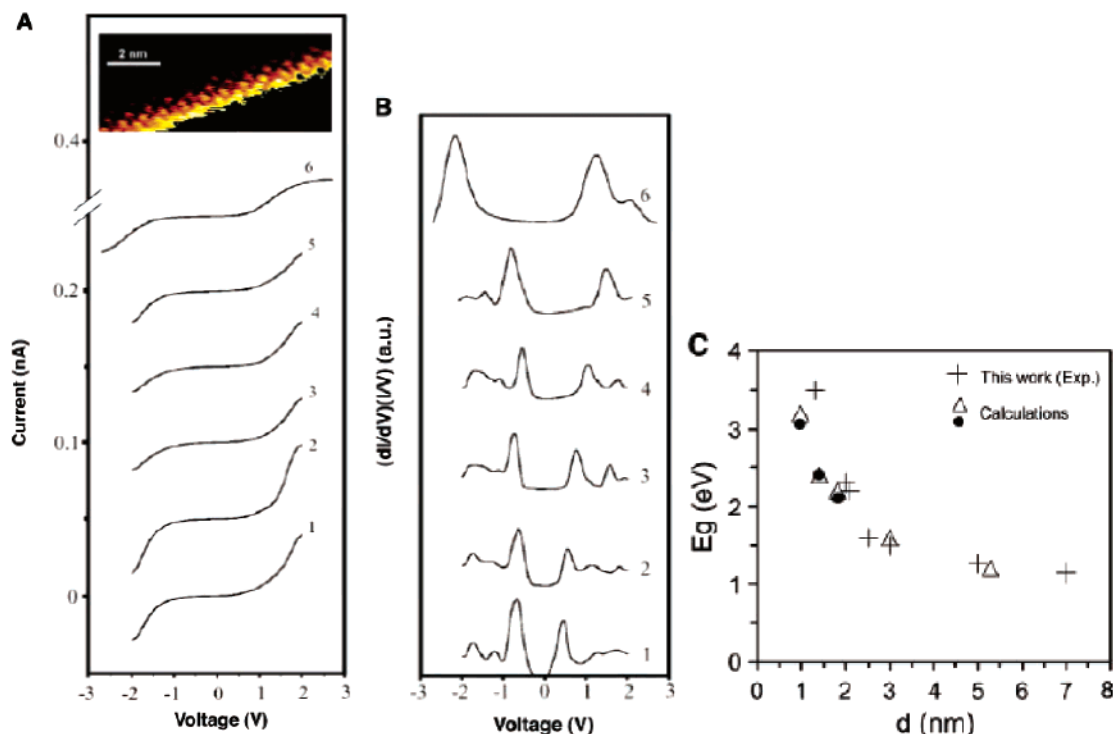
Recently, Lee and co-workers reported band gap opening of SiNWs due to quantum confinement effect when the diameter of SiNW shrinks to below 7 nm.<sup>123</sup> Scanning tunneling spectroscopy measurements were performed on individual oxide-removed SiNWs and were used to evaluate the electronic energy gaps as a function of nanowire diameter (Figure 103). The energy gap was found to increase with decreasing SiNW diameter from 1.1 eV for 7 nm to 3.5 eV for 1.3 nm in diameters, in agreement with previous theoretical predictions.

In addition, EELS spectra of individual SiNWs with different diameters at the Si  $L_{3,2}$ -edge have been obtained by Sun et al.<sup>375</sup> The results (Figure 104) revealed a threshold blue shift (e.g., 1 eV blue shift for a 9 nm SiNW) and a parabolic behavior for selected nanowires, indicating the widening of the band gap with decreasing nanowire diameters.

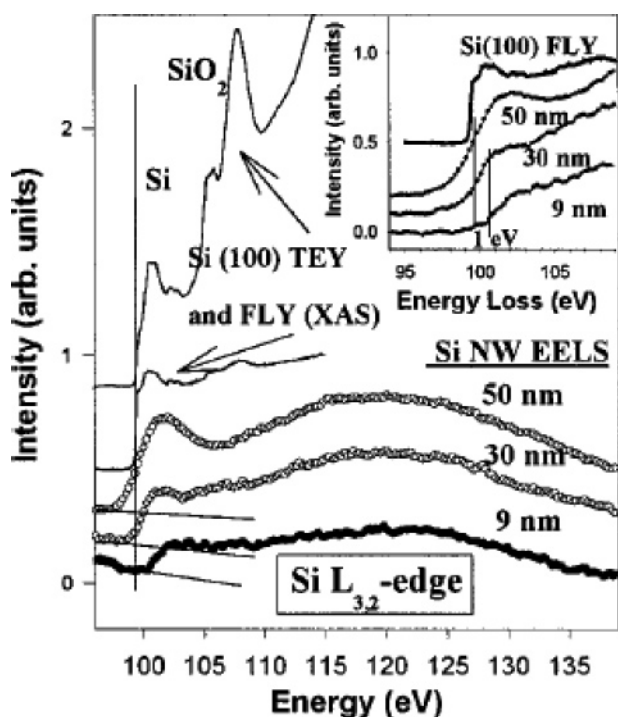
## 11.3. Theoretical Calculations

Zhao et al.<sup>378</sup> studied from first principles the structures of SiNWs grown along the 110 and 111 directions and their electronic and optical properties as a function of diameter. These properties are strongly influenced by quantum confinement and the electronic states can be described by those associated with a cylindrical potential well. Direct funda-





**Figure 103.** Electronic properties of the SiNW surfaces. (A)  $I$ - $V$  curves obtained by STS on six individual SiNWs. The diameters of wires 1–6 are 7, 5, 3, 2.5, 2, and 1.3 nm, respectively. The inset shows the atomically resolved STM image of wire 6. (B) Corresponding normalized tunneling conductances,  $(dI/dV)/(I/V)$ . The curves are offset vertically for clarity. (C) Experimental band gap versus diameter for SiNWs of wires 1–6 and an additional two wires not shown in A and B. Also shown are the calculated diameter-dependent band gaps (filled circles and triangles). (From ref 123 (<http://www.sciencemag.org>). Reprinted with permission from AAAS.)



**Figure 104.** EELS of three single Si nanowires of  $\sim 50$ ,  $\sim 30$ , and 9 nm from a HF-etched Si NW specimen. The XAFS of a Si(100) wafer recorded in TEY and FLY mode are also shown. The edge jump of the 50 nm wire was aligned to that of Si(100). The preedge background is also shown. A more detailed comparison of the edge jump is shown in the inset. (Reprinted with permission from ref 375. Copyright 2001 American Institute of Physics.)

mental band gaps are found at  $\Gamma$  for 110 and small 111 wires, which increase subquadratically as the diameter decreases. It was also found that Si [111] nanowires have a larger gap

than Si [110] nanowires, as expected from the effective-mass difference. In addition, anisotropy in the dielectric function is found in the nanowires with  $d \leq 2.2$  nm, where extra peaks in the absorption coefficient also begin to develop.

## 12. Fabrication of Nanodevices

The design and construction of nanoelectronic or nanophotonic devices such as field effect transistors, light-emitting diodes (LEDs), and quantum cascade lasers, etc., rely critically on our ability to fabricate functional heterostructures and interfaces with desirable characteristics. Needless to say the operating principles and performance of the resulting nanodevices depend on the chemical, physical, and biological properties of the nanomaterials which constitute the devices as well as the interfaces. For semiconductor nanodevices, the interface may include semiconductor homo- or hetero-junctions, dielectric–semiconductor junctions, and metal–semiconductor junctions, etc. Precise control over the composition and perfection of interfaces is required for the successful fabrication of high-performance nanodevices.

In this review, we have focused our attention on low-dimensional nanomaterials such as nanorods, nanowires, nanotubes, and nanowhiskers, etc., since the anisotropic properties and quantum-size effects are two of the many highly desirable attributes of low-dimensional nanomaterials in the design and fabrication of nanodevices. Nanoelectronic devices such as transistors, logic gates, tweezers, and sensors, etc., have been built from CNTs.<sup>386–390</sup> However, the electronic properties of CNTs are highly dependent on the tube diameters and their structures, both of which are difficult to control. By contrast, the diameters, structures, and compositions of nanowires are, relatively speaking, easier to control, making them good candidates for the fabrication of nanodevices.

Another focus of this review is silicon-based composite nanomaterials. Silicon-based nanotechnology is particularly promising since it is compatible with the conventional silicon microtechnology. Interfacing and integrating with the existing silicon-based microtechnology will encounter the least resistance among the many development paths of nanotechnology. To date, many prototype nanodevices such as transistors, diodes, switches, light-emitting diodes, lasers, and chemical and biological sensors, etc., have been fabricated from SiNWs and SiNDs. For example, dopants such as B and P can be introduced into SiNWs during growth, making them p- or n-type semiconductors, respectively.<sup>95</sup> This can be done with different nanowires or within the same nanowire (segmented). Wiring these prototypes together to form logic gates, memories, and circuitries will build the foundation for future nanocomputer and other devices. Since some nanowires, including SiNWs, can also be made to emit light or to lase,<sup>186</sup> it is conceivable that nanophotonics<sup>391</sup> will soon be integrated with nanoelectronics in silicon-based nanotechnology.

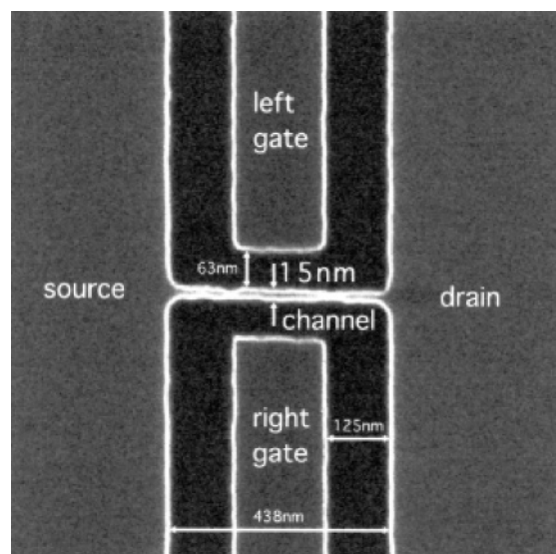
### 12.1. Top-Down Approach

The top-down approach seeks to fabricate nanodevices top-down by etching silicon (or other semiconductors) chips using lithography (either photolithography or electron lithography). Indeed, the top-down approach has been the method of choice in the semiconductor industry for making microelectronic and other devices for decades. Conventional photolithography can routinely mass produce silicon chips with 0.3  $\mu\text{m}$ , or 300 nm, features.

The semiconductor industry entered the *nanotechnology era* in the year 2000, and by 2004, the industry was shipping devices with physical gate dimension of less than 40 nm and insulator thickness of less than 1 nm. This is in line with the pace of Moore's law.<sup>392</sup> The current development of the state-of-the-art optical lithography at 193 nm wavelength is pushing the limit of 32 nm (half-pitch). Dimensions smaller than 32 nm are generally viewed as beyond the capabilities of optical lithography at 193 nm wavelength, unless high-index fluids, high-index lens materials, and higher-index resist can be developed. One way to extend the lifetime of optical projection lithography with immersion to 32 nm half-pitch and beyond is to divide the pattern into two or more masks. However, this latter strategy will undoubtedly increase the cost of manufacturing.

It is generally believed that extension of the roadmap for the semiconductor industry beyond 32 nm will probably require the development of "next-generation" lithography (NGL) technologies such as extreme ultraviolet lithography (EUV), maskless (ML2), and imprint lithography (to be discussed next). Because the "next-generation" lithographies will most likely require the development of substantially new infrastructure, implementation of these new technologies as viable manufacturing solutions will be a real challenge for the industry.<sup>393</sup>

Recent development in extreme ultraviolet lithography (EUVL) is expected to be used in manufacturing at 32 nm half pitch. The EUV lithography is a projection optical technology that uses 13.5-nm laser produced plasma. The laser wavelength is approaching the wavelengths of soft X-rays. At this wavelength, all materials are highly absorbing, so the imaging system must be composed of mirrors coated with multilayer structures designed to have high reflectivity at 13.5 nm wavelength.



**Figure 105.** SEM photograph of the Si nanowire and side gates fabricated by using inorganic electron beam (EB) resist process. The width, height, and length of the Si nanowire are 15, 20, and 438 nm, respectively. (Reprinted with permission from ref 394. Copyright 2000 Elsevier.)

For definitions or features finer than 32 nm, it is necessary to use electron beams or X-rays in the so-called "nan imprint lithography".<sup>343–345</sup> High-energy electron beams or X-rays (such as the highly collimated synchrotron radiations) can in theory provide definitions of a few nanometers. The state-of-the-art definition in nan imprint lithography (NIL) is about 5 nm.<sup>343–345</sup> It is obvious that "nan imprint" lithography can achieve much better resolution than extreme ultraviolet (EUV) lithography discussed earlier. However, it suffers from, among other things, cost effectiveness, mass production capability, and defect tolerance problems. The main reason is that nan imprint lithography is essentially a 1  $\times$  multilayer mold technology.

It is interesting to note that, at or below about 15 nm, quantum confinement sets in, making single-nanowire/nanotube single-electron nanodevices a reality. We shall now mention briefly one example of *single-electron* nanodevices here. Depicted in Figure 105 are the single-electron memory and single-electron transistor nanodevices fabricated by Tsutsumi et al. using an inorganic SiO<sub>2</sub> electron beam resist.<sup>394</sup> These single-electron nanodevices<sup>181,394,395</sup> are possible due to the carrier confinement and Coulomb blockade effects exhibited by the very narrow SiNWs and/or very small SiNDs in the *nanoregime*. Indeed, 15 nm wide silicon nanowire channel and 5–10 nm isolated silicon islands were used in the work of Tsutsumi, et al.<sup>394</sup> This is a fast-developing technology; the reader is referred to many excellent reviews and books in the literature.<sup>348–363,396</sup>

### 12.2. Bottom-Up Approach

Generally speaking, nanodevices fabricated by bottom-up approach will undergo the following processes: design and synthesis of nanoscale building materials, elucidation of the fundamental electronic, optical and other physical properties of these nanomaterials, fabrication of individual nanodevice nanocomponents, and the organization of various nanocomponents into increasingly complex integrated assemblies and eventually to functional nanodevices. Many efforts have been made on the first and second steps, in which

a wide variety of nanomaterials with controllable morphology, size, structure, and composition have been synthesized and their physical and chemical properties investigated. Single nanodevices such as field effect transistors, diodes, light-emitting diodes, and sensors, etc., using serial lithographic processing, such as electron-beam lithography, have also been fabricated (the fourth step). The last step, namely, the controlled assembly and integration of the various building blocks into functional systems, is still a formidable challenge. Nonetheless, some progress has been made. For example, electric fields<sup>341,397,398</sup> and microfluidic<sup>342,399</sup> and LB techniques<sup>337–340</sup> have recently been used to assemble silicon nanowires into high-density arrays, as discussed in section 10.

Many issues such as mass production and reproducibility, however, remain to be addressed. Finally, organizing various elements into basic units and interconnecting them to form functional nanodevices are yet two more hurdles in the bottom-up approach. The ultimate challenge, however, seems to be the interface of the nanodevices to the microworld, and eventually to the macroworld.

### 12.3. Hybrid Approach

Moore's law in semiconductor technology has been the guiding principle for the development of microelectronic industry for the past few decades.<sup>392</sup> As mentioned earlier, the current state-of-the-art definition or feature size is about 30 nm. Where will it end? It has been suggested that nanotechnology is a "disruptive" technology,<sup>400</sup> competing with the conventional, sustaining silicon microtechnology. In our view, nanotechnology is a "constructive" technology,<sup>401</sup> though still in its infancy, trying to integrate into, and merge with, the existing microtechnology. The complementarity and synergism of the two will benefit, and accelerate the developments of, both technologies. Hence the two are more appropriately termed "convergent" technologies.

It is our view that, at the scale of about 30 nm in feature size, the top-down approach of the existing lithography technologies will merge with the bottom-up strategy of the nanotechnology to form a new "hybrid" technology,<sup>401</sup> capitalizing on the strengths of both strategies and complementing one another. This large-scale merger may happen within the next decade or so.

Indeed, this hybrid approach has recently been demonstrated by the so-called grown-in-place approach<sup>93,94</sup> described in section 10.3. These examples demonstrated the growth of SiNWs or CNTs (the bottom-up approach) on a prefabricated Si wafer (the top-down approach). This in-situ growth of the active nanomaterials on a well-connected silicon chip alleviates the need to cut, assemble, and interface (the last three steps in the bottom-up approach, as per section 4.1) individual nanodevice units and take advantage of the desirable application-specific properties of the nanodevice elements.

### 12.4. Beyond Nanotechnologies

At the scale of about 3 nm in feature size, the hybrid technology discussed in the previous subsection will be challenged by "supramolecular" and "molecular" technologies epitomized by large-scale integration of single-molecule devices. Supramolecular chemistry has been well-developed over the past few decades;<sup>402</sup> however, large-scale integration

of supramolecules into nanosized devices is still many years away. Ultimately the supramolecular and molecular technologies will yield to subnanometer "atomic" or "nuclear" technologies at dimensions below 0.3 nm, whereby single-atom, single-electron, single-spin, single-photon devices are possible, revolutionizing various disciplines of science and technology, including, but not limited to, electronics, photonics, and spintronics. The last technology, spintronics, may involve electron or nuclear spins. Quantum computing will soon become a reality.<sup>403,404</sup> Sub-nanometer technologies, atomic and molecular technologies in particular, will be discussed in section 13.

With the tremendous increase in capacity (order-of-magnitude reduction in feature size and increase in speed) at each stage of the development, it will be affordable to build in redundancy (error tolerance), self-check, and self-repair mechanisms in the so-called "smart" devices. Furthermore, these nanosized or sub-nanosized molecular or atomic building blocks will be able to self-assemble, self-replicate, self-check, self-repair, and self-annihilate to form intelligent devices, just like genes, proteins, and enzymes do in living cells. Molecular or atomic recognition, self-scaling, precise positioning, and accurate manipulation of connections (by forming and breaking chemical bonds at specific sites, e.g., at the interface) of the building blocks are keys to a functional molecular or supramolecular device. Ultimately it may be possible, indeed both desirable and necessary, to fabricate nanodevices using nanomachines. Nanomachines can be designed to mass produce nanodevices from nanomaterials (as building blocks). By the same token, molecular machines can be designed to mass produce molecular devices from molecules and atoms, based on self-assembly, self-replicating, and complementarity, etc., principles and according to a set of engineering blueprints, in a way similar to living cells in producing proteins and enzymes from amino acids according to the DNA and RNA instructions.

Throughout the various stages of nano- or sub-nanotechnological developments, connection to the macroworld will probably rely to a large extent on the top-down approach, at least in the foreseeable future.

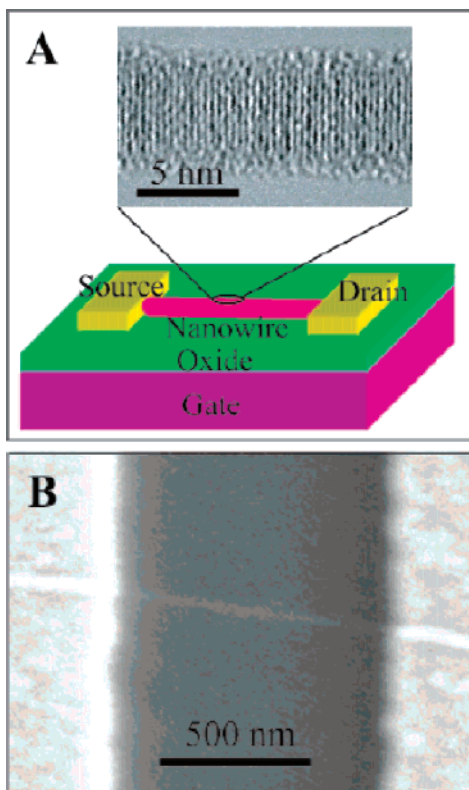
### 12.5. Nanodevices

In this section, we shall discuss recent developments in the fabrication of nanodevices based on silicon nanomaterials. Examples quoted here are meant to be representative rather than exhaustive since it is a fast-developing, multidisciplinary field.

#### 12.5.1. Nanoelectronics

Nanoelectronics is the most appealing application of nanotechnology, especially in view of the fact that conventional microelectronics technique (top-down approach) has almost reached its limit. When the smallest features on the current state-of-the-art, mass-produced FETs, the basic subunits in integrated electronic circuits, shrink to below 100 nm, the devices will become more difficult and costly to fabricate and may no longer function effectively due to the laws of quantum mechanics. To continue the miniaturization of circuit elements down to the nanometer scale, perhaps even to the molecular level, new nanometer-scale electronic devices would have to be fabricated. However, unlike today's FET's, which operate on the basis of the movement of masses of electrons in bulk matter, the new nanodevices take





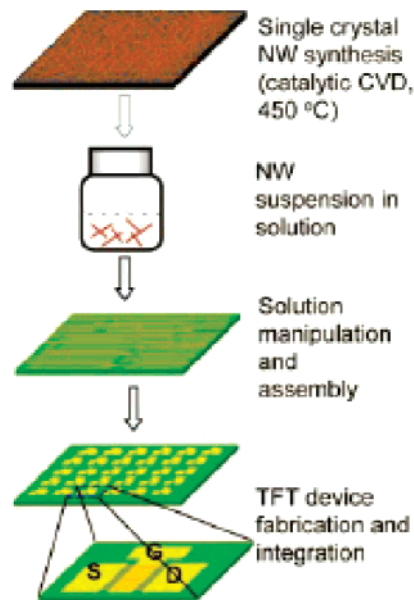
**Figure 106.** (A) Schematic representation of a SiNW FET showing the metal source and the drain electrodes with the NW and contacts on the surface of SiO<sub>2</sub>/Si substrate. Inset: High-resolution transmission electron micrograph of a 5 nm diameter SiNW. The scale bar is 5 nm. (B) SEM image of a SiNW FET device. (Reprinted with permission from ref 100. Copyright 2003 American Chemical Society.)

advantage of quantum mechanical phenomena, including quantum-size effect, discreteness of electrons, carrier confinement, Coulomb blockade, etc. Single-nanowire or nanodot, single-electron nanodevices<sup>181,394,395</sup> become possible. The reader is referred to the many papers and reviews dealing with these nanoelectronic devices, including single-electron devices and molecular electronic devices, in the literature.<sup>184,395,405–408</sup>

Single SWCNT field-effect transistors<sup>387,409</sup> have been fabricated by depositing SWCNT on Si/SiO<sub>2</sub>, which serve as a gate electrode, and connecting SWCNT by two metal electrodes. Low-temperature single-electron transistors<sup>410,411</sup> intramolecular metal–semiconductor diodes,<sup>259,412</sup> and intermolecular-crossed NT–NT diodes<sup>413</sup> have been achieved with CNTs.

Recently, SiNWs have also been used to fabricate nanoelectronics including FETs,<sup>28,95,96,100,102</sup> logic gates,<sup>414</sup> and bistable nanoscale switches.<sup>415</sup> A prototype SiNW FET device is shown in Figure 106. It was determined that the silicon nanowire devices can behave as excellent FETs, and moreover, the carrier mobilities in the silicon nanowire devices are comparable to or exceed the best achievable in planar silicon. A good review on SiNW and other semiconductor nanowire nanoelectronics has been given by Lieber.<sup>416,417</sup>

In addition, thin-film transistor (TFT) has also been fabricated using oriented Si nanowire films or CdS nanoribbons as semiconducting channels.<sup>418</sup> Figure 107 illustrates the NW–TFT fabrication process. The NWs were assembled into oriented NW thin films using a microfluidic technique or LB film technique to yield an electronic substrate. This



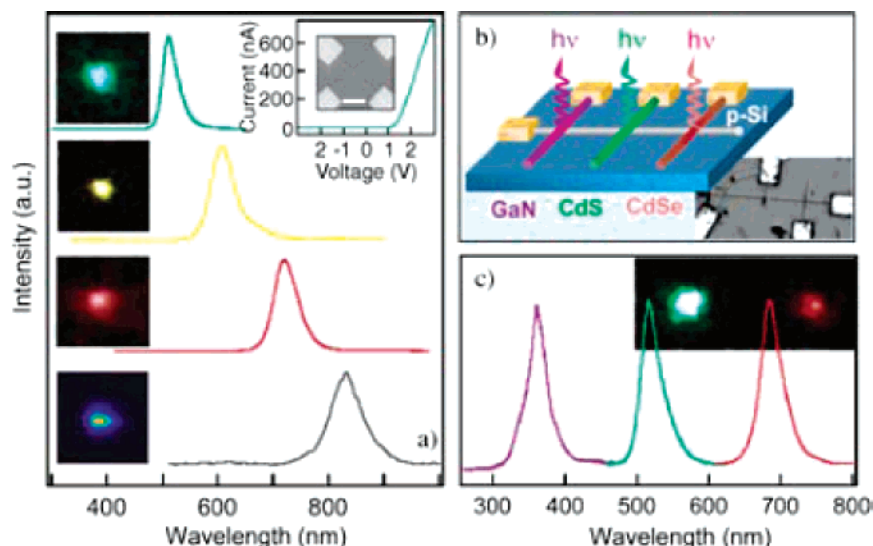
**Figure 107.** Diagram of NW–TFT fabrication process. In this approach, single-crystal NW materials are dispersed in a solution and aligned on the desired substrate to form a densely packed oriented NW thin film that is further processed via standard methods to form TFTs with the conducting channel parallel to the wire axis. (Reprinted by permission from Macmillan Publishers Ltd. (ref 418, <http://www.nature.com>), copyright 2003.)

substrate is processed using standard methods to produce NW–TFTs with conducting channels formed by multiple parallel single-crystal NW paths. In such NW–TFTs, charges travel from source to drain within single crystals, thus ensuring high carrier mobility. Thus high-performance TFTs can be produced on various substrates, including plastics, using a low-temperature assembly process.

### 12.5.2. Nanophotonics

Nanophotonics is another important application in nanotechnology. Unfortunately, though photonic devices can easily be coupled to silicon chips or fabricated from silicon-based materials, the light sources such as semiconductor lasers and LEDs cannot be built from silicon itself since silicon does not emit light efficiently. This is because the radiative recombination of the electron–hole pair is very slow in silicon and there are several other faster, alternative nonradiative pathways of recombination available. The slow radiative recombination in silicon is due to the fact that it is an “indirect band gap” semiconductor (as opposed to, say, GaAs, which is a “direct band gap” semiconductor and an efficient light emitter). This means that the net momentum of the recombined pair is different from that of the excited electron–hole pair, and hence the principle of conservation of momentum requires that the radiative recombination process must be coupled with certain lattice vibrations (phonons). As a result, bulk silicon has traditionally been considered a poor photonic material.

This view, however, is gradually changing. In the nanoregime, the law of conservation of momentum is relaxed as a result of the small sizes or the disordered state of the nanomaterial. As discussed in section 11.1, silicon nanodots, silicon nanowires, and certain disordered forms of silicon are known to exhibit efficient photoluminescence and electroluminescence properties. While the exact origin of these properties is still under investigation, it is generally believed



**Figure 108.** NanoLEDs: (a) Electroluminescence (EL) spectra from crossed p–n diodes of p-Si and n-CdS, CdSSe, CdSe, and InP, respectively (top to bottom). Insets to the left are the corresponding EL images for CdS, CdSSe, CdSe (all color CCD) and InP (liquid-nitrogen-cooled CCD) nanoLEDs. The top-right inset shows representative  $I$ – $V$  and SEM data recorded for a p-Si/n-CdS crossed NW junction (bar = 1  $\mu\text{m}$ ); spectra and images were collected at +5 V. (b) Schematic and the corresponding SEM image of a tricolor nanoLED array. The array was obtained by fluidic assembly and photolithography with  $\approx 5 \mu\text{m}$  separation between NW emitters. (c) Normalized EL spectra and color images from the three elements. (Reprinted with permission from ref 422. Copyright 2005 Wiley-VCH.)

that they arise from quantum-size effect or the confinement of the electrons and holes to very small dimensions. As described in section 11.2, the band gap of SiNWs increases from the bulk value of 1.1 to 3.5 eV as the diameter of the nanowire decreases from 7 to 1.3 nm, respectively. Thus, the color of the luminescence changes from red to yellow to green to blue as the nanowire gets thinner in this size range. Similar trend applies to SiNDs and porous silicon. For porous silicon, the particle size is inversely proportional to the extent of etching. Porous silicon that emits red, orange, yellow, green, and blue colors can now be prepared. Furthermore, when confined to very small dimensions, electrons and holes attract each other more strongly, thereby enhancing the radiative recombination process and thus the photoluminescence or electroluminescence.

In recent years, silicon quantum dots and quantum wells and porous silicon have been used to fabricate LEDs and other optoelectronic devices (see reviews<sup>419,420</sup> and references therein.). Silicon nanowires can also be used to assemble a p–n junction with other semiconductor nanowires in a crossed-nanowire device architecture which can be used to fabricate electroluminescence devices such as LEDs. For example, nanoLEDs can be assembled from n-type direct-band gap nanowires, such as gallium nitride, cadmium sulfide, and indium phosphide, in combination with the p-type indirect-band gap silicon nanowires (Figure 108). Indeed, such nanoLEDs, capable of simultaneously emitting ultraviolet, green, and red lights, have been fabricated by Lieber and co-workers<sup>421,422</sup> using multiple n-type gallium nitride, cadmium sulfide, and indium phosphide nanowires, respectively, across single p-type silicon nanowires.

This concept can also be extended to include fabrication of nanowire LEDs on planar silicon chips. For example, silicon nanowires can be lithographically patterned on planar silicon substrates and, subsequently, direct-band-gap material nanowires assembled over these “wires” to create nanoLED arrays, as has been demonstrated by Lieber and co-workers using cadmium sulfide as the direct-band-gap material.

It should be mentioned here that the first all-silicon integrated optoelectronic circuit was fabricated by Fauchet

and co-workers using a material described as “partially oxidized porous silicon” called “silicon-rich silicon oxide”. These authors showed that individually addressable arrays of these LED devices could be constructed, thereby demonstrating that an all-silicon optoelectronic technology is on the horizon.

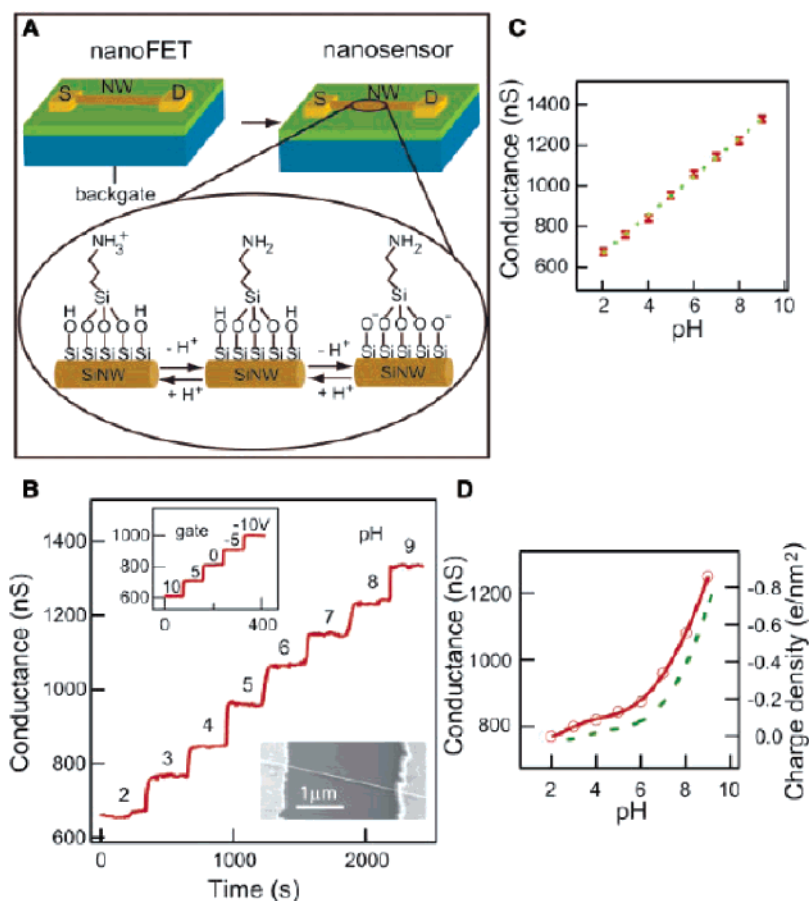
**12.5.2.1. Flat Panel Display.** It is well-known that nanotubes and nanowires with sharp tips are promising materials for field emission devices. Indeed, carbon nanotubes have already been used in large flat panel displays. Likewise, silicon nanowires and porous silicon (containing nanocrystals of silicon) can be used as large-area flat panel displays. The advantages of the silicon nanomaterials as field emission display nanomaterials include the following: (a) band gap opening from 1.1 to 3.8 eV for dimensions below 7 nm; (b) stable and uniform emission under low vacuum; (c) no need for back light; etc.<sup>423</sup>

### 12.5.3. Nanosensors

Another exciting application of nanotechnology is nanosensors in general and silicon-based nanosensors in particular.

Porous silicon is a useful nanosensor material. By measuring the change of the optical properties of porous silicon when a species is bound to its surface, the concentration of the species to be detected can be determined. For example, a biosensor based on induced wavelength shifts in the Fabry–Perot fringes of the visible-light reflection spectrum of derivatized thin films of porous silicon has been developed.<sup>424</sup> Binding of molecules induced changes in the refractive index of the porous silicon.<sup>425</sup> The validity and sensitivity of the system were demonstrated for small organic molecules (biotin and digoxigenin), 16-nucleotide DNA oligomers, and proteins (streptavidin and antibodies) at pico- and femtomolar concentrations. The sensor is also highly effective for detecting single-layered and multilayered molecular assemblies.

Silicon nanowire based FETs have also been configured as sensors for the detection of chemical and biological species. The conductance of nanowires will change in



**Figure 109.** NW nanosensor for pH detection. (A) Schematic illustrating the conversion of a NWFET into NW nanosensors for pH sensing. Also shown is the APTES-modified SiNW surface illustrating changes in the surface charge state with pH. (B) Real-time detection of the conductance for an APTES modified SiNW for pHs from 2 to 9. The pH values are indicated on the conductance plot. Inset: (top) Plot of the time-dependent conductance of a SiNW FET as a function of the back-gate voltage; (bottom) SEM image of a typical SiNW device. (C) Plot of the conductance versus pH. The red points are experimental data, and the dashed green line is linear fit of the data. (D) Conductance of unmodified SiNW (red) versus pH. The dashed green curve is a plot of the surface charge density for silica as a function of pH. (From ref 426 (<http://www.sciencemag.org>). Reprinted with permission from AAAS.)

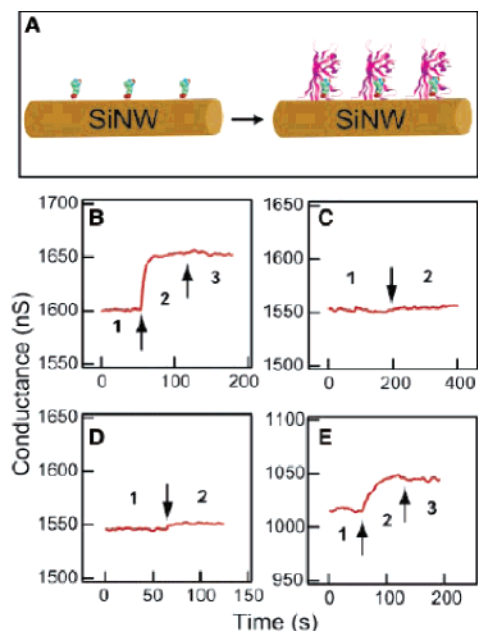
response to the binding of chemical and biological species on the nanowire surface; that is, molecular or macromolecular species “gate” the FET and thereby change the conductance.<sup>426</sup> Amine- and oxide-functionalized SiNWs exhibit pH-dependent conductance that is linear over a large dynamic range and can be related to the change in surface charge density during protonation and deprotonation processes (Figure 109). Biotin-modified SiNWs were used to detect streptavidin down to picomolar concentration range (Figure 110). Antigen-functionalized SiNWs showed reversible antibody binding and concentration-dependent detection in real time. The authors believe that the small size and capability of these semiconductor nanowires for sensitive, label-free, real-time detection of a wide range of chemical and biological species could be exploited in array-based screening and in vivo diagnostics.<sup>426</sup>

Recently, Lee and co-workers fabricated a series of sensors for gas, chemical, and bioanalytical applications using a bundle of silicon nanowires or nanowire films.<sup>427–429</sup> The sensor made by a bundle of HF-etched silicon nanowires exhibits a fast response and highly sensitive and reversible changes of the electrical resistance upon exposure to ammonia gas and water vapor.<sup>427</sup> Strands of aligned SiNWs with lengths over 2 mm and diameters of 35 nm were used to fabricate a multiwire strand of SiNWs into an electrode for cyclic voltammetric detection of bovine serum albumin.<sup>428</sup>

Lee and co-workers also used boron- or magnesium-modified Si nanowire films as sensors to measure the concentration of glucose or hydrogen peroxide in aqueous solution, respectively.<sup>429</sup> The B- or Mg-modified SiNW films were used as electrodes whose electrical resistances in the testing solutions are proportional to the logarithm of the concentration of the testing solution. It was reported that these sensors have a wide linear range (i.e., 0–10 mM glucose for B-modified SiNW film sensor, shown in Figure 111), high sensitivity ( $172 \text{ nA mmol}^{-1}$ ), good reproducibility, and long-term stability.<sup>429</sup>

A few cautionary notes are warranted here. First, for any nanosensor to be viable, it must have high sensitivity and selectivity, as well as good reliability in terms of stability and reproducibility. In particular, the sensing nanomaterial, which is the “brain” of the nanodevices, must have reproducibility, long-term stability and high sensitivity. In this regard, nanosensors or SiNW-FETs based on HF-etched SiNWs are problematic due to the instability of H-terminated SiNWs in water and some organic solvents, especially in the pH range of 4–10 (as discussed in sections 7.3, 7.4, and 8.2). Oxide-passivated or surface-functionalized SiNWs are relatively more stable, though their long-term stability in water or other solutions (especially under different pH and electrolyte conditions) also needs to be evaluated. Another aspect is the device principle and performance in the



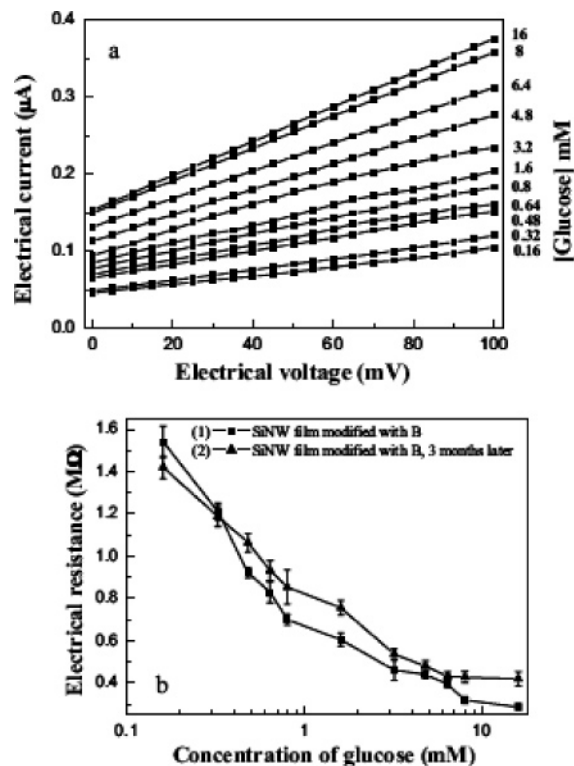


**Figure 110.** Real-time detection of protein binding. (A) Schematic representation of a biotin-modified SiNW (left) and the subsequent binding of streptavidin to the SiNW surface (right). (B) Plot of conductance versus time for a biotin-modified SiNW, where region 1 corresponds to buffer solution, region 2 corresponds to the addition of 250 nM streptavidin, and region 3 corresponds to pure buffer solution. (C) Conductance versus time for an unmodified SiNW. Regions 1 and 2 are the same as in B. (D) Conductance versus time for a biotin-modified SiNW, where region 1 corresponds to buffer solution and region 2 to the addition of a 250 nM streptavidin solution that was preincubated with 4 equiv of D-biotin. (E) Conductance versus time for a biotin-modified SiNW, where region 1 corresponds to buffer solution, region 2 corresponds to the addition of 25 pM streptavidin, and region 3 corresponds to pure buffer solution. Arrows mark the points when solutions were changed. (From ref 426 (<http://www.sciencemag.org>). Reprinted with permission from AAAS.)

nanorealm. For example, for nanodevices based on electrochemical principles, it has been pointed out that the detection of binding of molecules, charged or neutral, to the surface of SiO<sub>2</sub> by direct measurement of conductivity or electric field effect is not possible.<sup>430,431</sup> The underlying reason, according to these authors, is that “the SiO<sub>2</sub>/electrolyte is a nonpolarized interface which means that one or more charged species can cross this interface, effectively shorting out the interfacial capacitor that contains the immobilized charge of interest.” In ref 430, the authors expressed the opinion that “the hope for an immunoelectrode” is the discovery of “an interface with infinitely high charge transfer resistance,” in other words, “an ideal polarized (capacitive) interface.” Whether the electrochemistry-based nanosensors quoted in this subsection (as well as in section 12.5.5) satisfy these electrochemical criteria remains to be seen. Control experiments and long-term stability and reproducibility tests of the nanodevices can resolve most, if not all, of these and other relevant issues. On the other hand, in the uncharted territory of the nanoworld, surprising “nanoeffects” or “nanophenomena” that defy or challenge experience deduced from the macro- or microworld, as we know it, cannot be ruled out completely.

#### 12.5.4. Nanospintronics

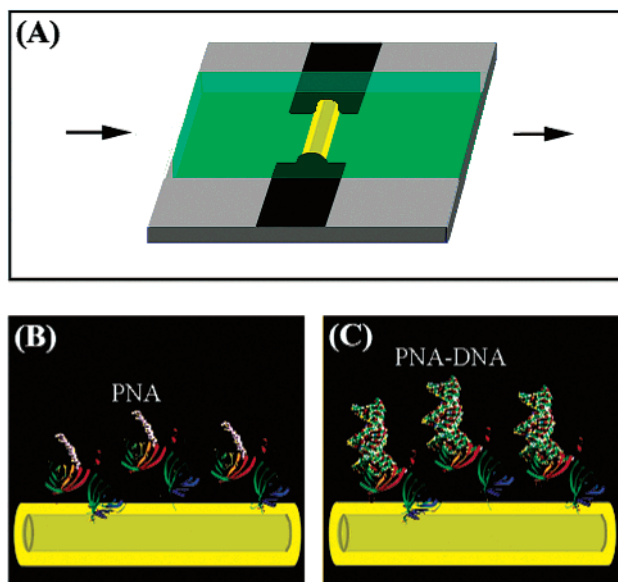
Spintronics<sup>432–435</sup> is a new and fast-growing branch of electronics in which electron spin, instead of its charge, is



**Figure 111.** (a) *I*–*V* curves of a B-modified SiNW film at various glucose concentrations. (b) Electrical resistance of a B-modified SiNW film versus glucose concentration. (Reprinted with permission from ref 429. Copyright 2005 Wiley-VCH.)

manipulated to perform certain functions. Initially, spintronics evolved from the development of advanced magnetic memory and sensors based on spin transports.<sup>436–438</sup> It was quickly expanded to include spins in semiconductors (SPINS), in the hope of developing new spin-based multifunctional devices such as spin-FET, spin-LED, spin-RTD (resonant tunneling device), optical switches operating at terahertz frequency, modulators, encoders, decoders, and quantum bits for quantum computation and communication.<sup>432–434</sup>

The silicon-based spintronics attract special interests due to compatibility with Si-based semiconductor applications.<sup>439</sup> Si-based spintronics could be achieved through hybrid approaches that integrate the metallic magnetic elements on top of conventional Si circuits, or by injecting spin-polarized electrons from metals into semiconductors.<sup>440</sup> The most direct method would be to induce ferromagnetism in a semiconductor at practical operating temperatures by introducing appropriate magnetic dopants such as Mn at levels of a few percent, producing a dilute magnetic semiconductor.<sup>441–444</sup> However, most ferromagnetic semiconductors are magnetic metal diluted III–V or II–VI semiconductor (instead of Si). Recently, DiTusa and co-workers have observed a clear signature of ferromagnetism in a Si-based magnetic semiconductor, albeit at a low temperature (53 K).<sup>445</sup> The authors demonstrated that Fe<sub>1–y</sub>Co<sub>y</sub>Si, an n-type narrow-gap magnetic semiconductor, exhibits an unusually large anomalous Hall effect that appears to derive from intrinsic band structure effects rather than impurity scattering as in conventional ferromagnets. This discovery of a Si-based magnetic semiconductor suggests routes for the realization of spin field effect transistors compatible with the existing microprocessor circuitry. It may be possible to utilize FeCoSi magnetic semiconductor layers as injectors and collectors for spin-polarized current in Si transistors.<sup>439</sup>



**Figure 112.** (A) Schematic of a sensor device consisting of a SiNW (yellow) and a microfluidic channel (green), where the arrows indicate the direction of sample flow. (B) SiNW surface with PNA receptor. (C) PNA–DNA duplex formation. (Reprinted with permission from ref 457. Copyright 2004 American Chemical Society.)

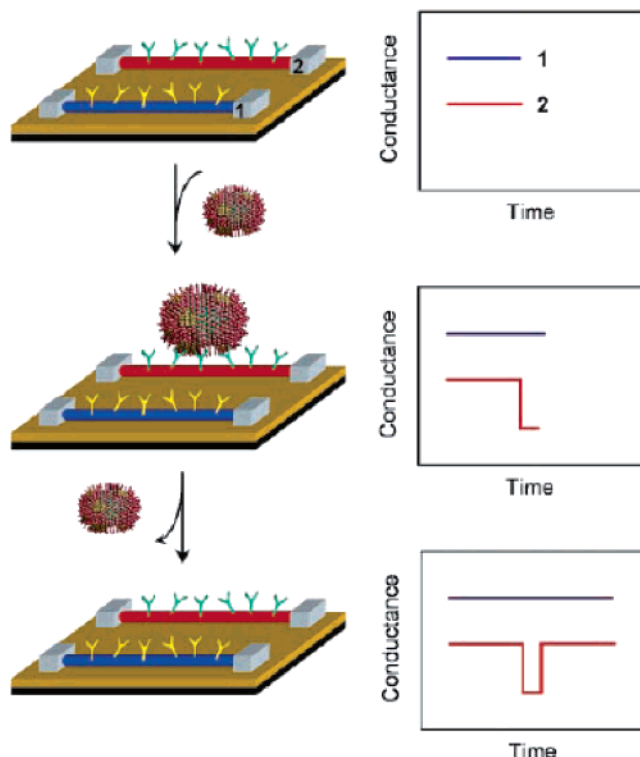
Since spintronics relies on the manipulation of electron spins, the first step in spintronics is the discovery of magnetic materials with interesting spin properties. Studies of the magnetic properties (including spin relaxation, coherence, etc.) of a material and our ability to modify or control such properties are prerequisites in the design and fabrication of spin nanodevices. In recent years, spin relaxation in Si heterostructures had been investigated by electron spin resonance in modulation doped Si/SiGe quantum wells.<sup>446–448</sup> Unfortunately, until now no spin phenomena have been observed in Si related nanowires or nanoparticles, although a number of ferromagnetic III–V and II–IV nanowires have been synthesized.<sup>449–456</sup>

Spintronics can also be based on nuclear spins rather than electron spins. However, this is beyond the scope of this review.

### 12.5.5. Nanobiology and Nanomedicine

Silicon nanowire FETs can be used for label free, direct real-time electrical detection of biomolecule binding.<sup>457–459</sup> SiNW-based FETs have the potential of very high sensitivity detection because of the depletion or accumulation of charge carriers caused by binding of a charged biological macromolecule at the surface of the SiNWs. The development of advanced biological sensors could impact significantly the areas of genomics, proteomics, biomedical diagnostics, and drug discovery.

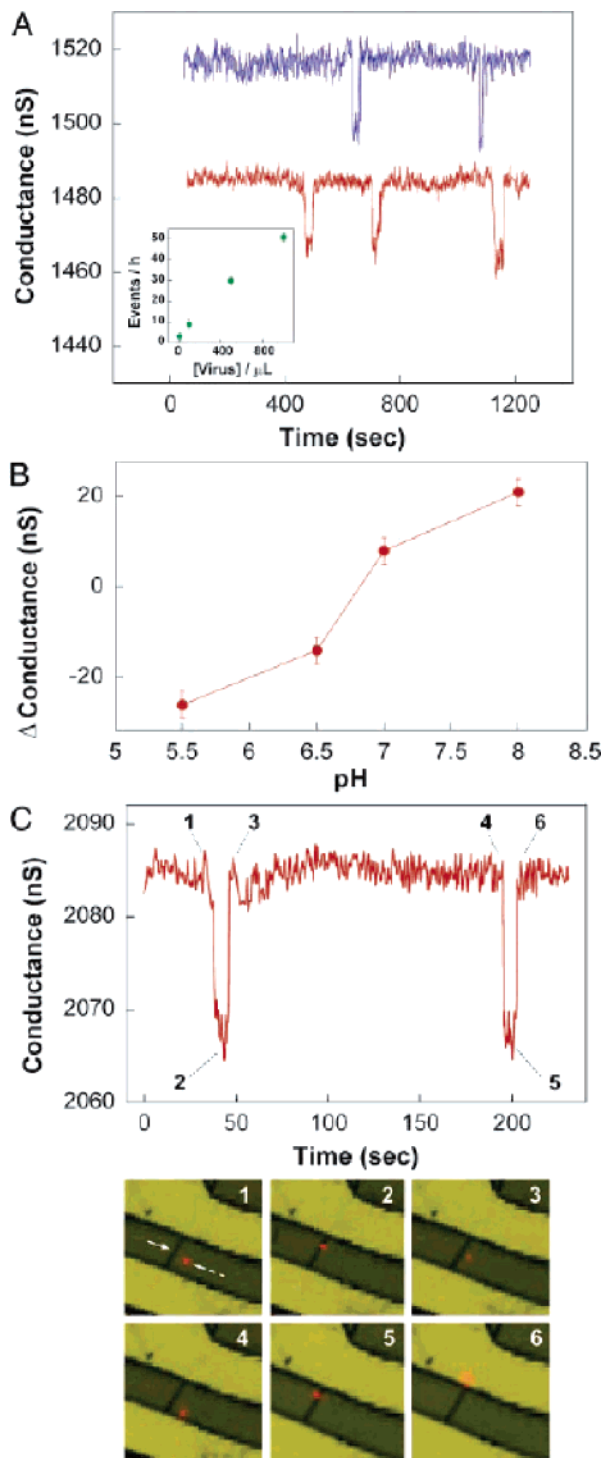
Silicon nanowire devices have been used to detect DNA, virus, and other biological macromolecules. Hahn and Lieber reported two-terminal silicon nanowire electronic devices that function as ultrasensitive and selective detectors of DNA.<sup>457</sup> Here, the surfaces of the silicon nanowire devices were modified with peptide nucleic acid receptors designed to recognize wild type versus the  $\Delta F508$  mutation site in the cystic fibrosis transmembrane receptor gene (Figure 112). Conductance measurements made while sequentially introducing wild type or mutant DNA samples exhibit a time-dependent increase in conductance, consistent with the



**Figure 113.** Nanowire-based detection of single viruses. (Left) Schematic shows two nanowire devices, 1 and 2, where the nanowires are modified with different antibody receptors. Specific binding of a single virus to the receptors on nanowire 2 produces a conductance change. (Right) Characteristic of the surface charge of the virus only in nanowire 2. When the virus unbinds from the surface, the conductance returns to the baseline value. (Reprinted with permission from ref 458. Copyright 2004 National Academy of Sciences, U.S.A.)

peptide nucleic acid (PNA)-DNA hybridization and enabled identification of fully complementary versus mismatched DNA samples. Concentration-dependent measurements showed that detection is sensitive at tens of femtomolar level. The authors believe that this nanowire-based approach represents a step forward for direct, label-free DNA detection with high sensitivity and good selectivity and could provide a pathway to integrated, high-throughput, multiplexed DNA detection for genetic screening and biothreat detection.

A direct, real-time electrical detection of single virus particles with high selectivity using silicon nanowire field effect transistors has also been reported.<sup>458</sup> Measurements made with SiNW arrays modified with antibodies for influenza A showed discrete conductance changes characteristic of binding and unbinding in the presence of influenza A virus (but not paramyxovirus or adenovirus). Simultaneous electrical and optical measurements using fluorescent-labeled influenza A virus were used to demonstrate conclusively that the conductance changes stemmed from the binding/unbinding of single viruses at the surface of SiNW devices (see Figure 113 and Figure 114). pH-dependent studies further showed that the detection mechanism is caused by a field effect and that the SiNW devices can be used to determine rapidly isoelectric points and variations in receptor–virus binding kinetics under different conditions. Finally, multiple viruses can be selectively detected in parallel using FET devices fabricated with SiNWs modified with antibodies specific for various distinct viruses. The possibility of large-scale integration of these SiNW-based nanodevices suggests the potential for simultaneous detection of a large number



**Figure 114.** Selective detection of single viruses. (A) Conductance vs time data recorded simultaneously from two silicon nanowire elements, red and blue plots, within a single device array after introduction of an influenza A solution. Inset: Frequency of single virus events as a function of virus solution concentration. (B) Conductance changes associated with single influenza A virus binding/unbinding as a function of solution pH. (C) Conductance (upper) and optical (lower) data recorded simultaneously vs time for a single silicon nanowire device after introduction of influenza A solution. Combined bright-field and fluorescence images correspond to time points 1–6 indicated in the conductance data; virus binding/unbinding appears as a red dot in the images. The solid white arrow in image 1 highlights the position of the nanowire device, and the dashed arrow indicates the position of a single virus. Images are  $8 \times 8 \mu\text{m}$ . All measurements were performed with solutions containing 100 viral particles/ $\mu\text{L}$ . (Reprinted with permission from ref 458. Copyright 2004 National Academy of Sciences, U.S.A.)

of different viruses at the single-virus level.

Most recently, Lieber and co-workers<sup>459</sup> reported a highly sensitive, label-free, multiplexed electrical detection method for cancer markers using a silicon-nanowire field effect device in which distinct nanowires and surface receptors are incorporated into arrays. Protein markers can be routinely detected at femtomolar concentrations, including detection of prostate specific antigen (PSA), PSA-alpha 1-antichymotrypsin, carcinoembryonic antigen (CEA), and mucin-1 down to 0.9 pg/mL in undiluted serum samples. In addition, SiNW nanodevices with nucleic acid receptors enabled real-time assays of the binding, activity, and small-molecule inhibition of telomerase using unamplified extracts from as few as ten tumor cells. The authors believe that the capability for multiplexed real-time monitoring of protein markers and telomerase activity with high sensitivity and selectivity in clinically relevant samples opens up possibilities for diagnosis and treatment of cancer and other diseases.

The cautionary notes at the end of section 12.5.3 also apply here.

### 13. Atomic- and Molecular-Scale Technologies

Though not the focus of this review, we shall discuss briefly here two sub-nanometer-scale technologies, namely, atomic- and molecular-scale technologies. We shall first describe various atomic- and molecular-scale imprinting techniques on surfaces in section 13.1, followed by single-atom or single-molecule chemistry, including reaction dynamics and spectroscopy, on various surfaces, in section 13.2. These technologies, made possible by the scanning probe microscopes, high-resolution electron microscopies, lasers, and other spectroscopic tools, are important not only in the further development of sub-nanotechnologies but also in probing fundamental chemical reaction dynamics and mechanisms at the atomic level, thereby revolutionizing how chemical research is done and how novel nanomaterials will be discovered and fabricated.

Specifically, with the advent of SPMs, single-atom trenches on the order of 0.1–0.3 nm in width can now be produced. As discussed in section 10.2.1, SPMs are powerful atomic-scale imaging tools. Not only surface structures, surface modification, and surface reconstructions can be imaged, adatoms, defects, stacking faults, and twinning, etc., on surfaces can also be visualized. In this section, we shall show further utilities of SPMs in manipulating individual atoms and molecules, in fabricating atomic-scale patterns on surfaces, and in studying fundamental chemical reactions on surfaces, one atom, one electron, or one bond at a time.

In a broader sense, atomic- and molecular-scale technologies at 0.3 and 3 nm, respectively, can also be viewed as hybrid sub-nanotechnologies in that sub-nanometer-scale objects such as atoms or molecules are being assembled (bottom-up approach), one at a time, on 2-D prefabricated surfaces (top-down approach).

#### 13.1. Atomic- and Molecular-Scale Imprinting on Surfaces

Using SPMs, various nano- or sub-nanoscaled imprinting, patterning, and lithography techniques have been developed.<sup>349,460–466</sup> Atomic-scaled features, down to one atom in width, can be “mechanically” scribed on surfaces. If the surfaces were wet with a reactive compound, either beforehand or afterward, simultaneous functionalization and im-



printing or patterning of the surfaces can be achieved. For example, scribing a silicon surface breaks through silicon's passivation layer (either hydrogen or oxide) to expose a highly reactive surface that reacts with the reactive reagent, inducing monolayer formation in the exposed region, thereby producing monolayer-covered imprints on the surface. Monolayers of 1-alkenes, 1-alkynes, alcohols, and alkyl halides, etc., have been produced on the reconstructed surfaces of Si(100)-(2 × 1) or Si(111)-(7 × 7).<sup>467</sup>

It should be emphasized that the above-mentioned techniques can be applied not only to pristine surfaces but also to monolayers already on surfaces. In addition, not only atoms can be extracted from, or deposited onto, surfaces (or adsorbed species on surfaces), dangling bonds<sup>468</sup> (see Figure 116 in section 13.2) or lone pairs of electrons<sup>469</sup> on the exposed atoms can also be seen after the passivating layer had been stripped (i.e., protective atoms extracted with the SPM tip).

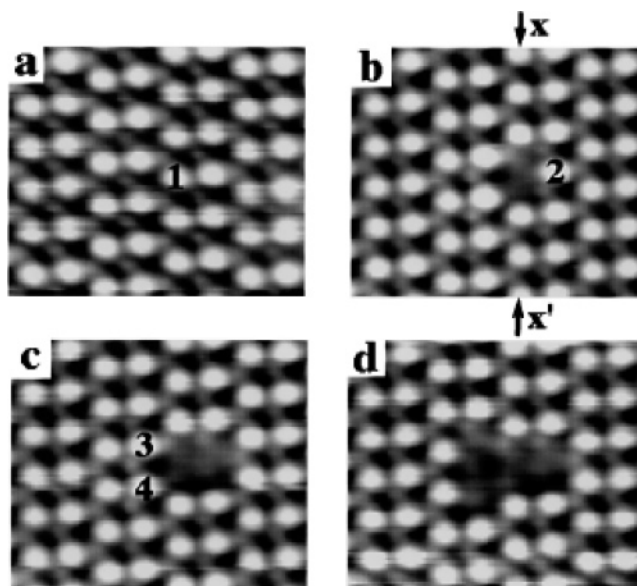
Instead of chemomechanical scribing, molecular-scale imprinting can also be achieved by highly localized atomic reactions (LAR) induced by photons, electrons, or heat. Here a loosely physisorbed self-assembled pattern can be imprinted onto a surface to form an identical, covalently bound, chemisorbed pattern. A beautiful example is the imprinting of a 12-membered ring of CH<sub>3</sub>Br physisorbed on Si(111)-(7 × 7) by photolysis (UV irradiation at 193 nm) or electron impact to form a 12-membered ring of chemisorbed Br atoms at 50 K.<sup>470</sup>

In any atomic- or molecular-scale imprinting, two minimum requirements must be met. First, the final imprint pattern must be identical or almost identical to the original physisorbed or scribed pattern. This is possible only if the "imprinting" process, which constitutes an induced chemical reaction, is a fully localized reaction at the atomic level (LAR).<sup>471</sup> Second, the nanopattern must have long-term stability. In any device, there will always be recurrent electron or photon flow which could cause substrate interactions, desorption induced by electronic transitions,<sup>472</sup> (the so-called DIET), and local heating, etc., thereby altering the nanopattern, or worse, the underlying nanostructure, and hence compromising the integrity of the device.

Finally, we should mention that atomic- and molecular-scale imprinting techniques discussed here are distinctly different from the nanomachining, nanomanipulating, and nanoassembling techniques discussed in section 10. The latter techniques deal with the manipulation or shaping of nanoobjects, while the former are techniques for nanoscale (down to single-atom scale) scribing on 2-D surfaces. Furthermore, atomic- and molecular-scale imprinting techniques are also different from nanofabrication techniques such as nanoimprint lithographies discussed in sections 10.7 and 12.1.

### 13.2. Single-Atom/Single-Molecule Chemistry: Reaction Dynamics and Spectroscopy

With the advent of SPMs and HRTEMs and sophisticated excitation sources (such as lasers and synchrotron radiations) and detection techniques, investigations of single-atom or single-molecule reactions, single-photon or single-electron spectroscopies are now possible. Reactions can now be studied, or induced, one electron, one atom, or one molecule at a time, and spectroscopies can now be observed, one electron or one photon at a time.<sup>317,473–479</sup> In this section, we shall discuss a few representative examples of atomic reactions on various surfaces. We shall demonstrate the



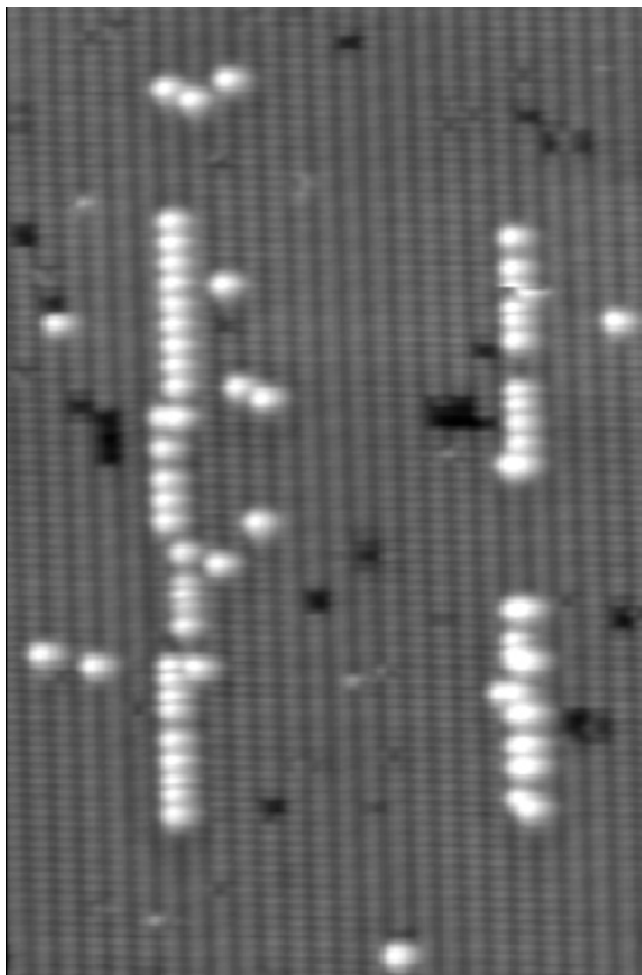
**Figure 115.** Sequence of STM images of the Ge(111)-c(2 × 8) surface (from a to d) during which four Ge atoms were extracted (area, 53 × 47 Å<sup>2</sup>; sample bias, +1 V; tunnel current, 1 nA). The selected atoms are indicated by numbers 1–4. (Reprinted with permission from ref 480 (<http://link.aps.org/abstract/PRL/v80/p3085>). Copyright 1998 by the American Physical Society).

utilities of SPMs in: (1) extracting atoms from, or depositing atoms onto, molecules or surfaces; (2) electronically or vibrationally exciting individual atoms and molecules; (3) inducing chemical reactions on surfaces, on adsorbed species, or between the adsorbates and the surface.

Direct SPM tip–surface interaction without any tunneling electrons or electric field effect allows the extraction of atoms from the surface in a controlled manner, as illustrated in Figure 115a–d, which shows the successive extractions of four germanium atoms from a Ge(111)-c(2 × 8) surface at room temperature.<sup>480</sup> In Figure 116, two lines of silicon dangling bonds on a H-passivated Si(100)-(2 × 1) surface were produced by extracting the hydrogen atoms with the STM tip.<sup>481</sup>

STM tip can also be used as an atomic size source of electrons for local electronic excitation. In fact, both electron and hole injections are possible. Molecular dynamics induced by electronic excitation with the STM tip include molecular movement, desorption from the surface, dissociation (bond breaking), and association (bond forming), etc. We shall give one representative example for each of these processes.

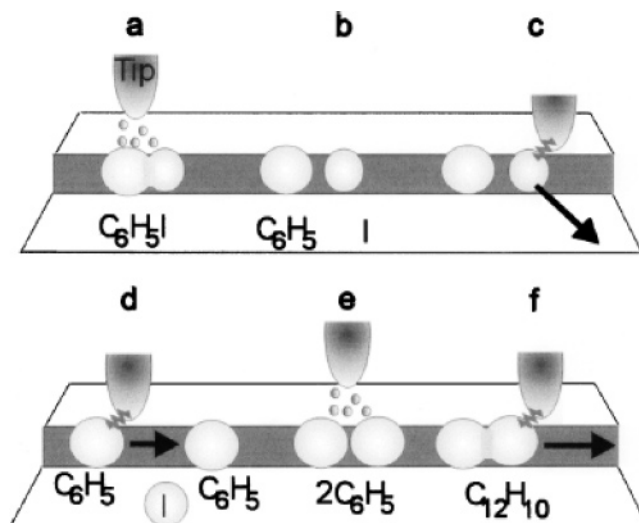
One example of electron-induced molecular movement is biphenyl adsorbed on Si(100)-(2 × 1) surface. At room temperature, the molecule was observed to adsorb in one of two configurations but fixed at one position at 35 K. This suggests that the molecule was pivoting about the two configurations at room temperature. Further experiments showed that it was possible to transform the bistable molecule into the fixed position by injecting electrons using the STM tip.<sup>482,483</sup> Though this particular example led to irreversible molecular movement, it was soon realized that reversible dynamic processes could be explored by lowering the temperature and by reducing the excitation energy. Here the bistable movement of the molecule between two configurations could be triggered by electron or hole attachment, thereby making it a reversible bistable switch or logic device.<sup>484</sup>



**Figure 116.** STM topography ( $50 \times 25 \text{ nm}^2$ ) of a hydrogenated Si-(100)-(2  $\times$  1) surface showing two lines of silicon dangling bonds (DBs) produced by extracting the hydrogen atoms with the STM tip. Kinks in the DB lines are mainly due to misalignment of the tip trajectory with the dimer rows. The right-hand line shows both a Peierls distortion and a section where the tip is inactive. (Reprinted with permission from ref 481. Copyright 2006 American Chemical Society.)

Electron-induced desorption and dissociation have been observed, depending upon the tip bias voltage, for chlorobenzene molecules adsorbed on Si(111)-(7  $\times$  7) surface.<sup>485,486</sup> The desorption mechanism was believed to be driven by the population of the anionic (or cationic) resonance state associated with the  $\pi$  system of the chemisorbed molecule upon electron excitation. In the latter case (dissociation), the dissociated chlorine atoms were found to be attached to neighboring silicon sites. The dissociation process was thus interpreted as a concerted mechanism involving electron attachment followed by C–Cl bond breaking and the formation of Si–Cl bonds at neighboring sites.

One of the most beautiful single-molecule reactions is the pioneering work by Hla and co-workers<sup>487</sup> on the synthesis of a biphenyl molecule from two iodobenzene molecules on a copper surface under STM. The STM sequence is illustrated schematically in Figure 117. Here the iodobenzene molecules were shown to adsorb preferentially on the step edges of a Cu(111) surface at 20 K. In a and b, STM tip-induced dissociation was achieved by injecting 1.5 eV electrons into an iodobenzene molecule, resulting in the cleavage of the C–I bond. In c, the dissociated iodine atom was removed



**Figure 117.** Schematic illustration of the STM tip-induced synthesis of a biphenyl molecule. (a, b) Electron-induced selective abstraction of iodine from iodobenzene. (c) Removal of the iodine atom to a terrace site by lateral manipulation. (d) Bringing together two phenyls by lateral manipulation. (e) Electron-induced chemical association of two phenyl groups to form the biphenyl. (f) Pulling the synthesized biphenyl molecule with the STM tip to confirm the association. (Reprinted with permission from ref 487. Copyright 2000 American Physical Society.)

to a terrace site by lateral movement. Bringing together two phenyl groups by lateral manipulation in d, followed by electron-induced coupling (by applying a 1.5 V pulse simultaneously to both phenyl groups) in e gave rise to the biphenyl molecule. The formation of the C–C bond in the resulting biphenyl molecule is confirmed by dragging laterally the product with the STM tip in f.

We should add that one of the problems with any single-molecule synthesis under STM is the positive identification of the products. Fortunately this can be alleviated in part by the use of the so-called inelastic electron tunneling spectroscopy (IETS) wherein the product(s) can be identified by vibrational spectroscopy.<sup>488,489</sup> The power of this technique is that different isotopes can be distinguished.

Other single-molecule reactions on various semiconductor and metal surfaces can be found in refs 471 and 481.

It is apparent that single-molecule synthesis, one atom or one bond at a time, is made possible by the ingenious sequence of the STM manipulations which allow bond breaking and bond forming in a highly controlled and precise manner. This opens up the new field of single-atom and single-molecule chemistry which will help propel the atomic- and molecular-scale technologies.

#### 14. Interconnection and Integration

Obviously large-scale interconnection and integration, and connection to the microworld and eventually to the macro-world, are challenges that must be overcome before any of these nanodevices could be put into use. Recently, Lieber's group developed a solution-based approach for hierarchical assembly of nanowires into integrated device arrays.<sup>337,339,490</sup> Nanowires were aligned with controlled nanometer- to micrometer-scale separation using the Langmuir–Blodgett technique, transferred to planar substrates in a layer-by-layer process to form parallel and crossed nanowire structures over centimeter length scales, and then patterned into repeating arrays of controlled dimensions and pitch using photolithog-

raphy. The centimeter-scale arrays containing thousands of single silicon nanowire field effect transistors with scalability to the 100 nm level. This approach allows the parallel and scalable integration of nanowire devices over large areas without the need to register individual nanowire–electrode interconnects. The scalable device characteristics were demonstrated by interconnecting a controlled number of nanowires per transistor in “pixellike” device arrays.

## 15. Conclusions and Future Prospects

In conclusion, nanotechnology is a revolution, not evolution, in science and technology. The advent of nanotechnology allows man to change the fundamental properties of matter, tailor make materials with desirable attributes, and fabricate functional devices of any dimensions. The nanorevolution will impact every aspect of human activities, not just in science and technology.

This review deals with all three aspects of the nanotechnological revolution, with special emphasis on building the materials base (especially silicon-based low-dimensional nanomaterials) for a wide variety of nanostructures potentially useful in future applications (the first aspect). The various manipulating techniques (the second aspect) and nanodevice fabrications (the third aspect) are also discussed, albeit briefly.

Silicon-based nanotechnology is highly promising since it is compatible with conventional silicon microtechnology. Needless to say the operating principles and performance of nanodevices in general, and silicon-based nanodevices in particular, depend on the chemical, physical, and biological properties of the nanomaterial components (the building blocks), especially at the interface, as well as on our ability to fabricate functional heterostructures and interfaces with desirable characteristics.

To build a nanodevice, one needs to control and manipulate the properties, sizes, and shapes of materials at the nanometer level. In this review, rational controls of the dimensions and orientation of SiNWs are discussed in section 6, followed by discussions on the surface treatments (etching) and the resulting surface speciation of SiNWs and SiNDs (section 7). The use of SiNWs as “platforms”, “templates”, or “molds” in the synthesis of other novel nanomaterials are discussed in section 8. A simple scheme, with special terms and symbols, is devised in section 5 to categorize various nanostructural types. A systematic discussion on the controlled syntheses of a wide variety of nanostructures is provided in section 9, followed by discussions on nanomachining and nanomanipulating techniques in section 10 and on quantum-size effects and properties such as bandgaps and photoluminescence in section 11. Finally, brief discussions on the fabrication of various nanodevice units, as well as the interconnection and integration of these nanodevices and their interface with the microworld, and eventually the macroworld, are topics of sections 12 and 14, respectively. While many nanodevices based on silicon nanomaterials have been fabricated, the issues of dispersity of SiNWs and related nanostructures as well as the long-term stability, sensitivity, and reproducibility of the nanodevices remain to be addressed.

The pros and cons of the bottom-up and top-down approaches to nanotechnology are also debated in section 12. While each approach has its advantages and disadvantages, it is our view that future development of nanotechnology will embrace both approaches with their relative contributions depending upon specific applications. In other

words, at the scale of about 30 nm in feature size, the top-down approach of the existing lithography technologies will probably merge with the bottom-up strategy of the nanotechnology to form a new hybrid technology (cf. section 12.3). At the scale of about 3 nm in feature size, this hybrid technology will be challenged by the emerging supramolecular and molecular technologies epitomized by large-scale integration of single-molecular devices. Ultimately the supramolecular and molecular technologies will yield to atomic or nuclear technologies at the dimension of below 0.3 nm, whereby single-atom, single-electron, single-spin, and single-photon devices become realities (cf. section 12.4).

In this context, atomic- and molecular-scale imprinting technologies as well as single-atom, single-molecule reaction dynamics and mechanisms and single-photon or single-spin spectroscopies are now realities. They are discussed briefly in section 13.

Finally, as stated earlier, the nanorevolution will impact every aspect of human life. One area of nanotechnology already having many major breakthroughs is nanomedicine.<sup>491,492</sup> The next decade will witness the explosive use of nanomaterials and nanodevices in the detection, monitoring, and treatment of diseases ranging from AIDS to diabetes to cancer. As highlighted in section 12.5.5, direct, real-time single-cell or single-virus detection is already a reality, and one can imagine that single-cell genetic engineering—the ultimate feat of nano-biotechnology—will eventually be possible.

## 16. Acronyms

1-D	one-dimensional
2-D	two-dimensional
3-D	three-dimensional
a-Si	amorphous silicon
AAO	anodized aluminum oxide
AFM	atomic force microscope
ALD	atomic layer deposition
ATR	attenuated total reflection
BHF	buffered HF solution
CEA	carcinoembryonic antigen
CNOs	carbon nanoions
CNTs	carbon nanotubes
CNW	carbon nanowire
c-Si	crystalline silicon
cSiNTs	crystalline silicon nanotubes
CVD	chemical vapor deposition
DB	dangling bond
DFT	density functional theory
DFTB-MD	density-functional tight-binding molecular dynamics
DIET	desorption induced by electronic transitions
DWCNTs	double-walled carbon nanotubes
EDX	energy dispersive X-ray spectroscopy
EELS	electron energy loss spectroscopy
EL	electroluminescence
EUVL	extreme UV lithography
fcc	face-centered cubic structure
FET	field effect transistor
FESEM	field emission scanning electron microscopy
FLY	fluorescence yield
FTIR	Fourier-transform infrared spectroscopy
GTBMD	generalized tight-binding molecular dynamics
HCNO	hydrocarbon nanoion
HCNT	hydrocarbon nanotube
HF calc	Hartree–Fock calculations
HFCVD	hot filament chemical vapor deposition
HOMO	highest occupied molecular orbital



HOPG	highly oriented pyrolytic graphite
HREELS	high-resolution electron energy loss spectroscopy
HRTEM	high-resolution transmission electron microscopy
IETS	inelastic electron tunneling spectroscopy
IRS	infrared spectroscopy
i-Si	intrinsic silicon
LAR	localized atomic reaction
LB	Langmuir–Blodgett
LEDs	light-emitting diodes
LEE	lithography and electrochemical etching
LEED	low-energy electron diffraction
LO	longitudinal-optic
LUMO	lowest unoccupied molecular orbital
MBE	molecular beam epitaxy
ML	monolayer
ML2	maskless lithography
MWCNTs	multiwalled carbon nanotubes
NC	nanocrystal
NCA	nanochannel alumina
ND	nanodots
NEXAFS	near-edge X-ray absorption fine structure
NGL	next-generation lithography
NIL	nanoimprint lithography
n-Si	n-type silicon
NR	nanorod
NS	nanoshell
NT	nanotube
NW	nanowire
OAG	oxide assisted growth
pc	polycrystalline
PDMS	poly(dimethylsiloxane)
PIM	polyicosahedral metal
PL	photoluminescence
PLA-CVD	pulsed laser ablation/chemical vapor deposition
PLY	photoluminescence yield
PNA	peptide nucleic acid
PSA	prostate specific antigen
p-Si	p-type silicon
QD	quantum dot
RCA	Clean Radio Corp. of America cleaning procedure for Si wafers
RIE	reactive ion (plasma) etching
RTD	resonant tunneling device
SAED	selected area electron diffraction
SAM	self-assembled monolayer
SCCM	standard cubic centimeter per minute at STP
SEM	scanning electron microscopy
SFIL	step-and-flash imprint lithography
SiCNTs	silicon carbide nanotubes
SiH	monohydride
SiH <sub>2</sub>	dihydride
SiH <sub>3</sub>	trihydride
SiNRs	silicon nanorods
SiNDs	silicon nanodots
SiNTs	silicon nanotubes
SiNWs	silicon nanowires
SLS	solution–liquid–solid
SOG	spin-on-glass
SOI	silicon oxide insulator
SPINS	spins in semiconductors
SPL	scanning probe lithography
SPM	scanning probe microscopy
STM	scanning tunneling microscopy
SWCNTs	single-walled carbon nanotubes
TEY	total electron yield
TEM	transmission electron microscopy
TFT	thin-film transistor
TO	transverse-optic
VLS	vapor–liquid–solid
VLSE	vapor–liquid–solid epitaxy
XAFS	X-ray absorption fine structure

XANES	X-ray absorption near edge spectroscopy
XEOL	X-ray excited optical luminescence

## 17. Acknowledgments

This review is based in part on the Keynote Lecture by B.K.T. at the ISCIC-5/ISCO-8 Symposium, Dec. 19–22, 2004, Hong Kong. This review is dedicated to the memory of Anna Tang Lee. B.K.T. is particularly grateful for the kind hospitality Professors S. T. Lee, N. B. Wong, R.Q. Zhang, and their colleagues extended to him during his visit to the City University of Hong Kong in 2002. X.H.S. appreciates P. Song's assistance and support during the preparation of this review. We also thank one of the reviewers for bringing refs 430 and 431 to our attention and the comments quoted at the end of section 12.5.3.

## 18. References

- (1) See, for example: (a) Amato, I. *Science* **1998**, 282, 402. (b) Judy, J. W. *Smart Mater. Struct.* **2001**, 10, 1115. (c) Heinrich, H.; Bauer, G.; Kuchar, F. E. *Physics and Technology of Submicron Structures*; Springer-Verlag: Berlin and Heidelberg, Germany, 1988.
- (2) (a) Keyes, R. W. *IBM J. Res. Dev.* **1988**, 24. (b) Ahmed, H.; Nakazato, K. *Microelectron. Eng.* **1996**, 32, 297. (c) Muller, D. A.; Sorsch, T.; Moccio, S.; Baumann, F. H.; Evans-Lutterodt, K.; Timp, G. *Nature* **1999**, 399, 758. (d) Service, R. F. *Science* **2001**, 293, 785.
- (3) (a) Lehn, J.-M. *Supramolecular Chemistry: Concepts and Perspectives*; VCH: Weinheim, Germany, 1995. (b) Vogtle, F. *Supramolecular Chemistry: An Introduction*; Wiley: Chichester, U.K., 1991. (c) Amabilino, D. B.; Stoddart, J. F. *Chem. Rev.* **1995**, 95, 2725. (d) Ungar, G.; Liu, Y. S.; Zeng, X. B.; Percec, V.; Cho, W. D. *Science* **2003**, 299, 1208.
- (4) Iijima, S. *Nature* **1991**, 354, 56.
- (5) Wildoer, J. W. G.; Venema, L. C.; Rinzler, A. G.; Smalley, R. E.; Dekker, C. *Nature* **1998**, 391, 59.
- (6) Odom, T. W.; Huang, J. L.; Kim, P.; Lieber, C. M. *Nature* **1998**, 391, 62.
- (7) Charlier, J. C.; Lambin, P. *Phys. Rev. B* **1998**, 57, R15037.
- (8) Zhou, G.; Duan, W. H.; Gu, B. L. *Chem. Phys. Lett.* **2001**, 333, 344.
- (9) Hamada, N.; Sawada, S.; Oshiyama, A. *Phys. Rev. Lett.* **1992**, 68, 1579.
- (10) Saito, R.; Dresselhaus, G.; Dresselhaus, M. S. *Physical Properties of Carbon Nanotubes*; Imperial College Press: London, 1998.
- (11) Ouyang, M.; Huang, J. L.; Cheung, C. L.; Lieber, C. M. *Science* **2001**, 292, 702.
- (12) Collins, P. C.; Arnold, M. S.; Avouris, P. *Science* **2001**, 292, 706.
- (13) Iijima, S.; Brabec, C.; Maiti, A.; Bernholc, J. *J. Chem. Phys.* **1996**, 104, 2089.
- (14) Thess, A.; Lee, R.; Nikolaev, P.; Dai, H. J.; Petit, P.; Robert, J.; Xu, C. H.; Lee, Y. H.; Kim, S. G.; Rinzler, A. G.; Colbert, D. T.; Scuseria, G. E.; Tomanek, D.; Fischer, J. E.; Smalley, R. E. *Science* **1996**, 273, 483.
- (15) Journet, C.; Maser, W. K.; Bernier, P.; Loiseau, A.; DelaChapelle, M. L.; Lefrant, S.; Deniard, P.; Lee, R.; Fischer, J. E. *Nature* **1997**, 388, 756.
- (16) Mintmire, J. W.; Dunlap, B. I.; White, C. T. *Phys. Rev. Lett.* **1992**, 68, 631.
- (17) Saito, R.; Fujita, M.; Dresselhaus, G.; Dresselhaus, M. S. *Appl. Phys. Lett.* **1992**, 60, 2204.
- (18) Saito, R.; Dresselhaus, M. G.; Dresselhaus, M. S. *Phys. Rev. B* **2000**, 61, 2981.
- (19) Saito, R.; Fujita, M.; Dresselhaus, G.; Dresselhaus, M. S. *Phys. Rev. B* **1992**, 46, 1804.
- (20) Deheer, W. A.; Chatelain, A.; Ugarte, D. *Science* **1995**, 270, 1179.
- (21) Wang, Q. H.; Setlur, A. A.; Lauerhaas, J. M.; Dai, J. Y.; Seelig, E. W.; Chang, R. P. H. *Appl. Phys. Lett.* **1998**, 72, 2912.
- (22) Choi, W. B.; Chung, D. S.; Kang, J. H.; Kim, H. Y.; Jin, Y. W.; Han, I. T.; Lee, Y. H.; Jung, J. E.; Lee, N. S.; Park, G. S.; Kim, J. M. *Appl. Phys. Lett.* **1999**, 75, 3129.
- (23) Wang, Q. H.; Yan, M.; Chang, R. P. H. *Appl. Phys. Lett.* **2001**, 78, 1294.
- (24) Terrones, M. *Annu. Rev. Mater. Res.* **2003**, 33, 419.
- (25) Morales, A. M.; Lieber, C. M. *Science* **1998**, 279, 208.
- (26) Zhang, Y. F.; Tang, Y. H.; Wang, N.; Yu, D. P.; Lee, C. S.; Bello, I.; Lee, S. T. *Appl. Phys. Lett.* **1998**, 72, 1835.
- (27) Holmes, J. D.; Johnston, K. P.; Doty, R. C.; Korgel, B. A. *Science* **2000**, 287, 1471.

- (28) Yu, J. Y.; Chung, S. W.; Heath, J. R. *J. Phys. Chem. B* **2000**, *104*, 11864.
- (29) Bohr, M. T. *IEEE Trans. Nanotechnol.* **2002**, *1*, 56.
- (30) Meyyappan, M.; Kelly, L. *Carbon Nanotubes: Science and Applications*; CRC Press: Boca Raton, FL, 2005.
- (31) Dresselhaus, M. S.; Dresselhaus, G.; Avouris, P. *Carbon Nanotubes*; Springer-Verlag: Berlin and Heidelberg, Germany, 2001.
- (32) Ebbesen, T. W. *Carbon Nanotubes: Preparation and Properties*; CRC Press: Boca Raton, FL, 1997.
- (33) Ajayan, P. M. *Chem. Rev.* **1999**, *99*, 1787.
- (34) Yakobson, B. I.; Smalley, R. E. *Am. Sci.* **1997**, *85*, 324.
- (35) Ebbesen, T. W. *Annu. Rev. Mater. Sci.* **1994**, *24*, 235.
- (36) Harris, P. J. F. *Carbon Nanotubes and Related Structures: New Materials for the Twenty-First Century*; Cambridge University Press: Cambridge, U.K., 1999.
- (37) Fagan, S. B.; Baierle, R. J.; Mota, R.; da Silva, A. J. R.; Fazzio, A. *Phys. Rev. B* **2000**, *61*, 9994.
- (38) Seifert, G.; Kohler, T.; Urbassek, H. M.; Hernandez, E.; Frauenheim, T. *Phys. Rev. B* **2001**, *63*, 193409.
- (39) Kang, J. W.; Seo, J. J.; Hwang, H. J. *J. Nanosci. Nanotechnol.* **2002**, *2*, 687.
- (40) Fagan, S. B.; Mota, R.; Baierle, R. J.; Paiva, G.; da Silva, A. J. R.; Fazzio, A. *J. Mol. Struct. (THEOCHEM)* **2001**, *539*, 101.
- (41) Barnard, A. S.; Russo, S. P. *J. Phys. Chem. B* **2003**, *107*, 7577.
- (42) Zhang, R. Q.; Lee, S. T.; Law, C. K.; Li, W. K.; Teo, B. K. *Chem. Phys. Lett.* **2002**, *364*, 251.
- (43) Zhang, R. Q.; Lee, H. L.; Li, W. K.; Teo, B. K. *J. Phys. Chem. B* **2005**, *109*, 8605.
- (44) Sha, J.; Niu, J. J.; Ma, X. Y.; Xu, J.; Zhang, X. B.; Yang, Q.; Yang, D. *Adv. Mater.* **2002**, *14*, 1219.
- (45) Jeong, S. Y.; Kim, J. Y.; Yang, H. D.; Yoon, B. N.; Choi, S. H.; Kang, H. K.; Yang, C. W.; Lee, Y. H. *Adv. Mater.* **2003**, *15*, 1172.
- (46) Mu, C.; Yu, Y. X.; Liao, W.; Zhao, X. S.; Xu, D. S.; Chen, X. H.; Yu, D. P. *Appl. Phys. Lett.* **2005**, *87*, 113104.
- (47) Hu, J. Q.; Bando, Y.; Liu, Z. W.; Zhan, J. H.; Golberg, D.; Sekiguchi, T. *Angew. Chem., Int. Ed.* **2004**, *43*, 63.
- (48) Teo, B. K.; Li, C. P.; Sun, X. H.; Wong, N. B.; Lee, S. T. *Inorg. Chem.* **2003**, *42*, 6723.
- (49) Peng, H. Y.; Wang, N.; Zheng, Y. F.; Lifshitz, Y.; Kulik, J.; Zhang, R. Q.; Lee, C. S.; Lee, S. T. *Appl. Phys. Lett.* **2000**, *77*, 2831.
- (50) Qin, L. C.; Zhao, X. L.; Hirahara, K.; Miyamoto, Y.; Ando, Y.; Iijima, S. *Nature* **2000**, *408*, 50.
- (51) Wang, N.; Tang, Z. K.; Li, G. D.; Chen, J. S. *Nature* **2000**, *408*, 50.
- (52) Stewart, J. J. P. *J. Comput. Chem.* **1989**, *10*, 209.
- (53) Dewar, M. J. S.; Thiel, W. *J. Am. Chem. Soc.* **1977**, *99*, 4899.
- (54) Gao, G. H.; Cagin, T.; Goddard, W. A. *Nanotechnology* **1998**, *9*, 184.
- (55) Mavrandonakis, A.; Froudakis, G. E. *Nano Lett.* **2003**, *3*, 1481.
- (56) Menon, M.; Richter, E.; Mavrandonakis, A.; Froudakis, G.; Andriotis, A. N. *Phys. Rev. B* **2004**, *69*, 115322.
- (57) Janzon, K. H.; Schafer, H.; Weiss, A. Z. *Anorg. Allg. Chem.* **1970**, *372*, 87.
- (58) Singh, A. K.; Kumar, V.; Briere, T. M.; Kawazoe, Y. *Nano Lett.* **2002**, *2*, 1243.
- (59) Singh, A. K.; Briere, T. M.; Kumar, V.; Kawazoe, Y. *Phys. Rev. Lett.* **2003**, *91*, 146802.
- (60) Masala, O.; Seshadri, R. *Annu. Rev. Mater. Res.* **2004**, *34*, 41.
- (61) Wagner, R. S. *Appl. Phys. Lett.* **1964**, *4*, 89.
- (62) Cui, Y.; Lahun, L. J.; Gudiksen, M. S.; Wang, J. F.; Lieber, C. M. *Appl. Phys. Lett.* **2001**, *78*, 2214.
- (63) Hanrath, T.; Korgel, B. A. *Adv. Mater.* **2003**, *15*, 437.
- (64) Lu, X. M.; Hanrath, T.; Johnston, K. P.; Korgel, B. A. *Nano Lett.* **2003**, *3*, 93.
- (65) Wang, N.; Tang, Y. H.; Zhang, Y. F.; Lee, C. S.; Lee, S. T. *Phys. Rev. B* **1998**, *58*, R16024.
- (66) Wang, N.; Zhang, Y. F.; Tang, Y. H.; Lee, C. S.; Lee, S. T. *Appl. Phys. Lett.* **1998**, *73*, 3902.
- (67) Lee, S. T.; Zhang, Y. F.; Wang, N.; Tang, Y. H.; Bello, I.; Lee, C. S.; Chung, Y. W. *J. Mater. Res.* **1999**, *14*, 4503.
- (68) Lee, S. T.; Wang, N.; Zhang, Y. F.; Tang, Y. H. *MRS Bull.* **1999**, *24*, 36.
- (69) Wang, N.; Tang, Y. H.; Zhang, Y. F.; Lee, C. S.; Bello, I.; Lee, S. T. *Chem. Phys. Lett.* **1999**, *299*, 237.
- (70) Zhang, Y. F.; Tang, Y. H.; Wang, N.; Lee, C. S.; Bello, I.; Lee, S. T. *J. Cryst. Growth* **1999**, *197*, 136.
- (71) Zhang, R. Q.; Lifshitz, Y.; Lee, S. T. *Adv. Mater.* **2003**, *15*, 635.
- (72) Zhang, Y. F.; Tang, Y. H.; Peng, H. Y.; Wang, N.; Lee, C. S.; Bello, I.; Lee, S. T. *Appl. Phys. Lett.* **1999**, *75*, 1842.
- (73) Zhang, R. Q.; Zhao, M. W.; Lee, S. T. *Phys. Rev. Lett.* **2004**, *93*, 095503.
- (74) Zhang, R. Q.; Chu, T. S.; Cheung, H. F.; Wang, N.; Lee, S. T. *Phys. Rev. B* **2001**, *64*, 11.
- (75) Wu, Y.; Cui, Y.; Huynh, L.; Barrelet, C. J.; Bell, D. C.; Lieber, C. M. *Nano Lett.* **2004**, *4*, 433.
- (76) Gu, Q.; Dang, H. Y.; Cao, J.; Zhao, J. H.; Fan, S. S. *Appl. Phys. Lett.* **2000**, *76*, 3020.
- (77) Kamins, T. I.; Williams, R. S.; Basile, D. P.; Hesjedal, T.; Harris, J. S. *J. Appl. Phys.* **2001**, *89*, 1008.
- (78) Kamins, T. I.; Li, X.; Williams, R. S. *Appl. Phys. Lett.* **2003**, *82*, 263.
- (79) Teo, B. K.; Sun, X. H.; Hung, T. F.; Meng, X. M.; Wong, N. B.; Lee, S. T. *Nano Lett.* **2003**, *3*, 1735.
- (80) Li, C. P.; Lee, C. S.; Ma, X. L.; Wang, N.; Zhang, R. Q.; Lee, S. T. *Adv. Mater.* **2003**, *15*, 607.
- (81) Peng, H. Y.; Pan, Z. W.; Xu, L.; Fan, X. H.; Wang, N.; Lee, C. S.; Lee, S. T. *Adv. Mater.* **2001**, *13*, 317.
- (82) Zhang, X. Y.; Zhang, L. D.; Meng, G. W.; Li, G. H.; Jin-Phillipp, N. Y.; Phillipp, F. *Adv. Mater.* **2001**, *13*, 1238.
- (83) Bogart, T. E.; Dey, S.; Lew, K. K.; Mohney, S. E.; Redwing, J. M. *Adv. Mater.* **2005**, *17*, 114.
- (84) Coleman, N. R. B.; Morris, M. A.; Spalding, T. R.; Holmes, J. D. *J. Am. Chem. Soc.* **2001**, *123*, 187.
- (85) Coleman, N. R. B.; O'Sullivan, N.; Ryan, K. M.; Crowley, T. A.; Morris, M. A.; Spalding, T. R.; Steytler, D. C.; Holmes, J. D. *J. Am. Chem. Soc.* **2001**, *123*, 7010.
- (86) Li, C. P.; Sun, X. H.; Wong, N. B.; Lee, C. S.; Lee, S. T.; Teo, B. K. *Chem. Phys. Lett.* **2002**, *365*, 22.
- (87) Wu, Y. Y.; Yan, H. Q.; Yang, P. D. *Top. Catal.* **2002**, *19*, 197.
- (88) Hochbaum, A. I.; Fan, R.; He, R. R.; Yang, P. D. *Nano Lett.* **2005**, *5*, 457.
- (89) Ge, S. P.; Jiang, K. L.; Lu, X. X.; Chen, Y. F.; Wang, R. M.; Fan, S. S. *Adv. Mater.* **2005**, *17*, 56.
- (90) Fuhrmann, B.; Leipner, H. S.; Hoche, H. R.; Schubert, L.; Werner, P.; Gosele, U. *Nano Lett.* **2005**, *5*, 2524.
- (91) Gao, D.; He, R. R.; Carraro, C.; Howe, R. T.; Yang, P. D.; Maboudian, R. *J. Am. Chem. Soc.* **2005**, *127*, 4574.
- (92) Wang, D.; Qian, F.; Yang, C.; Zhong, Z. H.; Lieber, C. M. *Nano Lett.* **2004**, *4*, 871.
- (93) Shan, Y. H.; Kalkan, A. K.; Peng, C. Y.; Fonash, S. J. *Nano Lett.* **2004**, *4*, 2085.
- (94) He, R. R.; Gao, D.; Fan, R.; Hochbaum, A. I.; Carraro, C.; Maboudian, R.; Yang, P. D. *Adv. Mater.* **2005**, *17*, 2098.
- (95) Cui, Y.; Duan, X. F.; Hu, J. T.; Lieber, C. M. *J. Phys. Chem. B* **2000**, *104*, 5213.
- (96) Cui, Y.; Lieber, C. M. *Science* **2001**, *291*, 851.
- (97) Tang, Y. H.; Sun, X. H.; Au, F. C. K.; Liao, L. S.; Peng, H. Y.; Lee, C. S.; Lee, S. T.; Sham, T. K. *Appl. Phys. Lett.* **2001**, *79*, 1673.
- (98) Tang, Y. H.; Sham, T. K.; Jurgensen, A.; Hu, Y. F.; Lee, C. S.; Lee, S. T. *Appl. Phys. Lett.* **2002**, *80*, 3709.
- (99) Ma, D. D.; Lee, C. S.; Lee, S. T. *Appl. Phys. Lett.* **2001**, *79*, 2468.
- (100) Cui, Y.; Zhong, Z. H.; Wang, D. L.; Wang, W. U.; Lieber, C. M. *Nano Lett.* **2003**, *3*, 149.
- (101) Zheng, G. F.; Lu, W.; Jin, S.; Lieber, C. M. *Adv. Mater.* **2004**, *16*, 1890.
- (102) Chung, S. W.; Yu, J. Y.; Heath, J. R. *Appl. Phys. Lett.* **2000**, *76*, 2068.
- (103) Zhou, G. W.; Li, H.; Sun, H. P.; Yu, D. P.; Wang, Y. Q.; Huang, X. J.; Chen, L. Q.; Zhang, Z. *Appl. Phys. Lett.* **1999**, *75*, 2447.
- (104) Byon, K.; Tham, D.; Fischer, J. E.; Johnson, A. T. *Appl. Phys. Lett.* **2005**, *87*, 193104.
- (105) Grundner, M.; Jakob, H. *Appl. Phys. A* **1986**, *39*, 73.
- (106) Graf, D.; Grundner, M.; R. S. *J. Appl. Phys.* **1990**, *68*, 155.
- (107) Burrows, V. A.; Chabal, Y. J.; Higashi, G. S.; Raghavachari, K.; Christman, S. B. *Appl. Phys. Lett.* **1988**, *53*, 998.
- (108) Higashi, G. S.; Chabal, Y. J.; Trucks, G. W.; Raghavachari, K. *Appl. Phys. Lett.* **1990**, *56*, 656.
- (109) Chabal, Y. J.; Higashi, G. S.; Raghavachari, K.; Burrows, V. A. *J. Vac. Sci. Technol. A* **1989**, *7*, 2104.
- (110) Jakob, P.; Chabal, Y. J. *J. Chem. Phys.* **1991**, *95*, 2897.
- (111) Hines, M. A.; Chabal, Y. J.; Harris, T. D.; Harris, A. L. *Phys. Rev. Lett.* **1993**, *71*, 2280.
- (112) Niwano, M.; Terash, M.; Shinohara, M.; Shoji, D.; Miyamoto, N. *Surf. Sci.* **1998**, *401*, 364.
- (113) Niwano, M.; Kageyama, J.; Kinashi, K.; Sawahata, J.; Miyamoto, N. *Surf. Sci.* **1994**, *301*, 245.
- (114) Sugiyama, K.; Igarashi, T.; Moriki, K.; Nagasawa, Y.; Aoyama, T.; Sugino, R.; Ito, T.; Hattori, T. *Jpn. J. Appl. Phys.* **1990**, *29*, 2401.
- (115) Ogawa, H.; Ishikawa, K.; Suzuki, M. T.; Hayami, Y.; Fujimura, S. *Surf. Sci. Lett.* **1993**, *302*, 245.
- (116) Sugita, Y.; Watanabe, S. *Jpn. J. Appl. Phys.* **1998**, *37*, 1193.
- (117) van der Zwan, M. L. W.; Bardwell, J. A.; Sproule, G. I.; Graham, M. J. *Appl. Phys. Lett.* **1994**, *64*, 446.
- (118) Bowler, D. R.; Owen, J. G.; Miki, K.; Briggs, G. A. D. *Phys. Rev. B* **1998**, *57*, 8790.



- (119) Houberts, R.; Memmert, U.; Behm, R. J. *Surf. Sci.* **1998**, *396*, 198.
- (120) Hahn, P. O. *Mater. Res. Soc. Symp. Proc.* **1986**, *54*, 645.
- (121) Hollinger, G.; Himpfel, F. J. *Vac. Sci. Technol.*, A **1983**, *1*, 640.
- (122) Sun, X. H.; Wang, S. D.; Wong, N. B.; Ma, D. D. D.; Lee, S. T.; Teo, B. K. *Inorg. Chem.* **2003**, *42*, 2398.
- (123) Ma, D. D. D.; Lee, C. S.; Au, F. C. K.; Tong, S. Y.; Lee, S. T. *Science* **2003**, *299*, 1874.
- (124) Kern, W.; Puotinen, D. A. *RCA Rev.* **1970**, *31*, 187.
- (125) Lide, D. R. *Handbook of Chemistry and Physics*, 83rd ed.; CRC Press: Boca Raton, FL, 2002–2003.
- (126) Trucks, G. W.; Raghavachari, K.; Higashi, G. S.; Chabal, Y. J. *Phys. Rev. Lett.* **1990**, *65*, 504.
- (127) Sacher, E.; Yelon, A. *Phys. Rev. Lett.* **1991**, *66*, 1647.
- (128) Trucks, G. W.; Raghavachari, K.; Higashi, G. S.; Chabal, Y. J. *Phys. Rev. Lett.* **1991**, *66*, 1648.
- (129) Kang, J. K.; Kusgrave, C. B. *J. Chem. Phys.* **2002**, *116*, 275.
- (130) Zhang, H.; Wang, X. M.; Zhang, K. C.; Teo, B. K. *J. Solid State Chem.* **2000**, *152*, 191.
- (131) Bensliman, F.; Aggour, M.; Ennaoui, A.; Matsumura, M. *Jpn. J. Appl. Phys. Part 2* **2000**, *39*, L1206.
- (132) Liu, F. M.; Ren, B.; Tian, Z. Q. *Spectrosc. Spectral Anal. (Beijing)* **2000**, *20*, 833.
- (133) Zhang, R. Q.; Zhao, Y. L.; Teo, B. K. *Phys. Rev. B* **2004**, *69*, 125319.
- (134) Chen, W. W.; Sun, X. H.; Wang, S. D.; Lee, S. T.; Teo, B. K. *J. Phys. Chem. B* **2005**, *109*, 10871.
- (135) Teo, B. K.; Chen, W. W.; Sun, X. H.; Wang, S. D.; Lee, S. T. *J. Phys. Chem. B* **2005**, *109*, 21716.
- (136) Garcia, S. P.; Bao, H.; Hines, M. A. *Surf. Sci.* **2003**, *541*, 252.
- (137) Dumas, P.; Chabal, Y. J.; Jakob, P. *Surf. Sci.* **1992**, *269/270*, 867.
- (138) Schmidt, D.; Niimi, H.; Hinds, B. J.; Aspnes, D. E.; Lucovsky, G. J. *Vac. Sci. Technol.*, B **1996**, *14*, 2812.
- (139) Teo, B. K.; Zhang, H. *Coord. Chem. Rev.* **1995**, *143*, 611.
- (140) Zhang, H.; Teo, B. K. *Inorg. Chim. Acta* **1997**, *265*, 213.
- (141) Teo, B. K.; Zhang, H. *Inorg. Chim. Acta* **2001**, *317*, 1.
- (142) Teo, B. K.; Zhang, H. *Angew. Chem., Int. Ed. Engl.* **1992**, *31*, 445.
- (143) Teo, B. K.; Dang, H.; Campana, C. F.; Zhang, H. *Polyhedron* **1998**, *17*, 617.
- (144) Teo, B. K.; Zhang, H. *J. Organomet. Chem.* **2000**, *614*, 66.
- (145) Teo, B. K.; Zhang, H.; Shi, X. B. *Inorg. Chem.* **1994**, *33*, 4086.
- (146) Teo, B. K.; Zhang, H. *J. Cluster Sci.* **2001**, *12*, 349.
- (147) Sun, X. H.; Li, C. P.; Wong, N. B.; Lee, C. S.; Lee, S. T.; Teo, B. K. *Inorg. Chem.* **2002**, *41*, 4331.
- (148) Sun, X. H.; Li, C. P.; Wong, N. B.; Lee, C. S.; Lee, S. T.; Teo, B. K. *J. Am. Chem. Soc.* **2002**, *124*, 14856.
- (149) Li, C. P.; Teo, B. K.; Sun, X. H.; Wong, N. B.; Lee, S. T. *Chem. Mater.* **2005**, *17*, 5780.
- (150) Kong, J.; Cassell, A. M.; Dai, H. J. *Chem. Phys. Lett.* **1998**, *292*, 567.
- (151) Ugarte, D. *Nature* **1992**, *359*, 707.
- (152) De Heer, W. A.; Ugarte, D. *Chem. Phys. Lett.* **1993**, *207*, 480.
- (153) Suslick, K. S.; Price, G. J. *Annu. Rev. Mater. Sci.* **1999**, *29*, 295.
- (154) Nishihara, H.; et al. *J. Chem. Soc., Faraday Trans.* **1991**, *87*, 1187.
- (155) Kiang, C. H.; Goddard, W. A. *Phys. Rev. Lett.* **1996**, *76*, 2515.
- (156) Zhang, P. H.; Crespi, V. H. *Phys. Rev. Lett.* **1999**, *83*, 1791.
- (157) (a) Ge, M. H.; Sattler, K. *Science* **1993**, *260*, 515. (b) Zhang, X. F.; Zhang, X. B.; Tendeloo, G. V.; Amelincx, S. M.; Beeck, O. D.; Van Landuyt, J. *J. Cryst. Growth* **1993**, *130*, 368.
- (158) Saito, Y. *Carbon* **1995**, *33*, 979.
- (159) Yudasaka, M.; Komatsu, T.; Ishihashi, T.; Achiba, Y.; Iijima, S. *J. Phys. Chem. B* **1999**, *102*, 4892.
- (160) Dai, H. J.; Rinzler, A. G.; Nikolaev, P.; Thess, A.; Colbert, D. T.; Smalley, R. E. *Chem. Phys. Lett.* **1996**, *260*, 471.
- (161) Hester, J. R.; Louchev, O. A. *Appl. Phys. Lett.* **2002**, *80*, 2580.
- (162) Hsin, Y. L.; Hwang, K. C.; Chen, F. R.; Kai, J. J. *Adv. Mater.* **2001**, *13*, 830.
- (163) Sano, N.; Wang, H.; Chowalla, M.; Alexandrou, I.; Amaratunga, G. A. J. *Nature* **2001**, *414*, 506.
- (164) Jeong, S.-H.; Ko, J.-H.; Park, J.-B.; Park, W. J. *Am. Chem. Soc.* **2004**, *126*, 15982.
- (165) Zhang, Y. F.; Tang, Y. H.; Zhang, Y.; Lee, C. S.; Bello, I.; Lee, S. T. *Chem. Phys. Lett.* **2000**, *330*, 48.
- (166) Harris, G. L. *Properties of Silicon Carbide*; INSPEC, Institution of Electrical Engineers: London, 1995.
- (167) Sun, X. H.; Li, C. P.; Wong, W. K.; Wong, N. B.; Lee, C. S.; Lee, S. T.; Teo, B. K. *J. Am. Chem. Soc.* **2002**, *124*, 14464.
- (168) Pan, Z. W.; Lai, H. L.; Au, F. C. K.; Duan, X. F.; Zhou, W. Y.; Shi, W. S.; Wang, N.; Lee, C. S.; Wong, N. B.; Lee, S. T.; Xie, S. S. *Adv. Mater.* **2000**, *12*, 1186.
- (169) Wang, Z. L.; Dai, Z. R.; Gao, R. P.; Bai, Z. G.; Gole, J. L. *Appl. Phys. Lett.* **2000**, *77*, 3349.
- (170) Zhang, Y.; Ichihashi, T.; Landree, E.; Nihey, F.; Iijima, S. *Science* **1999**, *285*, 1719.
- (171) Moro, L.; Paul, A.; Lorents, D. C.; Malhotra, R.; Ruoff, R. S.; Lazzeri, P.; Vanzetti, L.; Lui, A.; Subramoney, S. *J. Appl. Phys.* **1997**, *81*, 6141.
- (172) Sun, X. H.; Peng, H. Y.; Tang, Y. H.; Shi, W. S.; Wong, N. B.; Lee, C. S.; Lee, S. T.; Sham, T. K. *J. Appl. Phys.* **2001**, *89*, 6396.
- (173) Sun, X. H.; Sannaynaiken, R.; Naftel, S. J.; Tang, Y. H.; Zhang, P.; Kim, P. S.; Sham, T. K.; Fan, X. H.; Zhang, Y. F.; Lee, C. S.; Lee, S. T.; Wong, N. B.; Hu, Y. F.; Tan, K. H. *Chem. Mater.* **2002**, *14*, 2519.
- (174) Li, C. P.; Wang, N.; Wong, S. P.; Lee, C. S.; Lee, S. T. *Adv. Mater.* **2002**, *14*, 218.
- (175) Li, C. P.; Sun, X. H.; Wong, N. B.; Lee, C. S.; Lee, S. T.; Teo, B. K. *J. Phys. Chem. B* **2002**, *106*, 6980.
- (176) Wong, T. C.; Li, C. P.; Zhang, R. Q.; Lee, S. T. *Appl. Phys. Lett.* **2004**, *84*, 407.
- (177) Wilson, W. L.; Szajowski, P. F.; Brus, L. E. *Science* **1993**, *262*, 1242.
- (178) Littau, K. A.; Szajowski, P. J.; Muller, A. J.; Kortan, A. R.; Brus, L. E. *J. Phys. Chem.* **1993**, *97*, 1224.
- (179) Shimizuwayama, T.; Fujita, K.; Nakao, S.; Saitoh, K.; Fujita, T.; Itoh, N. *J. Appl. Phys.* **1994**, *75*, 7779.
- (180) Brus, L. E.; Szajowski, P. F.; Wilson, W. L.; Harris, T. D.; Schuppler, S.; Citrin, P. H. *J. Am. Chem. Soc.* **1995**, *117*, 2915.
- (181) Leobandung, E.; Guo, L. J.; Wang, Y.; Chou, S. Y. *Appl. Phys. Lett.* **1995**, *67*, 938.
- (182) Mutti, P.; Ghislotti, G.; Bertoni, S.; Bonoldi, L.; Cerofolini, G. F.; Meda, L.; Grilli, E.; Guzzi, M. *Appl. Phys. Lett.* **1995**, *66*, 851.
- (183) Min, K. S.; Shcheglov, K. V.; Yang, C. M.; Atwater, H. A.; Brongersma, M. L.; Polman, A. *Appl. Phys. Lett.* **1996**, *69*, 2033.
- (184) Tiwari, S.; Rana, F.; Hanafi, H.; Hartstein, A.; Crabbe, E. F.; Chan, K. *Appl. Phys. Lett.* **1996**, *68*, 1377.
- (185) Zhuang, L.; Guo, L. J.; Chou, S. Y. *Appl. Phys. Lett.* **1998**, *72*, 1205.
- (186) Pavesi, L.; Dal Negro, L.; Mazzoleni, C.; Franzo, G.; Priolo, F. *Nature* **2000**, *408*, 440.
- (187) Liz-Marzan, L. M.; Mulvaney, P. *J. Phys. Chem. B* **2003**, *107*, 7312.
- (188) Heitmann, J.; Muller, F.; Zacharias, M.; Gosele, U. *Adv. Mater.* **2005**, *17*, 795.
- (189) Kovalev, D.; Fujii, M. *Adv. Mater.* **2005**, *17*, 2531.
- (190) Birner, A.; Wehrspohn, R. B.; Gosele, U. M.; Busch, K. *Adv. Mater.* **2001**, *13*, 377.
- (191) Garrido, B.; Lopez, M.; Perez-Rodriguez, A.; Garcia, C.; Pellegrino, P.; Ferre, R.; Moreno, J. A.; Morante, J. R.; Bonafos, C.; Carrada, M.; Claverie, A.; de la Torre, J.; Souifi, A. *Nucl. Instrum. Methods Phys. Res., Sect. B* **2004**, *216*, 213.
- (192) Sopinsky, M.; Khomchenko, V. *Curr. Opin. Solid State Mater. Sci.* **2003**, *7*, 97.
- (193) Cullis, A. G.; Canham, L. T.; Calcott, P. D. J. *J. Appl. Phys.* **1997**, *82*, 909.
- (194) Lockwood, D. J. *Solid State Commun.* **1994**, *92*, 101.
- (195) Jung, K. H.; Shih, S.; Kwong, D. L. *J. Electrochem. Soc.* **1993**, *140*, 3046.
- (196) Canham, L. T.; Cox, T. I.; Loni, A.; Simons, A. J. *Appl. Surf. Sci.* **1996**, *102*, 436.
- (197) Ozin, G. A. *Adv. Mater.* **1992**, *4*, 612.
- (198) Yoffe, A. D. *Adv. Phys.* **1993**, *42*, 173.
- (199) Yoffe, A. D. *Adv. Phys.* **2001**, *50*, 1.
- (200) Sailor, M. J.; Lee, E. J. *Adv. Mater.* **1997**, *9*, 783.
- (201) Buriak, J. M. *Chem. Rev.* **2002**, *102*, 1271.
- (202) Mizuta, T.; Takeuchi, D.; Makimura, T.; Murakami, K. *Jpn. J. Appl. Phys., Part 1* **2002**, *41*, 5739.
- (203) Pettigrew, K. A.; Liu, Q.; Power, P. P.; Kauzlarich, S. M. *Chem. Mater.* **2003**, *15*, 4005.
- (204) Sweryda-Krawiec, B.; Cassagneau, T.; Fendler, J. H. *J. Phys. Chem. B* **1999**, *103*, 9524.
- (205) Yang, C. S.; Kauzlarich, S. M.; Wang, Y. C. *Chem. Mater.* **1999**, *11*, 3666.
- (206) Liang, H. P.; Wan, L. J.; Bai, C. L.; Jiang, L. *J. Phys. Chem. B* **2005**, *109*, 7795.
- (207) Rosemary, M. J.; MacLaren, I.; Pradeep, T. *Carbon* **2004**, *42*, 2329.
- (208) Hirsch, L. R.; Gobin, A. M.; Lowery, A. R.; Tam, F.; Drezek, R. A.; Halas, N. J.; West, J. L. *Ann. Biomed. Eng.* **2006**, *34*, 15.
- (209) Serksen, S. R.; Westcott, S. L.; Halas, N. J.; West, J. L. *Appl. Phys. Lett.* **2002**, *80*, 4609.
- (210) Tam, F.; Moran, C.; Halas, N. J. *J. Phys. Chem. B* **2004**, *108*, 17290.
- (211) Nehl, C. L.; Grady, N. K.; Goodrich, G. P.; Tam, F.; Halas, N. J.; Hafner, J. H. *Nano Lett.* **2004**, *4*, 2355.
- (212) Lim, Y. T.; Park, O. O.; Jung, H. T. *J. Colloid Interface Sci.* **2003**, *263*, 449.
- (213) Jiang, Z. J.; Liu, C. Y.; Liu, Y.; Zhang, Z. Y.; Li, Y. J. *Chem. Lett.* **2003**, *32*, 668.
- (214) Jiang, Z. J.; Liu, C. Y. *J. Phys. Chem. B* **2003**, *107*, 12411.
- (215) Jackson, J. B.; Halas, N. J. *J. Phys. Chem. B* **2001**, *105*, 2743.
- (216) Mayer, A. B. R.; Grebner, W.; Wannemacher, R. *J. Phys. Chem. B* **2000**, *104*, 7278.



- (217) Oldenburg, S. J.; Westcott, S. L.; Averitt, R. D.; Halas, N. J. *J. Chem. Phys.* **1999**, *111*, 4729.
- (218) Oldenburg, S. J.; Averitt, R. D.; Westcott, S. L.; Halas, N. J. *Chem. Phys. Lett.* **1998**, *288*, 243.
- (219) Averitt, R. D.; Westcott, S. L.; Halas, N. J. *Phys. Rev. B* **1998**, *58*, R10203.
- (220) Schueler, P. A.; Ives, J. T.; Delacroix, F.; Lacy, W. B.; Becker, P. A.; Li, J. M.; Caldwell, K. D.; Drake, B.; Harris, J. M. *Anal. Chem.* **1993**, *65*, 3177.
- (221) Moody, R. L.; Vodinh, T.; Fletcher, W. H. *Appl. Spectrosc.* **1987**, *41*, 966.
- (222) Radloff, C.; Halas, N. J. *Appl. Phys. Lett.* **2001**, *79*, 674.
- (223) Sun, X. H.; Wong, N. B.; Li, C. P.; Lee, S. T.; Kim, P. S. G.; Sham, T. K. *Chem. Mater.* **2004**, *16*, 1143.
- (224) Sun, X. H.; Wong, N. B.; Li, C. P.; Lee, S. T.; Sham, T. K. *J. Appl. Phys.* **2004**, *96*, 3447.
- (225) Tang, Y. H.; Zhang, Y. F.; Wang, N.; Lee, C. S.; Han, X. D.; Bello, I.; Lee, S. T. *J. Appl. Phys.* **1999**, *85*, 7981.
- (226) Peng, H. Y.; Wang, N.; Shi, W. S.; Zhang, Y. F.; Lee, C. S.; Lee, S. T. *J. Appl. Phys.* **2001**, *89*, 727.
- (227) Kohno, H.; Takeda, S. *Appl. Phys. Lett.* **1998**, *73*, 3144.
- (228) Qi, J. F.; Masumoto, Y. *Mater. Res. Bull.* **2001**, *36*, 1407.
- (229) Lago, R. M.; Tsang, S. C.; Lu, K. L.; Chen, Y. K.; Green, M. L. H. *J. Chem. Soc., Chem. Commun.* **1995**, 1355.
- (230) Che, G. L.; Lakshmi, B. B.; Martin, C. R.; Fisher, E. R. *Langmuir* **1999**, *15*, 750.
- (231) Satishkumar, B. C.; Vogl, E. M.; Govindaraj, A.; Rao, C. N. R. *J. Phys. D: Appl. Phys.* **1996**, *29*, 3173.
- (232) Jiang, K. Y.; Eitan, A.; Schadler, L. S.; Ajayan, P. M.; Siegel, R. W.; Grobert, N.; Mayne, M.; Reyes-Reyes, M.; Terrones, H.; Terrones, M. *Nano Lett.* **2003**, *3*, 275.
- (233) Haremza, J. M.; Hahn, M. A.; Krauss, T. D. *Nano Lett.* **2002**, *2*, 1253.
- (234) Svrcek, V.; Pham-Huu, C.; Ledoux, M. J.; Le Normand, F.; Ersen, O.; Joulie, S. *Appl. Phys. Lett.* **2006**, *88*, 033112.
- (235) Wang, J. W.; Kuimova, M. K.; Poliakoff, M.; Briggs, G. A. D.; Khlobystov, A. N. *Angew. Chem., Int. Ed.* **2006**, *45*, 5188.
- (236) Morgan, D. A.; Sloan, J.; Green, M. L. H. *Chem. Commun. (Cambridge)* **2002**, 2442.
- (237) Khlobystov, A. N.; Britz, D. A.; Briggs, G. A. D. *Acc. Chem. Res.* **2005**, *38*, 901.
- (238) Smith, B. W.; Monthieux, M.; Luzzi, D. E. *Nature* **1998**, *396*, 323.
- (239) Ulbricht, H.; Moos, G.; Hertel, T. *Phys. Rev. Lett.* **2003**, *90*, 095501.
- (240) Pickett, G. T.; Gross, M.; Okuyama, H. *Phys. Rev. Lett.* **2000**, *85*, 3652.
- (241) Hodak, M.; Girifalco, L. A. *Phys. Rev. B* **2003**, *67*, 075419.
- (242) Hodak, M.; Girifalco, L. A. *Phys. Rev. B* **2003**, *68*, 085405.
- (243) Khlobystov, A. N.; Porfyakis, K.; Kanai, M.; Britz, D. A.; Ardavan, A.; Shinohara, H.; Dennis, T. J. S.; Briggs, G. A. D. *Angew. Chem., Int. Ed.* **2004**, *43*, 1386.
- (244) Smith, B. W.; Luzzi, D. E.; Achiba, Y. *Chem. Phys. Lett.* **2000**, *331*, 137.
- (245) Khlobystov, A. N.; Britz, D. A.; Wang, J. W.; O'Neil, S. A.; Poliakoff, M.; Briggs, G. A. D. *J. Mater. Chem.* **2004**, *14*, 2852.
- (246) Britz, D. A.; Khlobystov, A. N.; Porfyakis, K.; Ardavan, A.; Briggs, G. A. D. *Chem. Commun. (Cambridge)* **2005**, 37.
- (247) Sloan, J.; Kirkland, A. I.; Hutchison, J. L.; Green, M. L. H. *Acc. Chem. Res.* **2002**, *35*, 1054.
- (248) Sloan, J.; Novotny, M. C.; Bailey, S. R.; Brown, G.; Xu, C.; Williams, V. C.; Friedrichs, S.; Flahaut, E.; Callender, R. L.; York, A. P. E. *Chem. Phys. Lett.* **2000**, *329*, 61.
- (249) Meyer, R. R.; Sloan, J.; Dunin-Borkowski, R. E.; Kirkland, A. I.; Novotny, M. C.; Bailey, S. R.; Hutchison, J. L.; Green, M. L. H. *Science* **2000**, *289*, 1324.
- (250) Sloan, J.; Wright, D. M.; Woo, H. G.; Bailey, S.; Brown, G.; York, A. P. E.; Coleman, K. S.; Hutchison, J. L.; Green, M. L. H. *Chem. Commun. (Cambridge)* **1999**, 699.
- (251) Friedrichs, S.; Sloan, J.; Green, M. L. H.; Hutchison, J. L.; Meyer, R. R.; Kirkland, A. I. *Phys. Rev. B* **2001**, *64*, 045406.
- (252) Hirahara, K.; Bando, S.; Suenaga, K.; Kato, H.; Okazaki, T.; Shinohara, H.; Iijima, S. *Phys. Rev. B* **2001**, *64*, 115420.
- (253) Dai, H. J.; Wong, E. W.; Lu, Y. Z.; Fan, S. S.; Lieber, C. M. *Nature* **1995**, *375*, 769.
- (254) Han, W. Q.; Fan, S. S.; Li, Q. Q.; Hu, Y. D. *Science* **1997**, *277*, 1287.
- (255) Zhang, Y.; Suenaga, K.; Colliex, C.; Iijima, S. *Science* **1998**, *281*, 973.
- (256) Gudiksen, M. S.; Lathon, L. J.; Wang, J.; Smith, D. C.; Lieber, C. M. *Nature* **2002**, *415*, 617.
- (257) Wu, Y. Y.; Fan, R.; Yang, P. D. *Nano Lett.* **2002**, *2*, 83.
- (258) Wu, Y.; Xiang, J.; Yang, C.; Lu, W.; Lieber, C. M. *Nature* **2004**, *430*, 61.
- (259) Hu, J. T.; Min, O. Y.; Yang, P. D.; Lieber, C. M. *Nature* **1999**, *399*, 48.
- (260) Zhan, J. H.; Bando, Y.; Hu, J. Q.; Liu, Z. W.; Yin, L. W.; Golberg, D. *Angew. Chem., Int. Ed.* **2005**, *44*, 2140.
- (261) Meng, X. M.; Hu, J. Q.; Jiang, Y.; Lee, C. S.; Lee, S. T. *Appl. Phys. Lett.* **2003**, *83*, 2241.
- (262) Zhou, X. T.; Zhang, R. Q.; Peng, H. Y.; Shang, N. G.; Wang, N.; Bello, I.; Lee, C. S.; Lee, S. T. *Chem. Phys. Lett.* **2000**, *332*, 215.
- (263) Lathon, L. J.; Gudiksen, M. S.; Wang, C. L.; Lieber, C. M. *Nature* **2002**, *420*, 57.
- (264) Hull, R.; Bean, J. C., Ed. *Germanium Silicon: Physics and Materials*; Academic: San Diego, 1999.
- (265) Wang, Z. Y.; Coffey, J. L. *Nano Lett.* **2002**, *2*, 1303.
- (266) Li, Q.; Wang, C. R. *J. Am. Chem. Soc.* **2003**, *125*, 9892.
- (267) Shi, W. S.; Peng, H. Y.; Xu, L.; Wang, N.; Tang, Y. H.; Lee, S. T. *Adv. Mater.* **2000**, *12*, 1927.
- (268) Choi, H. J.; Shin, J. H.; Suh, K.; Seong, H. K.; Han, H. C.; Lee, J. C. *Nano Lett.* **2005**, *5*, 2432.
- (269) Hu, J. Q.; Bando, Y.; Liu, Z. W.; Sekiguchi, T.; Golberg, D.; Zhan, J. H. *J. Am. Chem. Soc.* **2003**, *125*, 11306.
- (270) Zhan, J. H.; Bando, Y.; Hu, J. Q.; Sekiguchi, T.; Golberg, D. *Adv. Mater.* **2005**, *17*, 225.
- (271) Williams, R. S.; Medeiros-Ribeiro, G.; Kamins, T. I.; Ohlberg, D. A. *Ann. Rev. Phys. Chem.* **2000**, *51*, 527.
- (272) Voigtlander, B. *Surf. Sci. Rep.* **2001**, *43*, 127.
- (273) Hoepfener, S.; Maoz, R.; Cohen, S. R.; Chi, L. F.; Fuchs, H.; Sagiv, J. *Adv. Mater.* **2002**, *14*, 1036.
- (274) Liu, F.; Lagally, M. G. *Surf. Sci.* **1997**, *386*, 169.
- (275) Ogino, T.; Hibino, H.; Homma, Y.; Kobayashi, Y.; Prabhakaran, K.; Sumitomo, K.; Omi, H. *Acc. Chem. Res.* **1999**, *32*, 447.
- (276) Mo, Y. W.; Savage, D. E.; Swartzentruber, B. S.; Lagally, M. G. *Phys. Rev. Lett.* **1990**, *65*, 1020.
- (277) Ross, F. M.; Tersoff, J.; Tromp, R. M. *Phys. Rev. Lett.* **1998**, *80*, 984.
- (278) Kamins, T. I.; Carr, E. C.; Williams, R. S.; Rosner, S. J. *J. Appl. Phys.* **1997**, *81*, 211.
- (279) Hibino, H.; Shimizu, N.; Shinoda, Y. *J. Vac. Sci. Technol., A* **1993**, *11*, 2458.
- (280) Hibino, H.; Shimizu, N.; Shinoda, Y.; Ogino, T. *Mater. Res. Soc. Symp. Proc.* **1994**, *317*, 41.
- (281) Maoz, R.; Frydman, E.; Cohen, S. R.; Sagiv, J. *Adv. Mater.* **2000**, *12*, 725.
- (282) Maoz, R.; Frydman, E.; Cohen, S. R.; Sagiv, J. *Adv. Mater.* **2000**, *12*, 424.
- (283) Suto, S.; Sakamoto, K.; Wakita, T.; Hu, C.-W.; Kasuya, A. *Phys. Rev. B* **1997**, *56*, 7439.
- (284) Chen, D.; Sarid, D. *Surf. Sci. Rep.* **1995**, *329*, 206.
- (285) Klyachko, D.; Chen, D. M. *Phys. Rev. Lett.* **1995**, *75*, 3693.
- (286) Hashizume, T.; Wang, X. D.; Nishina, Y.; Shinohara, H.; Saito, Y.; Kuk, Y.; Sakurai, T. *Jpn. J. Appl. Phys.* **1992**, *31*, 880.
- (287) Suto, S.; Sakamoto, K.; Kondo, D.; Wakita, T.; Kimura, A.; Kakizaki, A. *Surf. Sci. Rep.* **1999**, *427-428*, 85.
- (288) Moriarty, P.; Upward, M. D.; Dunn, A. W.; Ma, Y.-R.; Beton, P. H.; Teehan, D. *Phys. Rev. B* **1998**, *57*, 362.
- (289) Seta, M. D.; Sanvitto, D.; Evangelisti, F. *Phys. Rev. B* **1999**, *59*, 9878.
- (290) Sakamoto, K.; Kondo, D.; Harada, M.; Kimura, A.; Kakizaki, A.; Suto, S. *Surf. Sci. Rep.* **1999**, *433-435*, 642.
- (291) Kondo, D.; Sakamoto, K.; Takeda, H.; Matsui, F.; Amemiya, K.; Ohta, T.; Uchida, W.; Kasuya, A. *Surf. Sci.* **2002**, *514*, 337.
- (292) Kondo, D.; Sakamoto, K.; Takeda, H.; Matsui, F.; Ohta, T.; Amemiya, K.; Uchida, W.; Kasuya, A. *J. Synchrotron Radiat.* **2001**, *8*, 505.
- (293) Sakamoto, K.; Kondo, D.; Takeda, H.; Sato, T.; Suga, S.; Matsui, F.; Amemiya, K.; Ohta, T.; Uchida, W.; Kasuya, A. *Surf. Sci.* **2001**, *493*, 604.
- (294) Hill, I. G.; McLean, A. B. *Phys. Rev. Lett.* **1999**, *82*, 2155.
- (295) Li, J. L.; Liang, X. J.; Jia, J. F.; Liu, X.; Wang, J. Z.; Wang, E. G.; Xue, Q. K. *Appl. Phys. Lett.* **2001**, *79*, 2826.
- (296) Miki, K.; Bowler, D. R.; Owen, J. H. G.; Briggs, G. A. D.; Sakamoto, K. *Phys. Rev. B* **1999**, *59*, 14868.
- (297) Shen, T. C.; Wang, C.; Tucker, J. R. *Phys. Rev. Lett.* **1997**, *78*, 1271.
- (298) Wang, J. Z.; Jia, J. F.; Liu, X.; Chen, W. D.; Xue, Q. K. *Phys. Rev. B* **2002**, *65*, 235303.
- (299) Zhachuk, R. A.; Teys, S. A.; Dolbak, A. E.; Olshanetsky, B. Z. *Surf. Sci. Rep.* **2004**, *565*, 37.
- (300) Stubenrauch, M.; Fischer, M.; Kremin, C.; Stoebenau, S.; Albrecht, A.; Nagel, O. *J. Micromech. Microeng.* **2006**, *16*, S82.
- (301) Kamins, T. I.; Li, X.; Williams, R. S. *Nano Lett.* **2004**, *4*, 503.
- (302) Martensson, T.; Svensson, C. P. T.; Wacaser, B. A.; Larsson, M. W.; Seifert, W.; Deppert, K.; Gustafsson, A.; Wallenberg, L. R.; Samuelson, L. *Nano Lett.* **2004**, *4*, 1987.
- (303) Li, W. Z.; Xie, S. S.; Qian, L. X.; Chang, B. H.; Zou, B. S.; Zhou, W. Y.; Zhao, R. A.; Wang, G. *Science* **1996**, *274*, 1701.

- (304) Su, M.; Li, Y.; Maynor, B.; Buldum, A.; Lu, J. P.; Liu, J. *J. Phys. Chem. B* **2000**, *104*, 6505.
- (305) Fan, S. S.; Chapline, M. G.; Franklin, N. R.; Tomblor, T. W.; Cassell, A. M.; Dai, H. J. *Science* **1999**, *283*, 512.
- (306) Mu, C.; Yn, Y. X.; Wang, R. M.; Wu, K.; Xu, D. S.; Guo, G. L. *Adv. Mater.* **2004**, *16*, 1550.
- (307) Schaffler, F. *Semicond. Sci. Technol.* **1997**, *12*, 1515.
- (308) Brunner, K. *Rep. Prog. Phys.* **2002**, *65*, 27.
- (309) Whall, T. E.; Parker, E. H. C. *Thin Solid Films* **2000**, *367*, 250.
- (310) Whall, T. E.; Parker, E. H. C. *J. Phys. D: Appl. Phys.* **1998**, *31*, 1397.
- (311) Xia, J. B.; Cheah, K. W. *Phys. Rev. B* **1997**, *56*, 14925.
- (312) Saeta, P. N.; Gallagher, A. C. *Phys. Rev. B* **1997**, *55*, 4563.
- (313) (a) Wang, P. J.; Fang, F. C.; Meyerson, B. S.; Nocera, J.; Parker, B. *Appl. Phys. Lett.* **1989**, *54*, 2701. (b) Ismail, K.; Le Goues, F. K.; Saenger, K. L.; Arafa, M.; Chu, J. O.; Mooney, P. M.; Meyerson, B. S. *Phys. Rev. Lett.* **1994**, *73*, 3447.
- (314) (a) Leskela, M.; Ritala, M. *Thin Solid Films* **2002**, *409*, 138. (b) Ritala, M.; Leskela, M. *Nanotechnology* **1999**, *10*, 19.
- (315) Steigmeier, E. F.; Morf, R.; Grutzmacher, D.; Auderset, H.; Delley, B.; Wessicken, R. *Appl. Phys. Lett.* **1996**, *69*, 4165.
- (316) Eigler, D. M.; Schweizer, E. K. *Nature* **1990**, *344*, 524.
- (317) Avouris, P. *Acc. Chem. Res.* **1995**, *28*, 95.
- (318) Lieber, C. M.; Kim, Y. *Adv. Mater.* **1993**, *5*, 392.
- (319) Requiha, A. A. G. *Proc. IEEE* **2003**, *91*, 1922.
- (320) Wang, Y.; Tang, Z. Y.; Kotov, N. A. *Abstr. Pap.—Am. Chem. Soc.* **2004**, *227*, U844.
- (321) Rubio-Sierra, F. J.; Heckl, W. M.; Stark, R. W. *Adv. Eng. Mater.* **2005**, *7*, 193.
- (322) Fahlbusch, S.; Mazerolle, S.; Breguet, J. M.; Steinecker, A.; Agnus, J.; Perez, R.; Michler, J. *J. Mater. Process. Technol.* **2005**, *167*, 371.
- (323) Li, X. D.; Wang, X. N.; Xiong, Q. H.; Eklund, P. C. *Appl. Phys. Lett.* **2005**, *87*, 233113.
- (324) Hsu, J. H.; Huang, M. H.; Lin, H. H.; Lin, H. N. *Nanotechnology* **2006**, *17*, 170.
- (325) Grier, D. G. *Nature* **2003**, *424*, 810.
- (326) Ashkin, A.; Dziedzic, J. M.; Bjorkholm, J. E.; Chu, S. *Opt. Lett.* **1986**, *11*, 288.
- (327) Ashkin, A. *Proc. Natl. Acad. Sci. U.S.A.* **1997**, *94*, 4853.
- (328) Ashkin, A. *IEEE J. Sel. Top. Quantum Electron.* **2000**, *6*, 841.
- (329) Svoboda, K.; Block, S. M. *Opt. Lett.* **1994**, *19*, 930.
- (330) Ke, P. C.; Gu, M. *Appl. Opt.* **1999**, *38*, 160.
- (331) Ghislain, L. P.; Switz, N. A.; Webb, W. W. *Rev. Sci. Instrum.* **1994**, *65*, 2762.
- (332) Rohrbach, A.; Stelzer, E. H. K. *Appl. Opt.* **2002**, *41*, 2494.
- (333) Litvinov, R. I.; Shuman, H.; Bennett, J. S.; Weisel, J. W. *Proc. Natl. Acad. Sci. U.S.A.* **2002**, *99*, 7426.
- (334) Gittes, F.; Schmidt, C. F. *Methods Cell Biol.* **1998**, *55*, 129.
- (335) Gittes, F.; Schmidt, C. F. *Opt. Lett.* **1998**, *23*, 7.
- (336) Pralle, A.; Prummer, M.; Florin, E. L.; Stelzer, E. H. K.; Horber, J. K. H. *Microsc. Res. Tech.* **1999**, *44*, 378.
- (337) Whang, D.; Jin, S.; Wu, Y.; Lieber, C. M. *Nano Lett.* **2003**, *3*, 1255.
- (338) Whang, D.; Jin, S.; Lieber, C. M. *Nano Lett.* **2003**, *3*, 951.
- (339) Jin, S.; Whang, D. M.; McAlpine, M. C.; Friedman, R. S.; Wu, Y.; Lieber, C. M. *Nano Lett.* **2004**, *4*, 915.
- (340) Tao, A.; Kim, F.; Hess, C.; Goldberger, J.; He, R. R.; Sun, Y. G.; Xia, Y. N.; Yang, P. D. *Nano Lett.* **2003**, *3*, 1229.
- (341) Duan, X. F.; Huang, Y.; Cui, Y.; Wang, J. F.; Lieber, C. M. *Nature* **2001**, *409*, 66.
- (342) Huang, Y.; Duan, X. F.; Wei, Q. Q.; Lieber, C. M. *Science* **2001**, *291*, 630.
- (343) Chou, S. Y.; Krauss, P. R.; Renstrom, P. J. *Science* **1996**, *272*, 85.
- (344) Chou, S. Y.; Krauss, P. R.; Renstrom, P. J. *J. Vac. Sci. Technol., B* **1996**, *14*, 4129.
- (345) Chou, S. Y. *MRS Bull.* **2001**, *26*, 512.
- (346) Colburn, M.; Johnson, S.; Stewart, M.; Damle, S.; Bailey, T. C.; Choi, B.; Wedlake, M.; Michaelson, T.; Sreenivasan, S. V.; Ekerdt, J.; Willson, C. G. *Proc. SPIE-Int. Soc. Opt. Eng.* **1999**, *3676*, 379.
- (347) Smith, B. J.; Stacey, N. A.; Donnelly, J. P.; Onsongo, D. M.; Bailey, T. C.; Mackay, C. J.; Resnick, D. J.; Dauksher, W. J.; Mancini, D. P.; Nordquist, K. J.; Sreenivasan, S. V.; Banerjee, S. K.; Ekerdt, J. G.; Willson, C. G. *Proc. SPIE-Int. Soc. Opt. Eng.* **2003**, *5037*, 1029.
- (348) Colburn, M.; Grot, A.; Amistoso, M. N.; Choi, B. J.; Bailey, T. C.; Ekerdt, J. G.; Sreenivasan, S. V.; Hollenhorst, J.; Willson, C. G. *Proc. SPIE-Int. Soc. Opt. Eng.* **2000**, *3997*, 453.
- (349) Piner, R. D.; Zhu, J.; Xu, F.; Hong, S. H.; Mirkin, C. A. *Science* **1999**, *283*, 661.
- (350) Ginger, D. S.; Zhang, H.; Mirkin, C. A. *Angew. Chem., Int. Ed.* **2004**, *43*, 30.
- (351) Wouters, D.; Schubert, U. S. *Angew. Chem., Int. Ed.* **2004**, *43*, 2480.
- (352) Kramer, S.; Fuierer, R. R.; Gorman, C. B. *Chem. Rev.* **2003**, *103*, 4367.
- (353) Aizenberg, J.; Black, A. J.; Whitesides, G. M. *Nature* **1999**, *398*, 495.
- (354) Aizenberg, J.; Black, A. J.; Whitesides, G. M. *Nature* **1998**, *394*, 868.
- (355) Pfeiffer, L.; West, K. W.; Stormer, H. L.; Eisenstein, J. P.; Baldwin, K. W.; Gershoni, D.; Spector, J. *Appl. Phys. Lett.* **1990**, *56*, 1697.
- (356) Flanders, D. C.; White, A. E. *J. Vac. Sci. Technol.* **1981**, *19*, 892.
- (357) Melosh, N. A.; Boukai, A.; Diana, F.; Gerardot, B.; Badolato, A.; Petroff, P. M.; Heath, J. R. *Science* **2003**, *300*, 112.
- (358) Gates, B. D.; Xu, Q. B.; Thalladi, V. R.; Cao, T. B.; Knickerbocker, T.; Whitesides, G. M. *Angew. Chem., Int. Ed.* **2004**, *43*, 2780.
- (359) Xu, Q. B.; Gates, B. D.; Whitesides, G. M. *J. Am. Chem. Soc.* **2004**, *126*, 1332.
- (360) Zach, M. P.; Ng, K. H.; Penner, R. M. *Science* **2000**, *290*, 2120.
- (361) Austin, M. D.; Ge, H. X.; Wu, W.; Li, M. T.; Yu, Z. N.; Wasserman, D.; Lyon, S. A.; Chou, S. Y. *Appl. Phys. Lett.* **2004**, *84*, 5299.
- (362) Austin, M. D.; Zhang, W.; Ge, H. X.; Wasserman, D.; Lyon, S. A.; Chou, S. Y. *Nanotechnology* **2005**, *16*, 1058.
- (363) Chou, S. Y. *Proc. IEEE* **1997**, *85*, 652.
- (364) Gates, B. D.; Xu, Q. B.; Stewart, M.; Ryan, D.; Willson, C. G.; Whitesides, G. M. *Chem. Rev.* **2005**, *105*, 1171.
- (365) Gates, B. D.; Xu, Q. B.; Love, J. C.; Wolfe, D. B.; Whitesides, G. M. *Annu. Rev. Mater. Res.* **2004**, *34*, 339.
- (366) Bratton, D.; Yang, D.; Dai, J. Y.; Ober, C. K. *Polym. Adv. Technol.* **2006**, *17*, 94.
- (367) Kleimann, P.; Badel, X.; Linnros, J. *Appl. Phys. Lett.* **2005**, *86*, 183108.
- (368) Choi, D. G.; Kirn, S.; Lee, E.; Yang, S. M. *J. Am. Chem. Soc.* **2005**, *127*, 1636.
- (369) Buuren, T. V.; Gao, Y.; Tiedje, T.; Dahn, J. R.; Way, B. M. *Appl. Phys. Lett.* **1992**, *60*, 3013.
- (370) Sham, T. K.; Jiang, D. T.; Coulthard, I.; Lorimer, J. W. Feng, X. H.; Tan, K. H.; Frigo, S. P.; Rosenberg, R. A.; Houghton, D. C.; Bryskiewicz, B. *Nature* **1993**, *363*, 331.
- (371) Littau, K. A.; Szajowski, P. J.; Muller, A. J.; Kortan, A. R.; Brus, L. E. *J. Phys. Chem.* **1993**, *97*, 1224.
- (372) Batson, P. E.; Heath, J. R. *Phys. Rev. Lett.* **1993**, *71*, 911.
- (373) Wilcoxon, J. P.; Samara, G. A. *Appl. Phys. Lett.* **1999**, *74*, 3164.
- (374) Lu, Z. H.; Lockwood, D. J.; Barbeau, J. M. *Nature* **1995**, *378*, 258.
- (375) Sun, X. H.; Tang, Y. H.; Zhang, P.; Naftel, S. J.; Sammynaiken, R.; Sham, T. K.; Peng, H. Y.; Zhang, Y. F.; Wong, N. B.; Lee, S. T. *J. Appl. Phys.* **2001**, *90*, 6379.
- (376) Sham, T. K.; Naftel, S. J.; Kim, P. S. G.; Sammynaiken, R.; Tang, Y. H.; Coulthard, I.; Moewes, A.; Freeland, J. W.; Hu, Y. F.; Lee, S. T. *Phys. Rev. B* **2004**, *70*, 045313.
- (377) Tilke, A. T.; Simmel, F. C.; Lorenz, H.; Blick, R. H.; Kotthaus, J. P. *Phys. Rev. B* **2003**, *68*, 075311.
- (378) Zhao, X. Y.; Wei, C. M.; Yang, L.; Chou, M. Y. *Phys. Rev. Lett.* **2004**, *92*, 236805.
- (379) Gilliland, G. D. *Mater. Sci. Eng., R* **1997**, *18*, 99.
- (380) Kanemitsu, Y. *Phys. Rep.* **1995**, *263*, 1.
- (381) Ludwig, M. H. *Crit. Rev. Solid State Mater. Sci.* **1996**, *21*, 265.
- (382) Kovalev, D.; Heckler, H.; Polisski, G.; Koch, F. *Phys. Status Solidi B* **1999**, *215*, 871.
- (383) Yu, D. P.; Hang, Q. L.; Ding, Y.; Zhang, H. Z.; Bai, Z. G.; Wang, J. J.; Zou, Y. H.; Qian, W.; Xiong, G. C.; Feng, S. Q. *Appl. Phys. Lett.* **1998**, *73*, 3076.
- (384) Ogüt, S.; Chelikowski, J. R.; Louie, S. G. *Phys. Rev. Lett.* **1997**, *79*, 1770.
- (385) Allan, G.; Delerue, C.; Lannoo, M. *Phys. Rev. Lett.* **1996**, *76*, 2961.
- (386) Baughman, R. H.; Zakhidov, A. A.; de Heer, W. A. *Science* **2002**, *297*, 787.
- (387) Tans, S. J.; Verschueren, A. R. M.; Dekker, C. *Nature* **1998**, *393*, 49.
- (388) Bachtold, A.; Hadley, P.; Nakanishi, T.; Dekker, C. *Science* **2001**, *294*, 1317.
- (389) Kim, P.; Lieber, C. M. *Science* **1999**, *286*, 2148.
- (390) Kong, J.; Franklin, N. R.; Zhou, C. W.; Chapline, M. G.; Peng, S.; Cho, K. J.; Dai, H. J. *Science* **2000**, *287*, 622.
- (391) Huang, M. H.; Mao, S.; Feick, H.; Yan, H. Q.; Wu, Y. Y.; Kind, H.; Weber, E.; Russo, R.; Yang, P. D. *Science* **2001**, *292*, 1897.
- (392) ITRS *International Technology Roadmaps for Semiconductors*, JEITA, Japan, 2005.
- (393) ITRS *Lithography*; JEITA, Japan, 2005.
- (394) Tsutsumi, T.; Suzuki, E.; Ishii, K.; Hiroshima, H.; Yamanaka, M.; Sakata, I.; Hazra, S.; Tomizawa, K. *Superlattices Microstruct.* **2000**, *28*, 453.
- (395) Kastner, M. A. *Rev. Mod. Phys.* **1992**, *64*, 849.
- (396) Gosser, K.; Dienststuhl, J.; Glosekotter, P. *Nanoelectronics and Nanosystems: From Transistors to Molecular and Quantum Devices*; Springer: Berlin, 2004.
- (397) Smith, P. A.; Nordquist, C. D.; Jackson, T. N.; Mayer, T. S.; Martin, B. R.; Mbindyo, J.; Mallouk, T. E. *Appl. Phys. Lett.* **2000**, *77*, 1399.



- (398) Diehl, M. R.; Yaliraki, S. N.; Beckman, R. A.; Barahona, M.; Heath, J. R. *Angew. Chem., Int. Ed.* **2001**, *41*, 353.
- (399) Messer, B.; Song, J. H.; Yang, P. D. *J. Am. Chem. Soc.* **2000**, *122*, 10232.
- (400) (a) Christiansen, C. *The Innovator's Dilemma*; Harvard Business School Press: Boston, 1997. (b) Jackson, J. *Disruptive Technologies, Wash. Technol.* **2003**, *17*, 20.
- (401) Teo, B. K.; Sun, X. H. *J. Cluster Sci.* **2006**, *17*, 529.
- (402) Lehn, J. M. *Science* **1993**, *260*, 1762.
- (403) Divincenzo, D. P. *Science* **1995**, *270*, 255.
- (404) Jaeger, G. *Quantum Information: An Overview*; Springer: Berlin, 2006.
- (405) Guo, L. J.; Leobandung, E.; Chou, S. Y. *Science* **1997**, *275*, 649.
- (406) GoldhaberGordon, D.; Montemerlo, M. S.; Love, J. C.; Opiteck, G. J.; Ellenbogen, J. C. *Proc. IEEE* **1997**, *85*, 521.
- (407) Takahashi, Y.; Ono, Y.; Fujiwara, A.; Inokawa, H. *J. Phys.: Condens. Matter* **2002**, *14*, R995.
- (408) Krieger, Y. G. *J. Struct. Chem.* **1993**, *34*, 896.
- (409) Martel, R.; Schmidt, T.; Shea, H. R.; Hertel, T.; Avouris, P. *Appl. Phys. Lett.* **1998**, *73*, 2447.
- (410) Tans, S. J.; Devoret, M. H.; Dai, H. J.; Thess, A.; Smalley, R. E.; Geerligs, L. J.; Dekker, C. *Nature* **1997**, *386*, 474.
- (411) Bockrath, M.; Cobden, D. H.; McEuen, P. L.; Chopra, N. G.; Zettl, A.; Thess, A.; Smalley, R. E. *Science* **1997**, *275*, 1922.
- (412) Yao, Z.; Postma, H. W. C.; Balents, L.; Dekker, C. *Nature* **1999**, *402*, 273.
- (413) Guo, L.; Ji, Y. L.; Xu, H. B.; Wu, Z. Y.; Simon, P. J. *Mater. Chem.* **2003**, *13*, 754.
- (414) Huang, Y.; Duan, X. F.; Cui, Y.; Lauhon, L. J.; Kim, K. H.; Lieber, C. M. *Science* **2001**, *294*, 1313.
- (415) Duan, X. F.; Huang, Y.; Lieber, C. M. *Nano Lett.* **2002**, *2*, 487.
- (416) Lieber, C. M. *MRS Bull.* **2003**, *28*, 486.
- (417) Huang, Y.; Lieber, C. M. *Pure Appl. Chem.* **2004**, *76*, 2051.
- (418) Duan, X. F.; Niu, C. M.; Sahi, V.; Chen, J.; Parce, J. W.; Empedocles, S.; Goldman, J. L. *Nature* **2003**, *425*, 274.
- (419) Soref, R. A. *Proc. IEEE* **1993**, *81*, 1687.
- (420) Koshida, N.; Matsumoto, N. *Mater. Sci. Eng., R* **2003**, *40*, 169.
- (421) Duan, X. F.; Huang, Y.; Agarwal, R.; Lieber, C. M. *Nature* **2003**, *421*, 241.
- (422) Huang, Y.; Duan, X. F.; Lieber, C. M. *Small* **2005**, *1*, 142.
- (423) Komode, T. Mitsushita Electric, Panasonic.
- (424) Lin, V. S. Y.; Motesharei, K.; Dancil, K. P. S.; Sailor, M. J.; Ghadiri, M. R. *Science* **1997**, *278*, 840.
- (425) Dancil, K. P. S.; Greiner, D. P.; Sailor, M. J. *J. Am. Chem. Soc.* **1999**, *121*, 7925.
- (426) Cui, Y.; Wei, Q. Q.; Park, H. K.; Lieber, C. M. *Science* **2001**, *293*, 1289.
- (427) Zhou, X. T.; Hu, J. Q.; Li, C. P.; Ma, D. D. D.; Lee, C. S.; Lee, S. T. *Chem. Phys. Lett.* **2003**, *369*, 220.
- (428) Shao, M. W.; Yao, H.; Zhang, M. L.; Wong, N. B.; Shan, Y. Y.; Lee, S. T. *Appl. Phys. Lett.* **2005**, *87*, 183106.
- (429) Shao, M. W.; Shan, Y. Y.; Wong, N. B.; Lee, S. T. *Adv. Funct. Mater.* **2005**, *15*, 1478.
- (430) Janata, J.; Blackburn, G. F. *Ann. N. Y. Acad. Sci.* **1984**, *428*, 286.
- (431) Janata, J. *Principles of Chemical Sensors*; Plenum Press: New York, 1989.
- (432) Wolf, S. A.; Awschalom, D. D.; Buhman, R. A.; Daughton, J. M.; von Molnar, S.; Roukes, M. L.; Chtchelkanova, A. Y.; Treger, D. M. *Science* **2001**, *294*, 1488.
- (433) Zutic, I.; Fabian, J.; Das Sarma, S. *Rev. Mod. Phys.* **2004**, *76*, 323.
- (434) Wolf, S. A.; Chtchelkanova, A. Y.; Treger, D. M. *IBM J. Res. Dev.* **2006**, *50*, 101.
- (435) Tanaka, M. *J. Cryst. Growth* **2005**, *278*, 25.
- (436) Moodera, J. S.; Mathon, G. *J. Magn. Magn. Mater.* **1999**, *200*, 248.
- (437) Moodera, J. S.; Nassar, J.; Mathon, G. *Annu. Rev. Mater. Sci.* **1999**, *29*, 381.
- (438) Hristoforou, E. J. *Optoelectron. Adv. Mater.* **2002**, *4*, 245.
- (439) Pearton, S. *Nat. Mater.* **2004**, *3*, 203.
- (440) Jansen, R. *J. Phys. D: Appl. Phys.* **2003**, *36*, R289.
- (441) Chambers, S. A.; Yoo, Y. K. *MRS Bull.* **2003**, *28*, 706.
- (442) Cibert, J.; Bobo, J. F.; Luders, U. C. *R. Phys.* **2005**, *6*, 977.
- (443) Dietl, T.; Ohno, H. *MRS Bull.* **2003**, *28*, 714.
- (444) Macdonald, A. H.; Schiffer, P.; Samarth, N. *Nat. Mater.* **2005**, *4*, 195.
- (445) Manyala, N.; Sidis, Y.; Ditusa, J. F.; Aeppli, G.; Young, D. P.; Fisk, Z. *Nat. Mater.* **2004**, *3*, 255.
- (446) Graeff, C. F. O.; Brandt, M. S.; Stutzmann, M.; Holzmann, M.; Abstreiter, G.; Schaffler, F. *Phys. Rev. B* **1999**, *59*, 13242.
- (447) Sandersfeld, N.; Jantsch, W.; Wilamowski, Z.; Schaffler, F. *Thin Solid Films* **2000**, *369*, 312.
- (448) Wilamowski, Z.; Jantsch, W. *Phys. Rev. B* **2004**, *69*, 035328.
- (449) Choi, H. J.; Seong, H. K.; Chang, J.; Lee, K. I.; Park, Y. J.; Kim, J. J.; Lee, S. K.; He, R. R.; Kuykendall, T.; Yang, P. D. *Adv. Mater.* **2005**, *17*, 1351.
- (450) Han, S. E.; Oh, H.; Kim, J. J.; Seong, H. K.; Choi, H. J. *Appl. Phys. Lett.* **2005**, *87*, 062102.
- (451) Ronning, C.; Gao, P. X.; Ding, Y.; Wang, Z. L.; Schwen, D. *Appl. Phys. Lett.* **2004**, *84*, 783.
- (452) Radovanovic, P. V.; Barrelet, C. J.; Gradecak, S.; Qian, F.; Lieber, C. M. *Nano Lett.* **2005**, *5*, 1407.
- (453) Wang, Q.; Sun, Q.; Jena, P. *Nano Lett.* **2005**, *5*, 1587.
- (454) Duan, J. H.; Yang, S. G.; Liu, H. W.; Gong, J. F.; Huang, H. B.; Zhao, X. N.; Tang, J. L.; Zhang, R.; Du, Y. W. *J. Cryst. Growth* **2005**, *283*, 291.
- (455) Ramlan, D. G.; May, S. J.; Zheng, J. G.; Allen, J. E.; Wessels, B. W.; Lauhon, L. J. *Nano Lett.* **2006**, *6*, 50.
- (456) Chang, Y. Q.; Wang, D. B.; Luo, X. H.; Xu, X. Y.; Chen, X. H.; Li, L.; Chen, C. P.; Wang, R. M.; Xu, J.; Yu, D. P. *Appl. Phys. Lett.* **2003**, *83*, 4020.
- (457) Hahm, J.; Lieber, C. M. *Nano Lett.* **2004**, *4*, 51.
- (458) Patolsky, F.; Zheng, G. F.; Hayden, O.; Lakadamyali, M.; Zhuang, X. W.; Lieber, C. M. *Proc. Natl. Acad. Sci. U.S.A.* **2004**, *101*, 14017.
- (459) Zheng, G. F.; Patolsky, F.; Cui, Y.; Wang, W. U.; Lieber, C. M. *Nat. Biotechnol.* **2005**, *23*, 1294.
- (460) Abbott, N. L.; Kumar, A.; Whitesides, G. M. *Chem. Mater.* **1994**, *6*, 596.
- (461) Xu, S.; Liu, G. Y. *Langmuir* **1997**, *13*, 127.
- (462) Liu, G. Y.; Xu, S.; Qian, Y. L. *Acc. Chem. Res.* **2000**, *33*, 457.
- (463) Lee, H. T.; Oh, J. S.; Park, S. J.; Park, K. H.; Ha, J. S.; Yoo, H. J.; Koo, J. Y. *J. Vac. Sci. Technol., A* **1997**, *15*, 1451.
- (464) Ara, M.; Graaf, H.; Tada, H. *Appl. Phys. Lett.* **2002**, *80*, 2565.
- (465) Lercel, M. J.; Redinbo, G. F.; Craighead, H. G.; Sheen, C. W.; Allara, D. L. *Appl. Phys. Lett.* **1994**, *65*, 974.
- (466) Perkins, F. K.; Dobisz, E. A.; Brandow, S. L.; Koloski, T. S.; Calvert, J. M.; Rhee, K. W.; Kosakowski, J. E.; Marrian, C. R. K. *J. Vac. Sci. Technol., B* **1994**, *12*, 3725.
- (467) Yang, L.; Lua, Y. Y.; Lee, M. V.; Linford, M. R. *Acc. Chem. Res.* **2005**, *38*, 933.
- (468) Soukiassian, L.; Mayne, A. J.; Carbone, M.; Dujardin, G. *Surf. Sci.* **2003**, *528*, 121.
- (469) Wang, Y. L.; Gao, H. J.; Guo, H. M.; Liu, H. W.; Batyrev, I. G.; McMahon, W. E.; Zhang, S. B. *Phys. Rev. B* **2004**, *70*, 073312.
- (470) Dobrin, S.; Lu, X. K.; Naumkin, F. Y.; Polanyi, J. C.; Yang, J. S. Y. *Surf. Sci.* **2004**, *573*, L363.
- (471) McNab, I. R.; Polanyi, J. C. *Chem. Rev.* **2006**, *106*, 4321.
- (472) Alavi, S.; Rousseau, R.; Lopinski, G. P.; Wolkow, R. A.; Seideman, T. *Faraday Discuss.* **2000**, *213*.
- (473) Avouris, P. *J. Phys. Chem.* **1990**, *94*, 2246.
- (474) Wolkow, R. A. *Annu. Rev. Phys. Chem.* **1999**, *50*, 413.
- (475) Hamers, R. J.; Coulter, S. K.; Ellison, M. D.; Hovis, J. S.; Padowitz, D. F.; Schwartz, M. P.; Greenleaf, C. M.; Russell, J. N. *Acc. Chem. Res.* **2000**, *33*, 617.
- (476) Rosei, F.; Schunack, M.; Naitoh, Y.; Jiang, P.; Gourdon, A.; Laegsgaard, E.; Stensgaard, I.; Joachim, C.; Besenbacher, F. *Prog. Surf. Sci.* **2003**, *71*, 95.
- (477) Eigler, D. M.; Schweizer, E. K. *Nature* **1990**, *344*, 524.
- (478) Dujardin, G.; Walkup, R. E.; Avouris, P. *Science* **1992**, *255*, 1232.
- (479) Nyffenegger, R. M.; Penner, R. M. *Chem. Rev.* **1997**, *97*, 1195.
- (480) Dujardin, G.; Mayne, A.; Robert, O.; Rose, F.; Joachim, C.; Tang, H. *Phys. Rev. Lett.* **1998**, *80*, 3085.
- (481) Mayne, A. J.; Dujardin, G.; Comtet, G.; Riedel, D. *Chem. Rev.* **2006**, *106*, 4355.
- (482) Mayne, A. J.; Lastapis, M.; Baffou, G.; Soukiassian, L.; Comtet, G.; Hellner, L.; Dujardin, G. *Phys. Rev. B* **2004**, *69*, 045409.
- (483) Cranney, M.; Mayne, A. J.; Laikhtman, A.; Comtet, G.; Dujardin, G. *Surf. Sci.* **2005**, *593*, 139.
- (484) Lastapis, M.; Martin, M.; Riedel, D.; Hellner, L.; Comtet, G.; Dujardin, G. *Science* **2005**, *308*, 1000.
- (485) Lu, P. H.; Polanyi, J. C.; Rogers, D. J. *Chem. Phys.* **1999**, *111*, 9905.
- (486) Sloan, P. A.; Hedouin, M. F. G.; Palmer, R. E.; Persson, M. *Phys. Rev. Lett.* **2003**, *91*, 118301.
- (487) Hla, S. W.; Bartels, L.; Meyer, G.; Rieder, K. H. *Phys. Rev. Lett.* **2000**, *85*, 2777.
- (488) Stipe, B. C.; Rezaei, M. A.; Ho, W. *Science* **1998**, *280*, 1732.
- (489) Lauhon, L. J.; Ho, W. *Phys. Rev. B* **1999**, *60*, R8525.
- (490) Whang, D.; Jin, S.; Lieber, C. M. *Jpn. J. Appl. Phys., Part 1* **2004**, *43*, 4465.
- (491) Shetty, R. *Nanotechnology: The Future in Medicine*, 2nd ed.; Mezcocore Technologies: Sainte Foy, Quebec, Canada, 2006.
- (492) Freitas, R. A. *Nanomedicine, Vol. I: Basic Capabilities*; Landes Bioscience: Georgetown, TX, 1999.